technische universität
dortmund

Dissertation zur Erlangung des
Doktorgrades der Naturwissenschaften

Applications and Extensions of Flow Equations to Closed and Open Quantum Systems

vorgelegt von
Gary Schmiedinghoff
geboren in Herdecke als Ferkinghoff

Condensed Matter Theory
Fakultät Physik
Technische Universität Dortmund

2022

Gutachter :	Prof. Dr. Götz S. Uhrig
	Prof. Dr. Frithjof Anders
	Prof. Dr. Kai P. Schmidt
Abgabedatum:	11. Juli 2022

Kurzfassung

Flussgleichungen, auch bekannt als kontinuierliche unitäre Transformationen, sind ein mächtiges Werkzeug, mit dem Hamilton-Operatoren und Observablen in eine effektive Basis transformiert werden können, wo sie eine zugänglichere Form annehmen. Jedoch versagen unitäre Transformationen häufig für nicht-Hermitesche Hamilton-Operatoren, die unter anderem in dissipativen Systemen auftauchen. Ferner haben Flussgleichungen oft Schwierigkeiten in der Nähe kritischer Punkte.

Diese Arbeit behandelt drei unabhängige Forschungsfragen zu Flussgleichungen:

Spinleitern sind zentrale Modelle für die Beschreibung stark korrelierter Quantensysteme. Eine weit entwickelte Methode zur Untersuchung solcher Systeme in zahlreichen Anregungskanälen ist resonante inelastische Röntgenstreuung, doch die theoretische Vorhersage der entsprechenden spektralen Dichten ist aufwendig. In dieser Arbeit berechnen wir die Spektraldichten einer Spin-1/2 Heisenberg-Leiter mit der Flussgleichungsmethode und sagen neuartige gebundene Drei-Triplon-Zustände voraus. Wir demonstrieren, dass diese gebundenen Zustände nur aufgrund von irreduziblen Drei-Triplon-Wechselwirkungen entstehen, indem wir die Vorteile unserer Methode ausnutzen.

Flussgleichungen versagen häufig in der Nähe von kritischen Punkten, da dort die Korrelationslänge divergiert. Die Methode könnte durch Anwendung im Impulsraum verbessert werden, da dort stark delokalisierte Physik leichter beschrieben werden kann. Hierzu untersuchen wir das Ising-Modell im transversalen Feld und zeigen, dass der Fluss zahlreicher Koeffizienten ein gemeinsames Konvergenzverhalten zeigt, was Aussicht auf deutliche Verbesserungen in zukünftigen Arbeiten gibt. Außerdem führen wir neue Trunkierungsschemata im Impulsraum ein, die nützlich für Niederenergiebeschreibungen sein können, und testen diese.

Ein weiteres Problem ist die Beschreibung offener Quantensysteme, das heißt Quantensysteme, die durch die Kopplung an ein externes Bad Dissipation erfahren. Dissipative Flussgleichungen bieten einen Rahmen, um die nicht-Hermiteschen Hamilton- und Lindblad-Operatoren zu behandeln, die in solchen Systemen auftauchen. Wir stellen einen neuartigen Generator vor, der auf dem teilchenzahlerhaltenden Generator aufbaut, und messen die Konvergenzgeschwindigkeit und die Genauigkeit bei Trunkierung im Vergleich zu Generatoren, die in der Vergangenheit vorgeschlagen worden sind. Wir zeigen, dass unser vorgeschlagener Generator hohe Konvergenzgeschwindigkeit und hervorragende Genauigkeit bietet. Darüber hinaus fassen wir die uns bekannten dissipativen Generatoren in ein allgemeines Schema zusammen, mit dem sich zahlreiche weitere Generatoren definieren lassen, die entweder auf bessere Konvergenzgeschwindigkeit oder Genauigkeit ausgelegt sind.

Abstract

Flow equations, also known as continuous unitary transformations, provide a powerful renormalization tool to transform a Hamiltonian and observables to an effective basis, where they take a more amenable form. However, unitary transformations often fail for non-Hermitian Hamiltonians, which appear, for instance, in dissipative systems. Furthermore, flow equation approaches often struggle in the vicinity of critical points.

This thesis aims to cover three separate problems regarding flow equations:

Spin ladders are crucial models for the description of strongly correlated quantum systems. An advanced method of probing such systems in various excitation channels is resonant inelastic X-ray scattering, but the theoretical prediction of the corresponding spectral densities is intricate. In this thesis, we compute the spectral densities of a spin-1/2 Heisenberg ladder with the flow equation method and predict novel three-triplon bound states. We demonstrate that these bound states only arise in the presence of irreducible three-triplon interactions by exploiting the strengths of our method.

Flow equations often fail in the vicinity of a critical point due to the divergent correlation length. The method could be improved by performing it in momentum space, where strongly delocalized physics can be described more easily. To this end, we investigate the transverse-field Ising model and show that the flows of various coefficients have a common convergence behavior, which offers a prospect for considerable improvements in future works. Additionally, we propose and test truncation schemes in momentum space, which could prove useful to describe low-energy physics.

Another current problem is the description of open quantum systems, i.e. quantum systems which are affected by dissipation because they couple to an external bath. Dissipative flow equations provide a framework to treat the non-Hermitian Hamiltonians and Lindbladians appearing in such systems. We propose a novel generator scheme based on the particle-conserving generator and benchmark the convergence speed and accuracy in spite of truncation compared to previously considered generators. We demonstrate that our proposed generator scheme provides high convergence speed and excellent accuracy. Furthermore, we encapsulate all currently known dissipative generator schemes in a universal framework, which can be used to propose various novel generator schemes favoring either convergence speed or accuracy.

Contents

Chapter 1

Motivation and Overview

Advances in the field of physics require a solid theoretical foundation and powerful theoretical tools, which can be used to predict novel phenomena. The scientific goal and the requirements for theoretical tools differ considerably between the various subfields of physics. For instance, a key goal of modern high energy physics is the discovery of a universal 'theory of everything' that describes the universe on a fundamental level. In condensed matter physics and specifically in the branch of solid-state physics, quantum mechanics already provides a microscopic theory on atomic and subatomic scales. The challenge of solid-state physics arises from the macroscopic number $N \approx 10^{23}$ of particles and the associated degrees of freedom. Even simple interactions between particles can lead to complex phenomena, which are not trivial to predict by understanding only the microscopic laws and material properties. The term 'emergence' has been introduced to describe such phenomena [1]. Some examples of emergent phenomena are magnetism, superconductivity and the various phases of ice. Complex behavior emerging from the interaction of seemingly simple microscopical constituents can also be observed outside of physics, for instance in the description of traffic jams, the spread of diseases, the planning of power grids or the formation of intelligence through a combination of macroscopically many (biological or artificial) neurons [1].

In principle, a description of emergent phenomena in a macroscopic system should be possible through a rigorous microscopical description. In practice, however, the microscopic differential equation systems are very complex and either not integrable inherently or too complicated to integrate. For instance, the Hilbert space of quantum mechanical solid-state systems either has infinite dimensions, for instance in the thermodynamic limit, or the number of dimensions increases exponentially with the number of particles. Historically, the development of powerful computer hardware and sophisticated numerical methods allowed for numerical solutions of various

physical systems, but in most cases only for relatively small system sizes. To tackle larger systems, physicists often resort to effective models, which only describe the most important degrees of freedom. The derivation of effective models, however, is not trivial. One can apply several strategies, such as perturbative expansions and other sophisticated approximations, which often incorporate educated guesses based on prior experience with similar problems. Universal schemes for finding effective models, especially for novel systems, can provide powerful tools for describing emergent phenomena in solid-state physics.

Such effective models in the field of solid-state physics are often obtained by utilizing the fact that solid materials have low temperature compared to the intrinsic energy scales of the material, so low energy processes dominate. Powerful tools to describe low-energy physics are provided by renormalization methods, which obtain an effective model by rescaling the system to low energies. By using these techniques, several systems can be categorized into universality classes which, despite their microscopical differences, exhibit the same macroscopic behavior close to the phase transition where the correlation length diverges [2]. However, typical scaling approaches suffer from the fact that high-energy contributions are neglected completely, which prevents them from describing phenomena such as high-temperature superconductivity or heavy fermions [3].

These scaling approaches can be generalized using a renormalized perturbative expansion retaining the full Hilbert space at the cost of a more complex set of scaling equations [3]. Such a generalization is provided by **continuous unitary transformations (CUT)**, also known as **flow equations**, which transform an initial Hamiltonian and observables continuously to their effective form. The method has been introduced by Wegner in 1994 for condensed matter physics [4] and independently by Glazek and Wilson for high-energy physics under the name of similarity renormalization scheme [5,6]. Similar flow equations have already been studied in 1990 by the mathematicians Brockett, Chu and Driessel who named the technique **double bracket flow** [7–9]. The CUT method has since been refined and applied to various fields of condensed matter physics including some strong-coupling problems.
For instance, flow equations have been applied successfully to the Anderson model [10, 11], the spin-boson model [12], electron-phonon interactions [13, 14], quantum systems including an environment [15, 16], spin chains with and without frustration [17–20], the quantum sine-Gordon models [21, 22], Shastry-Sutherland lattices [23], spin ladders in copper nitrate [24] and coupled spin ladders in the compound $BiCu_2PO_6$ [25]. Flow equations have also been applied in combination with other formalisms, such as Floquet theory [26, 27].

One challenge in the application of flow equations is the fact that the equations are not always closed or contain too many degrees of freedom. While renormalizing

generators that conserve band-diagonality [17, 28] tackle this problem, one often requires physically justifiable truncation schemes to obtain closed and numerically solvable flow equations. One can reduce the degrees of freedom with a description in second quantization [4], but even then a truncation scheme is typically necessary to reduce the number of tracked operators to a finite set of operator monomials. Various truncation schemes have been established, including schemes based on the range of processes in real-space [29], perturbation theory [17] or scaling arguments such as the operator product expansion [21, 22] or the scaling dimension [30, 31]. Truncations based on perturbative expansions have proven especially fruitful [32].

The aim of this thesis is to push the capabilities of the flow equation method further, both by applying it to calculate intricate spectroscopic properties and by introducing new CUT schemes. To that end, we study three different problems. First, we apply an established CUT scheme to predict novel phenomena that are observable with spectroscopic experiments. Second, a momentum-space scheme for hard-core particles is introduced, which aims to circumvent the limitations of conventional approaches close to the critical point. Third, an existing generator scheme is generalized to dissipative systems and non-Hermitian Hamiltonians. The following three sections introduce the three studied problems in more detail.

1.1 Dynamic Properties of Heisenberg Ladders

The inner structure and intrinsic forces of a solid-state system can be studied experimentally through scattering experiments like **inelastic neutron scattering (INS)** [33, 34]. Such experiments align a collimated beam of particles at a sample of the studied material and measure the intensities of the scattered particles. During the scattering process, the particles transfer a part of their kinetic energy and momentum to the sample. By examining the intensities resolved over various transferred momenta and energies and by comparing the data with theoretical predictions, important features of the material can be revealed. Spectral densities, which can be measured with such experiments for various observables, give insight into the density of elementary excitations and their interactions. For spin excitations, the INS method is limited to spin 1, i.e. the **non-spin-conserving (NSC)** channel.

In the past, the flow equation method has been used extensively to calculate spectral properties which can be observed by INS on quantum systems such as spin chains [35] and spin ladders [36]. While other methods such as exact diagonalization [37–40], numerical renormalization groups (NRG) [41] and density matrix renormalization groups (DMRG) [42, 43] can be used to compute spectral densities, the flow equation method offers some distinct advantages. For instance, flow equations allow the computation of true continua with high resolution instead of discrete

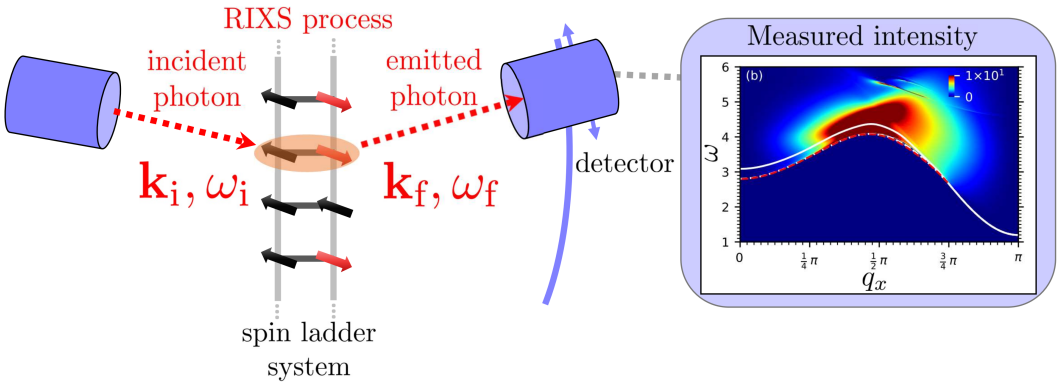

Figure 1.1: Schematic setup of RIXS experiment. The sample, e.g. a spin ladder material, is excited resonantly at the core-level energy of an electron by an incident photon with momentum $\mathbf{k}_\mathrm{i}$ and energy ω_i. A direct or indirect RIXS process (see Sec. 3.2.3 for details) occurs. The transferred momentum $\mathbf{q}$ and energy ω are determined by measuring the momentum $\mathbf{k}_\mathrm{f}$ and energy ω_f of the emitted photon.

energies. Furthermore, it is possible to select individual excitation channels and to selectively enable or disable irreducible multi-particle interactions [44].

An even more powerful method that has seen rapid progress is **resonant inelastic X-ray scattering (RIXS)**, where one scatters X-ray beams at a sample and tunes the energy to the X-ray transitions of core-level electrons to resonantly enhance the cross section [45–49]. Compared with INS, this method offer worse energy resolution, but covers a larger region of the scattering phase space, can resolve weaker signals, requires smaller sample volumes, and an X-ray radiation source is also cheaper to maintain than typical thermal neutron sources for INS [45]. Furthermore, one can probe the **spin-conserving (SC)** channel, which is not accessible by INS, allowing one to study additional excitations and discover novel physics. The theoretical prediction of the RIXS response, however, is more involved. It can be described with high accuracy by the leading orders of the **ultra-short core-hole lifetime (UCL) approximation** [37,45,47,48,50], which contain more complicated observables than the INS response. The experiment is outlined in Fig. 1.1 .

One aim of this thesis is to apply the flow equation method to calculate the response functions of a spin-1/2 Heisenberg ladder in RIXS and INS experiments. To achieve this, we compute the structure factor for both the SC and NSC observables relevant for RIXS. We predict three-triplon bound states for realistic spin ladders and propose materials and experimental settings to verify our findings. Moreover, we demonstrate that the three-triplon bound states only arise due to irreducible three-triplon interactions and discuss how these interactions arise during the CUT. Finally, we extend the calculations in the UCL approximation to the second leading order and discuss the arising new features.

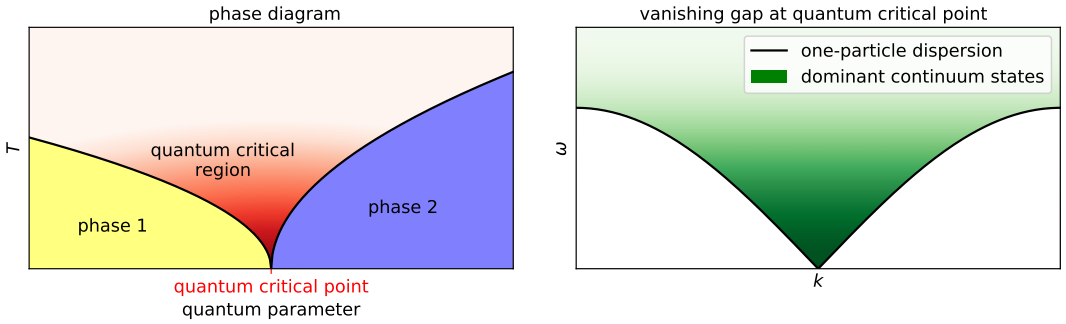

Figure 1.2: Left: Schematic phase diagram with a quantum critical point at vanishing temperature and a quantum critical region at finite temperature. Typical quantum parameters are coupling strengths or doping ratios. Such phase diagrams can be observed, for instance, for dimerized antiferromagnets [51]. Right: Gapless one-particle dispersion. Due to the vanishing gap, the lower edge of multi-particle continua coincides with or intersects the dispersion. The green coloring indicates that low-energy continuum states around the minimum of the dispersion dominate the low-temperature physics.

1.2 Momentum Space Flow Equations with Hard-Core Constraint

One central field of solid-state physics is the description of quantum criticality, i.e. the description of phase transitions governed by quantum fluctuations at zero temperature [51]. Quantum criticality is the norm rather than the exception for one-dimensional and quasi-one-dimensional systems [52]. One finds such systems in a diverse range of materials, such as carbon nanotubes, stripes in cuprate high-temperature superconductors, confined ultracold atomic gases and quantum spin chains [53]. At a second-order quantum phase transition, the correlation length ξ of the system diverges and local excitations can become maximally delocalized [54]. Fig. 1.2 schematically depicts the occurrence of a quantum critical point. Furthermore, gapless systems can arise when global continuous symmetries are broken by long-range order [55–57].

Many truncation schemes utilize the spatial extension of processes, i.e. local operators are considered during integration but strongly delocalized operators are truncated [58, 59]. This poses a problem close to critical points, where the diverging correlation length does not allow an accurate description with local operators. As a consequence, in many cases the flow does not converge or the physical properties are not captured correctly close to the second-order quantum phase transition.

To tackle this problem, one can employ a CUT in momentum space by performing a Fourier transformation before setting up the flow equations. Strongly delocalized processes in real space correspond to strongly localized processes in momentum space, allowing one to describe such delocalized processes with a finite amount of

operators in momentum space. One challenge of this approach is the fact that the initial Hamiltonian often contains interactions of small range in real-space, which are strongly delocalized in momentum space. This increases the amount of tracked contributions in momentum space significantly and therefore partially offsets the advantage of the momentum-space approach. For elementary excitations with trivial bosonic or fermionic operators, the commutation relation in real space is preserved in momentum space. More intricate excitations, such as hard-core bosons, can have distinctly more involved commutators in momentum space. This can increase the number of relevant processes further and render the application of flow equations in momentum space significantly more challenging.

In this work, we study the application of flow equations for hard-core bosons in momentum space. We discuss a one-dimensional Ising chain in a transverse magnetic field, which hosts hard-core bosonic excitations and a quantum critical point. We introduce truncation schemes in momentum space that could provide powerful tools in the future, but at the current stage do not offer significant improvements over other traditional truncation schemes. Furthermore, we investigate the asymptotic convergence behavior of non-particle-conserving operator terms in momentum space. Our computations show that they can be described with a small number of convergence exponents, which could lead to powerful analytical or numerical descriptions in the future.

1.3 Dissipative Flow Equations

One of the most fundamental approximations in physics is to model a system isolated from the rest of the universe. The assumption behind this is convincing: In many cases, the system of interest does not interact with the environment in a significant way or can be isolated well enough in an experimental setting. However, these interactions do not vanish completely and can still influence the system, i.e. by introducing dissipation. In quantum mechanics, such systems that are in interaction with an environment or bath are called open quantum systems [60]. One important difference to closed systems is the fact that in closed quantum systems the time evolution is unitary and its generator is the Hermitian Hamilton operator, also called Hamiltonian. Contrary to this, the most general description of open quantum systems

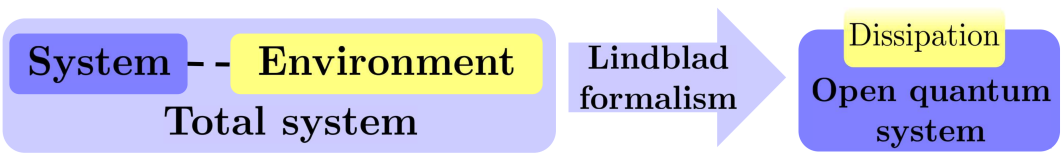

Figure 1.3: Schematic idea of the Lindblad formalism. Instead of describing the total system, the environment is incorporated in the open quantum system through dissipative terms.

with Markovian baths is given by the Lindblad (or Gorini-Kossakowski-Sudarshan-Lindblad) master equations [60]. For these systems, the time evolution is non-unitary and the generator is the non-Hermitian Lindblad operator, also called Lindbladian, with complex eigenvalues. The imaginary parts of the eigenvalues encode relaxations and dissipations. The basic idea is outlined in Fig. 1.3.

Some prominent examples of open quantum systems are radioactive decays [61], exciton polaritons [62], cold gases with losses [63], circuit QED arrays [64], trapped ions [65] and Rydberg atoms [66]. Non-Hermitian operators also appear in other contexts outside of Markovian baths [67–69]. For instance, they arise in effective approximations such as the Dyson-Maleev representation, which replaces spin operators by effective bosonic operators but leads to a non-Hermitian representation on the full bosonic Hilbert space [70, 71]. Open quantum systems are an active field of research and important for the understanding of novel quantum phenomena [72–75]. Understanding the dissipative effects in these systems on a quantitative level is crucial in non-equilibrium physics in general and specifically for quantum coherent control in quantum information processing and for any pump-probe setups.

It is important to develop new, robust and efficient tools for describing open quantum systems. Some of the methods introduced to this end are quantum trajectories [76], tensor networks [77, 78], quantum algorithms [79] and extensions of mean field theories [80, 81]. Many approaches in the past attempted to describe the unitary dynamics of the full system, i.e the system plus environment, by decoupling the small system from the environment [11, 12, 14–16, 82–85]. This approach is limited considerably by the size of the full system. It is more effective to solve only the non-unitary dynamics of the microscopic system, specifically, while the effects of the environment are described by the Lindblad master equations.

Historically, the application of flow equations was restricted to Hermitian matrices and non-Hermitian matrices with real eigenvalues. They were therefore unable to treat the non-Hermitian matrices and complex eigenvalues encountered in dissipative open quantum systems. Rosso et al. introduced three novel generator schemes in 2020, which extend the scope of flow equations to non-Hermitian matrices, labelled **dissipative flow equations** [86]. They demonstrated that the formalism works for various systems and compared the convergence speeds of their proposed generators. However, the field of dissipative flow equations is still in its infancy and efficient schemes are crucial to push the field forward.

In this thesis, we introduce a novel generator scheme by generalizing the **particle-conserving (pc-)generator** to dissipative flow equations. We extend the scope of previous research, which focused on convergence speed [86], to the equally important accuracy of the flows in spite of truncation. Since truncations are necessary for

almost all relevant applications of flow equations, a generator scheme must minimize truncation errors to capture the physics correctly. We prove important properties of our proposed generator scheme and benchmark the convergence speed as well as truncation errors for various systems. Finally, we compare all results with the results for the generator suggested before and thereby show that our generator is a good tradeoff, because it combines excellent accuracy with good convergence speed.

1.4 Structure of This Thesis

We cover the basic principles of CUT in Chap. 2 , which are relevant for all following chapters. The flow equation approach is explained in Sec. 2.1 and extended to second quantization in Sec. 2.2 . We introduce common generator schemes, most notably the pc-generator, in Sec. 2.3 . Common truncation schemes are presented in Sec. 2.4 and symmetries are discussed in Sec. 2.5 . The **residual-off-diagonality (ROD)** is defined in Sec. 2.6, which provides a very useful convergence measure.

In Chap. 3 we calculate the dynamic properties of a spin-1/2 Heisenberg ladder for RIXS experiments. The physical model is defined in Sec. 3.1 , where the concept of triplon excitations and bound states are also explained. Sec. 3.2 covers experimental probing methods and the corresponding excitation channels relevant for an experimental verification of our findings, while Sec. 3.3 discusses the theoretical and numerical methods utilized for computing the relevant response functions. We report our findings in Sec. 3.4 and summarize the central results in Sec. 3.5 .

Truncations in momentum space for hard-core bosons are studied in Chap. 4 . We define the physical model in Sec. 4.1 and discuss advantages and challenges of a momentum-space approach in Sec. 4.2 . In Sec. 4.3 we investigate strategies to exploit the momentum-space description. The findings are concluded in Sec. 4.4.

We investigate the generalization of the pc-generator to dissipative flow equations in Chap. 5 . The Lindblad master equations are introduced in Sec. 5.1 and non-unitary flow equations are discussed in Sec. 5.2 . We show the limitations of the pc-generator in Sec. 5.3 and generalize it to a more suitable form for dissipative flow equations in Sec. 5.4 . The three previously suggested generators are discussed in Sec. 5.5 and compared to our proposed generator analytically in Sec. 5.6. All four generators are benchmarked numerically in Sec. 5.7 . We conclude our findings in Sec. 5.8 .

The central findings of Chap. 3 to Chap. 5 are summarized and an outlook for future scientific research is given in the final conclusion in Chap. 6 .

Chapter 2

Continuous Unitary Transformations (Flow Equations)

In this chapter we introduce the basic idea of CUTs, derive the flow equations and introduce generator and truncation schemes relevant for the rest of this thesis.

2.1 Flow Equation Approach

The Hamiltonians of physical many-body systems are often established in an unamenable form, e.g. in second quantization with creation and annihilation operators of particles which are not conserved. To arrive at a more tractable form, e.g. a Hamiltonian with (quasi-)particle conservation, one typically changes the basis by a discrete unitary transformation

$$H_{\text{eff}} = UHU^\dagger \quad \text{with} \quad U^\dagger = U^{-1}\,. \tag{2.1.1}$$

The difficulty lies in finding an appropriate unitary transformation operator U. Some standard cases can be solved by generic approaches such as Fourier transformations and Bogoliubov transformations [87], but for more complicated systems finding a suitable unitary transformation is not trivial.

The flow equation scheme provides a systematic approach for finding appropriate transformations. To this end, it generalizes the discrete unitary transformation to a continuous unitary transformation (CUT) by introducing the continuous flow parameter ℓ [4, 5, 17, 28]

$$H(\ell) = U[H(\ell)]H(0)U^\dagger[H(\ell)] \quad \underset{\ell\to\infty}{\longrightarrow} \quad H(\infty) = H_{\text{eff}}\,, \tag{2.1.2}$$

where H_{eff} is a more tractable form than $H(0)$. In principle, H_{eff} can be determined by finding the transformation for $\ell \to \infty$. At first glance, this seems like an un-

necessary complication of the initial problem, but often in physics a complicated generalization allows for an elegant simplification. We use the notation $U[H(\ell)]$ to emphasize that the unitary matrix $U(\ell)$ depends on $H(\ell)$, because it is chosen at each ℓ such that it transforms $H(\ell)$ closer to the final form H_{eff}. The idea behind this can be illustrated by an analogy to rotations in high-dimensional spaces. By changing the generator of the rotation, i.e. the instantaneous rotation axis, one can optimize the orientation of the rotation at each ℓ. This is a vital asset of the CUT, which allows for advantageous properties when transforming complicated systems which can only be treated approximately.

Continuing with this analogy, the rotation axis is defined by the generator, so it is reasonable to express the unitary matrix $U(\ell)$ by the Antihermitian generator $\eta(\ell)$

$$U(\ell) = \mathcal{T}_\ell \exp\left[\int_0^\ell \eta[H(\ell')]\mathrm{d}\ell'\right], \quad \eta^\dagger(\ell) = -\eta(\ell)\,, \tag{2.1.3}$$

where $\mathcal{T}_\ell$ is the ℓ-ordered product. By inserting (2.1.3) in (2.1.2) and differentiating with respect to ℓ, one obtains the flow equations

$$\partial_\ell H(\ell) = \big[\,\eta[H(\ell)], H(\ell)\,\big]\,. \tag{2.1.4}$$

One can also transform observables O to the new basis with the transformation

$$\partial_\ell O(\ell) = \big[\,\eta[H(\ell)], O(\ell)\,\big]\,. \tag{2.1.5}$$

By introducing (2.1.4) and (2.1.5), the problem of finding the transformation U is replaced by choosing an appropriate generator scheme $\eta[H(\ell)]$ and solving the flow equations. The flow equations can sometimes be solved analytically, but most commonly they must be integrated numerically. To set up the flow equations, one can recursively insert $H(\ell)$ in (2.1.4), starting with the initial Hamiltonian $H(0)$, to find the new terms that arise during the flow. In most cases, the flow equations are not closed, i.e. the number of terms is infinite. Therefore, a truncation scheme must be applied to limit the number of tracked terms.

The workflow of the CUT or flow equation method can be broken down to

1. choosing a generator and truncation scheme,
2. evaluating the commutator, often multiple times, to set up the flow equations,
3. analytically or numerically integrating the flow equations.

This simple recipe can be expanded to improve the computational efficiency and accuracy of the CUT approach. The most common variants are [88]

- **Self-similar CUT (sCUT)**
  In sCUT, the Hamiltonian is approximated by a finite basis of operators in second quantization, enabling normal-ordering and distinction of interactions by the number of involved quasi-particles. Using second quantization also enables one to track multiple matrix elements of the Hamiltonian in a single operator, see Sec. 2.2.1 . A finite operator basis can often only be obtained by introducing a truncation scheme. This truncation scheme can be based on a small perturbation parameter [3,14] or the range in real-space [59]. Aside from this truncation, no perturbative expansion is performed.

- **Graph-theory based CUT (gCUT)**
  The gCUT method [89] can be seen as an expansion of the exact linked-cluster expansion [90] for ground-state properties. The flow equations of the Hamiltonian are decomposed into finite graphs, which can be solved numerically on the matrix level. The non-perturbative effective Hamiltonian is obtained by combining the results of all graphs. The accuracy is controlled by the maximum size of the considered graphs.

- **Perturbative CUT (pCUT)**
  This method, which was introduced by Knetter and Uhrig [17,91,92], performs a perturbative expansion up to very high orders to calculate flow equations that can be integrated analytically. The remaining task is the calculation of the matrix elements which appear in the effective Hamiltonian.

- **Enhanced perturbative CUT (epCUT)**
  By combining the representation of the Hamiltonian in second quantization and the explicit numerical integration of the flow equations from sCUT with the perturbative expansion of pCUT, the epCUT method [32] can derive a series expansion of H_{eff} for a larger class of models than pCUT. The operator monomials are expanded perturbatively, such that only contributions which are relevant to the targeted quantities in the desired order n of x^n are tracked.

- **Directly evaluated enhanced perturbative CUT (deepCUT)**
  The deepCUT [32] is a non-perturbative twin of the epCUT, which utilizes the perturbative expansion to determine which contributions are relevant for the targeted quantities in the desired order, but integrates the obtained differential equation system directly without any expansion. Thereby, all tracked flows are considered up to infinite order in x. This scheme is explained in more detail in Sec. 2.4.3 .

In this work, we apply the deepCUT scheme in Chap. 3 . In Chap. 4 and Chap. 5 we work on fundamental extensions in momentum space and for dissipative systems, which are not directly restricted to a single CUT scheme.

2.2 Flow Equations in Second Quantization

While (2.1.4) is the most straight-forward implementation of flow equations, a description in second quantization is often more advantageous, see Sec. 2.2.1 . In second quantization, the Hamiltonian and generator can be expressed in an operator basis $\{\hat{A}_i\}$ [4]

$$\hat{H}(\ell) = \sum_i h_i(\ell)\hat{A}_i \,, \tag{2.2.6a}$$

$$\hat{\eta}(\ell) = \sum_i \eta_i(\ell)\hat{A}_i = \sum_i h_i(\ell)\hat{\eta}[\hat{A}_i] \,, \tag{2.2.6b}$$

where each $\hat{A}_i$ is a normal-ordered monomial of creation ($\hat{a}_i^\dagger$) and annihilation ($\hat{a}_i$) operators, e.g. a hopping term $\hat{a}_i^\dagger a_j$. Only the coefficients $h_i(\ell)$ and $\eta_i(\ell)$ depend on ℓ, while the operator basis $\{\hat{A}_i\}$ remains constant during the flow. In (2.2.6b), we assume for simplicity that the coefficients $\eta_i(\ell)$ depend directly on the corresponding $h_i(\ell)$, i.e. $\eta_i(\ell)$ and $h_i(\ell)$ only differ by a factor that is constant for each A_i. We explicitly denote operators by hat symbols in (2.2.6) to distinguish them from scalars, but in the following equations, the hat symbols are omitted for brevity.

To set up the flow equations in second quantization, one can evaluate the commutator (2.1.4), which yields a linear superposition of operator monomials. The monomials are then compared with the basis monomials $\{A_i\}$ and the prefactors can be defined as the elements of the tensor D_{ijk} of contributions, i.e.

$$[\hat{\eta}[A_j], A_k] = \sum_i D_{ijk} A_i \,. \tag{2.2.7}$$

The contributions D_{ijk} are then used to set up the flow equations

$$\boxed{\partial_\ell h_i(\ell) = \sum_{jk} D_{ijk}\, h_j(\ell) h_k(\ell) \,.} \tag{2.2.8}$$

For observables $O(\ell) = \sum_i o_i(\ell)\tilde{A}_i$ one obtains O_{eff} in the effective basis by simultaneously integrating

$$\boxed{\partial_\ell o_i(\ell) = \sum_{jk} \tilde{D}_{ijk} h_j(\ell) o_k(\ell) \,,} \tag{2.2.9}$$

where the tilde over $\tilde{D}_{ijk}$ and $\tilde{A}$ denote the fact that the observable may use a different basis than the Hamiltonian. For bilinear Hamiltonians, i.e. Hamiltonians containing only operator monomials of up to two bosonic or fermionic operators, the process is simpler. In that case, the evaluation of the commutator (2.1.4) and the integration of the flow equations can be performed directly on the matrix $\mathbf{M}(\ell)$ with

$$H(\ell) = \boldsymbol{a}^\dagger \mathbf{M}(\ell) \boldsymbol{a} \,, \quad \boldsymbol{a} := \left(a_0, a_1, ..., a_0^\dagger, a_1^\dagger, ...\right)^{\mathrm{T}} \,. \tag{2.2.10}$$

2.2.1 Advantages of the Description in Second Quantization

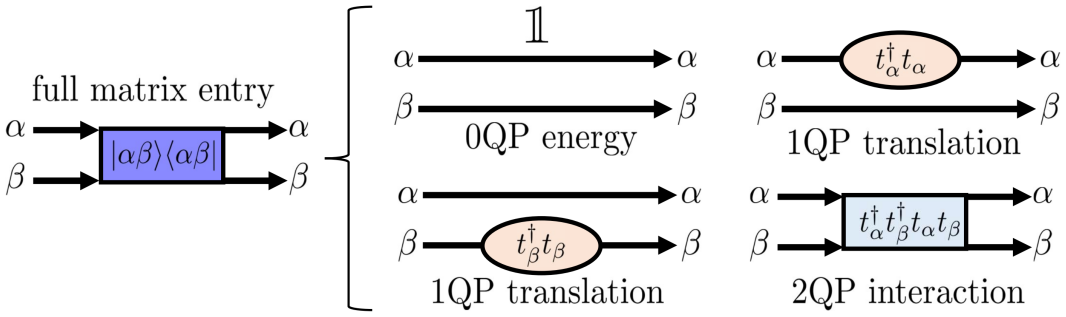

Figure 2.1: Diagrammatic representation of the irreducible processes constituting the diagonal matrix element $|\alpha\beta\rangle\langle\alpha\beta|$ to the two-particle state $|\alpha\beta\rangle$ with the corresponding creation ($t_\alpha^\dagger$) and annihilation operators (t_α), which act on states with a minimum of 0/1/2 quasiparticles.

The first form of the flow equations (2.1.4) treats H in matrix form with elements $h_{nj} = \langle n|H|j\rangle$, where $|n\rangle$ is a basis in Hilbert space. This poses the problem that the matrix dimension D increases exponentially with the system size N. Therefore, the flow equations track an exponentially large number of matrix elements or, even worse, the flow equations are not closed at all. This renders the numerical integration of the flow equations impossible for most macroscopic systems.

Often, it is advantageous to formulate the flow equations in second quantization (2.2.8), where one tracks the coefficients $h_i(\ell)$ of operator monomials A_i to obtain tractable flow equations [4, 29, 59, 92, 93]. In that case, the number of tracked coefficients is not determined by D but rather by the size of the basis $\{A_i\}$. Because one monomial creates contributions to a multitude of matrix elements $h_{nj} = \langle n|H|j\rangle$, even a small number of tracked monomials describes processes on a large section of the Hilbert space. A suitable truncation scheme, see Sec. 2.4 , finds a finite number of monomials that provide an accurate approximation in the thermodynamic limit $N \to \infty$. Therefore, these monomials can be used to compute true continua, rather than a discrete set of energies, which is a distinct advantage of this formalism.

The tradeoff is that many matrix elements are only captured partially. For instance, a matrix element between two-particle states can be decomposed into various irreducible interaction processes. For illustration, the processes constituting a diagonal element to a two-particle state are shown in Fig. 2.1. If one wishes to fully capture many-particle processes, the number of required monomials rises rapidly.

The different scaling of the basis size with and without second quantization can be illustrated by a simple example. Consider a one-dimensional chain of N localized spin-1/2 particles. Obviously, the Hilbert space has dimension 2^N and accordingly, the Hamiltonian H without truncation is of dimension $D = 2^N$. Therefore, one needs to track $D_{\text{direct}} = D^2 = 4^N$ matrix elements $h_{nj} = \langle n|H|j\rangle$. Using second quantization, the number of possible n-to-m-particle processes is given by the $\binom{N}{n}$ possible combinations of n annihilation operators on N sites and the $\binom{N}{m}$ possible

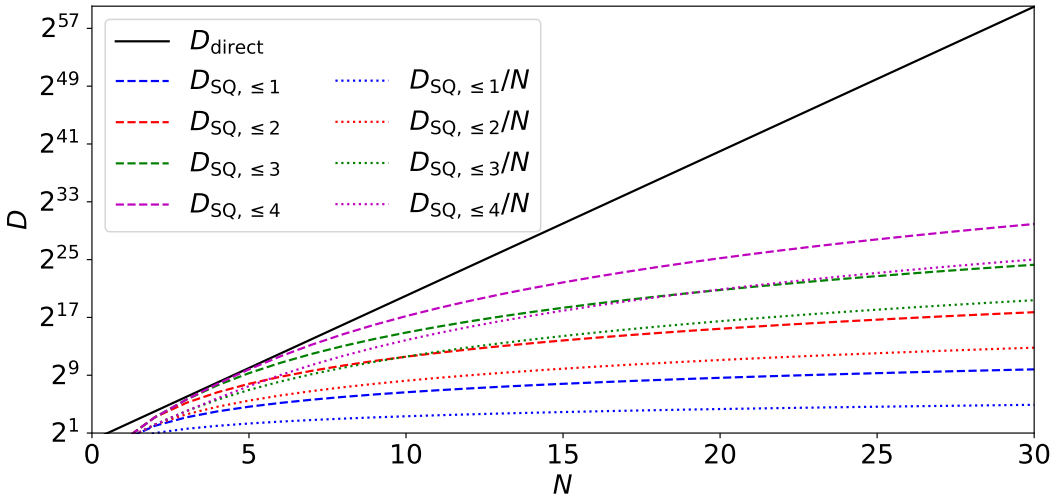

Figure 2.2: Number of tracked coefficients without ($D_{\text{direct}} = 4^N$) and with ($D_{\text{SQ},\,\leq k} = \sum_{n,m=1}^{k} \binom{N}{n}\binom{N}{m}$) second quantization up to k-particle processes. The dotted lines roughly approximate the dimension $D_{\text{SQ symm},\,\leq k} \approx D_{\text{SQ},\,\leq k}/N$ when translation symmetry is utilized.

combinations of m creation operators, i.e. $D_{\text{SQ},\,n\to m} = \binom{N}{n}\binom{N}{m}$ coefficients must be tracked. If one attempts to track all contributions with $n, m \in \{1, 2, ..., k\}$, the number of tracked coefficients if $D_{\text{SQ},\,\leq k} = \sum_{n,m=1}^{k} \binom{N}{n}\binom{N}{m}$.
The number of tracked coefficients in each case is plotted in Fig. 2.2 up to $k = 4$. The direct description using the matrix elements $h_{nj} = \langle n|H|j\rangle$ always requires more coefficients than the description in second quantization. One commonly wants to describe a system as close as possible to the thermodynamic limit $N \to \infty$, but focusing on processes between at most 2 or 3 particles, i.e. low-energy processes, in which case the advantage of the description in second quantization is even more pronounced. Note that this argument holds even without utilizing symmetries, see Sec. 2.5 , or sophisticated truncation schemes, see Sec. 2.4 , which both drastically reduce the matrix dimension. For instance, by using translation symmetry, which can be done trivially in second quantization, the number of tracked coefficients is reduced by a factor N for a one-dimensional system with N sites. This causes a significantly better scaling and makes the description in second quantization even more efficient.

2.3 Generator Schemes

The choice of the generator scheme $\eta[H]$ strongly affects the properties of the flow equations and of the resulting effective Hamiltonian. Therefore, an appropriate scheme must be chosen for a given problem. In this section, we present some common generator schemes and discuss their properties. These schemes or dissipative generalizations based on them will be utilized in this thesis. The dependencies on ℓ

are not denoted explicitly for brevity.

2.3.1 Particle-Conserving (pc-)Generator

In this section, we introduce the **particle-conserving (pc-)generator**, which has been proposed by Mielke for banded matrices [28] and independently by Knetter and Uhrig for many-particle systems [17]. We treat the Mielke variant first, because its definition is less universal, but we label both schemes pc-generator in this thesis because the central idea is extremely similar and the Mielke definition can be understood as a special case of the Knetter and Uhrig definition.

2.3.1.1 Formulation by Mielke

Mielke proposed the generator

$$\eta^{\mathrm{M}}[H] = H^+ - H^- \,, \tag{2.3.11a}$$
$$\eta^{\mathrm{M}}_{nj}[H] = \mathrm{sign}(n-j)\, h_{nj} \,, \tag{2.3.11b}$$

where H^+ and H^- are the upper and lower triangular part of H [28, 94] and η^{M}_{nj} are the matrix elements of η^{M}. The idea is that if the diagonal elements h_{nn} are sorted in ascending order and one chooses a negative sign for the lower triangular matrix, the flow converges to stable fixed points corresponding to diagonal matrices, see below. If the diagonal elements are not sorted, they will be sorted by the flow. Alternatively one can use a different definition

$$\eta^{\mathrm{M}}_{nj}[H] = \mathrm{sign}(h_{nn} - h_{jj}) h_{nj} \,. \tag{2.3.12}$$

Note that using (2.3.12) is equivalent to using the first definition (2.3.11) and ensuring the ordering $h_{nn} > h_{jj}\ \forall n > j$ at each value of ℓ by swapping the basis vectors, if necessary. This can, however, change the structure and band-diagonality of the matrix. For simplicity, we will continue with the first definition (2.3.11).

The Mielke generator induces the flow equations

$$\partial_\ell h_{nj} = \sum_k \Big(\eta_{nk} h_{kj} - h_{nk} \eta_{kj} \Big) \tag{2.3.13a}$$
$$= \sum_k \Big(\mathrm{sign}(n-k)\, h_{nk} h_{kj} - \mathrm{sign}(k-j)\, h_{nk} h_{kj} \Big) \tag{2.3.13b}$$
$$= -|h_{nn} - h_{jj}| h_{nj} + \sum_{k \notin \{j,n\}} \Big(\mathrm{sign}(n-k) + \mathrm{sign}(j-k) \Big) h_{nk} h_{kj} \tag{2.3.13c}$$
$$\Rightarrow \partial_\ell h_{nn} = 2 \sum_{k \neq n} \mathrm{sign}(n-k)\, |h_{nk}|^2 \,. \tag{2.3.13d}$$

By analyzing these flow equations, we can learn some important properties of the Mielke generator.

1) **Convergence to Fixed Point**

The flow always converges to a diagonal matrix, even if it contains degeneracies. We prove this by summing over the flow of the first r diagonal elements

$$\partial_\ell \left(\sum_{n=1}^{r} h_{nn} \right) = \sum_{n=1}^{r} \sum_{k>r} -2|h_{nk}|^2 \leq 0 \,. \tag{2.3.14}$$

With this, $\sum_{n=1}^{r} h_{nn}$ cannot increase. At the same time, for a physical ground state to exist, H needs to be bounded from below, so the variational principle reveals that the sum cannot be lower than the sum of the lowest r eigenvalues

$$\sum_{n=1}^{r} h_{nn} \geq \sum_{n=1}^{r} \lambda_n \tag{2.3.15}$$

and therefore the derivative must vanish for $\ell \to \infty$

$$\lim_{\ell\to\infty} \partial_\ell \sum_{n=1}^{r} h_{nn} = 0 \,. \tag{2.3.16}$$

The fixed points of the flow equations (2.1.4) are matrices H for which the generator η vanishes, i.e. matrices with vanishing off-diagonal elements

$$\lim_{\ell\to\infty} |h_{nk}|^2 = 0 \,. \tag{2.3.17}$$

2) **Renormalization of Energies**

If the matrix H is close to diagonal, i.e. the off-diagonal elements $|h_{nj}| \ll 1 \,\forall n \neq j$, then the off-diagonal elements converge like

$$h_{nj} \propto \exp\Big(-|h_{nn}(\infty) - h_{jj}(\infty)|\ell \Big) =: \exp\Big(-|\Delta E_{nj}|\ell \Big) \tag{2.3.18}$$

because only the first summand in (2.3.13c) is of order $\mathcal{O}(h_{nj})$, while the second summand is of order $\mathcal{O}(h_{nj}^2)$ and therefore negligible. One can approximate $h_{nn}(\ell) \approx h_{nn}(\infty)$ in the nearly diagonal case as well, because (2.3.13d) reveals that the error of this approximation is of order $\mathcal{O}(h_{nj}^2)$.

This means that the off-diagonal elements of the Mielke generator converge to 0 (or in more colloquial terms "are rotated to 0") with a linear dependence on the energy differences ΔE_{nj} in the exponential argument. This is an important renormalizing property of the generator, as physical states with large energy differences are separated from each other first and states energetically close to each other are separated later. While this property can increase the computation time, it also causes off-diagonal elements h_{nj} with high distance $|n-j|$ to the diagonal to vanish quickly before accumulating significant renormalizations. This is relevant for truncation schemes, in which those off-diagonal elements far away from the diagonal are neglected during the integration of the flow equations. The truncation error is discussed in detail in the context of dissipative flow equations in Chap. 5 .

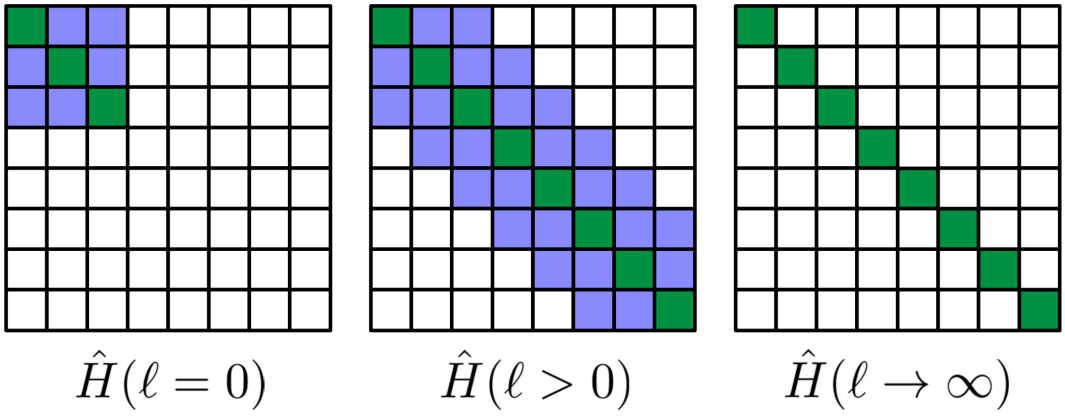

Figure 2.3: Schematic flow of the matrix elements induced by pc-generator in the Mielke formulation (2.3.11). Green squares indicate finite diagonal elements and blue squares indicate finite off-diagonal elements. The band diagonality is preserved, but new elements can arise during the flow. The final matrix is diagonal.

3) **Preservation of Band-Diagonality**

The band-diagonality of the matrix is preserved. One can prove this quickly by analyzing (2.3.13c). We assume

$$h_{nj}(0) = 0 \quad , \forall |j-n| > \Delta \in \mathbb{N}_0 \,, \tag{2.3.19}$$

so that the initial matrix $H(0)$ is band-diagonal with band-width Δ. We want to show $\partial_\ell h_{nj}{=}0 \; \forall |j-n| > \Delta$, since this implies that the elements $h_{nj} \; \forall |j-n| > \Delta$ stay at 0. We assume $n < j$ for simplicity. The case $n > j$ is analogous, as H is Hermitian and hence $h_{nj} = h^*_{jn}$. We take (2.3.13c) and apply the assumptions

$$\partial_\ell h_{nj} = -|h_{nn} - h_{jj}| \underbrace{h_{nj}}_{=0} + \sum_{k \notin \{j,n\}} \underbrace{\Big(\operatorname{sign}(n-k) + \operatorname{sign}(j-k)\Big)}_{=0 \text{ if } k \in [n,j]} h_{nk} h_{kj} \tag{2.3.20a}$$

$$= \sum_{k<n} 2 h_{nk} \underbrace{h_{kj}}_{=0} - \sum_{k>j} 2 \underbrace{h_{nk}}_{=0} h_{kj} \quad , \forall |j-n| > \Delta \,. \tag{2.3.20b}$$

In the last step we use that the summation $k < n$ implies $|k-j| > \Delta$ and $k > j$ implies $|k-n| > \Delta$, respectively. Note that we only assume band-diagonality for the initial matrix $\ell = 0$, but our derivation holds not only for $\ell = 0$, but for all $\ell > 0$, since both $\partial_\ell h_{nj}$ and h_{nj} stay 0 during the complete flow.

The preservation of band-diagonality, which is shown schematically in Fig. 2.3, is a great advantage of the Mielke generator. It reduces the number of new contributions appearing during the flow, which in turn reduces the computational cost and the error introduced by truncations.

4) **Energy Ordering**

The Mielke generator (2.3.11) sorts the eigenvalues $h_{nn}(\infty) \geq h_{jj}(\infty)$ for all

$n > j$. In other words, attractive fixed points of the flow must obey

$$\operatorname{sign}(n-j) = \operatorname{sign}(h_{nn}(\infty) - h_{jj}(\infty))\,. \tag{2.3.21}$$

This can cause problems if the diagonal elements are not sorted initially or if they lose their ordering during the flow. Even for the adapted version (2.3.12), which does not explicitly sort the diagonal, such violation of the ordering can cause massive reorderings of the matrix elements, during which the off-diagonal elements can temporarily increase and the band-diagonality is no longer preserved [93].

5) **Units**
From the definition (2.3.11) of the Mielke generator, one can tell that η has the dimension of an energy and hence the flow parameter ℓ has the dimension of an inverse energy. This corresponds to the linear energy dependence in the asymptotic behavior (2.3.18).

2.3.1.2 Formulation by Knetter and Uhrig

When appyling the Mielke generator from Sec. 2.3.1.1 , one can always decide not to include all off-diagonal matrix elements in η^{M}, but rather a selected choice of elements that should vanish in H_{eff}. One can formalize this generalization of the Mielke generator by introducing the more general pc-generator

$$\eta^{\mathrm{pc}}_{nj}[H] = \operatorname{sign}(q_{nn} - q_{jj}) h_{nj}\,, \tag{2.3.22}$$

where one can use any diagonal operator Q with diagonal elements q_{nn} to selectively decouple blocks of H [17, 95]. The operator Q is not transformed during the flow. In this way, the flow converges to a block diagonal H_{eff} instead of a diagonal one, where the blocks consist of states with constant q_{nn}. An alternative definition is

$$\eta^{\mathrm{pc}}_{nj}[H] = \sum_j \sum_{\substack{i \\ i>j}} H^i_j - H^j_i\,, \tag{2.3.23}$$

where H^i_j is the block of H which transforms states with $q = j$ to states with $q = i$. Additionally, the sign of the generator elements $\eta^{\mathrm{pc}}_{nj}[H]$ can be controlled by the choice of the elements q_{nn} of Q.

Originally, Knetter and Uhrig formulated this generator for the purpose of decoupling subspaces with different numbers of quasi-particles, in which case q_{nn} counts the number of quasi-particles [17, 91]. In this case the flow converges at a quasi-particle-conserving H_{eff}, which is the motivation for the name "particle-conserving generator". Because the basic properties of the more general definition (2.3.22) of the pc-generator are essentially the same as those of the Mielke formulation (2.3.11), we do not repeat the properties discussed in Sec. 2.3.1.1 . However, we want to highlight a few interesting aspects arising from the generalization.

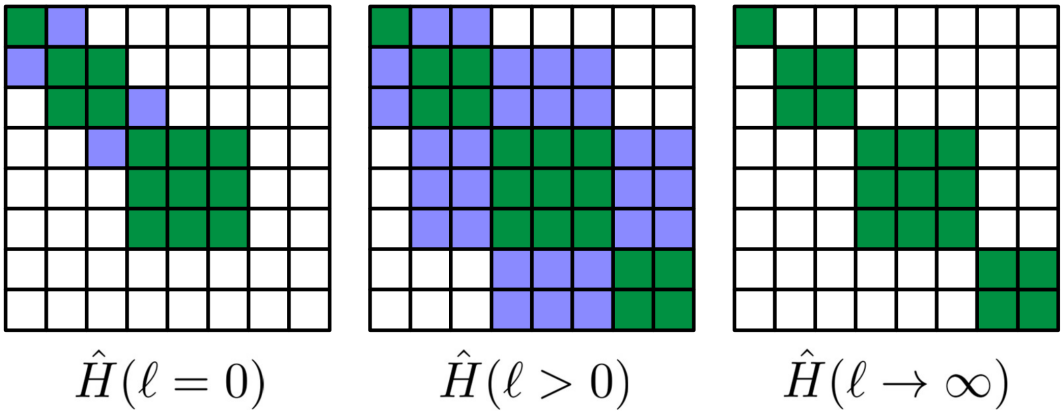

Figure 2.4: Schematic flow of the matrix elements induced by pc-generator in the more general formulation by Knetter and Uhrig (2.3.22). Green squares indicate finite block diagonal elements and blue squares indicate finite off-diagonal elements. The block band-diagonality is preserved, but new elements can arise during the flow. The final matrix is block diagonal. A block is defined by elements with identical q_{nn}, e.g. with an identical number of quasi-particles.

6) **Interpretation of Block Band-Diagonality**
Similar to the Mielke formulation, the pc-generator in the Knetter/Uhrig formulation preserves the block band-diagonality of H and therefore reduces the computational cost and truncation errors. Fig. 2.4 depicts the conservation of band-diagonality schematically. The physical interpretation of the conservation of block band-diagonality depends on the choice of Q.
In the case of many-particle systems, where Q counts the number of quasi-particles, this implies that if the initial Hamiltonian $H(0)$ only contains terms which change the quasi-particles number by a maximum number of $n_{\max}$, then the pc-generator ensures that $H(\ell)$ cannot contain terms which change the number of quasi-particles by more than $n_{\max}$ [44]. As another example, if one applies CUT in Floquet theory, the maximum change $n_{\max}$ of the phase factor $\exp(\mathrm{i}n_{\max}\omega t)$ is preserved [26].

7) **Generalized Energy Ordering**
We stressed in Sec. 2.3.1.1 that the Mielke generator (2.3.11) assumes an ordered diagonal, i.e. $\operatorname{sign}(n-j) = \operatorname{sign}(h_{nn}(\infty) - h_{jj}(\infty))$. For the pc-generator this is generalized to

$$\operatorname{sign}(q_{nn} - q_{jj}) = \operatorname{sign}(h_{nn}(\infty) - h_{jj}(\infty))\,. \tag{2.3.24}$$

For example, assume that Q counts the number of quasi-particles. In this case the pc-generator attempts to sort the energies h_{nn} in a way that states with more quasi-particles always have higher energies. This must not always be true, however, as the energy bands can overlap (either initially or at some point during the flow), which is shown schematically in Fig. 2.5. In this case, the pc-generator has to perform significant reorderings, which can lead to a rising off-diagonal and

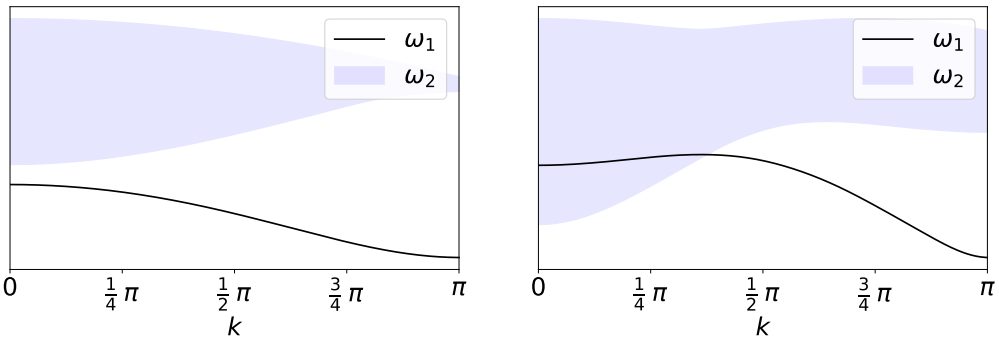

Figure 2.5: Schematic examples of a system where the one-particle dispersion and the two-particle continuum (left) are separated or (right) cross one another.

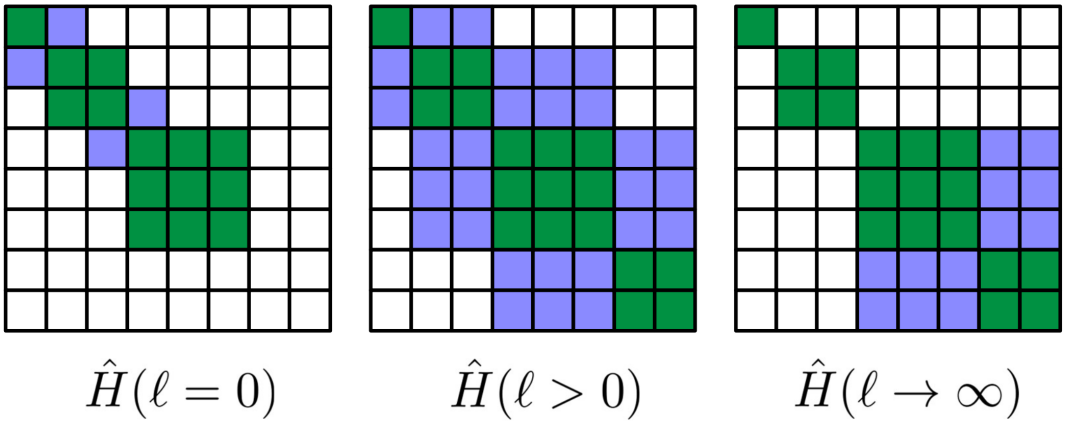

Figure 2.6: Schematic flow of the matrix elements induced by ps-generator (2.3.25). Green squares indicate finite block diagonal elements and blue squares indicate finite off-diagonal elements. The block band-diagonality is preserved, but new elements can arise during the flow. The final matrix is block diagonal up to the selected number of quasi-particles.

causes numerical problems, possibly leading to a divergent flow.

2.3.2 Particle-Sorting (ps-)Generator

While the formulation (2.3.22) of the pc-generator generalizes the Mielke formulation (2.3.12) to allow decoupling based on blocks with constant Q, it does not allow to choose blocks which should not be decoupled from any other blocks with different q_{nn}. This can cause problems if the subspaces overlap energetically and can cause a diverging flow when approximations are used [59]. Fischer, Duffe and Uhrig proposed a solution to this problem with the particle-sorting generator scheme

$$\eta^{\mathrm{ps}}_{(k:n)}[H] = \sum_{\substack{j \\ j \leq k}} \sum_{\substack{i \\ i > j}} \left(H^i_j - H^j_i \right) , \tag{2.3.25}$$

which only decouples the subspaces with up to k quasi-particles [96, 97] from other subspaces. The flow is depicted schematically in Fig. 2.6.

Note that one can use the basic principle of the Mielke formulation (2.3.11) of the pc-generator and generalize it beyond the scope of the Knetter/Uhrig formulation (2.3.22) and the ps-generator (2.3.25). For instance, one can define a generator $\eta_{nj}[H] = h_{nj}q_{nj}$, where q_{nj} takes a constant value depending on the states and energies h_{nn} and h_{jj}. The pc- and ps-generator are merely two schemes which have proven versatile enough for many-body physics and are relevant for the scope of this thesis.

2.3.3 Wegner Generator

The original generator proposed by Wegner [4]

$$\eta^{\text{Wegner}} = [H_{\text{diag}}, H_{\text{off-diag}}]\,, \tag{2.3.26a}$$
$$\eta^{\text{Wegner}}_{nj} = (h_{nn} - h_{jj})h_{nj}\,, \tag{2.3.26b}$$

has less advantageous convergence properties than the pc-generator, see below. Nevertheless, it is a powerful tool that has been used successfully, for instance, for the description of sine-Gordon models [21,22]. It is calculated by taking the commutator of the diagonal and off-diagonal parts of the Hamiltonian $H = H_{\text{diag}} + H_{\text{off-diag}}$. Just like for the pc-generator the terms 'diagonal' and 'off-diagonal' are not restrictive. One is free to include only specific terms of H in $H_{\text{off-diag}}$ that should converge to 0 during the flow, while all other terms are kept in H_{diag}. Note that the definition (2.3.26) is quite similar to the definition of the Mielke generator (2.3.12) which does not require ordered eigenvalues, but the Wegner generator introduces an additional scaling with the value of the difference $h_{nn} - h_{jj}$. The Wegner generator induces the flow equations

$$\partial_\ell h_{nj} = \sum_k \Big((h_{nn} - h_{kk})h_{nk}h_{kj} - (h_{kk} - h_{jj})h_{nk}h_{kj} \Big) \tag{2.3.27a}$$
$$= -(h_{nn} - h_{jj})^2 h_{nj} + \sum_{k\notin\{n,j\}} (h_{nn} + h_{jj} - 2h_{kk})h_{nk}h_{kj} \tag{2.3.27b}$$
$$\Rightarrow\ \partial_\ell h_{nn} = \sum_{k\neq n} 2(h_{nn} - h_{kk})|h_{nk}|^2\,. \tag{2.3.27c}$$

In the following, we list some important properties of these flow equations.

1) **Convergence to Fixed Point**

The squared Frobenius norm of the diagonal component

$$||H_{\text{diag}}||^2 = \sum_n |h_{nn}|^2 = 2\sum_{nj} \big(h_{nn} - h_{jj}\big)^2 |h_{nj}|^2 \geq 0 \tag{2.3.28}$$

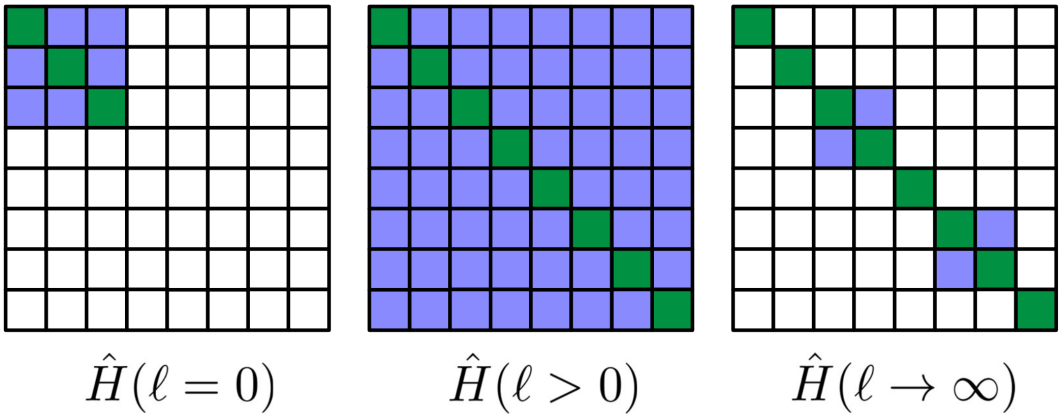

Figure 2.7: Schematic flow of the matrix elements induced by the Wegner-generator. Green squares indicate finite diagonal elements and blue squares indicate finite off-diagonal elements. The block band diagonality is not preserved and new elements can arise during the flow. The final matrix is diagonal apart from degeneracies.

increases during the flow, but is also bounded from above and must therefore converge. The fixed points are matrices H which can only have finite off-diagonals if the off-diagonal elements connect degenerate energies

$$h_{nj}(\infty) = 0 \quad \forall n \neq j : h_{nn}(\infty) \neq h_{jj}(\infty)\,. \tag{2.3.29}$$

Convergence has been proven originally for finite matrices [4] and later for infinite systems [93] and self-similar truncation [98].

2) **Renormalization of Energies**
If H is already close to diagonal form, i.e. all $|h_{nj}| \ll 1$ for $n \neq j$, then the off-diagonal elements converge with

$$h_{nj} \propto \exp\Big(- \big(h_{nn}(\infty) - h_{jj}(\infty)\big)^2 \ell \Big) =: \exp\Big(- |\Delta E_{nj}|^2 \ell \Big)\,. \tag{2.3.30}$$

The reason for this is that the first summand in (2.3.27b) is of order $\mathcal{O}(h_{nj})$ and the second summand is of order $\mathcal{O}(h_{nj}^2)$, hence the second summand is neglegible. One can approximate the diagonal elements as converged $h_{nn}(\ell) \approx h_{nn}(\infty)$ since their flow (2.3.27c) is of order $\mathcal{O}(h_{nj}^2)$.

3) **Band-Diagonality not Preserved**
Contrary to the pc-generator, the Wegner generator does not systematically preserve the band-diagonality of H. This is shown schematically in Fig. 2.7 and causes a relatively high computational cost and larger truncation errors compared to the pc-generator.

4) **Units**
In definition (2.3.26) of the Wegner generator, one can see that the generator η has the dimension of a squared energy, which corresponds to the quadratic

energy prefactor in (2.3.30). Consequently, the flow parameter ℓ is measured in units of inverse squared energies. The fact that ℓ scales differently for different generators is important if one compares the flow of different generators or of systems with different energy scales. In those cases, one cannot directly compare the convergence speed based on the flow parameter ℓ.

2.4 Truncation Schemes

One central caveat of the CUT method is the fact that the flow equations are not guaranteed to be closed for infinite systems, i.e. systems in the thermodynamic limit. Even if the Hilbert space is finite or the flow equations are closed, they can be too numerous for numerical integration. If one still wants to use CUTs for such systems, an appropriate truncation scheme must be applied to obtain a numerically solvable set of differential equations, while still capturing the relevant physics. For small systems, one may analyze each contribution manually to determine which monomials should be included in the calculation, but a more general scheme is necessary for larger systems. Here, we present three strategies for finding an appropriate truncation scheme.

2.4.1 Truncation by Scaling Arguments

One can use scaling arguments to find a suitable truncation scheme. For instance, if the gap is found at $\omega(k = 0) = \Delta$, the relevant low-energy physics is described by processes at $k \approx 0$. To determine how relevant certain processes are in this area, one can rescale the momenta $k \to \lambda k$ with a factor $\lambda \in]0, 1[$. For hard-core particles, for instance, one can show by rescaling the hard-core commutator that monomials consisting of $2n$ operators scale with λ^{n-1}, i.e. monomials with few operators are most relevant, see Sec. 4.2.5 for a thorough calculation. Using this truncation scheme, it is reasonable to only track monomials consisting of $2n < 2n_{\max}$ operators.

2.4.2 Truncation by Real-Space Extension

For quantum systems with energy gap Δ on a lattice, correlation functions (such as spin-spin correlations) decay exponentially with the correlation length ξ. The energy gap Δ between the ground state and the energetically lowest excited state is connected to the correlation length ξ by

$$\Delta \propto \xi^{-z} \tag{2.4.31}$$

with the dynamical critical exponent z [54]. This justifies a truncation scheme based on the spatial extension of operator monomials. An extension is defined for each monomial and all terms beyond a maximum extension d are truncated [29]. The extension can be defined in several ways. Reischl proposed the maximal taxi cab

distance between the sites on which the local creation and annihilation operators act, i.e. the leftmost and rightmost operator on a one-dimensional lattice [29]. The absolute position is not relevant for systems with translation invariance. But for the calculation of response functions, the absolute position can be relevant, in which case it can be useful to define the range by the sum of distances between a central site and all local operators.

This truncation scheme can be combined with the scaling arguments discussed in Sec. 2.4.1 . For hard-core particles, one can show using scaling arguments that low-energy physics is dominated by processes on a low number of particles, so monomials consisting of a small number $2n$ of local creation and annihilation operators are more relevant. Hence, it is reasonable to only include monomials up to a maximum particle number N, i.e. $n \leq N$, and to use a $2N$-tuple $\mathbf{d} = (d_2, ..., d_{2N})$ of maximal extensions [59]. The extensions d_0 and d_1 are omitted because monomials consisting of less than two operators have extension zero. A monomial of n particles is tracked only if it fulfills $n \leq 2N$ and has maximal extension d_n.

Truncation based on real-space range must be used with care when the correlation length ξ becomes large, for instance close to a second order quantum phase transition, where long-range processes become relevant and ξ diverges. For example, for a one-dimensional spin-chain with $z = 1$ one finds

$$\xi = \frac{v}{\Delta} \tag{2.4.32}$$

with the spin-wave velocity v in absence of a gap. To capture all relevant correlations, one should choose a minimum extension

$$d_{\min} \overset{!}{\gtrapprox} \xi = \frac{v}{\Delta} \,. \tag{2.4.33}$$

To check if this condition is fulfilled, one has to calculate v for a given system. This can be achieved by approximating the dispersion $\omega(k)$ at the gap

$$\min_k \omega(k) = \omega(k_0) = \Delta \tag{2.4.34}$$

in leading order by using the approximation

$$\omega(k) \approx \sqrt{\Delta^2 + v^2(\delta k)^2} \quad , \delta k := k - k_0 \tag{2.4.35a}$$

$$\Rightarrow |v| = \lim_{\delta k \to 0} \frac{\sqrt{\omega^2(k) - \Delta^2}}{|\delta k|} \,. \tag{2.4.35b}$$

This yields the condition

$$d_{\min} \overset{!}{\gtrapprox} \lim_{\delta k \to 0} \frac{\sqrt{\omega^2(k)/\Delta^2 - 1}}{|\delta k|} \,. \tag{2.4.36}$$

For a numerical implementation on a discrete lattice, this condition can be checked by evaluating ω at the k-value closest to k_0. Alternatively, $\omega(k)$ can be interpolated in a small area around k_0.

We stress that truncation with a maximal extension $d_{\max} = \max_n(d_n)$ can be applied on a system in the thermodynamic limit $N \to \infty$ and is different from a calculation on a finite system of size N with periodic boundary conditions. The periodic boundaries fold back terms in the commutator (2.2.7) so that otherwise truncated terms are still tracked [58], e.g. a monomial $t_0 t_9$ on a system with $N = 10$ does not have extension 9, but 1. The flow equations of the finite system with periodic boundaries are identical to the equations for the infinite system only if the system size N is large enough [58], i.e. for 1-dimensional systems if

$$N \geq N_{\text{eff}} = 3d_{\max} + 1\,. \tag{2.4.37}$$

In that sense, the finite system with $N \geq N_{\text{eff}}$ and the infinite system are equivalent for the truncated CUT, even though their eigenvalues without truncation, for instance obtained by exact diagonalization, are distinct. One advantage of this fact is that the CUT results can be used to calculate true continua on the infinite system without discretization in k, because the truncated CUT can be performed on a system in the thermodynamic limit $N \to \infty$. This is a major advantage over the discrete eigenvalues one obtains using other methods such as exact diagonalization.

2.4.3 Truncation by Perturbative Expansion (epCUT and deepCUT)

If the Hamiltonian H can be expanded in a small perturbation parameter x, it is reasonable to truncate terms based on their order $\mathcal{O}(x^n)$. This approach was introduced by Knetter and Uhrig, labelled pCUT [17, 91, 92], and in second quantization by Krull, labelled epCUT [32]. We focus on the epCUT variant for now, because of the advantages of the description in second quantization, which are outlined in Sec. 2.2.1 .

We assume that the initial Hamiltonian can be expanded in orders of x

$$H(0) = \sum_{m=0}^{n} x^m H^{(m)}(0)\,. \tag{2.4.38}$$

Most commonly, the initial Hamiltonian takes the form $H(0) = H^{(0)}(0) + xH^{(1)}(0)$, i.e. only terms in order $\mathcal{O}(x^0)$ and $\mathcal{O}(x^1)$ appear. We assume that either the local Hilbert space on each site is finite or that $H^{(0)}$ is a sum of local bilinear terms of bosonic or fermionic operators. A (block-)diagonal $H^{(0)}$ is desirable, but not required. We aim to track the flow up to order $\mathcal{O}(x^n)$

$$H(\ell) = \sum_{m=0}^{n} x^m H^{(m)}(\ell)\,. \tag{2.4.39}$$

With the expansion of $H^{(m)}(\ell)$ in the operator basis $\{A_i\}$, see Sec. 2.2 , we obtain an expansion of the coefficients $h_i(\ell)$ in x

$$h_i(\ell) = \sum_{m=0}^{n} x^m f_i^{(m)}(\ell)\,. \tag{2.4.40}$$

Inserting this into the flow equations (2.2.8) yields

$$\partial_\ell \sum_{m=0}^{n} x^m f_i^{(m)}(\ell) = \sum_{jl} D_{ijl} \sum_{p,q=0}^{n} x^{p+q} f_j^{(p)}(\ell) f_l^{(q)}(\ell) \,. \tag{2.4.41}$$

The contributions D_{ijl} do not depend on the orders m, p, q, but only on the commutation relation (2.2.7) between the corresponding basis monomials. By comparing individual orders in x, one obtains the flow equations

$$\partial_\ell f_i^{(m)}(\ell) = \sum_{jl} D_{ijl} \sum_{p+q=m} x^{p+q} f_j^{(p)}(\ell) f_l^{(q)}(\ell) \,. \tag{2.4.42}$$

All contributions to order m consist of either commutations of $H^{(0)}$ with a term of order m or of commutation of two terms with orders $p, q < m$. This defines a hierarchy of the coefficients because higher-order coefficients do not influence lower-order coefficients.

Taking the full flow (2.4.42) into account is inefficient, as many terms do not contribute to the target quantity, e.g. the ground state energy or dispersion, in order $\mathcal{O}(x^n)$. The epCUT approach aims to identify contributions $f_i^{(m)}$ which are required to obtain the flow to the target quantity in the target order and to truncate all other contributions. The flow equations (2.4.42) are then solved for all relevant $f_i^{(m)}(\ell)$. The algorithm for identifying only the relevant orders is explained in detail in Ref. [32].

The deepCUT scheme improves this approach [32]. The expansion to find the relevant contributions $f_i^{(m)}$ is still applied, but instead of integrating the individual orders $f_i^{(m)}(\ell)$ in (2.4.42), the flow equations (2.2.8) are integrated for the full monomial coefficients $h_i(\ell)$. This way, all relevant terms are considered in infinite order in x, which drastically increases the accuracy of the results [32], while the number of tracked coefficients is still minimized to only the minimum amount to obtain exact results of the target quantities up to order $\mathcal{O}(x^n)$.

Note that for discrete lattice systems, the small expansion parameter x often appears in the processes spanning over multiple sites. We will discuss examples of such models in Sec. 3.1.1 and Sec. 4.1.1 . For such systems, the minimum order n in x and the spatial extension of a process are often identical, so the truncation approach based on the order in n is similar to truncation based on real-space distance, see Sec. 2.4.2 . For this reason, the deepCUT approach can yield accurate results even in the high-perturbation regime $x \gtrapprox 1$ because only high-range effects are truncated [32]. However, note that deepCUT does not only truncate based on the order $\mathcal{O}(x^n)$, but performs an expansion so that the number of tracked monomials is reduced as far as possible, while the target quantity is still described in the desired order. Therefore, a true deepCUT approach is more efficient and accurate than a naive truncation based on the spatial extension.

In this work, the deepCUT scheme is applied to a spin ladder in Chap. 3 , for which a truncation in order $\mathcal{O}(x^n)$ truncates all terms of spatial extension above n.

2.5 Symmetries

The computational cost of the integration of the flow equations can be reduced significantly by making use of inherent symmetries of the Hamiltonian and algebraic symmetries.

2.5.1 Symmetries of the Hamiltonian

Numerically, symmetries can be implemented by treating the coefficients $\{h_i\}$ of multiple monomials $\{A_i\}$, which can be transformed into one another using symmetry transformation, as a single value in the flow equations (2.2.8). However, when calculating the tensor elements D_{ijk}, care must be taken to only count each unique contribution once.

We show explicitly how to adapt the tensor D_{ijk} when applying symmetries. We introduce the set

$$S[A_i] = \{A_j | A_j \cong A_i\} \,. \tag{2.5.43}$$

of all monomials A_j that can be obtained by applying symmetry transformations of the system on A_i. If $A_j \in S[A_i]$, then the coefficients of A_j and A_i must be identical. We define the number of monomials in the set

$$s[A_i] = \left|S[A_i]\right| \,. \tag{2.5.44}$$

Furthermore, we choose one representative $R_{\mathfrak{i}} \in S[A_i]$ from each set as a reference operator. The different index notation $\mathfrak{i}$ is used to imply that we have less representatives $R_{\mathfrak{i}}$ than operators A_i. We introduce the set of indices i corresponding to the representative $\mathfrak{i}$

$$I[R_{\mathfrak{i}}] = \{i | A_i \in S[R_{\mathfrak{i}}]\} \,. \tag{2.5.45}$$

At the beginning of the numerical treatment one must calculate all symmetry sets $S[R_{\mathfrak{i}}]$ and their sizes $s[R_{\mathfrak{i}}]$ by applying all symmetry transformations of the Hamiltonian multiple times on the operator basis. Typical transformations include translation, mirroring, rotations in spin-space and calculating the adjoint. The symmetry groups must then be considered in the flow equations (2.2.8) for the coefficients $h_{\mathfrak{i}}(\ell)$ of the representative $R_{\mathfrak{i}}$

$$\partial_\ell h_{\mathfrak{i}}(\ell) = \sum_{\mathfrak{j}} D_{\mathfrak{ijl}} h_{\mathfrak{j}}(\ell) h_{\mathfrak{l}}(\ell) \,. \tag{2.5.46}$$

with

$$D_{\mathfrak{ijl}} = \frac{1}{s[R_{\mathfrak{i}}]} \sum_{\substack{i \in I[R_{\mathfrak{i}}] \\ j \in I[R_{\mathfrak{j}}] \\ k \in I[R_{\mathfrak{l}}]}} D_{ijk} \,. \tag{2.5.47}$$

Note that it does not suffice to calculate only the commutators $[R_\mathrm{j}, R_\mathrm{l}]$ of the representatives in (2.2.7) to obtain the tensor D_ijl. However, it suffices to calculate the commutators $[R_\mathrm{j}, A_l]$, $\forall A_l \in S[R_\mathrm{l}]$, where only one of the representatives is expanded to the full group, rather than $[A_j, A_l]$, $\forall A_j \in S[R_\mathrm{j}], A_l \in S[R_\mathrm{l}]$, where both representatives are expanded.

2.5.2 Algebraic Symmetries

In addition to real symmetries between fundamentally different monomials, algebraic symmetries occur where one monomial can be notated in different fashions because of its algebra, i.e. because certain operators commute with one another. Let us consider a bosonic or hard-core bosonic algebra, where all annihilators commute with one another $[b_i, b_j] = 0$ and all creators commute with one another $[b_i^\dagger, b_j^\dagger] = 0$. Therefore terms such as

$$b_i^\dagger b_j^\dagger = b_j^\dagger b_i^\dagger \tag{2.5.48}$$

must share the same coefficient. While this equivalence is trivial analytically, it must be kept in mind for numerical implementations where one attempts to make use of the symmetries of H. If a symmetry transformation on A_i yields an algebraically equivalent version of A_i, rather than a truly new operator, then this symmetry transformation does not increase the group size $s[A_i]$. The algebraic group size $s_\mathrm{alg}[A_i]$ indicates the number of operators that are algebraically equivalent to A_i and is calculated for each basis monomial A_i. For instance, the algebraic group size of $b_i^\dagger b_j^\dagger$ is $s_\mathrm{alg}[b_i^\dagger b_j^\dagger] = 2$ for $i \neq j$ and $s_\mathrm{alg}[b_i^\dagger b_j^\dagger] = 1$ for $i = j$.

Tab. 2.1 shows possible group sizes for some simple bilinear and quartic monomials, which will be relevant in Chap. 4 . The column for index transformations only lists transformations which are independent from one another. These transformations can be applied one after another to calculate the whole set of algebraically equivalent monomials. The last column lists the possible algebraic group sizes $s_\mathrm{alg}[A_i]$. Note

A_i	Equivalent	Transformation	Possible $s_\mathrm{alg}[A_i]$
$b_i^\dagger b_j^\dagger$	$\cong b_j^\dagger b_i^\dagger$	$i \leftrightarrow j$	1, 2
$b_i^\dagger b_j^\dagger b_m b_n$	$\cong b_j^\dagger b_i^\dagger b_m b_n$	$i \leftrightarrow j$	1, 2, 4
	$\cong b_i^\dagger b_j^\dagger b_n b_m$	$m \leftrightarrow n$	
$b_i^\dagger b_j^\dagger b_m^\dagger b_n$	$\cong b_j^\dagger b_i^\dagger b_m^\dagger b_n$	$i \leftrightarrow j$	1, 3, 6
	$\cong b_i^\dagger b_m^\dagger b_j^\dagger b_n$	$j \leftrightarrow m$	

Table 2.1: Possible algebraic symmetries for selected bilinear and quartic monomials.

that the concrete value of $s_{\text{alg}}[A_i]$ depends on the values of the operator indices. In general, the algebraic group size $s_{\text{alg}}[A_i]$ can be calculated for a given monomial A_i by the formula

$$s_{\text{alg}} = \frac{N_c! N_a!}{\prod_i n_{c,i} \prod_i n_{a,i}} \tag{2.5.49}$$

where N_c (N_a) is the total number of creation (annihilation) operators found in the monomial while $n_{c,i}$ ($n_{a,i}$) is the number of creation (annihilation) operators with the same numerical index. We omit $[A_i]$ for sake of brevity. For example, the monomial $b_1^\dagger b_1^\dagger b_2^\dagger b_4$ has $N_c = 3$ creators and $N_a = 1$ annihilators. It consists of one creator $b_1^\dagger$ appearing twice and one unique creator $b_2^\dagger$ as well as one unique annihilator b_4. Therefore, we find $n_{c,1} = 2$, $n_{c,2} = 1$ and $n_{a,1} = 1$, which leads to $s_{\text{alg}} = \frac{3!\cdot 1!}{2\cdot 1\cdot 1} = 3$ possible permutations.

2.6 Termination Criterion: Residual-Off-Diagonality

In numerical calculations, one cannot perform the integration of (2.1.4) up to $\ell \to \infty$, but must stop at a finite ℓ_{fin} with $H(\ell_{\text{fin}}) \approx H_{\text{eff}}$. To determine whether the integration can be stopped, it is useful to define a measure of convergence. A well-established measure is the *residual-off-diagonality* (ROD) [44]

$$\text{ROD}[H] = \frac{1}{D}\sqrt{\sum_i \sum_{j\neq i} |h_{ij}|^2}\,, \tag{2.6.50}$$

of a D-dimensional matrix H, which measures the geometric norm of all off-diagonal elements. As the flow converges to a stable fixed point, the ROD converges to 0. Note that this formula can easily be adapted to

1. second quantization, in which case h_{ij} is replaced by the coefficients h_i of the operator monomials

$$\text{ROD}[H] = \sqrt{N \sum_i \frac{|h_i|^2}{N^{n(A_i)}}}\,. \tag{2.6.51}$$

   Here, one divides the summands by the system size N to the power of $n(A_i)$, which is the number of creation and annihilation operators that A_i consists of.

2. variants where not all off-diagonal elements are rotated away. In this case only the components which are supposed to be rotated away are included in the summation. To do this automatically, one can also define the ROD by the generator norm

$$\text{ROD}[H] = ||\eta||_2 = \frac{1}{D}\sqrt{\sum_{i,j} |\eta_{ij}|^2}\,. \tag{2.6.52}$$

This definition is equivalent to (2.6.50) if all generator elements fulfill either $|\eta_{nj}| = |h_{nj}|$ or $\eta_{nj} = 0$. This definition stresses that a vanishing ROD corresponds to a vanishing flow, i.e. $\eta = 0$ corresponds to $\partial_\ell H = 0$ in (2.1.4).

Chapter 3

Dynamic Correlations of Spin-1/2 Heisenberg Ladders

The previous chapter introduced important basics of the flow equation method, also known as CUT, and various important concepts such as truncation schemes. These methodical basics are applied in Chap. 3 to Chap. 5, which cover the three scientific problems of this thesis.

In this chapter, we apply the flow equation method to theoretically predict three-triplon bound states formed unambiguously by irreducible three-triplon interactions in realistic spin ladders that can be found in cuprates, i.e. compounds containing copper cations. We calculate the relevant structure factors and suggest experimental settings in which they can be measured to confirm our predictions. We perform the computations using the deepCUT scheme, see Sec. 2.4.3 , and Lanczos tridiagonalization [99]. Parts of the results presented in this chapter have been published in Ref. [44].

The chapter is structured in the following way: we define the spin-1/2 Heisenberg ladder and discuss the theoretical description of triplon excitations in Sec. 3.1 . Experimental methods to probe the system are explained in Sec. 3.2 and theoretical methods to predict the experimental results are introduced in Sec. 3.3, including the application of deepCUT in Sec. 3.3.2 . The results for various excitation channels are discussed in Sec. 3.4 . We conclude our findings and compare the predicted responses in the excitation channels in Sec. 3.5 .

3.1 Antiferromagnetic Spin-1/2 Heisenberg Ladder

3.1.1 Basic Model

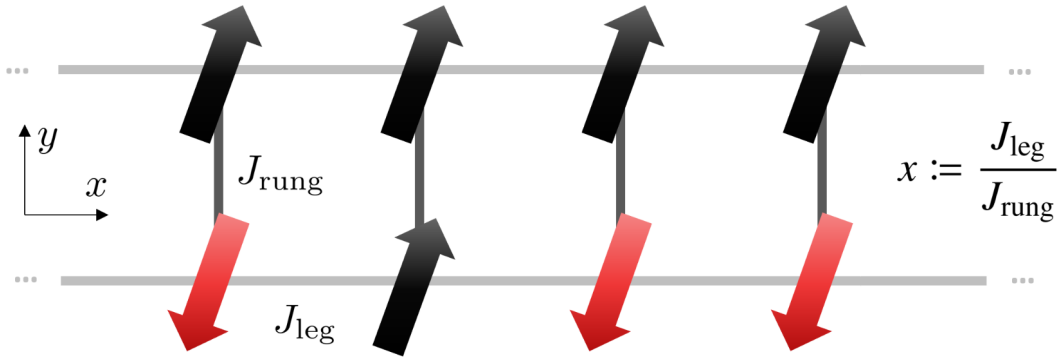

Figure 3.1: The antiferromagnetic two-leg spin-1/2 Heisenberg ladder. The spins are placed on the vertices of the spin ladder. The superexchange coupling to nearest neighbors in x-direction has strength J_{leg}, the coupling in y-direction J_{rung}. The relative coupling strength is parametrized by $x := J_{\text{leg}}/J_{\text{rung}}$.

We consider the **quasi-one-dimensional antiferromagnetic spin-1/2 ladder in the Heisenberg model**

$$H = \sum_{i=1}^{N} \left(J_{\text{rung}} \boldsymbol{S}_{i,1} \cdot \boldsymbol{S}_{i,2} + J_{\text{leg}} \sum_{\tau=0,1} \boldsymbol{S}_{i,\tau} \cdot \boldsymbol{S}_{i+1,\tau} \right) \tag{3.1.1}$$

with the vector spin operator $\boldsymbol{S}_{i,\tau}$ at the vertex intersecting rung i and leg $\tau \in \{0, 1\}$ and the next-neighbor superexchange interaction J_{rung} and J_{leg} in y- and x-direction, respectively. The ladder contains N rungs and the total spin of this system is a conserved quantity. Since global energy prefactors do not change the qualitative physics, the only free parameter of interest is the coupling ratio $x := J_{\text{leg}}/J_{\text{rung}}$, where $x = 0$ corresponds to the trivial case of N isolated **dimers**. Note that in some studies, the authors define x differently, since they focus on the regime close to isolated spin chains $x \gg 1$. In this thesis, we focus on the strongly dimerized regime $x \approx 0$ and the intermediate regime $x \approx 1$.

Spin ladders are of interest due to their relation to high-temperature superconductors and because they are an entangled magnetic many-body system that does not exhibit any long-range order [100, 101]. Heisenberg spin ladders are realized in cuprates to a high degree of accuracy with $x \gtrapprox 1$ [101].

Tab. 3.1 lists various cuprates that host spin ladders with either dominant rung couplings or dominant leg couplings. The corresponding value of x is specified for each material.

Cuprate	$x \approx$	Reference	Notes
$(5IAP)_2CuBr_4{\cdot}2H_2O$	0.077	[102]	
$KCuCl_3$	0.096-0.25	[103, 104]	best agreement with experiments when no diagonal interaction
$Cu_2(C_5H_{12}N_2)_2Cl_4$	0.2	[105]	plus small ferromagnetic diagonal interaction
$(C_5H_{12}N)_2CuBr_4$	0.29	[106]	
$La_6Ca_8Cu_{24}O_{41}$	1.0	[107]	plus small ring coupling
$(La,Ca)_{14}Cu_{24}O_{41}$	1-1.2	[108]	
$BiCu_2PO_6$	1.2	[36]	plus multiple further couplings
$Sr_{14}Cu_{24}O_{41}$	1.2	[49]	
$La_4Sr_{10}Cu_{24}O_{41}$	1.5	[109]	plus small ring coupling
$CaCu_2O_3$	12	[110]	

Table 3.1: Examples of cuprates that host spin ladders with various values of x. Dominant rung couplings correspond to $x < 1$ and dominant leg couplings correspond to $x > 1$. When possible, x is taken directly from the reference, otherwise it is calculated from $x = J_{\text{leg}}/J_{\text{rung}}$ rounded to two significant digits with J_{leg} and J_{rung} taken from the corresponding reference.

3.1.2 Triplons as Elementary Excitations

In this work, we start in the diagonal basis of the spin ladder with $x = 0$ and treat the leg terms through an expansion in x. For small x, the spin ladder dimerizes. The elementary excitations of dimerized systems in the strong coupling limit are quasi-particles known as **triplons** [111]. Since each dimer consists of two spins with $S = 1/2$, the combined spin divides into a singlet ($S_s = 0$) and triplet ($S_t = 1$). By defining the singlet state as the vacuum state, one can introduce triplon creation operators $(t^\alpha)^\dagger$ and annihilation operators t^α with flavors $\alpha \in \{x, y, z\}$ for a single dimer

$$|s\rangle = \quad |0\rangle = \frac{1}{\sqrt{2}}(|\uparrow\downarrow\rangle - |\downarrow\uparrow\rangle)\,, \tag{3.1.2a}$$

$$|x\rangle = (t^x)^\dagger\,|0\rangle = -\frac{1}{\sqrt{2}}(|\uparrow\uparrow\rangle - |\downarrow\downarrow\rangle)\,, \tag{3.1.2b}$$

$$|y\rangle = (t^y)^\dagger\,|0\rangle = \frac{\mathrm{i}}{\sqrt{2}}(|\uparrow\uparrow\rangle + |\downarrow\downarrow\rangle)\,, \tag{3.1.2c}$$

$$|z\rangle = (t^z)^\dagger\,|0\rangle = \frac{1}{\sqrt{2}}(|\uparrow\downarrow\rangle + |\downarrow\uparrow\rangle)\,. \tag{3.1.2d}$$

This definition of the operators t^α differs from the bond-operator representation [112, 113], which introduces an additional abstract state. Note that for all multiplet arrangements resulting from spin addition the multiplet with maximum total spin is symmetric under parity transformations (e.g. exchanging the two spins with one another) and the multiplets alternate between symmetric and antisymmetric configu-

ration under parity transformations. Therefore, the triplet states are symmetric and the singlet states are antisymmetric. This can also be verified by explicitly switching the spins in (3.1.2).

As a consequence of the different parity of singlet and triplet states, whenever the number of triplons in the spin-ladder system changes by an odd number, the parity of the system changes as well. Note that in this context, the parity of the spin ladder describes the (anti-)symmetry with respect to a reflection along the symmetry axis parallel to the x-axis, i.e. the transformation $\tau \leftrightarrow \bar{\tau} := 1 - \tau$ switching the two legs. A state of even parity remains unchanged after such a reflection, while a state of odd parity changes by a factor -1. The parity is relevant for the experimental selection of the excitation channels, see Sec. 3.2.1 .

To describe not only one but all dimerized rungs of the spin ladder, we reintroduce the indices i for the rung and τ for the leg in the operators $t^{\alpha}_{i,\tau}$. The triplon operators satisfy the hard-core boson commutation relation

$$\left[t_i^{\alpha}, t_j^{\beta\,\dagger}\right] = \delta_{i,j}\left(\delta_{\alpha,\beta}\left(\mathbb{1} - \sum_{\gamma} t_i^{\gamma\,\dagger} t_i^{\gamma}\right) - t_i^{\beta\,\dagger} t_i^{\alpha}\right) \tag{3.1.3}$$

including the triplon flavors $\alpha, \beta, \gamma \in \{x, y, z\}$. Triplon exitations also appear in other dimerized systems, such as Shastry-Sutherland magnets [23, 114, 115]. In Chap. 4 we will introduce a physical system which exhibits elementary excitations that can be described by flavorless hard-core bosons with a similar algebra (4.1.10a), which can be derived from (3.1.3) by applying the constraint $\alpha = \beta = \gamma$.

One can express the system (3.1.1) with triplon operators by using the relations

$$2S^{\alpha}_{i,1} = + t_i^{\alpha} + t_i^{\alpha\,\dagger} - \mathrm{i}\sum_{\beta\gamma} \epsilon_{\alpha\beta\gamma} t_i^{\beta\,\dagger} t_i^{\gamma}\,, \tag{3.1.4a}$$

$$2S^{\alpha}_{i,2} = - t_i^{\alpha} - t_i^{\alpha\,\dagger} - \mathrm{i}\sum_{\beta\gamma} \epsilon_{\alpha\beta\gamma} t_i^{\beta\,\dagger} t_i^{\gamma} \tag{3.1.4b}$$

to replace all spin operators and obtain

$$\frac{H}{J_{\mathrm{rung}}} = H^{(0)} + H^{(1)} \tag{3.1.5}$$

with

$$H^{(0)} = -\frac{3}{4}\sum_i \mathbb{1} + \sum_{i,\alpha} t_i^{\alpha\,\dagger} t_i^{\alpha}\,, \tag{3.1.6}$$

and

$$
\begin{aligned}
H^{(1)} = +\frac{x}{2}\Bigg[& \sum_{i,\alpha}\left(t_i^{\alpha\,\dagger}t_{i+1}^{\alpha} + t_{i+1}^{\alpha\,\dagger}t_i^{\alpha}\right) \\
& + \sum_{i,\alpha\neq\beta} t_i^{\alpha\,\dagger}t_{i+1}^{\beta\,\dagger}t_i^{\beta}t_{i+1}^{\alpha} \\
& - \sum_{i,\alpha\neq\beta} t_i^{\alpha\,\dagger}t_{i+1}^{\alpha\,\dagger}t_i^{\beta}t_{i+1}^{\beta} \\
& + \sum_{i,\alpha}\left(t_i^{\alpha\,\dagger}t_{i+1}^{\alpha\,\dagger} + t_i^{\alpha}t_{i+1}^{\alpha}\right)\Bigg] .
\end{aligned}
\tag{3.1.7a}
$$

Completely localized triplon excitations, which are restricted to a single rung without influencing neighboring rungs, only appear for $x = J_{\text{leg}}/J_{\text{rung}} = 0$. For $x > 0$, the triplons smear out over multiple rungs due to the finite leg couplings. Therefore, triplon excitations become more delocalized for increasing x. The extent of the delocalization is characterized by the correlation length ξ (See Sec. 2.4.2 for a brief discussion of correlation lengths). If x becomes too large and the energy gap closes, i.e. $\min_k \omega(k) \to 0$, a quantum phase transition occurs, the ground state is no longer described by the triplon vacuum state and triplons are no longer the elementary excitations of the system. In that case, the triplon picture no longer describes the system well. Furthermore, the correlation length diverges when the gap closes, see (2.4.32). For the simple Heisenberg ladder presented here, however, the gap only closes at $x \to \infty$ [116, 117]. Therefore, the triplon picture works for all finite x. The only restriction is that if one uses perturbative approaches in x in order $o_{\max}$, i.e. order $\mathcal{O}(x^{o_{\max}})$, which only consider effects spanning over a maximum of $o_{\max}$ rungs, then strongly delocalized triplons cannot be described correctly and the method fails for large values of x.

By examining the terms appearing in the Hamiltonian (3.1.7a), one can also ascertain that the number of triplons is in fact not a conserved quantity. On the one hand, this is a caveat, because a basis transformation is required to obtain delocalized, conserved quasi-particles. On the other hand, by transforming to a basis of conserved quasi-particles, this allows the observation of excitations consisting of various conserved quasi-particles. Since the parity is a conserved quantity, similar to the total spin of the system, the number of local triplons in the initial basis can only change by even numbers.

3.1.3 n-Triplon Bound States

Fig. 3.2 depicts the emergence of bound states in spin ladders. For increasing $x = J_{\text{leg}}/J_{\text{rung}}$, the triplon excitations in the conserving basis are delocalized over an increasing number of rungs and the attractive triplon interactions increase in

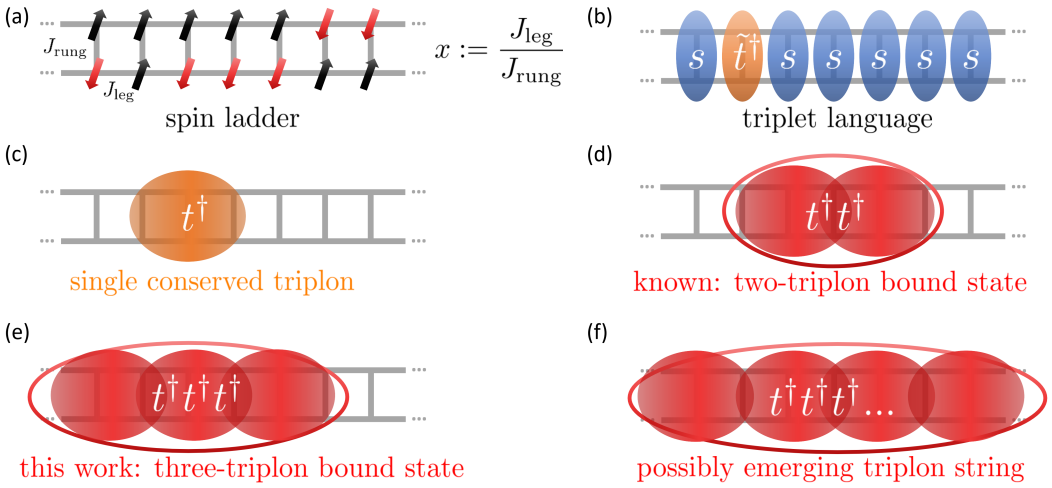

Figure 3.2: Emergence of multi-triplon bound states in spin ladders. (a) The $S = 1/2$ spins interact with their next neighbors with coupling strengths J_{leg} and J_{rung}. (b) For $x = J_{\text{leg}}/J_{\text{rung}} = 0$ the spins on each rung form a singlet (blue ellipses) in the ground state. The elementary excitations are local $S = 1$ triplons (orange ellipse). (c) For $x > 0$ the elementary excitations are delocalized $S = 1$ triplons. (d) Attractive two-triplon interactions lead to $S \in \{0, 1\}$ two-triplon bound states (red double-ellipse). (e) Strong three-triplon interactions lead to $S = 0$ three-triplon bound states, see Sec. 3.4.3 . (f) Strings of bound states containing n triplons are predicted for ladders with additional diagonal couplings (not shown). The emergence of three-triplon bound states without diagonal couplings suggests n-strings even without diagonal couplings. We also published this figure in Ref. [44].

strength. The two-triplon interactions lead to the formation of $S \in \{0, 1\}$ two-triplon bound states. Two-triplon bound states have been experimentally observed mediated by a phonon in infrared absorption for bound states with $S = 0$ [108] and using **inelastic neutron scattering (INS)** (see Sec. 3.2.2) for $S = 1$ [109]. Two-triplon bound states are also well established theoretically [111, 118, 119]. The color code (orange for free triplons and red for bound triplons) is also used in the result Sec. 3.4 .

Three-triplon bound states, however, have not been observed before in such systems. They have only been observed in completely frustrated Heisenberg spin ladders with antiferromagnetic diagonal couplings, where they result from two-triplon interactions [120]. We will show in Sec. 3.4.3 that for the Heisenberg ladder (3.1.1), three-triplon bound states result as a consequence of irreducible three-triplon interactions and cannot be formed by only two-body interactions.

Further n-triplon bound states with $n > 3$ are theoretically possible, as well, but the theoretical prediction is not possible with the currently available computational power when using the methods covered in this chapter. Nevertheless, triplon strings of many bound triplons offer an exciting prospect, especially since they generalize the concept of Bethe strings, which have already been detected in spin chains [121, 122],

	$S_{\text{tot}} = 0$ (SC)	$S_{\text{tot}} = 1$ (NSC)
three triplons odd parity		
two triplons even parity		
one triplon odd parity		
zero triplons even parity	ground state	

Table 3.2: The excitation channels are characterized by the parity and total spin. Both spin and parity are specified relative to the ground state, so the ground state is even by definition and no one-triplon $S = 0$ states or zero triplon $S = 1$ states exist. White shading indicates unphysical states, light blue shading indicates possible states and green shading indicates the ground state. Note that multi-triplon states containing $n > 3$ triplons and total spin $1 < S \leq n$ could, in principle, also be studied, but are beyond the scope of this thesis.

to a much broader class of non-integrable solid-state systems.

3.2 Experimentally Probing the System

3.2.1 Excitation Channels

The total spin and the parity, i.e. reflection symmetry with respect to the transformation $\tau \leftrightarrow \bar{\tau}$, are conserved quantities of the system. When probing the system from the ground state, one can selectively study subspaces of the full Hilbert space that have a total spin and parity that corresponds to the excitation one introduces to the system by probing.

The parity of the system depends on the number of triplon excitations, since each singlet has odd parity and each triplon even parity. The parity of the ground state can be either even or odd, depending on the number of rungs, but for the sake of simplicity we define parity with respect to the ground state, therefore defining the ground state to be of even parity. Each time a triplon is added to the system, one odd singlet is replaced by an even triplon, changing the total parity. Therefore, states with an even (odd) number of triplon have even (odd) parity. By choosing a probing method which either changes or preserves parity, one can selectively observe the channel with an even or odd number of triplons, respectively.

The ground state has a total spin of $S_0 = 0$, so the total spin is always determined by the number of triplons. A single triplon carries a spin of $S_1 = 1$. For $n > 1$ triplons, the total spin can be combined to $S_n \in \{0, 1, ..., n\}$. In this work, we focus on the **spin-conserving (SC) channel** $S = 0$ and a single **non-spin-conserving (NSC) channel** with $S = 1$.

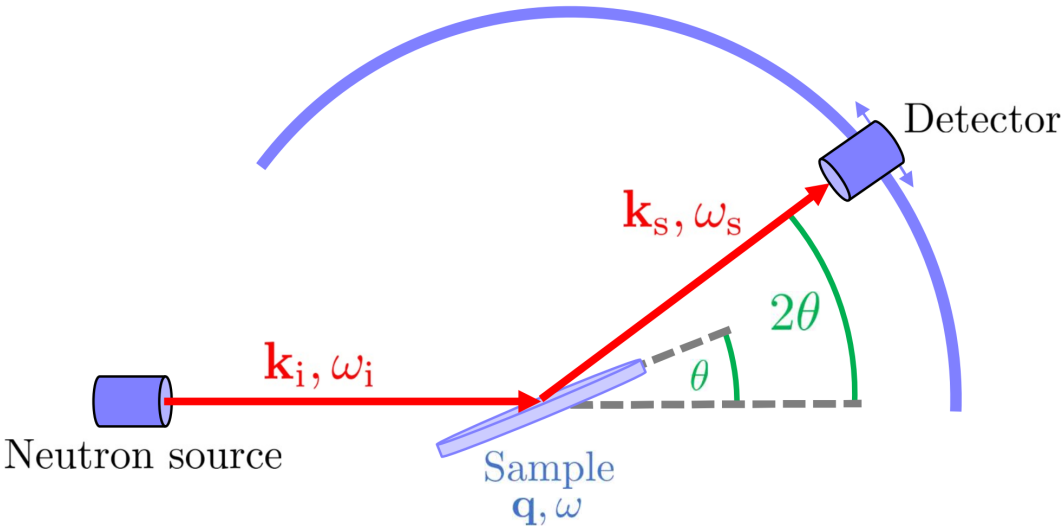

Figure 3.3: Schematic experimental setup of an inelastic neutron scattering experiment. The incident neutrons with frequency ω_i and momentum $\boldsymbol{k}_\mathrm{i}$ are scattered, transferring ω and $\boldsymbol{q}$ to the sample, and are measured in the detector with a scattered frequency ω_s and momentum $\boldsymbol{k}_\mathrm{s}$. Different $\boldsymbol{q}$ can be selected by rotating sample and detector by the angle θ and 2θ, respectively.

The different channels are illustrated in Tab. 3.2. An established method of experimentally probing the system is a scattering experiment, in which massive particles or photons are scattered at a sample of the material. By using such experiments, magnetic properties like spin correlation functions and features of the excitations can be studied [123, 124]. Depending on the experimental setup and the scattered particles, various channels and energy scales can be studied. In the following sections, we will introduce three probing techniques that are of interest for the theoretical predictions in this chapter.

3.2.2 Inelastic Neutron Scattering

INS is a standard technique for studying magnetic properties of solid-state systems, with the first experiments having been performed in the 1930s [33, 34]. The magnetic moment of the neutrons allows them to interact with unpaired electrons in magnetic atoms, opening up measurements of the magnetic properties of the studied sample. In contrast to charged particles, Coulomb interactions can be neglected when scattering neutral neutrons. The microscopic structure of the sample can be resolved by neutrons with wavelengths of approximately $10^{-10}\,\mathrm{m}$, which corresponds to energies in the order of meV. Such neutrons are called thermal neutrons and are commonly created using a nuclear research reactor or a particle accelerator. These facilities are expensive and the neutron flux is quite low. This limits the utility of INS, especially for small cross sections.

The basic experimental setup is shown in Fig. 3.3. A collimated neutron beam

is focused on the sample, where the neutrons and the sample interact with each other. The incident frequency ω_i (directly connected to the energy $E_\mathrm{i} = \hbar\omega_\mathrm{i}$) and momentum $\boldsymbol{k}_\mathrm{i}$ changes during the scattering process to the scattered frequency ω_s and momentum $\boldsymbol{k}_\mathrm{s}$. The transferred momenta $\boldsymbol{q} = \boldsymbol{k}_\mathrm{i} - \boldsymbol{k}_\mathrm{s}$ and $\omega = \omega_\mathrm{i} - \omega_\mathrm{s}$ determine the intensities of the scattered neutrons and are directly connected to the physical processes in the sample. By measuring the intensities of the scattered neutrons with a detector, one can obtain information about the microscopic structure of the sample.

For the spin-ladder system (3.1.1), which extends macroscopically in x-direction, but only has two different spins in y-direction, q_y is restricted to the two cases

$$q_y = 0 \qquad \text{parity conserved}\,, \tag{3.2.8a}$$

$$q_y = \frac{\pi}{a} \qquad \text{parity changes}\,. \tag{3.2.8b}$$

Keeping the channels in Tab. 3.2 in mind, this implies that one can select whether to probe an even ($q_y = 0$) or odd ($q_y = \pi/a$) number of triplons.

The differential cross section for the solid angle element $\mathrm{d}\Omega$ is

$$\frac{\mathrm{d}^2\sigma}{\mathrm{d}\Omega\mathrm{d}\omega} \propto \sqrt{\frac{\omega_\mathrm{f}}{\omega_\mathrm{i}}} S_\mathrm{DSF}(\boldsymbol{q},\omega) \tag{3.2.9}$$

with the **dynamic structure factor (DSF)** at zero temperature

$$S_\mathrm{DSF}(\boldsymbol{q},\omega) = \frac{1}{2\pi}\int_{-\infty}^{\infty} \mathrm{d}t e^{\mathrm{i}\omega t}\langle S^z(-\boldsymbol{q},t)\hat{S}^z(\boldsymbol{q},0)\rangle \tag{3.2.10a}$$

$$= \frac{1}{N}\sum_f \left|\left\langle f\middle|\sum_{i,\tau} e^{\mathrm{i}\boldsymbol{q}\boldsymbol{R}_{i,\tau}} S_i^z\middle|g\right\rangle\right|^2 \delta(\omega_\mathrm{f} - \omega_\mathrm{g} + \omega)\,, \tag{3.2.10b}$$

which can be expressed as the Fourier transform of the spin-spin correlation function $\langle S^z(-\boldsymbol{q},t)S^z(\boldsymbol{q},0)\rangle$ [125]. The symbols $|g\rangle$ and $|f\rangle$ are the ground state and final state with respective energies ω_g and ω_f. Correlation functions for other flavors than z can be considered, as well, but do not reveal any further information for a system with spin isotropy. To predict the results of INS measurements, we will focus on the DSF defined above. We will also consider other relevant structure factors, therefore it makes sense to define the general form of structure factors

$$S(\boldsymbol{q},\omega) = \frac{1}{N}\sum_f \left|\left\langle f\middle|\sum_{i,\tau} e^{\mathrm{i}\boldsymbol{q}\boldsymbol{R}_{i,\tau}} O\middle|g\right\rangle\right|^2 \delta(\omega_\mathrm{f} - \omega_\mathrm{g} + \omega)\,, \tag{3.2.11}$$

which can be evaluated for other observables O, as well.

The DSF measured by INS experiments covers only the NSC channel with transferred spin $S = 1$. To study the SC channel, one needs to employ other experimental techniques, e.g. electromagnetic scattering techniques, one of which we discuss in the following section.

3.2.3 Resonant Inelastic X-Ray Scattering

Historically, electromagnetic light (i.e. photons) in the X-ray frequency range has seen widespread use in medical screening, but has also been used in elastic X-ray spectroscopy by the Bragg brothers as early as 1912 [126]. **Resonant inelastic X-ray scattering (RIXS)** is a specialized application of X-ray scattering, where the X-ray energy corresponds to the X-ray transitions of core-level electrons of the studied material, which leads to a resonant enhancement of the cross section by several orders of magnitude [45]. During scattering, energy, momentum and polarization are transferred from the incident photon to the sample and therefore to the material's inherent excitations. By selectively changing the properties of the incident photons in the RIXS experiment, specific edges with unique scattering properties can be probed [127]. This allows one to study the subset of excitations that appear in the selected probing channel. Of particular interest to us is the fact that the SC channel can be probed by RIXS. While RIXS does not provide the same energy resolution as INS, it covers a wider scattering phase space and requires only small sample volumes [45].

The basic idea of the experimental setup is similar to the INS setup in Fig. 3.3. While photons are used instead of neutron, RIXS experiments also measure the amplitude of the scattered X-rays for various transferred energies ω and momenta $\boldsymbol{q}$. During the scattering process, excitations in the material can be created by direct or indirect RIXS processes.

A direct RIXS process is shown in Fig. 3.4. When a photon of momentum $\boldsymbol{k}_\mathrm{i}$ and energy ω_i hits the probe, it can excite a core-level electron to an empty state in the valence band. The empty core level can now be filled by one of various other electrons from occupied states with different energies and momenta. When the core-level state is filled, a photon of momentum $\boldsymbol{k}_\mathrm{f}$ and energy ω_f is emitted, which can then be measured by the detector.

An indirect RIXS process is shown in Fig. 3.5. In an indirect RIXS process the same electron that is excited decays back to the core-level. The energy and momentum scattering occurs due to Coulomb interactions of the core hole (or the excited electron) and the valence electrons.

By tuning the incident energy ω_i to the binding energy of specific core-level electrons in specific atoms and choosing appropriate polarization, those electrons can be excited selectively [127]. Since those energies appear as singular edges in the absorption rate, see Fig. 3.6, it is common to refer to the excited core-level by the corresponding edge. For example, when one mentions probing at the Cu K-edge, then that person refers to exciting the 1s electrons of Cu atoms.

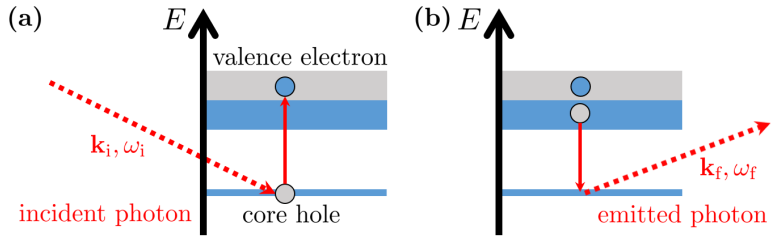

Figure 3.4: Direct RIXS process, where (a) a photon of momentum $\boldsymbol{k}_\mathrm{i}$ and energy ω_i excites a core-level electron to an unoccupied state in the valence band. (b) An electron from an occupied state decays to the core level, emitting a photon of momentum $\boldsymbol{k}_\mathrm{f}$ and energy ω_f in the process. [45–49]

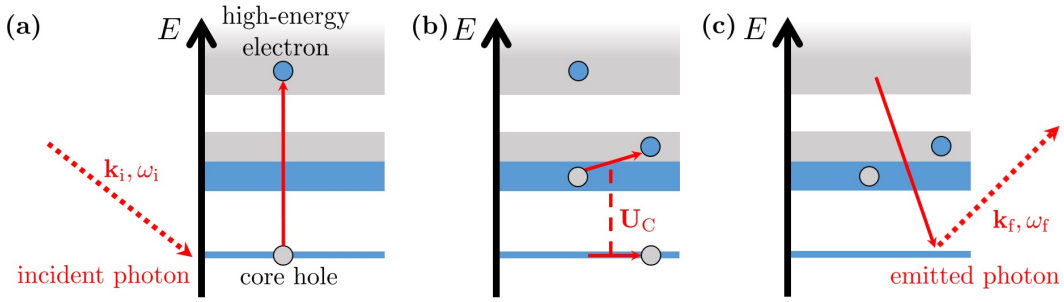

Figure 3.5: Indirect RIXS process, where (a) a photon of momentum $\boldsymbol{k}_\mathrm{i}$ and energy ω_i excites a core-level electron to an unoccupied high-energy state. (b) In the intermediate state, the Coulomb interaction U_C between the core-level hole and an electron in the conduction band leads to an excitation of the electron. (c) In the final state, the high-energy electron decays back into the core-level and a photon of momentum $\boldsymbol{k}_\mathrm{f}$ and energy ω_f is emitted. [45–49]

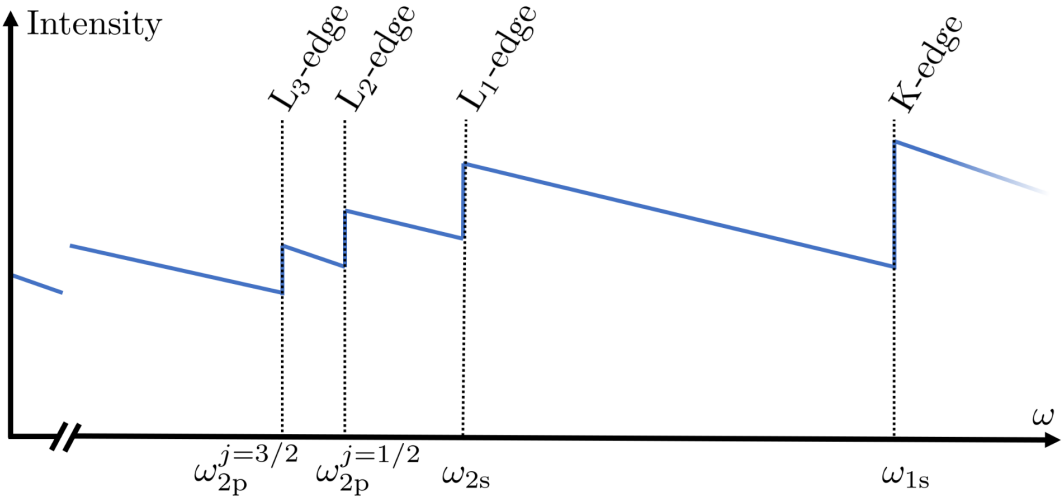

Figure 3.6: Schematic plot of X-ray absorption edges arising when the absorbed energy ω resonantly excites a core-level electron. The vertical, dotted lines mark the core-level energies. Note that the energies $\omega_{2\mathrm{p}}^{j=3/2}$ at the L_3-edge and $\omega_{2\mathrm{p}}^{j=1/2}$ at the L_2-edge are clearly separated in presence of strong spin-orbit coupling, e.g. in Cu atoms [50].

Different edges have different properties. For example, probing the Cu K-edge or oxygen K-edge in cuprates leads purely to SC excitations [46,128], while probing the Cu L_3-edge leads to both SC and NSC contributions [129, 130].

Two important advantages of RIXS experiments over INS experiments are the high cross section at large energies and the fact that the SC channel can be probed separately from the NSC channel [45]. Probing at the Cu K-edge also provides enough initial momentum to induce significant momentum transfer $\boldsymbol{q}$. The full response function, however, is more challenging to calculate than the DSF (3.2.10), which is the response function of INS experiments. This increases the computational complexity of theoretical predictions. In the following, we will discuss how to calculate the leading orders in core-hole lifetime of the RIXS response both in the SC and the NSC channel.

3.2.3.1 Indirect RIXS Response

The RIXS response of the indirect process can be approximated using the **ultrashort core-hole lifetime (UCL) approximation** [37, 45, 47, 48, 50]. The full derivation is presented in App. A. While the NSC channel is described well by the DSF (3.2.10), the RIXS response in first order in the SC channel is given by the more complicated **dynamic exchange structure factor (DESF)** at zero temperature

$$S_{\mathrm{DESF}}(\boldsymbol{q},\omega) = \frac{1}{N}\sum_f \left|\left\langle f\middle|\sum_{i,\tau} e^{\mathrm{i}\boldsymbol{q}\boldsymbol{R}_{i,\tau}} O^{\mathrm{ex}}_{i,\tau}\middle|g\right\rangle\right|^2 \delta(\omega_{\mathrm{f}}-\omega_{\mathrm{g}}+\omega)\,, \tag{3.2.12a}$$

$$O^{\mathrm{ex}}_{i,\tau} = \mathbf{S}_{i,\tau}\cdot\left[J_{\mathrm{leg}}\left(\mathbf{S}_{i+1,\tau}+\mathbf{S}_{i-1,\tau}\right)+J_{\mathrm{rung}}\mathbf{S}_{i,\bar{\tau}}\right] \tag{3.2.12b}$$

with the spin exchange observable $O^{\mathrm{ex}}_{i,\tau}$. For efficient numerical calculations, it is useful to work with observables of fixed parity. For this reason, we introduce the observable

$$O^{\mathrm{ex}}_{i,\pm} = O^{\mathrm{ex}}_{i,1} \pm O^{\mathrm{ex}}_{i,2} \tag{3.2.13}$$

with the two cases

$$O^{\mathrm{ex}}_{i,+} = J_{\mathrm{leg}}\sum_\tau \mathbf{S}_{i,\tau}\cdot\left(\mathbf{S}_{i+1,\tau}+\mathbf{S}_{i-1,\tau}\right)+2J_{\mathrm{rung}}\mathbf{S}_{i,1}\cdot\mathbf{S}_{i,2}\,, \tag{3.2.14a}$$

$$O^{\mathrm{ex}}_{i,-} = J_{\mathrm{leg}}\sum_\tau \mathbf{S}_{i,\tau}\cdot\left(\mathbf{S}_{i+1,\tau}+\mathbf{S}_{i-1,\tau}\right)(-1)^{\tau-1} \tag{3.2.14b}$$

and obtain

$$S^{\pm}_{\mathrm{DESF}}(q_x,\omega) = \frac{1}{N}\sum_f \left|\left\langle f\middle|\sum_{i} e^{\mathrm{i}q_x R_i} O^{\mathrm{ex}}_{i,\pm}\middle|g\right\rangle\right|^2 \delta(\omega_{\mathrm{f}}-\omega_{\mathrm{g}}+\omega)\,. \tag{3.2.15}$$

The even DESF $S^{+}_{\mathrm{DESF}}(q_x,\omega)$ describes excitations of an even number of triplons, while $S^{-}_{\mathrm{DESF}}(q_x,\omega)$ describes excitations of an odd number of triplons. Tab. 3.3 depicts how the different channels of the spin ladder (3.1.1) can be probed using INS

	$S = 0$ (SC)	$S = 1$ (NSC)
three triplons odd parity	RIXS	INS, RIXS
two triplons even parity	RIXS	INS, RIXS
one triplon odd parity		INS, RIXS
zero triplons even parity	ground state	

Table 3.3: The excitation channels are characterized by the parity and total spin. Both spin and parity are specified relative to the ground state, so the ground state is even by definition and no one-triplon $S = 0$ states or zero-triplon $S = 1$ states exist. While INS can only probe the NSC channel with the observable $S^z_{i,\tau}$, RIXS has a rich spectrum in both the SC and NSC channel, which is described by various observables.

and RIXS at the Cu K-edge. Just like for the INS, q_y is restricted to the two cases described in (3.2.8) and can be used to selectively probe an even or odd number of triplons. Note that (3.2.13) does not require a normalizing prefactor $1/2$ because the structure factor is only proportional to the experimental response and global prefactors do not change the relative weights at different values of ω and $\boldsymbol{q}$.

The observables $O^{\Delta S,k}_{i,\tau,\sigma}$ for higher orders of the UCL expansion in the SC and NSC channel, respectively, are

$$O^{\mathrm{SC},k}_{i,\tau} = \left(J_{\mathrm{rung}} \boldsymbol{S}_{i,\tau} \cdot \boldsymbol{S}_{i,\bar{\tau}} + J_{\mathrm{leg}} \boldsymbol{S}_{i,\tau} \cdot \left(\boldsymbol{S}_{i+1,\tau} + \boldsymbol{S}_{i-1,\tau} \right) \right)^k , \; k \geq 1 \tag{3.2.16}$$

and

$$O^{\mathrm{NSC},k}_{i,\tau} = S^z_{i,\tau} \left(J_{\mathrm{rung}} \boldsymbol{S}_{i,\tau} \cdot \boldsymbol{S}_{i,\bar{\tau}} + J_{\mathrm{leg}} \boldsymbol{S}_{i,\tau} \cdot \left(\boldsymbol{S}_{i+1,\tau} + \boldsymbol{S}_{i-1,\tau} \right) \right)^k , \; k \geq 0 , \tag{3.2.17}$$

which is derived in App. A. The index σ used in App. A is neglected here because it no longer appears in the observables. Note that the NSC observable is non-Hermitian for $k > 0$. The two leading orders in each channel are

$$O^{\mathrm{NSC},0}_{i,\tau} = S^z_{i,\tau} , \tag{3.2.18a}$$

$$O^{\mathrm{NSC},1}_{i,\tau} = S^z_{i,\tau} \left(J_{\mathrm{rung}} \boldsymbol{S}_{i,\tau} \cdot \boldsymbol{S}_{i,\bar{\tau}} + J_{\mathrm{leg}} \boldsymbol{S}_{i,\tau} \cdot \left(\boldsymbol{S}_{i+1,\tau} + \boldsymbol{S}_{i-1,\tau} \right) \right) , \tag{3.2.18b}$$

$$O^{\mathrm{SC},1}_{i,\tau} = \left(J_{\mathrm{rung}} \boldsymbol{S}_{i,\tau} \cdot \boldsymbol{S}_{i,\bar{\tau}} + J_{\mathrm{leg}} \boldsymbol{S}_{i,\tau} \cdot \left(\boldsymbol{S}_{i+1,\tau} + \boldsymbol{S}_{i-1,\tau} \right) \right) , \tag{3.2.18c}$$

$$O^{\mathrm{SC},2}_{i,\tau} = \left(J_{\mathrm{rung}} \boldsymbol{S}_{i,\tau} \cdot \boldsymbol{S}_{i,\bar{\tau}} + J_{\mathrm{leg}} \boldsymbol{S}_{i,\tau} \cdot \left(\boldsymbol{S}_{i+1,\tau} + \boldsymbol{S}_{i-1,\tau} \right) \right)^2 . \tag{3.2.18d}$$

Note that $O^{\mathrm{NSC},0}_{i,\tau}$ corresponds to the DSF observable and $O^{\mathrm{SC},1}_{i,\tau}$ to the DESF observable. Analogous to (3.2.15), it is useful to calculate the response function for

(anti-)symmetrized observables $O_{i,\pm}^{(\mathrm{N})\mathrm{SC},k} = O_{i,1}^{(\mathrm{N})\mathrm{SC},k} \pm O_{i,2}^{(\mathrm{N})\mathrm{SC},k}$. The symmetric observable excites an even number of triplons and the antisymmetric observable excites an odd number of triplons. The (anti-)symmetrized response for a general observable O can be calculated with the

$$S^{\pm}(q_x,\omega) = \frac{1}{N}\sum_f \left|\left\langle f\right|\sum_i e^{\mathrm{i}q_x R_i} O_{i,\pm}^{\Delta S,k}\left|g\right\rangle\right|^2 \delta(\omega_\mathrm{f} - \omega_\mathrm{g} + \omega)\,, \tag{3.2.19a}$$

$$O_{i,\pm}^{\Delta S,k} = O_{i,1}^{\Delta S,k} \pm O_{i,2}^{\Delta S,k}\,. \tag{3.2.19b}$$

In the following calculations for general observables, we use the symbol $O_i^{\pm}$ instead of $O_{i,\pm}^{\Delta S,k}$ for brevity.

3.2.4 Terahertz Spectroscopy

To verify our findings in the SC channel, see Sec. 3.4.3 , a third experimental method with higher energy resolution is necessary, which is briefly presented in this section. This method is **terahertz spectroscopy**, which utilizes strong electromagnetic fields and has been used successfully in the past to observe Bethe strings [121]. In principle, any probing in the terahertz frequency range of $0.1 - 20\,\mathrm{THz}$ can be considered terahertz spectroscopy, but the term often refers to time-resolved THz spectroscopy, where THz pulses are generated and detected in a synchronous, coherent manner using visible or near-IR laser pulses [131].

A distinct advantage of THz spectroscopy is the time-resolution, which is not directly relevant for our work here. Furthermore, it is possible to measure not only the intensity of the electric field, but both the amplitude and phase of each spectral component of the pulse. Most importantly, THz experiments offer a much higher energy resolutions than RIXS, which allows one to distinguish features with similar energies. While RIXS experiments offer typical energy resolutions of (10-100) meV [130, 132], THz spectroscopy can achieve resolutions below 1 MHz [133, 134], which corresponds just a few neV. However, THz spectroscopy does not allow high momentum transfer, which limits the covered scattering phase space.

3.3 Calculating the Response

The DESF is usually calculated using exact diagonalization [37–40] or density matrix renormalization groups [43]. In this work, we apply the deepCUT scheme with an expansion in x and the ps-generator (2.3.25) to separate subspaces of different number of triplons to arrive at high resolution results of the DESF. One additional advantage of this approach is the fact that n-particle interactions can be activated and deactivated selectively. In the following, the necessary analytical equations and numerical methods to compute spectral weights are presented.

3.3.1 Green's Function

The structure factor (3.2.19) can be expressed in terms of a Green's function

$$S^{\pm}(q_x,\omega) = -\frac{1}{\pi}\mathrm{Im}[G^{\pm}(q_x,\omega)] \tag{3.3.20}$$

at temperature $T = 0$ in accordance with the fluctuation-dissipation theorem [135]. One can calculate the Green's function by using the resolvent

$$G^{\pm}(q_x,\omega) = \left\langle g \middle| \left(O^{\pm}_{q_x}\right)^{\dagger} \frac{1}{\omega - H(q_x) - E_0 + i0^+} O^{\pm}_{q_x} \middle| g \right\rangle, \tag{3.3.21}$$

$$O^{\pm}_{q_x} = \frac{1}{\sqrt{N}} \sum_i O^{\pm}_i e^{\mathrm{i}q_x R_i} \tag{3.3.22}$$

with the Hamiltonian H, the ground state energy E_0 and the Fourier transformed observables $O^{\pm}_{q_x}$.

3.3.2 Separating Triplon Spaces using deepCUT

We apply the deepCUT scheme, see Sec. 2.4.3 , to separate the n-triplon spaces in the effective Hamiltonian $H_{\mathrm{eff}}(q_x)$, i.e. the Hamiltonian in an effective basis. To this end, we transform both the Hamiltonian $H(q_x)$ and the observable $O^{\pm}_{q_x}$ and obtain the effective operators $H_{\mathrm{eff}}(q_x)$ and $O^{\pm}_{q_x,\mathrm{eff}}$. The ground state in the effective basis is the triplon vacuum state $|g_{\mathrm{eff}}\rangle$ and the resolvent can be expressed as

$$G^{\pm}(q_x,\omega) = \left\langle g_{\mathrm{eff}} \middle| \left(O^{\pm}_{q_x,\mathrm{eff}}\right)^{\dagger} \frac{1}{\omega - H_{\mathrm{eff}}(q_x) - E_0 + i0^+} O^{\pm}_{q_x,\mathrm{eff}} \middle| g_{\mathrm{eff}} \right\rangle. \tag{3.3.23}$$

The effective Hamiltonian $H_{\mathrm{eff}}(q_x)$ conserves the number of triplons, which makes the evaluation of the fraction significantly easier, since the calculation can be performed for each n-triplon subspace separately. Since the momentum q_x and energy ω are conserved by $H_{\mathrm{eff}}(q_x)$ and $O^{\pm}_{q_x,\mathrm{eff}}$ creates triplon excitations of total momentum q_x, as well, one can also perform the calculations for different q_x separately. The calculations for different ω, however, cannot be separated completely, because $O^{\pm}_{q_x,\mathrm{eff}}$ does not create excitations of a single specific energy ω, but of various energies at once.

The effective exchange observable $O^{\pm}_{q_x,\mathrm{eff}}$ consists of operator monomials that create or annihilate multiple triplons. Since it is applied to the vacuum ground state $|g\rangle$ in (3.3.23), one only needs to consider contributions that create a fixed number of n triplons at once. Effectively, one can calculate the full Green's function by summing over all n-triplon Green's functions up to a certain $n_{\max}$

$$G^{\pm}(q_x,\omega) = \sum_{n=1}^{n_{\max}} G^{\pm}_{n\ \mathrm{triplons}}(q_x,\omega)\,. \tag{3.3.24}$$

One can also choose to selectively calculate the Green's function $G^{\pm}_{n\ \mathrm{triplons}}(q_x,\omega)$ for a specific number of triplons n to examine the response in this channel. This is useful

if the energy continua of channels with an even (odd) number of triplons overlap, in which case multiple channels lead to spectral weight in the same region of phase space. Furthermore, one can selectively enable or disable m-triplon interactions for various m in $H_{\text{eff}}(q_x)$ to investigate the effects of those interactions. Being able to selectively choose the number of excited triplons and considered interactions is a fundamental advantage of the flow equation method over other methods such as exact diagonalization.

3.3.3 Lanczos Tridiagonalization

We employ the

Lanczos Algorithm

$$|\Psi_0\rangle = O^{\pm}_{q_x,\text{eff}}\,|g\rangle\ , \tag{3.3.25a}$$

$$|\Psi_1\rangle = (H_{\text{eff}}(q_x) - a_0)\,|\bar{\Psi}_0\rangle\ , \tag{3.3.25b}$$

$$|\Psi_{n+1}\rangle = (H_{\text{eff}}(q_x) - a_n)\,|\bar{\Psi}_n\rangle - b_n^2\,|\bar{\Psi}_{n-1}\rangle \quad \forall n \in \mathbb{N}_+\,, \tag{3.3.25c}$$

$$|\bar{\Psi}_n\rangle = \frac{|\Psi_n\rangle}{b_n} \qquad \forall n \in \mathbb{N}_0 \tag{3.3.25d}$$

with the

Lanczos Coefficients (LC)

$$a_n(q_x) = \frac{\langle\Psi_n|\,H_{\text{eff}}(q_x)\,|\Psi_n\rangle}{\langle\Psi_n|\Psi_n\rangle} \qquad \forall n \in \mathbb{N}_0\,, \tag{3.3.26a}$$

$$b_0^2(q_x) = \langle\Psi_0|\Psi_0\rangle\ , \tag{3.3.26b}$$

$$b_n^2(q_x) = \frac{\langle\Psi_n|\Psi_n\rangle}{\langle\Psi_{n-1}|\Psi_{n-1}\rangle} \qquad \forall n \in \mathbb{N}_+ \tag{3.3.26c}$$

to calculate a tridiagonal expression for the effective Hamiltonian

$$H_{\text{eff}}(q_x) = \begin{pmatrix} a_0(q_x) & b_0(q_x) & 0 & \cdots \\ b_0(q_x) & a_1(q_x) & b_1(q_x) & \cdots \\ 0 & b_1(q_x) & a_2(q_x) & \cdots \\ \vdots & \vdots & \vdots & \ddots \end{pmatrix} \tag{3.3.27}$$

in the Krylov subspace that is created by repeatedly applying H_{eff} on $|\Psi_0\rangle$ [99]. The central idea of the Lanczos algorithm is finding the most important eigenvalues and eigenvectors of the matrix $H_{\text{eff}}(q_x)$, which in most cases are the most extreme eigenvalues, without diagonalizing the full matrix. The multiplication step $(H_{\text{eff}}(q_x) - a_n)\,|\bar{\Psi}_n\rangle$ in the algorithm (3.3.25) reveals that the Lanczos method is an adaption of the more naive power method $|\Psi_n\rangle = H^n_{\text{eff}}(q_x)\,|\Psi_0\rangle$.

When performing Lanczos tridiagonalization, one commonly samples a random initial state $|\Psi_0\rangle$ so that it is preferably not orthogonal to any eigenvector of $H_{\text{eff}}(q_x)$.

This ensures that all eigenvectors and -values can be acquired by repeatedly applying $H_{\text{eff}}(q_x)$. In the Green's function (3.3.23), the resolvent is applied to the initial state $O^{\pm}_{q_x,\text{eff}}|g\rangle$. Therefore, only states accessible from $|\Psi_0\rangle = O^{\pm}_{q_x,\text{eff}}|g\rangle$ are relevant for the computation of the Green's function.

To obtain results for fixed momenta q_x, the calculation is performed in momentum space in the basis of Fourier transformed n-triplon states. In real space, the n-triplon states can be denoted $|r_0,\alpha_0\rangle ... |r_{n-1},\alpha_{n-1}\rangle$ with triplons of flavors α_i at rungs r_i with $r_{i+1} > r_i \; \forall i \in \mathbb{N}_0$. The Fourier transformed states are

$$|q_x,\alpha_0\rangle = \frac{1}{\sqrt{N}} \sum_{r_0} e^{\mathrm{i}q_x r_0} |r_0,\alpha_0\rangle \,, \tag{3.3.28a}$$

$$|q_x,\alpha_0\rangle|d_1,\alpha_1\rangle = \frac{1}{\sqrt{N}} \sum_{r_0} e^{\mathrm{i}q_x \frac{r_0+r_1}{2}} |r_0,\alpha_0\rangle|r_1,\alpha_1\rangle \,, \tag{3.3.28b}$$

$$|q_x,\alpha_0\rangle ... |d_n,\alpha_n\rangle = \frac{1}{\sqrt{N}} \sum_{r_0} e^{\mathrm{i}q_x \frac{r_0+...+r_n}{n+1}} |r_0,\alpha_0\rangle ... |r_n,\alpha_n\rangle \tag{3.3.28c}$$

with the distance $d_i := r_i - r_{i-1} \; \forall i \in \mathbb{N}_+$ between two consecutive triplons in real space. Note that only the space index r_0 is replaced by a momentum q_x, while the information about the relative distances d_i between the triplons still exists in the momentum space basis states.

When a numerically small coefficient $|b_n| < 10^{-8}$ is obtained at any point of the Lanczos tridiagonalization, we assume that we have completely exhausted the Krylov space and terminate the algorithm. Since the Hilbert space is infinite and the Krylov space can be infinite as well, an additional termination criterion is necessary. We assume that states with high distances d_i between triplons do not contribute to the spectral weight in a significant way, which is justified by the fact that the initial Hamiltonian (3.1.1) consists of highly localized interactions. After switching to the effective basis using deepCUT, $H_{\text{eff}}(q_x)$ contains delocalized interactions spanning multiple rungs, but unless x is chosen to be very large, the interaction strength decreases quickly with the number of spanned rungs. Furthermore the deepCUT method performs a truncation by an expansion in x, which effectively only considers interactions spanning a maximum number of rungs, so $H_{\text{eff}}(q_x)$ is already localized because of the deepCUT truncation scheme. To utilize this, we introduce a maximum distance $d_{\max}$ and truncate states that do not fulfill

$$d_i \leq d_{\max} \quad \forall i \in N_+ \,. \tag{3.3.29}$$

In this way, we only consider states where the triplons are close enough to each other. Typical values of $d_{\max}$ in our calculations are 2000 for two triplons and 1000 for three triplons. For one triplon, the value of $d_{\max}$ is irrelevant and only one Lanczos coefficient appears, i.e. the Hamilton operator can be evaluated directly. After performing a deepCUT of order o in the perturbation parameter x on the

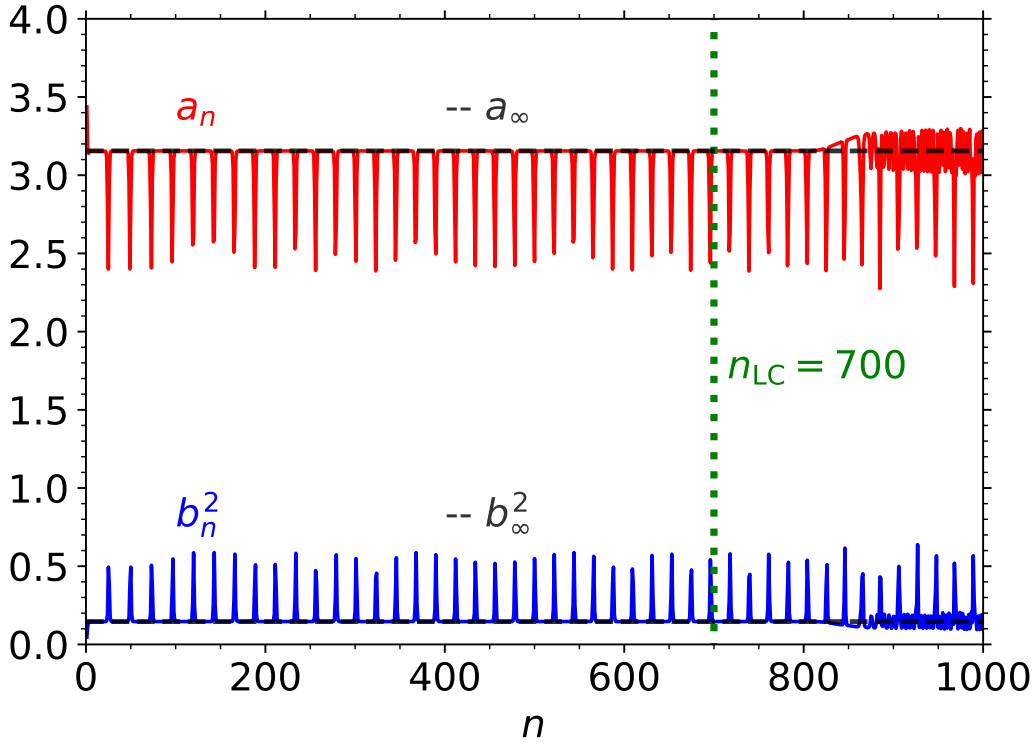

Figure 3.7: An example of calculated Lanczos coefficients a_n and b_n^2 for the observable $O^+_{q_x,\text{eff}}$ in two-triplon space at $q_x = \pi/a$ for the perturbation parameter $x = 1.0$, perturbation order $o = 10$ and maximum distance $d_{\max} = 2000$. Despite the critical limit of coefficients being $n_{\text{LC,crit}} = 200$, first significant errors appear only at $n_{\text{LC}} > 800$. Because we manually choose a single limit $n_{\text{LC, max}}$ of used coefficients that must be valid for multiple values of q_x, $n_{\text{LC}} = 700$ was chosen for this dataset. The horizontal dashed lines mark the calculated values of a_∞ and b_∞.

spin ladder (3.1.5) in triplon language, triplon jump processes $t^\dagger_{i+\Delta} t_i$ spanning over $|\Delta| \leq o$ rungs can appear in H_{eff}. Therefore, when one calculates at least

$$n_{\text{LC}} > n_{\text{LC, crit}} = \frac{d_{\max}}{o} \tag{3.3.30}$$

Lanczos coefficients, the truncation in d_i introduces errors to the Lanczos coefficients. However, even beyond $n_{\text{LC,crit}}$ one can calculate multiple coefficients with negligibly small errors. Since a higher number of calculated Lanczos coefficients leads to a higher accuracy of the calculated spectral weights, we continue the calculation beyond $n_{\text{LC,crit}}$ and manually check how many coefficients n_{LC} can be used for the calculation of the response (3.2.19). We choose the number of coefficients n_{LC} such that qualitative deviations from the quasi-periodic behavior are cut off. Typical values are $n_{\text{LC}}/n_{\text{LC,crit}} = 2$–$6$, but how many values can be used in a specific case depends on various parameters like x and q_x.

Fig. 3.7 shows an example of calculated coefficients a_n and b_n^2 for $o = 10$ and $d_{\max} = 2000$. After a very short initial convergence to the horizontal dashed lines,

the Lanczos coefficients show a quasi-periodic behavior. Most of the coefficients are on the dashed lines, but periodically some coefficients show a short peak of varying amplitude. At around $n_{\mathrm{LC}} > 800$, clear deviations from the quasi-periodic behavior can be observed, which arise due to the truncation errors of $d_{\max}$. For the dataset shown here, the maximum number of considered Lanczos coefficients is set to $n_{\mathrm{LC}} = 700$, which is significantly lower than the point where the first clear errors appear. We choose $n_{\mathrm{LC}} = 700$ for this dataset because we manually choose a single value of n_{LC} for all datasets which share the same observable, x, o and $d_{\max}$ but differ in q_x. Manually choosing an individual n_{LC} for each value of q_x would be an immense effort without providing significant increases in accuracy. We show in Sec. D.1 for one example that the choice of n_{LC} is large enough so that the result does not suffer from any perceptible errors.

We also calculate the convergence values a_∞ and b_∞ of a_n and b_n respectively, which are depicted by dashed lines in Fig. 3.7. In some cases, the Lanczos coefficients converge nicely to these values and do not show quasi-periodic deviations, in which case it is easy to determine a_∞ and b_∞ automatically by using the last coefficients a_n and b_n. For quasi-periodic cases like the one depicted in Fig. 3.7 we perform a slightly more involved calculation to automatically determine a_∞ and b_∞. We explain the automated method exemplarily for a_∞ (the method for b_∞ works analogously):

1. Consider an interval of consecutive Lanczos coefficients $a_n,\ n \in [200, n_{\mathrm{LC}}]$ starting at 200 to exclude any initial convergence behavior.
2. Sort the coefficients a_n in the interval by size, yielding sorted coefficients $a'_n,\ n' \in [0, n_{\mathrm{sorted}}]$ with $n_{\mathrm{sorted}} = n_{\mathrm{LC}} - 200$.
3. Determine the median $\bar{a} := a_{n_{\mathrm{sorted}}/2} =: a_{\bar{n}}$.
4. Average over an interval of 51 coefficients around the median to obtain an approximation of the convergence value $a_\infty = \frac{1}{51} \sum_{n=\bar{n}-25}^{\bar{n}+25} a'_n$.

The explicit numbers 200 and 51 in the above algorithm were chosen because they proved reliable for our data, but other values can be a valid choice depending on the number of calculated Lanczos coefficients. To ensure that the algorithm works correctly for all calculations, we manually compare the horizontal lines for a_∞ and b_∞ with the actual coefficients a_n and b_n in similar plots to Fig. 3.7 . If we observe a discrepancy, we tune the starting point of the interval and the number of averaged coefficients until a_∞ and b_∞ coincide well with the trend of a_n and b_n. An additional clue for wrong values of a_∞ and b_∞ is obtained by examining the calculated spectral weights (3.2.19) after performing the continued fraction expansion, see Sec. 3.3.4 . If the calculated weights fluctuate immensely, the convergence values are most likely not calculated correctly.

The convergence values of the Lanczos coefficients are related to the upper energy $\omega_{\max}$ and lower energy $\omega_{\min}$ of the corresponding n-triplon continuum [99]

$$\omega_{\max}(q_x) = a_\infty(q_x) + 2b_\infty(q_x)\,, \tag{3.3.31a}$$

$$\omega_{\min}(q_x) = a_\infty(q_x) - 2b_\infty(q_x)\,. \tag{3.3.31b}$$

One can calculate the bare continuum edges without multi-triplon interactions by iterating the calculation

$$\omega^{\text{bare}}_{\max,\text{n}}(q_x) = \max_k(\omega_{n-1}(q_x - k) + \omega_1(k))\,, \tag{3.3.32a}$$

$$\omega^{\text{bare}}_{\min,\text{n}}(q_x) = \min_k(\omega_{n-1}(q_x - k) + \omega_1(k)) \tag{3.3.32b}$$

from $n = 2$ up to the desired number of triplons. Note that it is desirable to use a very high discretization in q_x to calculate the bare continua. Otherwise, significant errors arise for large n and steep dispersions $\omega_1(q_x)$. Using the Lanczos coefficients and (3.3.31), one can obtain the full continuum limits including interactions. Attractive triplon interactions decrease the energies of the lower edge and repulsive interactions increase the energies of the upper edge.

To find the correct edges of the three-triplon continuum, one must calculate the Lanczos coefficients and determine a_∞ and b_∞ with (3.3.31). The three-triplon continuum includes states of three freely scattering triplons and states of one free triplon scattering with a two-triplon bound state. Because of the bound two-triplon states, which include energetic contributions from two-triplon interactions, the true three-triplon continuum edges cannot be calculated trivially with (3.3.32).

The two-triplon continuum consists only of two freely scattering triplons. Therefore, one can calculate the continuum edges directly by applying (3.3.32)

$$\omega_{\max,2}(q_x) = \max_k(\omega_1(q_x - k) + \omega_1(k))\,, \tag{3.3.33a}$$

$$\omega_{\min,2}(q_x) = \min_k(\omega_1(q_x - k) + \omega_1(k))\,. \tag{3.3.33b}$$

We omit the superscript 'bare' in this case because these terms already describe the true two-triplon continuum edges. Two-triplon interaction processes do not move the two-triplon continuum edges, but rather introduce two-triplon bound states with fixed discrete energies (but different energies for different q_x) outside of the continuum. Since the true continuum in the two-triplon case can be calculated using (3.3.32), the relations (3.3.31) can be rearranged to

$$a_\infty(q_x) = \frac{\omega_{\max}(q_x) + \omega_{\min}(q_x)}{2}\,, \tag{3.3.34a}$$

$$b_\infty(q_x) = \frac{\omega_{\max}(q_x) - \omega_{\min}(q_x)}{4}\,, \tag{3.3.34b}$$

and then be used to determine a_∞ and b_∞. We apply this method to calculate a_∞ and b_∞ in the two-triplon channel and also use these results to check the results of

our automated algorithm for a_∞ and b_∞. These check verify that our automated algorithm yields correct results.

To make large values of $d_{\max}$ and therefore high accuracy feasible, we highly optimized the computation of the Lanczos algorithm. To this end, a sparse matrix representation $(H_{\text{eff}})_{nj} = \langle \Phi_n | H_{\text{eff}} | \Phi_j \rangle$ is prepared in advance by applying H_{eff} once on each relevant basis state in the truncated Krylov space. The matrix products $H_{\text{eff}} | \Phi_n \rangle$ are parallelized in C++ with the Eigen library [136] and OpenMP [137]. For different values of q_x, only the exponents of the Fourier transformed states (3.3.28) differ. Therefore, we can first calculate a general matrix representation for general q_x, where we keep track of the phase factors $\frac{r_0+\ldots+r_n}{n+1}$ in the exponents so that we can quickly calculate the matrix representations for specific q_x. This works well in the two-triplon channel when we calculate the spectral weight for a large amount of different q_x. For the results presented in this thesis, we use 51 values of q_x for low-resolution plots and 201 values for high-resolution plots. For these calculations, the general matrix representation significantly reduced the computation time. For the three-triplon channel, however, the general matrix representation requires too much internal memory and cannot be used for high $d_{\max}$ with the hardware available to us. Therefore, we calculate a new matrix representation for each q_x directly without using the general matrix representation in three-triplon space. We also use various further micro optimizations in our code to increase the attainable maximum value of $d_{\max}$.

3.3.4 Continued Fraction Expansion with Square-Root Terminator

The tridiagonal form (3.3.27) of $H_{\text{eff}}(q_x)$ allows the evaluation of (3.3.23) with a continued fraction expansion [99, 138] of the resolvent

$$G^{\pm}(q_x, \omega) = \cfrac{b_0^2(q_x)}{\omega - a_0(q_x) - \cfrac{b_1^2(q_x)}{\omega - a_1(q_x) - \ldots}}, \tag{3.3.35}$$

which can be expressed as a recursion

$$G_n = \frac{b_n^2}{\omega - a_n - G_{n+1}} \tag{3.3.36}$$

with $G^{\pm}(q_x, \omega) = G_0$. The explicit notation of q_x, ω and $\pm$ in the recursion (3.3.36) is omitted for brevity.

Divergences in $\text{Re}(G)$ correspond to peaks in $\text{Im}(G)$ due to the Kramers-Kronig-relation

$$\text{Re}(G)(q_x, \omega) = -2P \int_{-\infty}^{\infty} \frac{\mathrm{d}\omega'}{2\pi} \frac{\text{Im}(G)(q_x, \omega')}{\omega - \omega'} \tag{3.3.37}$$

with the principal value P of the integral. One can approximate the imaginary part $\mathrm{Im}[G^{\pm}(q_x,\omega)]$, and hence $S^{\pm}(q_x,\omega)$ according to (3.3.20), by a finite number of delta peaks by calculating (3.3.35) explicitly for a finite number of Lanczos coefficients. The number of considered delta peaks increases with the number of calculated Lanczos coefficients and the peaks can be broadened artificially, see Sec. 3.3.6 . However, approximating the continuous weight with a multitude of peaks is not the optimal approach, even if many coefficients are known. One can instead exploit the fact the Lanczos coefficients converge to a_∞ and b_∞ to perform an effective calculation for a quasi-infinite number of coefficients. To that end, one can introduce a terminator G_∞ to the continued fraction expansion

$$G = \cfrac{b_0^2}{\omega - a_1 - \cfrac{}{\ddots - G_\infty}} \,. \tag{3.3.38}$$

Assuming that the Lanczos coefficients converge to a_∞ and b_∞, one can expect the continued fraction terms G_n to similarily converge to

$$G_\infty = \cfrac{b_\infty^2}{\omega - a_\infty - \cfrac{b_\infty^2}{\ddots}} = \frac{b_\infty^2}{\omega - a_\infty - G_\infty} \tag{3.3.39}$$

$$\Leftrightarrow 0 = G_\infty^2 - G_\infty(\omega - a_\infty) + b_\infty^2 \tag{3.3.40}$$

$$\Leftrightarrow G_\infty = \frac{\omega - a_\infty}{2} \pm \sqrt{\frac{(\omega - a_\infty)^2}{4} - b_\infty^2} \,. \tag{3.3.41}$$

Using the relations (3.3.34), we can infer

$$\frac{(\omega - a_\infty)^2}{4} - b_\infty^2 \begin{cases} \leq 0 & ,\omega \in [\omega_{\min}, \omega_{\max}] \\ > 0 & \text{else} \end{cases} \tag{3.3.42}$$

and see that G_∞ is complex in the continuum energy range $[\omega_{\min}, \omega_{\max}]$. Thus, one can obtain a continuous expression of the spectral weight (3.3.20) for all continuum energies $\omega \in [\omega_{\min}, \omega_{\max}]$, including energies $\omega \notin \{a_i\}$ not covered explicitly by the calculated Lanczos coefficients. The particular choice of a terminator above is called **square-root terminator** with the sign of the square-root for the physical solution determined by ω

$$G_\infty = \begin{cases} \frac{\omega - a_\infty}{2} - \sqrt{\left(\frac{\omega - a_\infty}{2}\right)^2 - b_\infty^2} & ,\omega > \omega_{\max} \,, \\ \frac{\omega - a_\infty}{2} - \mathrm{i}\sqrt{b_\infty^2 - \left(\frac{\omega - a_\infty}{2}\right)^2} & ,\omega \in [\omega_{\min}, \omega_{\max}] \,, \\ \frac{\omega - a_\infty}{2} + \sqrt{\left(\frac{\omega - a_\infty}{2}\right)^2 - b_\infty^2} & ,\omega < \omega_{\min} \,. \end{cases} \tag{3.3.43}$$

As the name and the square-root in the formula imply, this terminator reproduces square-root divergences excellently. It is therefore of great use in one-dimensional and quasi-one-dimensional systems like spin ladders, which typically exhibit square-root divergences.

Recall that the spectral density $S^{\pm}(q_x, \omega)$ is related to the imaginary part of the Green's function according to (3.3.20). The total spectral weight $I_{\text{cont}}(q_x)$ of the continuum for total momentum q_x is obtained by integration over the continuous spectral density $S^{\pm}(q_x, \omega)$

$$I_{\text{cont}}(q_x) = \int_{\omega_{\min}}^{\omega_{\max}} S^{\pm}(q_x, \omega) \mathrm{d}\omega \,. \tag{3.3.44}$$

3.3.5 Finding (Anti-)Bound States

Bound states are found at energies $\omega < \omega_{\min}$ and antibound states at energies $\omega > \omega_{\max}$ outside of the continuum. In the following, we only refer to bound states, but the statements are true for antibound states as well. Their spectral weight can be calculated using

$$I_{\text{bound}}(\omega_m) = \frac{b_0^2}{|f'(\omega_m)|}, \quad 0 = f(\omega_m) = \omega_m - a_0 - \frac{b_1^2}{\omega - a1 - ...} \tag{3.3.45}$$

where ω_m are the roots of the denominator. Finding these roots, however, can prove quite difficult. One can attempt to find them by searching for singularities of the real parts of the Green's function or by explicitly looking for roots of $f(\omega_m)$. A more reliable solution for finding (anti-)bound states, however, is exact diagonalization, where one calculates all eigenenergies ω_m and the corresponding eigenstates $|\psi_m\rangle$ of $H_{\text{eff}}(q_x)$ directly. The caveat is that this does not capture the effect of the terminator. The computation of the diagonalization is more efficient if performed on the tridiagonal form (3.3.27). Furthermore, since the exact diagonalization is performed on the effective Hamiltonian obtained by deepCUT, it is possible to selectively calculate bound states consisting of a chosen number of triplons and a chosen total spin. The spectral weight of the bound state is computed using

$$I_{\text{bound}}(\omega_m) = |\langle \psi(\omega_m) | \psi_0 \rangle|^2 \tag{3.3.46}$$

with the eigenstate $|\psi(\omega_m)\rangle$ to the eigenvalue ω_m and the initial state $|\Psi_0\rangle = O^{\pm}_{q_x,\text{eff}} |g\rangle$ that also appears in the Lanczos algorithm (3.3.25).

3.3.6 Artificial Lorentz Broadening

As an alternative approach for calculating the spectral weights, one can introduce a small imaginary part δ^+ to the energies

$$z = \omega + \mathrm{i}\delta^+ \tag{3.3.47}$$

to cause an artificial Lorentzian broadening of the peaks of the continued fraction

$$G = \lim_{\delta^+ \to 0^+} \frac{b_0^2}{\omega + \mathrm{i}\delta^+ - a_1 - \frac{b_1^2}{\ddots}} = \lim_{z \to \omega} \frac{b_0^2}{z - a_1 - \frac{b_1^2}{\ddots}} \,. \tag{3.3.48}$$

This way, the continuum and bound states can be calculated as a continuous function without the use of a terminator or exact diagonalization. Broadening is especially useful for plotting bound states, which would otherwise be infinitely narrow delta peaks. The disadvantage of this approach is the fact that the continuum is plotted as a spectrum of broadened delta-peaks, rather than a smooth function. This becomes especially noticeable for a small number of considered Lanczos coefficients, where one obtains a strongly fluctuating continuum.

In this thesis, we only use Lorentz broadening to plot the (anti-)bound states outside of the continuum. The continuum is calculated and plotted using the square-root terminator (3.3.43) and the energies and weights of bound states are calculated using exact diagonalization. Instead of introducing the broadening using (3.3.47), we plot the bound state at energy ω_m with weight $I_{\text{bound}}(\omega_m)$ using the Lorentz function

$$L(\omega) = \frac{1}{\pi} \frac{I_{\text{bound}}(\omega_m)\gamma}{(\omega - \omega_m)^2 - \gamma^2} \quad , \gamma = 5 \cdot 10^{-4} \,. \tag{3.3.49}$$

Note that we use Lorentz broadening for the bound states, because it is typical for lifetime effects. For experimental purposes, however, we presume that Gaussian broadening caused by the finite precision of the measuring instruments are the more dominant broadening effect.

3.4 Results

3.4.1 Preliminary Considerations

Two central findings that are discussed in the following sections are the existence of three-triplon bound states and their relation to three-triplon interactions. For readers without prior experience with the flow equation method, it might seem peculiar that three-triplon processes emerge in the natural basis of the spin ladder, although no such processes occur in the initial Hamiltonian (3.1.5). App. B provides two exemplary calculations, which demonstrate how three-triplon interactions emerge in the effective Hamiltonian H_{eff}.

The deepCUT is performed with a program by Nils Drescher, which is explained in detail in his PhD thesis [88]. For all considered parameter ranges, we attempt a deepCUT calculation up to order 10, but in some cases the maximum convergent order lies below 10. Furthermore, the maximum distance $d_{\max}$ in (3.3.29) must be reduced for more than two triplons due to high memory demands, leading to fewer Lanczos coefficients n_{LC}. The numerical parameters are not listed explicitly in the following plots, but a comprehensive list can be found in App. C. For most data sets, we use perturbation parameters $x \in \{0.25, 0.5, 1.2, 2.0\}$. The value $x = 1.2$ is chosen instead of $x = 1.0$ because this better represents the experimentally relevant range in cuprates, in particular for the telephone number compound $La_{5.2}Ca_{8.8}Cu_{24}O_{41}$,

see Tab. 3.1 at the beginning of this chapter. App. C provides slices of the heatmaps presented in the following sections, which allows one to more easily discern the form of the spectral density.

3.4.2 Non-Spin-Conserving Channel in Order $k = 0$

The NSC channel with excitations of total spin $S = 1$ can be probed with INS and the corresponding spectral density up to two triplons has been calculated in the past [32,111]. However, RIXS offers a larger cross section at high energies, potentially allowing one to probe excitations in three-triplon space. Furthermore, higher order contributions beyond the observable $S^z_{i,\tau}$ can be probed by RIXS and are superposed with the leading order contribution. For these reasons, and to discuss differences between the NSC and SC channel, we study the leading order NSC response in this section.

The leading order ($k = 0$) observable in the NSC channel is described by the observable

$$O^{\mathrm{NSC},0}_{i,\pm} = S^z_{i,\tau} \pm S^z_{i,\bar{\tau}}\,. \tag{3.4.50}$$

Fig. 3.8 ($x \in \{0.25, 0.5\}$) and Fig. 3.10 ($x \in \{1.2, 2\}$) show the weights for the even observable $O^{\mathrm{NSC},0}_{i,+} = S^z_{i,1} + S^z_{i,2}$ in two-triplon space. Note that the ω axis does not start at 0 in order to show only the energy range in which significant contributions of the selected channel appear. The continuum edges are highlighted with solid white lines and the bound states are marked by dashed red lines. With increasing x, the energetic range of the two-triplon continuum increases. Furthermore, the spectral weight increases and shifts towards larger q_x. The boundaries are non-monotonic for $x \gtrapprox 1$. A bound state can be observed for a small $x = 0.25$ at $q_x \gtrapprox 0.6\pi/a$. For larger x, the bound state emerges from the continuum for smaller q_x ($q_x \gtrapprox 0.2\pi/a$ at $x = 2$) and the bound state weight increases. The formation of a bound state below the continuum implies attractive two-triplon interactions in the effective basis. The left panel of Fig. 3.12 shows that the relative weight of the bound state compared to the continuum at the same momentum q_x is large for all considered values of x and a wide range of q_x. The bound state weight is most dominant for small x and $q_x = \pi/a$. The energies of the lower continuum edge and the bound state are separated well, which enables one to detect the bound state in an experimental setting with reasonable energy resolution [108,109]. Note that it is trivial to determine that this bound state is a two-triplon $S = 1$ bound state because the NSC two-triplon channel was selected. Furthermore, our approach allows us to trivially distinguish between bound state and continuum.

The spectral weight of the odd NSC observable $O^{\mathrm{NSC},0}_{i,-} = S^z_{i,1} - S^z_{i,2}$ for one and three triplons is depicted in Fig. 3.9 ($x \in \{0.25, 0.5\}$) and Fig. 3.11 ($x \in \{1.2, 2\}$). The one-triplon dispersion (bottom row) is monotonically decreasing for smaller

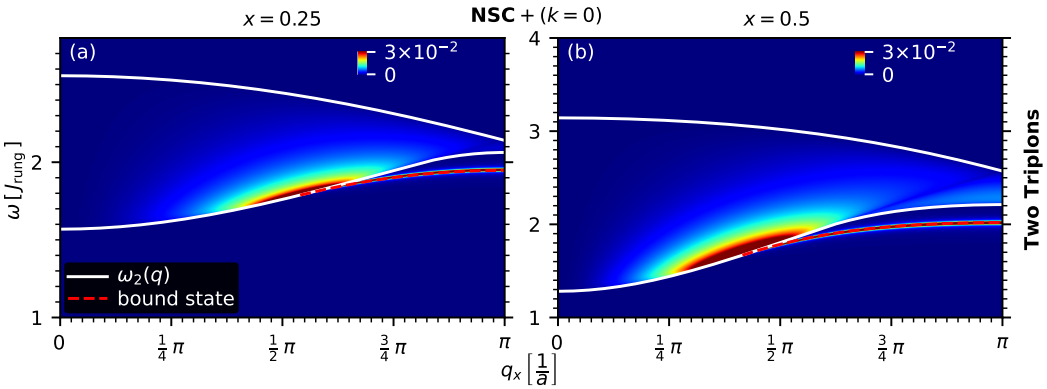

Figure 3.8: Spectral density $S(q_x, \omega)$ of the leading NSC observable $O^{\mathrm{NSC},0}_{i,+} = S^z_i$ (DSF, see (3.2.10) and (3.2.18)) in two-triplon space for perturbation parameters $x \in \{0.25, 0.5\}$.

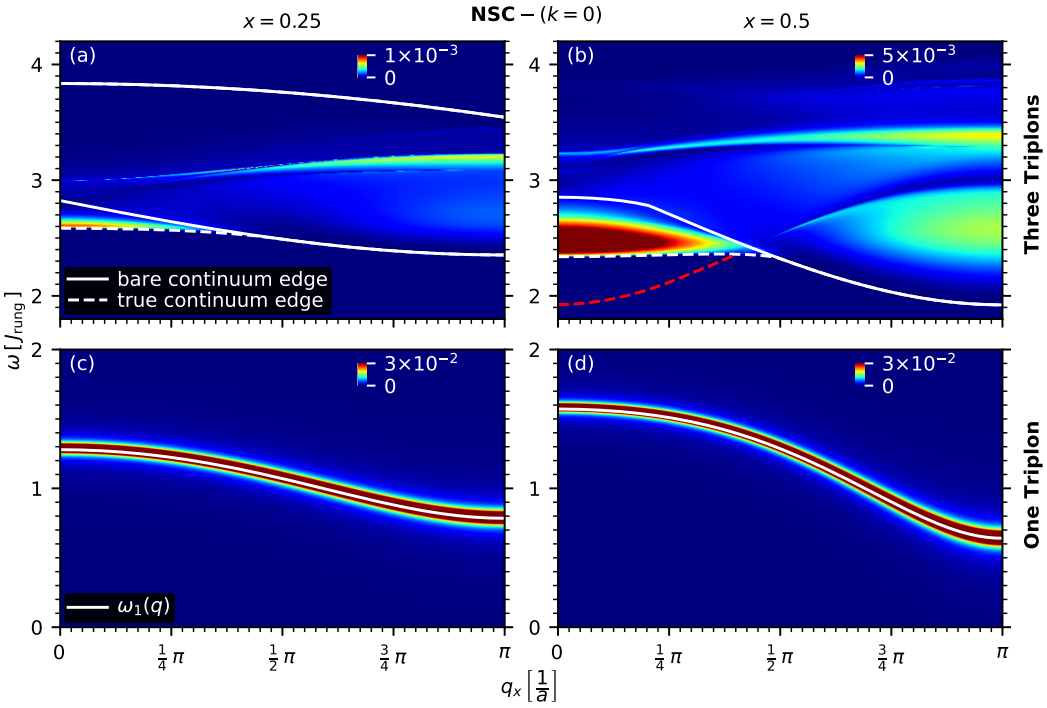

Figure 3.9: Spectral density $S(q_x, \omega)$ of the leading NSC observable $O^{\mathrm{NSC},0}_{i,-} = S^z_i$ (DSF, see (3.2.10) and (3.2.18)) in one-triplon space and three-triplon space for perturbation parameters $x \in \{0.25, 0.5\}$.

$x \in \{0.25, 0.5\}$, but non-monotonic for larger $x \in \{1.2, 2\}$, which is in accordance with the non-monotonic two-triplon continuum for $x \in \{1.2, 2\}$. With increasing x, the energy gap $\omega(q_x = \pi/a)$ decreases and the spectral weight shifts towards higher q_x. The three-triplon response (top row) is depicted near the lower continuum edge, where the spectral weight dominates. The solid white line depicts the bare continuum edge (3.3.32) and the dashed white line depicts the true continuum edge (3.3.31). For $x \in \{0.25, 0.5\}$, one finds a dominant spectral feature at the lower continuum edge close to $q_x = 0$. A three-triplon bound state is found for $x = 0.5$ at

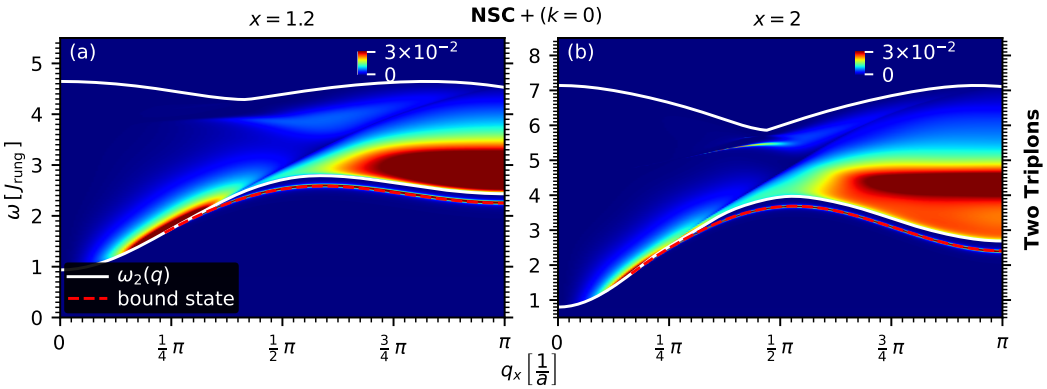

Figure 3.10: Spectral density $S(q_x, \omega)$ of the leading NSC observable $O^{\mathrm{NSC},0}_{i,+} = S^z_i$ (DSF, see (3.2.10) and (3.2.18)) in two-triplon space for perturbation parameters $x \in \{1.2, 2\}$.

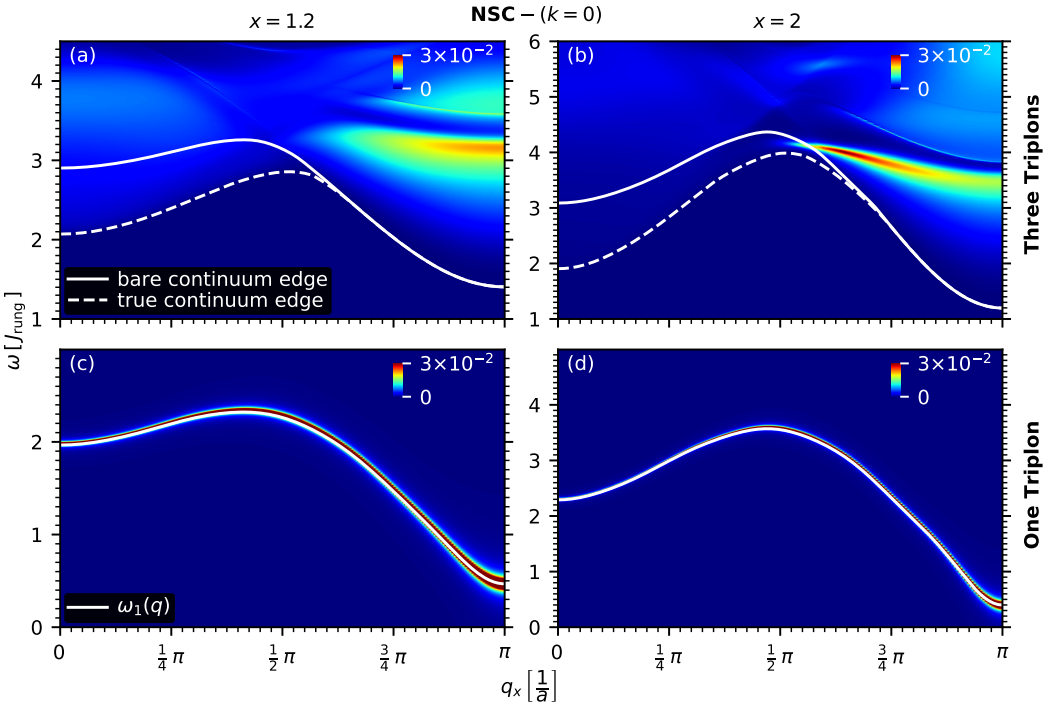

Figure 3.11: Spectral density $S(q_x, \omega)$ of the leading NSC observable $O^{\mathrm{NSC},0}_{i,-} = S^z_i$ (DSF, see (3.2.10) and (3.2.18)) in one-triplon space and three-triplon space for perturbation parameters $x \in \{1.2, 2\}$.

small q_x, but the weight of this bound state is negligible, rendering an experimental detection virtually impossible. It stands out, however, that a thin feature emerges in the continuum at the imagined continuation of the bound state into the continuum. For increasing x, two distinct dominant features can be found at larger $q_x \in [\pi/2, \pi]$. The three-triplon weight increases with x. Note that sometimes different color scales of the heat map are chosen for different x in order to better accentuate the relevant features. Therefore, features of the same color in different plots do not always represent the same spectral density.

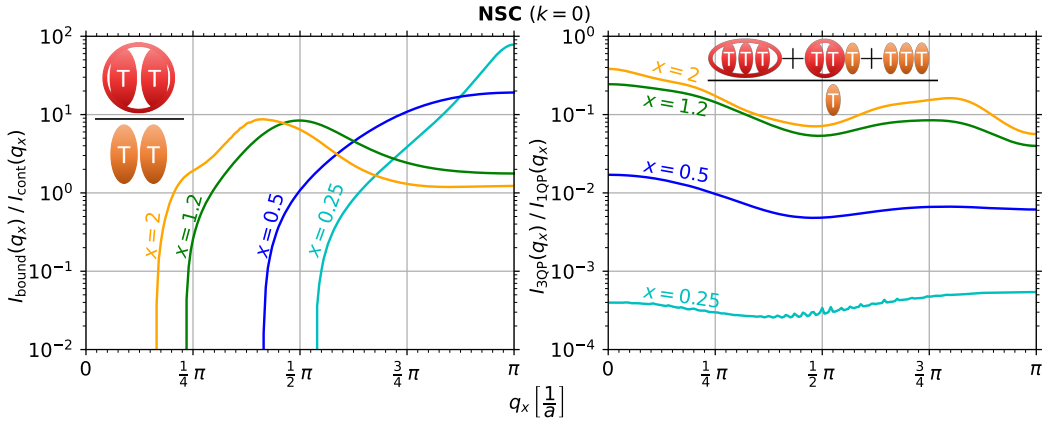

Figure 3.12: Left: Ratio of bound-state weight to integrated continuum weight of the leading NSC observable $O^{\text{NSC},0}_{i,+}$ (DSF, see (3.2.10) and (3.2.18)) in two-triplon space for various x and q_x. Right: Ratio of integrated three-triplon continuum weight to one triplon weight for the NSC observable $O^{\text{NSC},0}_{i,-}$.

The one-triplon and three-triplon weights are both measured in the same channel with $q_y = \pi$, so the weights could overlap in principle. The right panel of Fig. 3.12 shows that the one-triplon weight dominates over the three-triplon weight, especially for small x. This does not pose a problem in experimental settings, because the one-triplon dispersion and three-triplon continuum are energetically separated for $x \in \{0.25, 0.5, 1.2\}$. For $x = 2$, the energies overlap at $q_x \lessapprox 0.35\pi/a$, but all significant three-triplons weight is found at larger energies or momenta. Fig. 3.13 depicts the dispersion, two-triplon continuum, three-triplon continuum and all found bound states. In that figure, the overlap of one-triplon energies and three-triplons energies for $x = 2$ can be observed more explicitly.

To conclude this section, the leading order of the NSC channel provides some dominant features up to three-triplon space, which are well separated energetically. RIXS experiments have a high cross section even for larger energies, so we surmise that an experimental verification is possible even of the three-triplon features, for which an INS is less feasible. A dominant bound state with $S = 1$ arises in two-triplon space, but no three-triplon bound state of significant weight is found.

3.4.3 Spin-Conserving Channel in Order $k = 1$

The SC channel cannot be probed by INS, but can be studied with RIXS. In this section, we discuss the leading order results in the SC channel, which are also published in Ref. [44]. The leading order ($k = 1$) of the SC channel is described by the observable

$$O^{\text{SC},1}_{i,\pm} = \sum_{\tau} \left[J_{\text{rung}} \boldsymbol{S}_{i,\tau} \cdot \boldsymbol{S}_{i,\bar{\tau}} + J_{\text{leg}} \boldsymbol{S}_{i,\tau} \cdot \left(\boldsymbol{S}_{i+1,\tau} + \boldsymbol{S}_{i-1,\tau} \right) \right] (-1)^{\tau} . \tag{3.4.51}$$

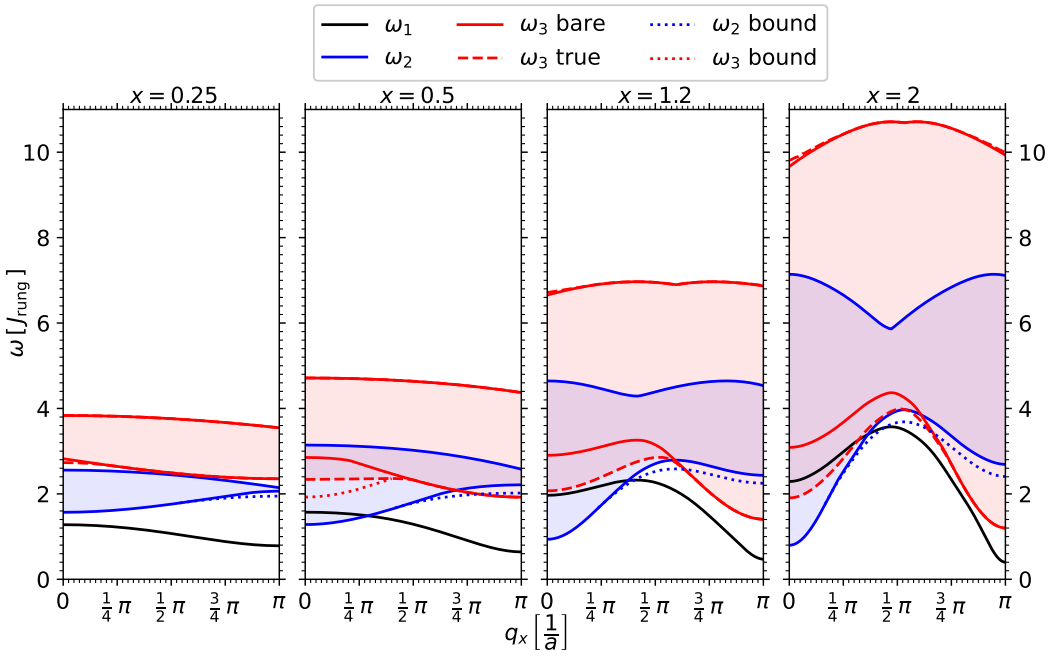

Figure 3.13: Continua and bound states up to three-triplon space in the NSC channel for perturbation parameters $x \in \{0.25, 0.5, 1.2, 2\}$. Solid lines depict bare continuum edges, dashed lines mark the true three-triplon continuum including binding effects and dotted lines depict bound states.

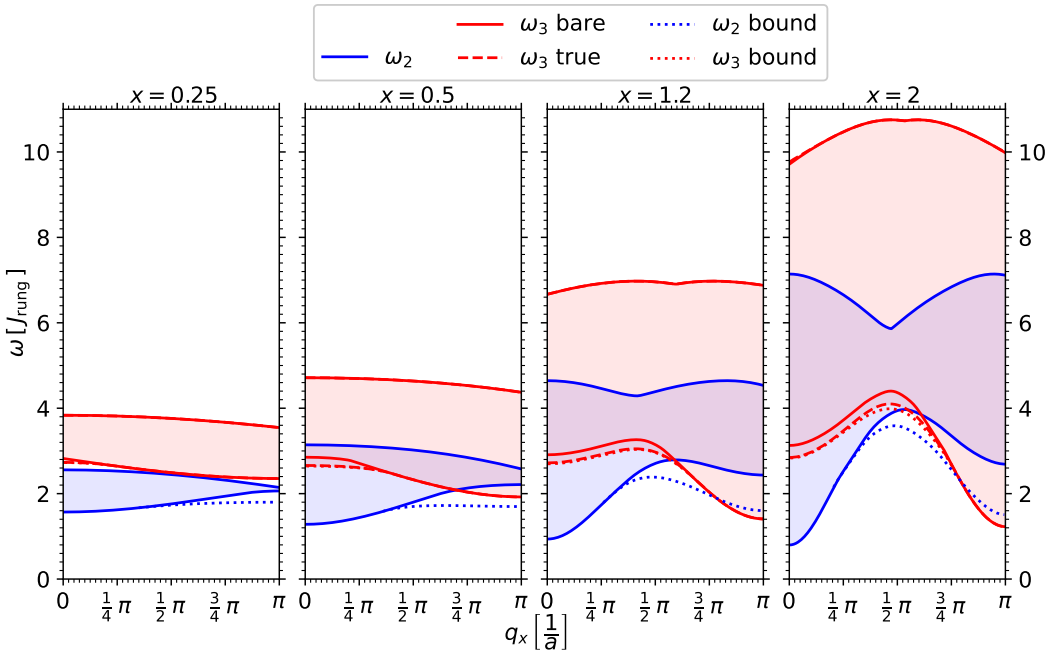

Figure 3.14: Continua and bound states up to three-triplon space in the SC channel for perturbation parameters $x \in \{0.25, 0.5, 1.2, 2\}$. Solid lines depict the dispersion and bare continuum edges, dashed lines mark the true three-triplon continuum including binding effects and dotted lines depict bound states.

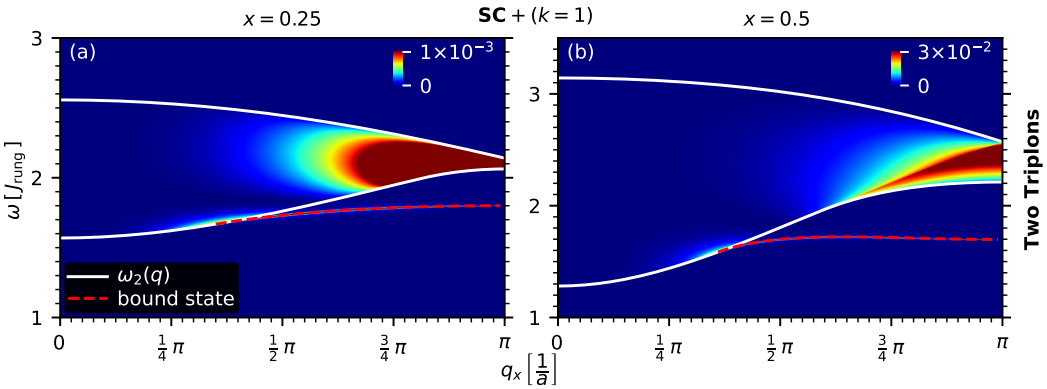

Figure 3.15: Spectral density $S(q_x, \omega)$ of the leading SC observable $O^{\mathrm{SC},1}_{i,+}$ (DESF, see (3.2.15)) in two-triplon space for perturbation parameters $x \in \{0.25, 0.5\}$.

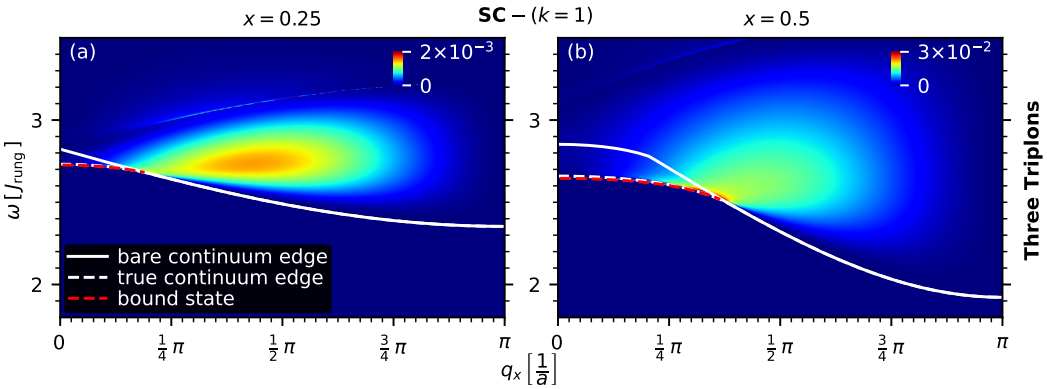

Figure 3.16: Spectral density $S(q_x, \omega)$ of the leading SC observable $O^{\mathrm{SC},1}_{i,-}$ (DESF, see (3.2.15)) in three-triplon space for perturbation parameters $x \in \{0.25, 0.5\}$.

Fig. 3.14 depicts the continua and bound states in the SC channel. Note that no one-triplon response occurs, because a single $S_1 = 1$ triplon cannot have a total spin of 0 and hence cannot be excited in the SC channel. When comparing the relevant energies in Fig. 3.14 with the NSC channel depicted in Fig. 3.13, one finds that the bound states have different energies. A two-triplon bound state can have a total spin $S_2 \in \{0, 1, 2\}$ due to the superposition of two $S_1 = 1$ triplons. The $S_2 = 0$ two-triplon bound state has less energy than the $S_2 = 1$ two-triplon bound state, similar to the lower energy of a singlet state compared to a triplet state in a single dimer. The $S_2 = 2$ two-triplon bound state cannot be probed with the observables presented in this work and hence will not be discussed. A three-triplon bound state appears in the SC channel for all x, which will be discussed in more detail below. Note that the bare continua are identical in the SC and NSC channel, but the true lower edge of the three-triplon continuum is found at smaller energies in the NSC channel than in the SC channel. The reason for this is that the true lower edge of the three-triplon continuum is formed by the combination of a two-triplon bound state and a free triplon. Combinations of three free triplons are possible, as well, but are already captured by the bare continuum edges. In the NSC channel, a total spin

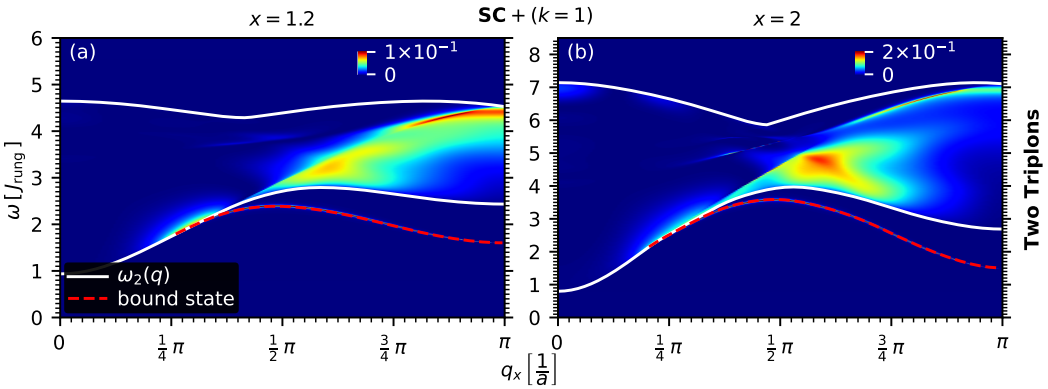

Figure 3.17: Spectral density $S(q_x, \omega)$ of the leading SC observable $O^{\mathrm{SC},1}_{i,+}$ (DESF, see (3.2.15)) in two-triplon space for perturbation parameters $x \in \{1.2, 2\}$.

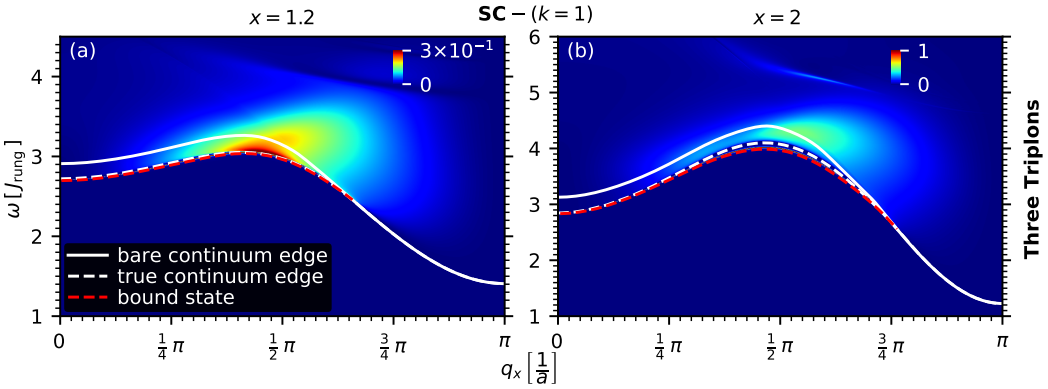

Figure 3.18: Spectral density $S(q_x, \omega)$ of the leading SC observable $O^{\mathrm{SC},1}_{i,-}$ (DESF, see (3.2.15)) in three-triplon space for perturbation parameters $x \in \{1.2, 2\}$.

of $S_3 = 1$ can be achieved by combining a single $S_1 = 1$ triplon with a two-triplon bound state of $S_2 \in \{0, 1, 2\}$, so the low-energy $S_2 = 0$ two-triplon bound state from the SC channel contributes to the NSC three-triplon continuum. In the SC channel, however, a total spin of $S_3 = 0$ can only be achieved by combining a single $S_1 = 1$ triplon with a two-triplon bound state of $S_2 = 1$, so only the two-triplon bound state of the NSC channel contributes, which has higher energy and leads to a higher minimal energy of the three-triplon continuum.

The two-triplon spectral density of the even SC observable in order $k = 1$ $O^{\mathrm{SC},1}_{i,+} = 2J_{\mathrm{rung}}\boldsymbol{S}_{i,1} \cdot \boldsymbol{S}_{i,2} + J_{\mathrm{leg}}\boldsymbol{S}_{i,1} \cdot \left(\boldsymbol{S}_{i+1,1} + \boldsymbol{S}_{i-1,1}\right) + J_{\mathrm{leg}}\boldsymbol{S}_{i,2} \cdot \left(\boldsymbol{S}_{i+1,2} + \boldsymbol{S}_{i-1,2}\right)$ is depicted in Fig. 3.15 ($x \in \{0.25, 0.5\}$) and Fig. 3.17 ($x \in \{1.2, 2\}$). For $x = 0.25$, most spectral weight is found around $q_x \approx \pi/a$ and in the bound state, which is also situated at large q_x. With increasing x, the overall spectral weight increases and the distribution inside the continuum changes. With larger x more continuum weight is found at $q_x \approx 0.5\pi/a$ at the lower continuum edge while the upper continuum edge retains significant weight at $q_x \approx \pi/a$. Most weight, however, transfers towards the $S = 0$ two-triplon bound state. While the weight of this bound state is small

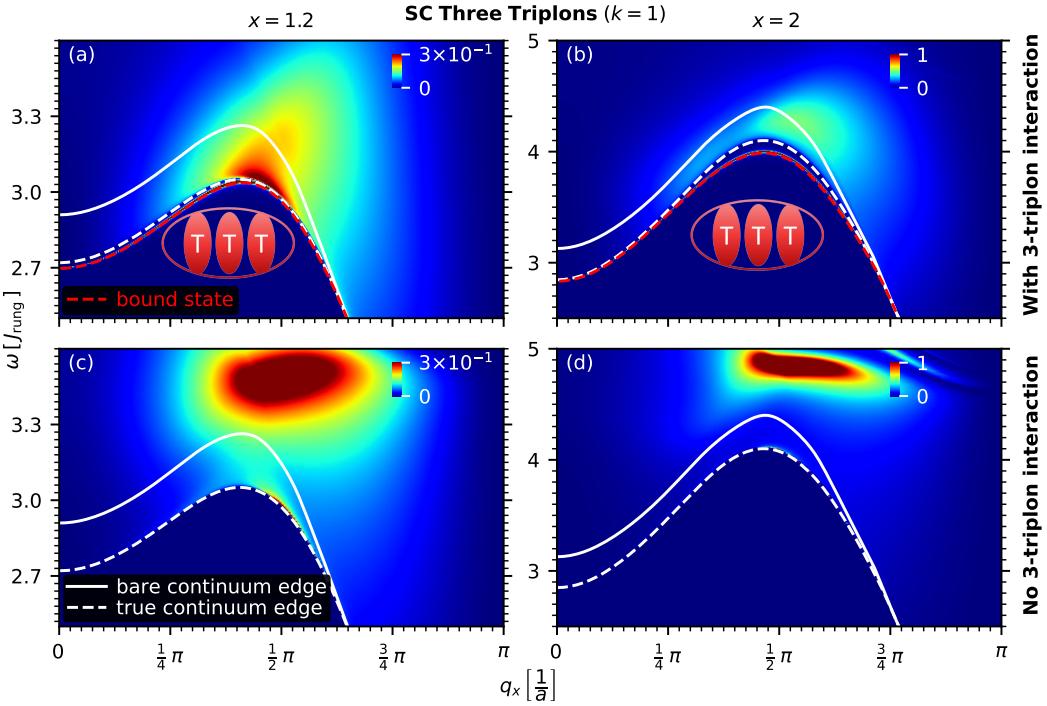

Figure 3.19: Spectral density $S(q_x, \omega)$ of the leading odd SC observable $O^{\text{SC},1}_{i,-}$ (DESF, see (3.2.15)) in three-triplon space for perturbation parameters $x \in \{1.2, 2\}$ with and without activated three-triplon interactions.

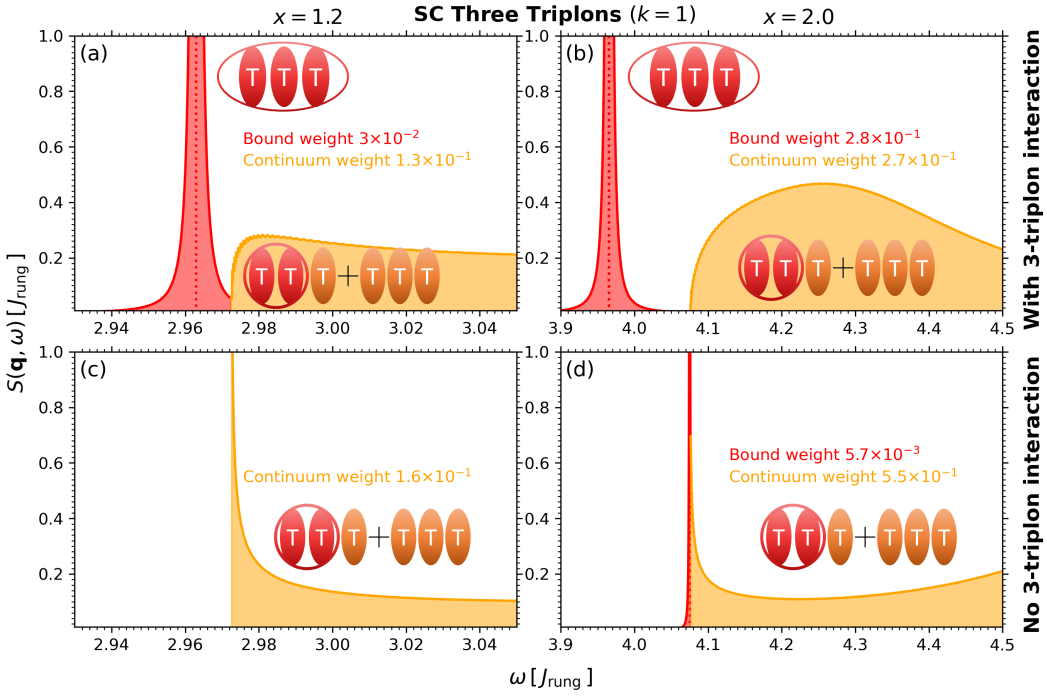

Figure 3.20: Spectral density $S(\omega)$ at $q_x = 0.5\pi/a$ of the leading odd SC observable $O^{\text{SC},1}_{i,-}$ (DESF, see (3.2.15)) in three-triplon space for perturbation parameters $x \in \{1.2, 2\}$ with and without activated three-triplon interactions at fixed momentum $q_x = \pi/2$.

compared to the continuum weight at $x = 0.25$, it is absolutely dominant at $x = 2$.

The three-triplon spectral density of the odd SC observable in order $k = 1$ $O^{\mathrm{SC},1}_{i,-} = J_{\mathrm{leg}}\boldsymbol{S}_{i,1} \cdot \left(\boldsymbol{S}_{i+1,1} + \boldsymbol{S}_{i-1,1}\right) - J_{\mathrm{leg}}\boldsymbol{S}_{i,2} \cdot \left(\boldsymbol{S}_{i+1,2} + \boldsymbol{S}_{i-1,2}\right)$ is shown in Fig. 3.16 ($x \in \{0.25, 0.5\}$) and Fig. 3.18 ($x \in \{1.2, 2\}$). Note that the deepCUT for these calculations does not converge in order 10 for the (3:n)-generator, which separates all triplon-spaces up to three triplons. To achieve the best possible accuracy, we combine the one-triplon and two-triplon contributions to H_{eff} obtained with the (2:n)-generator in order 10 with the three-triplon contributions of the the highest convergent order of the (3:n)-generator. The highest convergent order for each case can be found in Tab. C.1 in App. C.

The attractive two-triplon interactions, which lead to the formation of two-triplon bound states, also shift the lower edge of the bare three-triplon continuum (3.3.32) towards smaller energies for the true three-triplon continuum (3.3.31). Note that three-triplon interactions are not considered when calculating the three-triplon continuum edges. While three-triplon interactions can shift the weight inside of the continuum, the only energetically new contributions are obtained through bound states with discrete energy for a given q_x.

With increasing x, the three-triplon spectral weight is shifted towards the lower continuum edge around $q_x \approx 0.5\pi/a$. The overall spectral weight increases with x. This is not captured quite clearly in the plot, since most weight is found in the three-triplon bound state, which is very close to the continuum edge and plotted as a Lorentzian of small width $\gamma = 5 \cdot 10^{-4}$, see Sec. 3.3.6 .

In Fig. 3.19, we investigate the spectral weight around the lower continuum edge for $x \in \{1.2, 2\}$ and compare the results with the full H_{eff} (panels a-b) with results after disabling irreducible three-triplon interactions (panels c-d). For the results including three-triplon interactions, one finds a $S = 0$ three-triplon bound state, highlighted by a dashed red line, appearing directly below the continuum edge at $q_x < 0.65\pi/a$ for $x = 1.2$ and at $q_x < 0.75\pi/a$ for $x = 2.0$. One could argue that the close vicinity of the bound state to the lower continuum limit suggests that it appears only due to a numerical error: After all, if one eigenenergy ω_m of the tridiagonalized Hamiltonian is found ever so slightly below the lower continuum edge, it is interpreted as a bound state. Hence, an error in the calculation of the Lanczos coefficients or an error in the calculation of the lower continuum edge could lead to a continuum contribution detected incorrectly as a bound state. To preclude such an error, we checked the Lanczos coefficients and the continuum limits by using the relations (3.3.34) and (3.3.31) and by plotting the Lanczos coefficients a_n and b_n explicitly like in Fig. 3.7. The conclusion of all these checks is that a three-triplon bound state indeed emerges below the three-triplon spectrum.

The bottom row (panels c-d) of Fig. 3.19 depicts the same phase space as the upper row after disabling all three-triplon interactions in the H_{eff}. Consequently, these plots show only the effects of one-triplon energies and two-triplon interactions. Without the three-triplon interactions, no three-triplon bound state appears and most of the spectral weight is found at larger energies. Conversely, it can be deduced that the strongly attractive three-triplon interactions lead to the spectral weight shifting towards the lower continuum edge and to the emergence of the bound state. The two-triplon interactions alone are not strong enough to form a three-triplon bound state.

This is a tremendously interesting results when contraposed to classical particles, i.e. not quasi-particles, which are described purely by two-particle interactions. These two-particle interactions alone can create many-particle bound states of more than two particles, e.g. an atom with multiple electrons or even a macroscopic solid-state system. For triplon quasi-particles, which are the elementary excitation in the spin ladder discussed in this chapter, we find a three-triplon bound state which emerges only if three-triplon interactions are considered explicitly. One could argue that these are not true three-particle states, because they are described in an effective quasi-particle basis and three delocalized triplons in that effective basis correspond to a vast number of local triplets in the original basis. However, the initial local triplet basis is only introduced because it is a simple starting point for setting up the Hamiltonian of the spin ladder. In the local triplet basis, the number of quasi-particles is not conserved and hence one cannot speak of bound n-triplet states in a meaningful way. The natural basis to describe the spin ladder is the basis which conserves the number of quasi-particles: The effective triplon basis that we obtain by applying the deepCUT method.

In Fig. 3.19, it is quite difficult to discern the exact form and the size of the spectral weight around the lower continuum edge because of the close vicinity of the bound state. To enable a closer investigation, Fig. 3.20 depicts a smaller energy range and a single momentum $q_x = 0.5\pi/a$. Again, the top row depicts the results for the full H_{eff} while the bottom row depicts the results with disabled three-particle interactions. The numerical values of the bound state weight and of the full continuum are depicted explicitly, including continuum energies which are outside of the plotted range of ω. The weight of the bound state is significant compared to the continuum weight and is even slightly larger for $x = 2$. For increasing x, one finds the distance between bound state and continuum increasing, making the bound state more distinct and easier to discern, which is important for experimental verification. Slight ripples can be observed in the continuum weight, which are an artifact of the continued fraction expansion. If one calculates the lower continuum edge and the limit Lanczos coefficients (3.3.34) incorrectly, these ripples become very distinct.

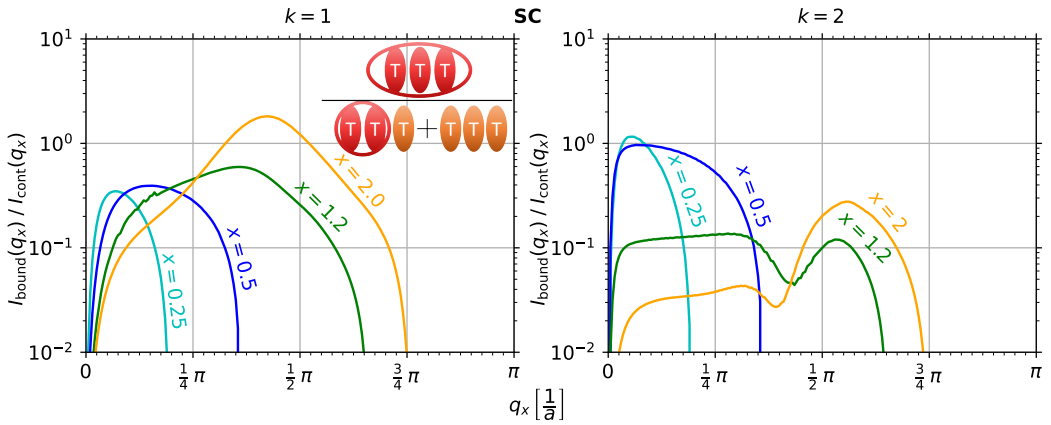

Figure 3.21: Left: Ratio of bound weight to integrated continuum weight of the leading SC observable $O^{\text{SC},1}_{i,-}$ (DESF, see (3.2.15)) in three-triplon space for various x and q_x. The continuum weight has contributions from (i) three asymptotically scattering triplons and (ii) one triplon plus a two-triplon bound state. Right: The same ratio for the second leading order $O^{\text{SC},2}_{i,-}$, discussed in Sec. 3.4.5 .

The slight inaccuracy of the lower continuum limit at $q_x = 0.5\pi/a$, which leads to the ripples observed here, is significantly smaller than the energetic distance between bound state and continuum.

In the bottom row of Fig. 3.20, a square-root divergence of the continuum weight occurs at the lower continuum edge. Surprisingly, in (d) it appears as if a three-triplon bound state exists for $x = 2$ even without three-triplon interactions. However, this pseudo bound state is so close to the continuum limit that it can be the results of calculating a slightly too large value of the lower continuum edge. The weight of the pseudo bound state is not significant compared to the continuum and the distinct square-root divergence at the lower continuum edge can still be observed, which is not the case when a true bound state emerges in (a-b). Therefore, it is reasonable to assume that no actual bound state appears in (d). One could manually lower the continuum edge so that this pseudo bound state does not appear, but for the purpose of this discussion we use the continuum limits that are calculated by the automated method presented in Sec. 3.3.3 .

To show that the bound states carry significant weight for various x and q_x, we calculate the ratio of bound state weight (3.3.46) to continuum weight (3.3.44) and show the results in the left panel of Fig. 3.21. When this ratio is high, this means that at the given q_x the bound state is dominant and can be discerned more easily in an experimental setting. We find that with increasing x the bound weight becomes more significant and that the maximum of the ratio moves towards larger q_x. In all four considered cases, the relative maximum is found in the range $q_x \in [0, 0.5\pi/a]$. The value of the maximum ratio is in the range $I_{\text{bound}}/I_{\text{cont}} \approx 20\% - 105\%$.

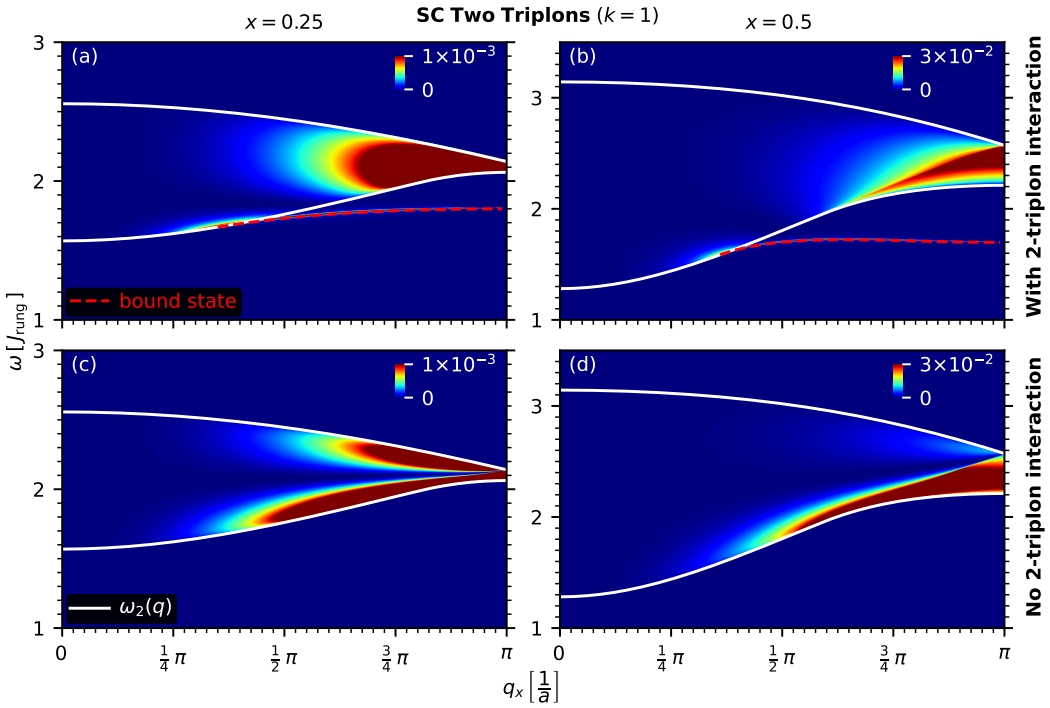

Figure 3.22: Spectral density $S(q_x, \omega)$ of the leading even SC observable $O^{\mathrm{SC},1}_{i,+}$ (DESF, see (3.2.15)) in two-triplon space for perturbation parameters $x \in \{0.25, 0.5\}$ with (a-b) and without (c-d) activated two-triplon interactions.

While the weight of the bound state is significant, the small energetic difference to the lower continuum edge, which also carries significant weight, complicates experimental verification. RIXS experiments are able to probe the SC channel with substantial momentum transfer, but the energy resolution of current instruments is not high enough to distinguish between the three-triplon bound state and the continuum. A solution to this problem are THz experiments, which offer a higher energy resolution. However, they do not transfer significant momentum, which is a problem because the bound state is most dominant at $q_x \approx 0.5\pi/a$. To circumvent this problem, one can use a spin ladder with a slight distortion with periodicity of four ranges. That way, the states $q_x \in \{0.25\pi/a, 0.5\pi/a, 0.75\pi/a\}$ are folded back to the center of the Brillouin zone. This enables one to detect the bound state even without substantial momentum transfer. However, we stress that to probe the SC channel, a momentum transfer of at least $q_y = \pi/a$ is necessary.

To further demonstrate how disabling interactions affects the spectral weight, Fig. 3.22 (for $x \in \{0.25, 0.5\}$) and Fig. 3.23 (for $x \in \{1.2, 2\}$) compare the two-triplon results with and without activated two-triplon interations. As expected, the $S = 0$ two-triplon bound state appears only if two-triplon interactions are activated. Without two-triplon interactions, no bound state emerges and the spectral weight is distributed more broadly in the continuum.

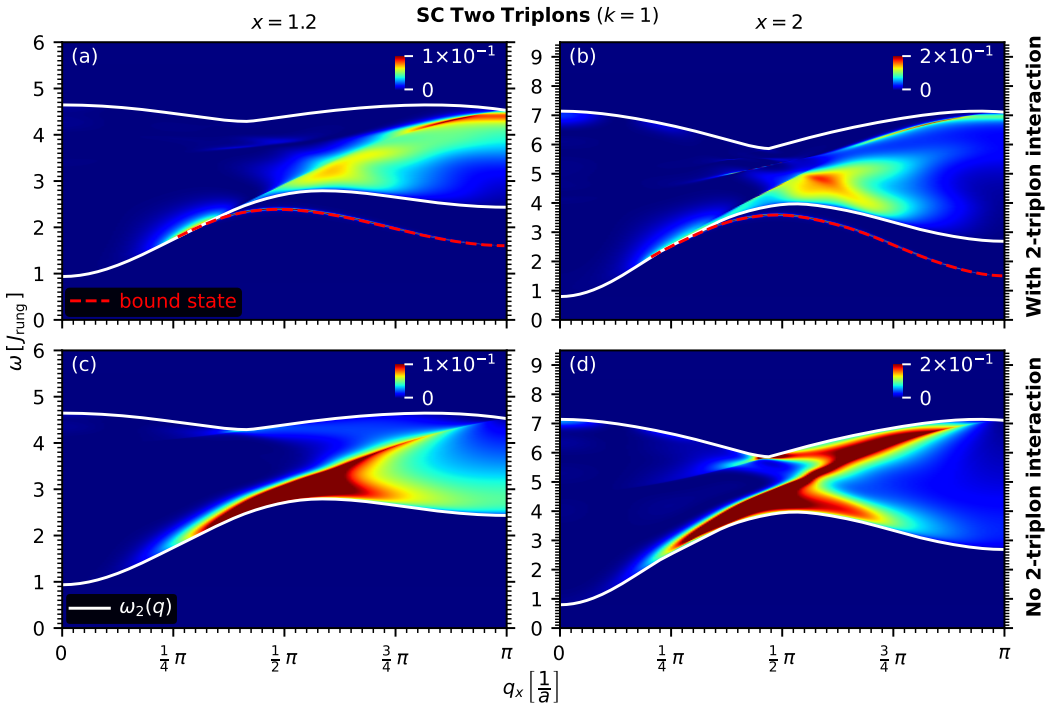

Figure 3.23: Spectral density $S(q_x, \omega)$ of the leading even SC observable $O^{\mathrm{SC},1}_{i,+}$ (DESF, see (3.2.15)) in two-triplon space for perturbation parameters $x \in \{1.2, 2\}$ with (a-b) and without (c-d) activated two-triplon interactions.

To conclude this section, we find that a three-triplon bound state arises in the SC channel, which is not accessible to INS, but to RIXS. This bound state arises as a consequence of genuine three-triplon interactions, which is a novel phenomenon compared to many-particle bound states which arise solely due to two-particle interactions. The bound state is energetically close to the continuum edge, but becomes more distinct for larger x, where the energetic distance and the spectral weight of the bound state increase. The vicinity to the continuum edge renders the experimental resolution with RIXS difficult, but THz spectroscopy on distorted spin ladders offers a solution for experimental verification. We also found a two-triplon bound state and various continuum features which should be easily distinguishable for RIXS.

3.4.4 Non-Spin-Conserving Channel in Order $k = 1$

In Sec. 3.4.2 , we discussed the leading order ($k = 0$) of the NSC channel. In this section, we investigate the next leading order of the UCL expansion, see Sec. 3.2.3.1 . The second leading order ($k = 1$) observable in the NSC channel is

$$O^{\mathrm{NSC},1}_{i,\pm} = \sum_{\tau} \left[J_{\mathrm{rung}} \boldsymbol{S}_{i,\tau} \cdot \boldsymbol{S}_{i,\bar{\tau}} + J_{\mathrm{leg}} \boldsymbol{S}_{i,\tau} \cdot \left(\boldsymbol{S}_{i+1,\tau} + \boldsymbol{S}_{i-1,\tau} \right) \right] S^z_{i,\tau} (-1)^{\tau} \,. \tag{3.4.52}$$

The absolute value of the spectral weight cannot be compared directly due to the nontrivial prefactors arising in the expansion, but the qualitative distribution provides insights to the shape of the spectral density observed in RIXS experiments.

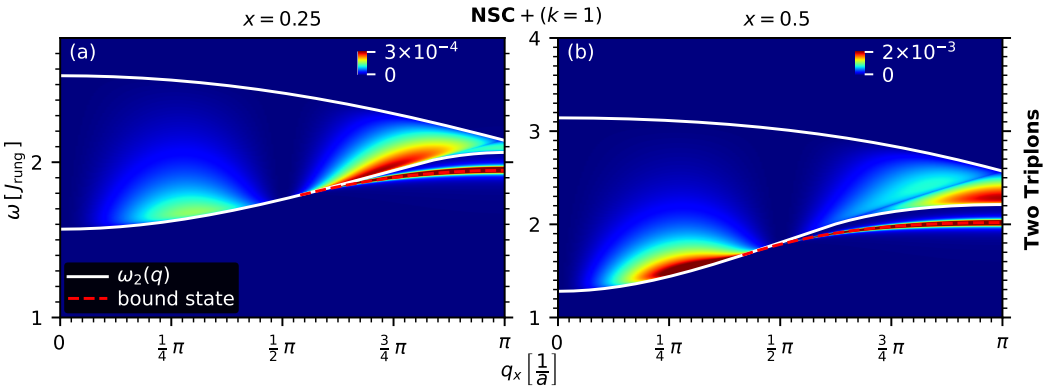

Figure 3.24: Spectral density $S(q_x, \omega)$ of the second leading NSC observable $O^{\mathrm{NSC},1}_{i,+}$ (see (3.2.19)) in two-triplon space for perturbation parameters $x \in \{0.25, 0.5\}$.

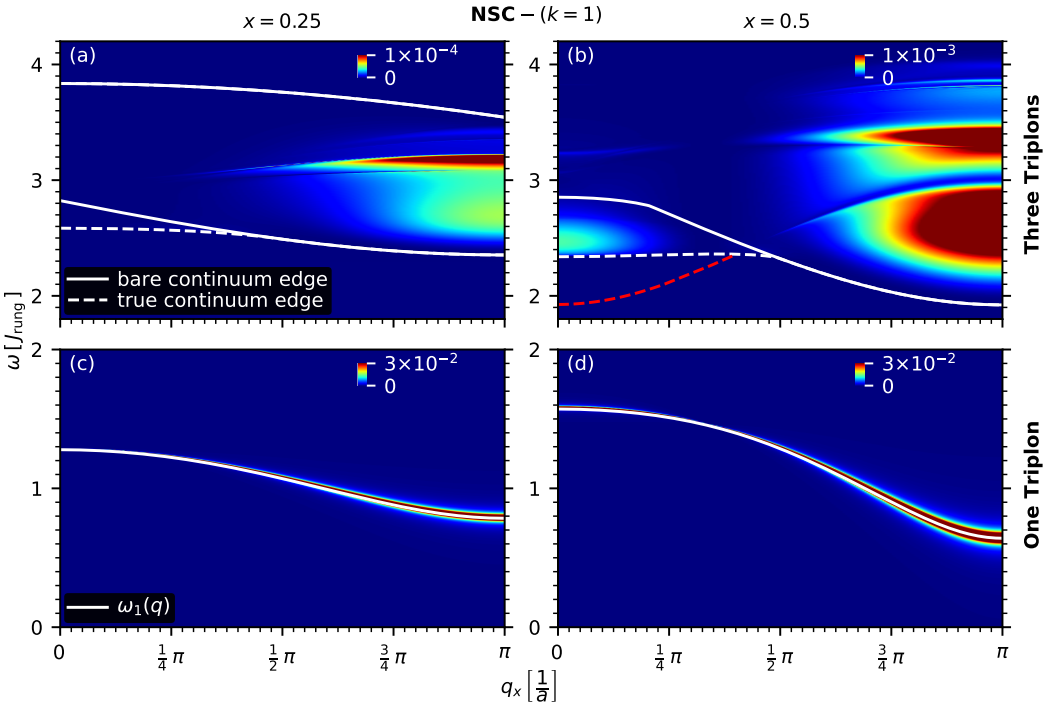

Figure 3.25: Spectral density $S(q_x, \omega)$ of the second leading NSC observable $O^{\mathrm{NSC},1}_{i,-}$ (see (3.2.19)) in one-triplon space and three-triplon space for perturbation parameters $x \in \{0.25, 0.5\}$.

Fig. 3.24 ($x \in \{0.25, 0.5\}$) and Fig. 3.26 ($x \in \{1.2, 2\}$) show the weights for the even observable $O^{\mathrm{NSC},1}_{i,+}$ in two-triplon space. Compared to the leading order ($k = 0$) results in Fig. 3.8 ($x \in \{0.25, 0.5\}$) and Fig. 3.10 ($x \in \{1.2, 2\}$), the spectral weight is shifted towards $q_x = 0$ and $q_x = \pi/a$, i.e. away from $q_x \approx 0.5\pi/a$. The leading order shows a single dominant feature at $q_x \approx 0.5\pi/a$ for $x \leq 0.5$, which is split into two features in the second leading order. Overall, one should expect larger spectral weight at the extreme values $q_x \approx \pi/a$ and $q_x \approx 0.25\pi/a$ than the first order results suggest.

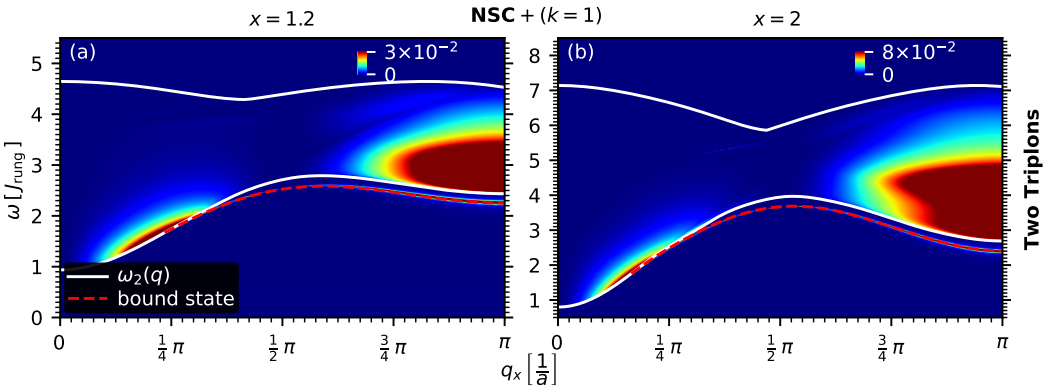

Figure 3.26: Spectral density $S(q_x, \omega)$ of the second leading NSC observable $O^{\mathrm{NSC},1}_{i,+}$ (see (3.2.19)) in two-triplon space for perturbation parameters $x \in \{1.2, 2\}$.

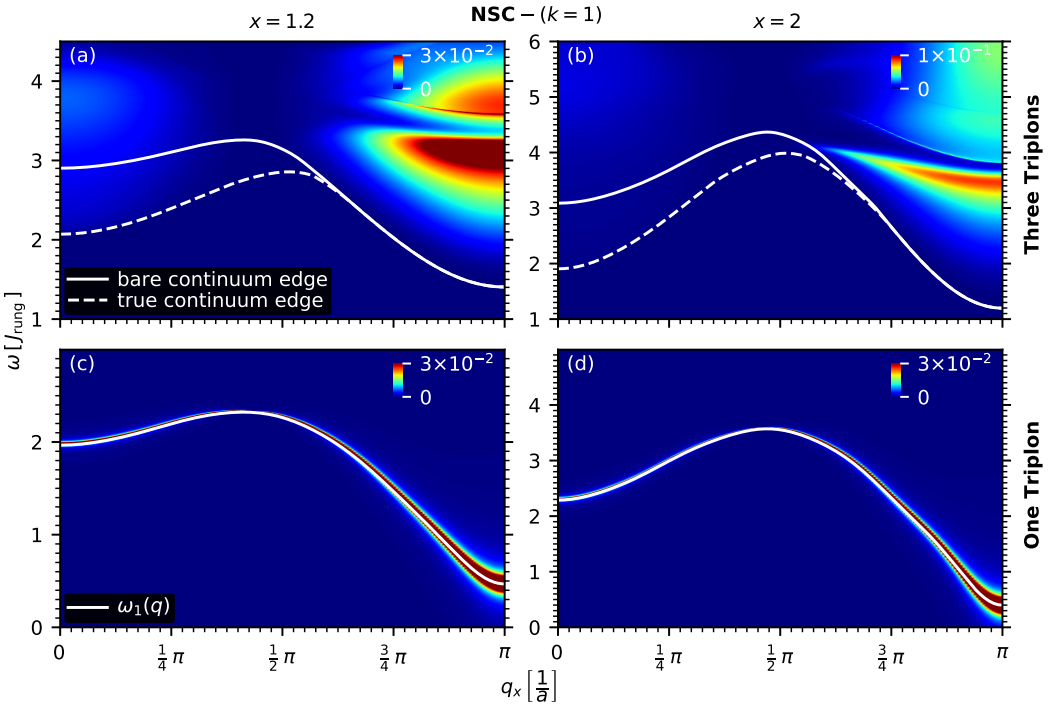

Figure 3.27: Spectral density $S(q_x, \omega)$ of the second leading NSC observable $O^{\mathrm{NSC},1}_{i,-}$ (see (3.2.19)) in one-triplon space and three-triplon space for perturbation parameters $x \in \{1.2, 2\}$.

Fig. 3.25 ($x \in \{0.25, 0.5\}$) and Fig. 3.27 ($x \in \{1.2, 2\}$) show the weights for the odd observable $O^{\mathrm{NSC},1}_{i,-}$, which can be compared to the leading order results in Fig. 3.9 ($x \in \{0.25, 0.5\}$) and Fig. 3.11 ($x \in \{1.2, 2\}$). In one-triplon space, the spectral weight is shifted towards $q_x = \pi/a$. In three-triplon space, the weight is also shifted towards large q_x, with multiple features arising, which are clearly separated energetically. The shape of the features is similar to the shape in the leading order.

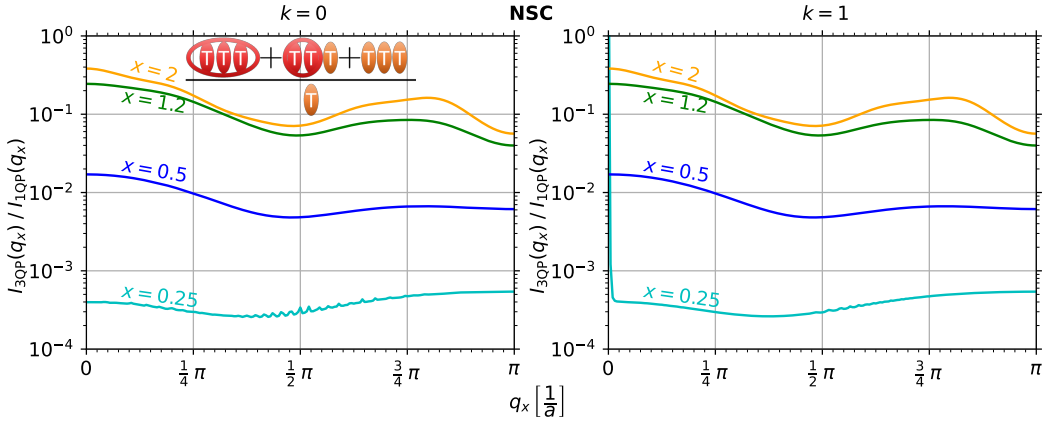

Figure 3.28: Left: Ratio of integrated three-triplon continuum weight to one-triplon weight for the leading NSC observable $O^{\mathrm{NSC},0}_{i,-}$ (see (3.2.19))) for various x and q_x. The same data as in the right panel of Fig. 3.12 is shown. Right: Ratio for the second leading NSC observable $O^{\mathrm{NSC},1}_{i,-}$. The data is identical to the leading order results aside from small fluctuations for $x = 0.25$.

The right panel of Fig. 3.28 depicts the ratio of integrated spectral weight in the three-triplon channel to the integrated weight in the one-triplon channel. A comparison with the leading order ($k = 0$) results in the left panel reveals that, aside from slight fluctuations, the relative spectral weight is identical.

To conclude this section, the second order calculation in the NSC channels reveals that one should expect more spectral weight at $q_x \approx \pi/a$ than the leading order results suggest. Furthermore, two distinct continuum features arise in the space of two-triplon states for $x \in \{0.25, 0.5\}$, while the leading order results suggest only a single feature.

3.4.5 Spin-Conserving Channel in Order $k = 2$

In Sec. 3.4.3 , we discussed the leading order ($k = 1$) of the SC channel. In this section, we investigate the next leading order of the UCL expansion, see Sec. 3.2.3.1 . The second leading order ($k = 2$) observable in the SC channel is

$$O^{\mathrm{SC},2}_{i,\pm} = \sum_{\tau} \left[J_{\mathrm{rung}} \boldsymbol{S}_{i,\tau} \cdot \boldsymbol{S}_{i,\bar{\tau}} + J_{\mathrm{leg}} \boldsymbol{S}_{i,\tau} \cdot \left(\boldsymbol{S}_{i+1,\tau} + \boldsymbol{S}_{i-1,\tau} \right) \right]^2 (-1)^{\tau} . \tag{3.4.53}$$

Like in the previous section, the absolute value of the spectral weight cannot be compared directly due to the nontrivial prefactors arising in the expansion, but the qualitative distribution gives insights about the overall spectral weight observed in RIXS experiments.

Fig. 3.29 ($x \in \{0.25, 0.5\}$) and Fig. 3.31 ($x \in \{1.2, 2\}$) show the weights for the even observable $O^{\mathrm{SC},2}_{i,+}$ in two-triplon space, which can be compared to the leading order results in Fig. 3.15 and Fig. 3.17. For $x = 0.25$, the spectral weight is shifted significantly towards smaller $q_x \in [0, 0.35\pi/a]$ with a large feature extending from $q_x = 0$ to the intersection point of the bound state and the continuum. For larger x, the continuum weight is also shifted towards smaller q_x, but less distinctly than for $x = 0.25$. For instance, for $x \in \{1.2, 2\}$ the continuum weight at the intersection point with the bound state increases in the $k = 2$ correction, while for $x = 0.5$ a novel weak feature arises at $q_x \in [0, 0.25\pi/a]$.

Fig. 3.30 ($x \in \{0.25, 0.5\}$) and Fig. 3.32 ($x \in \{1.2, 2\}$) show the weights for the odd observable $O^{\mathrm{SC},2}_{i,-}$ in three-triplon space. Compared to the leading order results in Fig. 3.16 and Fig. 3.18, the qualitative shape of the spectral weight in the continuum changes only marginally. An interesting shift of weight occurs, however, in the bound state. This is depicted in the right panel of Fig. 3.21, which shows the ratio of bound weight to integrated continuum weight for various x and q_x. Compared to the ratios of the leading order depicted in the left panel of Fig. 3.21, the highest ratio of bound weight arises for $x \in \{0.25, 0.5\}$ close to $q_x = 0$. This is a vital finding, because a dominant three-triplon bound state at $x \leq 1$ opens up new materials for which the bound state can be verified experimentally. The caveat is that for small x, the bound state has energy even closer to the continuum edge, making it more difficult to resolve it unambiguously in an experimental setting. As discussed in Sec. 3.4.3 , this problem can be circumvented with THz spectroscopy, which has a higher energy resolution than RIXS. Since the relative bound weight in the right panel of Fig. 3.21 is most dominant at $q_x \approx 0$ for $x = \{0.25, 0.5\}$, the marginal momentum transfer of THz spectroscopy poses less of a problem than for $x = \{1.2, 2\}$. However, note that THz spectroscopy is not described by the same structure factor as RIXS experiment.

To conclude this section, the second order results in the SC channel predict more spectral weight around $q_x \approx 0$ in two-triplon space than the leading order

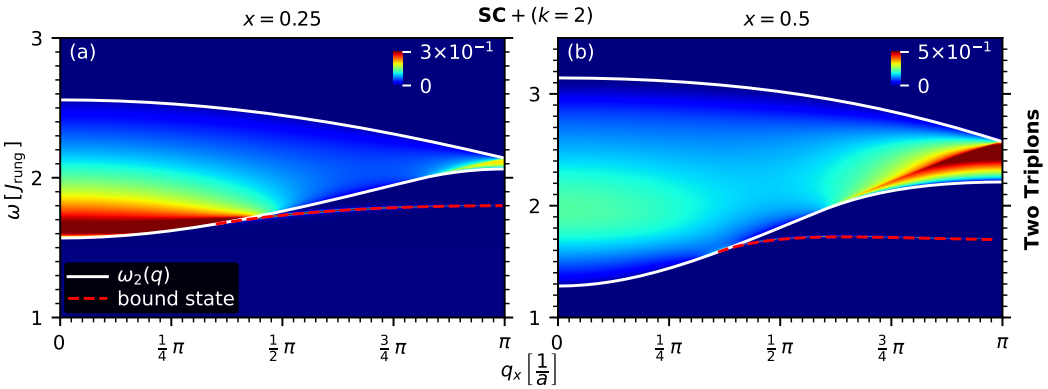

Figure 3.29: Spectral density $S(q_x, \omega)$ of the second leading SC observable $O^{\mathrm{SC},2}_{i,\pm}$ (see (3.2.19)) in two-triplon space for perturbation parameters $x \in \{0.25, 0.5\}$.

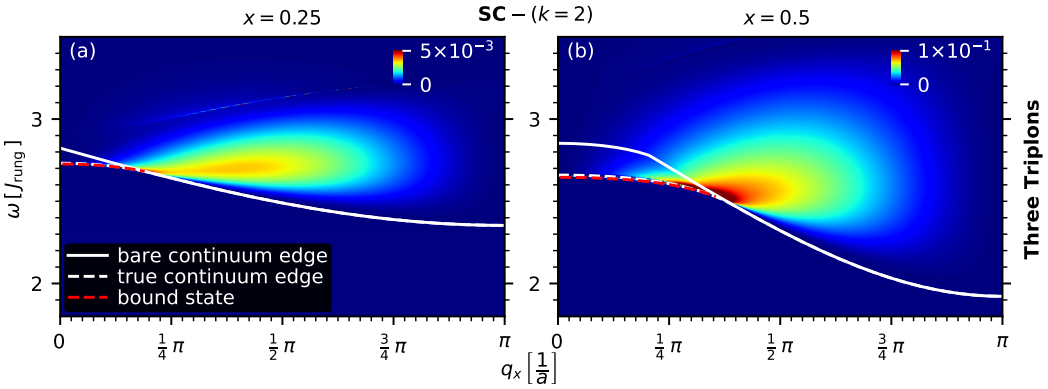

Figure 3.30: Spectral density $S(q_x, \omega)$ of the second leading SC observable $O^{\mathrm{SC},2}_{i,\pm}$ (see (3.2.19)) in three-triplon space for perturbation parameters $x \in \{0.25, 0.5\}$.

suggests. Furthermore, three-triplon bound states with dominant weight compared to the continuum are predicted for $x < 1$, while the leading order only suggests dominant bound states for $x \geq 1$. The three-triplon bound states at small x have the most dominant weight at $q_x \approx 0$, which is useful for THz spectroscopy, which offers high energy resolution but only marginal momentum transfer. However, the requirement of high energy resolution is even more important for small x, because the energy of three-triplon bound state and continuum are even closer to one another.

3.4.6 Comparison with Exact Diagonalization

In the previous sections, we presented the two leading order results in the SC channel and NSC channel. In this section, we compare the results obtained by deepCUT with results calculated by exact diagonalization (ED) [49] to emphasize the advantages of our approach and corroborate the results. We also discuss the accuracy of the deepCUT results in more detail in App. D.

Comparing the deepCUT results with ED results serves two purposes: (i) one can

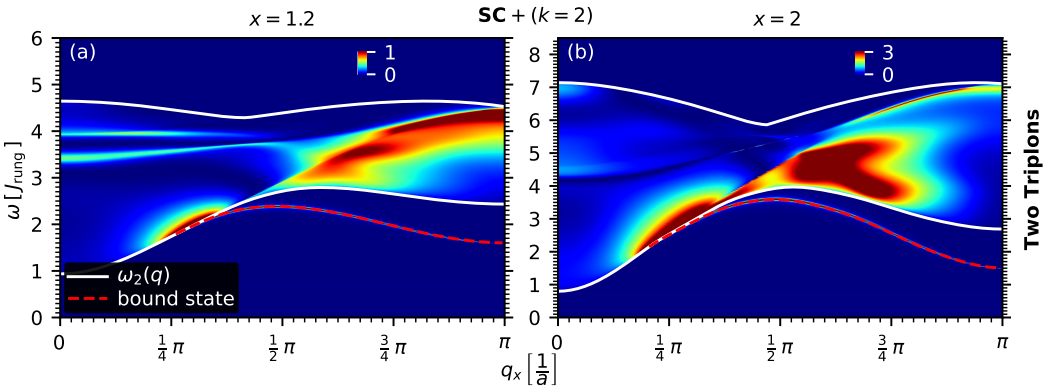

Figure 3.31: Spectral density $S(q_x, \omega)$ of the second leading SC observable $O^{\mathrm{SC},2}_{i,\pm}$ (see (3.2.19)) in two-triplon space for perturbation parameters $x \in \{1.2, 2\}$.

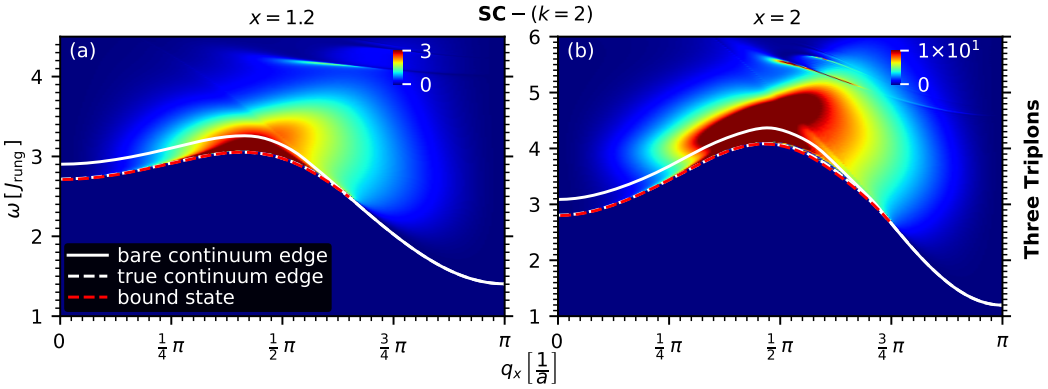

Figure 3.32: Spectral density $S(q_x, \omega)$ of the second leading SC observable $O^{\mathrm{SC},2}_{i,\pm}$ (see (3.2.19)) in three-triplon space for perturbation parameters $x \in \{1.2, 2\}$.

check whether the deepCUT results strongly contradict the ED results, which would be a clue for an error in the deepCUT approach, and (ii) one can compare properties of the methods. Fig. 3.33 shows ED data for $x = 1$ [49]. Note that in the ED calculation, N stands for the number of considered spins, so up to $N/2 = 14$ rungs are considered. Naively, this appears to be a larger system than the one considered in the deepCUT calculation. The deepCUT is evaluated up to order o10, so processes spanning up to 10 rungs are considered. The difference, however, is that deepCUT considers a system in thermodynamic limit and truncation occurs only in the triplon operators in second quantization. Due to translational symmetry, the effect of these operators is considered on the full system.

The first thing one notices when observing Fig. 3.33 is the fact that the ED-results are much more coarse than the deepCUT results discussed in previous sections. This is a consequence of the finite system size, which limits the resolution of the ED approach. The discretization of q_x is naturally limited by $N/2$. Significant finite size effects arise, which becomes apparent when comparing the results for different N. For instance, in panel (e), one observes two dominant features in two-triplon space

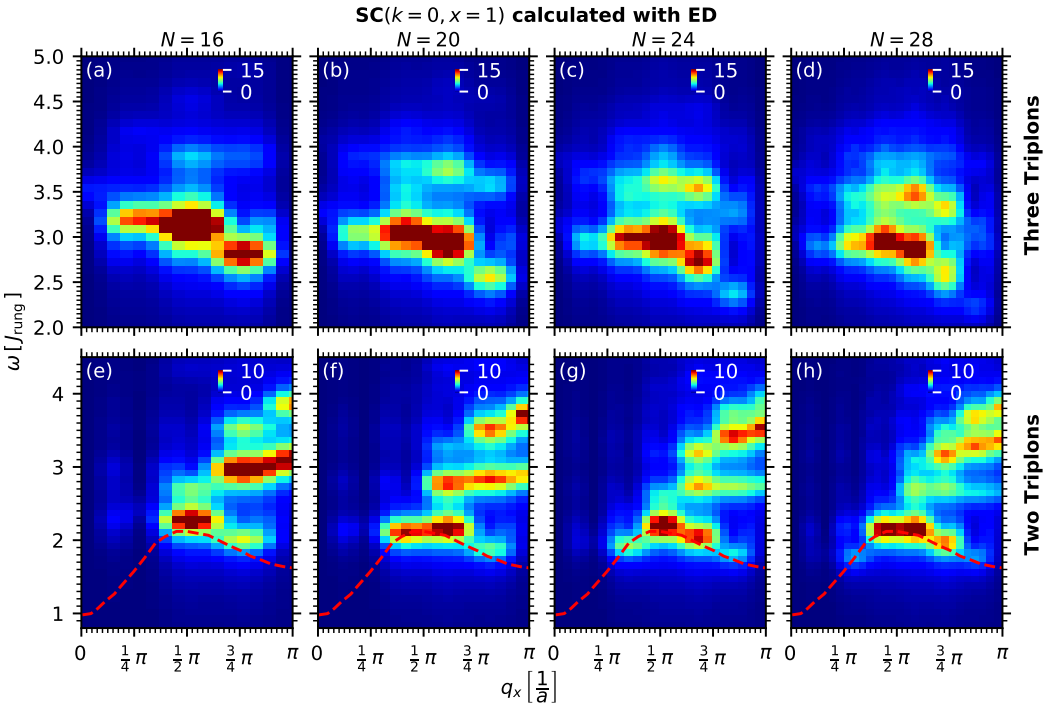

Figure 3.33: Spectral density in the SC channel for $x = 1$ calculated with exact diagonalization (data kindly provided by Umesh Kumar [49]) with various number of considered sites N, i.e. $N/2$ considered rungs, in two-triplon space ($q_y = 0$) and three-triplon space ($q_y = \pi/a$). The theoretical bound state curve is plotted as a red dashed line.

for $N = 16$. Increasing N in (f-h) changes the number and shape of the dominant features. In (f), the two features are flatter and a third dominant feature at higher energies arises. In (g) the middle features loses significant spectral weight. In (h) the middle feature has insignificant weight compared to the other features and the top feature splits into two features of different energies. The author of the ED data confirmed that this are indeed discretization artifacts. In the ED calculation, the two-triplon bound state is not calculated explicitly and the results do not explicitly reveal that it is a bound state without knowledge of the continuum limits. The energy-momentum relation is approximated by an analytical expression [49].

Fig. 3.34 shows a direct comparison of the ED results with $x = 1$ and $N = 28$ to the deepCUT results. The deepCUT results in panel (b) and (d) have an exceedingly better resolution that can be increased even further without performing the deepCUT calculation a second time. To double the resolution in q_x, one can perform the Lanczos tridiagonalization, see Sec. 3.3.3 , twice as often, which is only computationally expensive for three or more triplons. To double the resolution in ω one can perform the continued fraction expansion, see Sec. 3.3.4 , twice as often, which does not cost significant computation time. At worst, the computational cost of the deepCUT approach increases linearly with the resolution, while the dimension of the Hilbert space in ED scales exponentially with the system size. Both ED and

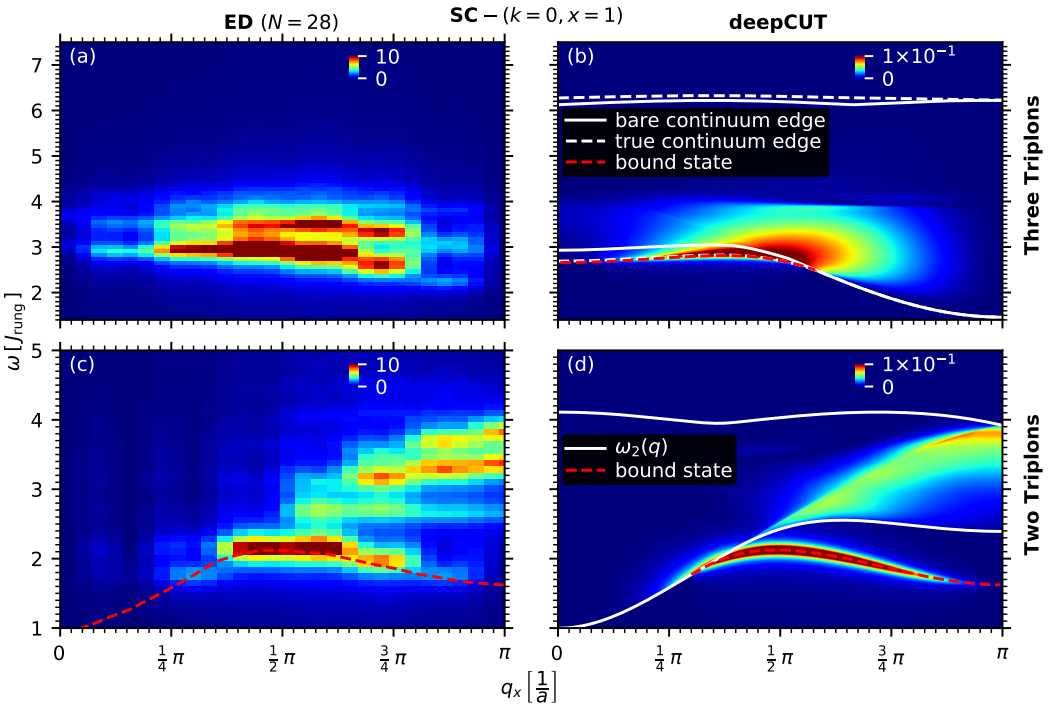

Figure 3.34: Spectral density (left column) in the SC channel for $x = 1$ calculated with exact diagonalization (data kindly provided by Umesh Kumar [49]) with $N = 28$ considered sites, i.e. $N/2 = 14$ considered rungs, in two-triplon space ($q_y = 0$) and three-triplon space ($q_y = \pi/a$). The data is compared with the (right column) deepCUT results, where the bound state is plotted with Gaussian broadening for easier comparison.

deepCUT yield significant features in the same area of phase space, which is expected. However, ED yields features with multiple maxima, while deepCUT yields fewer but continuous features. In panel (c), for instance, one finds 3-4 separate features around $\omega/J_{\text{rung}} \in [2.5, 4]$ and $q_x \in [0.5\pi/2, \pi/a]$, while panel (d) shows only two significant features, the bound state and a long feature in the continuum.

To conclude, the deepCUT approach provides several benefits over ED. One obtains outstanding resolution without finite size artifacts (but with finite-range effects) and can distinguish contributions from different numbers of quasi-particles. The true continuum limits and the dispersion relation of bound states are obtained directly by the method and bound states can be distinguished unambiguously from the continuum. Furthermore, one can selectively disable n-triplon interactions, which was used in Sec. 3.4.3 .

3.5 Concluding Discussion of the Response Function

In this chapter, we applied the deepCUT method to calculate spectral features of a spin-1/2 Heisenberg ladder (3.1.1) in both the NSC channel and the SC channel up to three-triplon space. The SC channel cannot be probed by INS experiments, but is accessible to RIXS. Convergence in high orders of the deepCUT expansion is more difficult when more triplons are considered. To calculate three-triplon contributions with high accuracy, we combine results in high expansion order o10, obtained with the (2:n)-generator, with the highest converged order of the (3:n)-generator.

The RIXS response can be described by the UCL expansion, with the first leading order in the SC channel being relevant for INS experiments. We calculated the two leading orders, both for the SC channel and the NSC channel. The second leading order describes the dominant corrections to the leading order.

In the NSC channel, our results for the leading order observable $O^{\mathrm{NSC},0}_{i,\tau} = S_{i,\tau}$ coincide with prior findings for INS experiments [32, 111]. We showed that the flow equation method provides a substantially higher resolution than exact diagonalization, partially because it allows one to calculate true continua, which are less prone to discretization errors. RIXS experiments make it possible to study the spectral weight even for larger energies in the three-triplon channel with a reasonably large cross section. The spectral feature in the NSC channel are separated well enough energetically to be captured as separate features by RIXS measurements. The second leading order NSC observable $O^{\mathrm{NSC},1}_{i,\pm} = S_{i,\tau}\left[J_{\mathrm{rung}}\boldsymbol{S}_{i,\tau}\cdot\boldsymbol{S}_{i,\bar{\tau}} + J_{\mathrm{leg}}\boldsymbol{S}_{i,\tau}\cdot\left(\boldsymbol{S}_{i+1,\tau}+\boldsymbol{S}_{i-1,\tau}\right)\right]$ introduces a shift of spectral weight towards large $q_x \approx \pi/a$. For $x \in \{0.25, 0.5\}$, we find novel spectral features in two-triplon space.

The leading order results in the SC channel are described by the observable $O^{\mathrm{SC},1}_{i,\tau} = J_{\mathrm{rung}}\boldsymbol{S}_{i,\tau}\cdot\boldsymbol{S}_{i,\bar{\tau}} + J_{\mathrm{leg}}\boldsymbol{S}_{i,\tau}\cdot\left(\boldsymbol{S}_{i+1,\tau}+\boldsymbol{S}_{i-1,\tau}\right)$. We calculated the response and showed the emergence of a three-triplon bound state. The surprising revelation is that this bound state only emerges due to genuine, i.e. irreducible, three-triplon interactions. In nature, multi-particle bound states usually arise due to two-body interactions. We showed that three-triplon interactions are necessary to form this bound state by selectively deactivating these interactions, which is possible due to the decoupling of n-particle subspaces by deepCUT. The spectral weight of the three-triplon bound state is significant and even dominates the continuum weight for $x = 2$ and $q_x \approx 0.42\pi/a$. By evaluating the second leading order observable $O^{\mathrm{SC},2}_{i,\tau}$, we showed that significant bound weight can be found for $x = 0.25$ at marginal momentum transfer $q_x \approx 0$. Note, however, that the odd parity channel, i.e. the channel with an odd number of triplon excitations, can only be probed with $q_y = \pi/a$, so a finite momentum transfer or some difference in the structure is still required.

The most significant finding is the emergence of three-triplon bound states due to irreducible three-triplon interactions. RIXS experiments can probe the phase space of the bound state, but the energy resolution of around $(10 - 100)\,\mathrm{meV}$ [130, 132] is not high enough to properly distinguish the bound state from the lower three-triplon continuum edge, which also carries significant weight. THz spectroscopy offers higher energy resolution below 1 neV [133,134], but only transfers marginal momentum. The dominant bound weight at $q_x \approx 0$ for $x = 0.25$ in the second leading order could allow one to measure the bound state with small momentum transfer. Alternatively, one could attempt to probe the bound state at $x = 2$ and $q_x \approx 0.42\pi/a$ with THz spectroscopy for a distorted spin ladder with periodicity of four rungs, which folds $q_x \in \{0.25\pi/a, 0.5\pi/a, 0.75\pi/a\}$ back to the center of the Brillouin zone. Tab. 3.1, which can be found at the beginning of this chapter, lists candidates of cuprates for experimental verification. With the steady improvement of experimental techniques, we are hopeful of verifications of our findings in the near future.

Future theoretical studies could investigate the RIXS response for more complex systems, e.g. spin ladders with diagonal couplings between nearest-next neighbors or coupled spin ladders. Furthermore, one could investigate more terms of the UCL expansion, such as the cross term neglected in our calculation, see App. A, or consider the full response by summing over the leading orders with known coefficients (calculated from the core-hole lifetime). Additionally, a fascinating question is whether n-triplon bound states with $n > 3$ triplons arise in spin ladders. Such n-triplon strings would provide a generalization of Bethe string [121, 122]. Different from Bethe strings, they would not be restricted to integrable systems such as spin chains.

Our results show that the CUT method, and specifically deepCUT as a highly optimized variant, is very powerful and the effective quasi-particle-conserving basis provides many advantages. The selective disabling of three-triplon interactions allowed us to show unambiguously that they are necessary to form three-triplon bound states. We were able to trivially separate continua from bound states and different excitation channels from one another and sum rule checks verified that no significant spectral weight was neglected. The results are real continua in high resolution, which do not show significant discretization artifacts. Even in four-triplon space, which is too large to treat with high accuracy, we were able to obtain a rough approximation of the spectral weight, see App. D. The approach described in this chapter opens novel ways to study complex bound states, which are also relevant in other fields, for instance for finding bound states in superconducting nanowires for quantum computing [139], topological bound states in non-Hermitian systems of photonic lattices [140] and for the discovery of three-body correlations in ultracold atoms [141]. In the following chapters, we will lay the groundwork to extend the CUT method to a wider class of problems.

Chapter 4

Hard-Core Flow Equations in Momentum-Space

In the previous chapter, the flow equation method was applied to compute the dynamic response of a spin ladder in RIXS experiments and predict three-triplon bound states. Our results show the strengths of the method. However, flow equations have already been applied to spin ladders numerous times in the past, albeit only for the simple INS observable. In Chap. 4 to Chap. 5, the focus is shifted to methodical improvements of flow equations in order to treat a wider class of problems.

In this chapter we study flow equations for hard-core systems using the pc-generator in momentum space with the goal of finding strategies to apply the mechanism to gapless quantum systems, for instance systems at a quantum critical point. To this end, a one-dimensional spin model is studied. Our numerical computations show that a direct implementation of the flow equation method in momentum space is considerably more costly than in real space, but principally possible. However, both the real-space and momentum-space CUT do not converge in the vicinity of the quantum critical point other than for extremely small system sizes. We introduce truncation schemes in momentum space and study their effect on the flow. However, no significant improvement over spatial truncation schemes is found at the current stage. Further analyses show that close to the fixed point, many coefficient converge with the same speed. This finding could be used in the future for analytic and numerical simplifications.

We introduce the physical model and discuss the analytical dispersion in Sec. 4.1. In Sec. 4.2 we discuss how applying a CUT for hard-core particles in momentum space offers both benefits and challenges. We investigate different strategies in Sec. 4.3 and conclude our findings in Sec. 4.4 .

4.1 Transverse-Field Ising Model

4.1.1 Model in Real Space

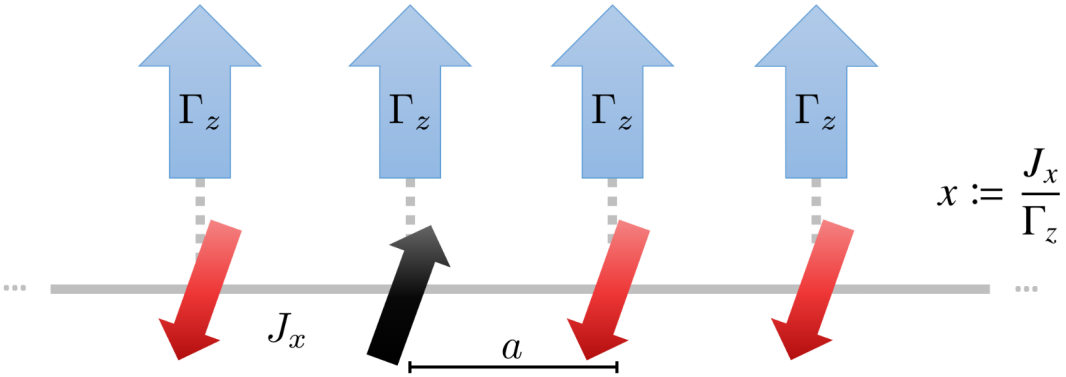

Figure 4.1: Schematic representation of the TFIM model (4.1.2). The spin-1/2 particles are fixed on equidistant sites of distance a on a one-dimensional chain and the x-components S_x of next neighbors interact with strength J_x, while the z-components S_z are coupled to a magnetic field Γ_z. Black arrows represents spin-up, red arrows spin-down and blue arrows represent the magnetic field.

The generalized Heisenberg spin chain in a magnetic field [142] is defined as

$$H = \boldsymbol{\Gamma} \sum_{i=0}^{N-1} \boldsymbol{S}_i - \sum_{i,j=0}^{N-1} \sum_{\alpha,\beta\in\{x,y,z\}} 2J_{ij}^{\alpha\beta} S_i^{\alpha} S_j^{\beta} \tag{4.1.1}$$

with spin operators $\boldsymbol{S}_i$ on sites $i \in \{0, 1, ..., N-1\}$ and elements S_i^{α} with $\alpha \in \{x, y, z\}$. The external magnetic field is parametrized by $\boldsymbol{\Gamma}$ and the interactions between pairs of spins are described by $J_{ij}^{\alpha\beta}$. The prefactor 2 in the interaction term is chosen to compensate for the quadratic factor $(1/2)^2$ from the spins compared to the linear factor $1/2$ in the field term. This system cannot be solved exactly, apart from special cases [143]. In the following investigation, we focus on an exactly solvable special case, the **transverse-field Ising model** (TFIM)

$$H = \Gamma_z \sum_{i=0}^{N-1} S_i^z - 2J_x \sum_{i=0}^{N-1} S_i^x S_{i+1}^x \,, \tag{4.1.2}$$

which has already been studied extensively [54, 144–146] in the past and is depicted in Fig. 4.1 . The TFIM describes a one-dimensional spin chain with next-neighbor interaction of the x-components S_i^x and interactions with a magnetic field in z-direction, i.e. transversal with respect to the next-neighbor interaction, and periodic boundaries $\boldsymbol{S}_N = \boldsymbol{S}_0$. The ratio $x := J_x/\Gamma_z$ is the only relevant quantum parameter governing the phase of the system at temperature $T = 0$, since a global prefactor of the energy do not affect the phase.

The TFIM has been studied in the past using various methods, including CUT in real space, which utilizes a transformation to string operators [35]. For $|x| < 1$, all spins are aligned antiparallel to the magnetic field in the ground state. For $|x| > 1$ the spins obey ferromagnetic ordering in x-direction for $x > 1$ or antiferromagnetic ordering for $x < -1$ in the ground state. Note that the aim of this chapter is not to contribute novel findings about the TFIM, but rather to use it as a toy model to study the applicability of truncation schemes in momentum space. Considering a one-dimensional system provides two major advantages: numerical calculations are less computationally expensive and quantum critical effects are more dominant [52]. In particular, the TFIM hosts flavorless hard-core bosons, see below, which provide a distinct challenge in momentum space.

The commutation relation of the spin operators in natural units, i.e. $\hbar = 1$, is

$$[S_j^\alpha, S_l^\beta] = i\delta_{j,l} \sum_{\gamma\in\{x,y,z\}} \epsilon_{\alpha\beta\gamma} S_i^\gamma \,. \tag{4.1.3}$$

One can transform to ladder operators

$$S_j^\pm = S_j^x \pm \mathrm{i} S_j^y = (S_j^\mp)^\dagger \tag{4.1.4}$$

by using the relations

$$S_j^x \overset{(4.1.4)}{=} \frac{1}{2}(S_j^+ + S_j^-)\,, \tag{4.1.5}$$

$$S_j^\pm S_j^\mp = (S_j^x)^2 + (S_j^y)^2 \mp \mathrm{i}\underbrace{[S_j^x, S_j^y]}_{\overset{(4.1.3)}{=}\mathrm{i}S_j^z} = \underbrace{\boldsymbol{S}_i^2}_{\frac{3}{4}} - \underbrace{(S_j^z)^2}_{\frac{1}{4}} \pm S_j^z = \frac{1}{2} \pm S_j^z \,. \tag{4.1.6}$$

The ladder operators fulfill the (anti-)commutation relations

$$[S_j^-, S_l^+] = \mathrm{i}\underbrace{[S_j^x, S_l^y]}_{\overset{(4.1.3)}{=}\mathrm{i}\delta_{j,l}S_j^z} - \mathrm{i}\underbrace{[S_j^y, S_l^x]}_{\overset{(4.1.3)}{=}-\mathrm{i}\delta_{j,l}S_j^z} = -2\delta_{j,l}S_j^z \overset{(4.1.6)}{=} \delta_{j,l}(1 - 2S_j^+ S_j^-)\,, \tag{4.1.7a}$$

$$[S_j^\pm, S_l^\pm] = \pm\mathrm{i}\underbrace{[S_j^x, S_l^y]}_{\overset{(4.1.3)}{=}\mathrm{i}\delta_{j,l}S_j^z} \pm \mathrm{i}\underbrace{[S_j^y, S_l^x]}_{\overset{(4.1.3)}{=}-\mathrm{i}\delta_{j,l}S_j^z} = 0\,, \tag{4.1.7b}$$

$$\{S_j^\pm, S_j^\pm\} = \underbrace{\{S_j^x, S_j^x\}}_{\frac{1}{2}} - \underbrace{\{S_j^y, S_j^y\}}_{\frac{1}{2}} = 0\,. \tag{4.1.7c}$$

On can use (4.1.5) to describe the system (4.1.2) in the eigenbasis of S_i^z, where the ladder operators act similar to creation and annihilation operators

$$\frac{H}{\Gamma_z} = \sum_{i=0}^{N-1} \left(S_i^+ S_i^- - \frac{1}{2} \right) - \frac{x}{2} \sum_{i=0}^{N-1} \left(S_i^+ S_{i+1}^- + S_i^+ S_{i+1}^+ + \mathrm{h.c.} \right) . \tag{4.1.8}$$

For the discussion of this system, it is useful to use operators similar to the triplon operators (3.1.2) introduced in Chap. 3 . To that end, we apply the **Matsubara-Matsuda transformation** [147]

$$S^+ = b^\dagger \,, \tag{4.1.9a}$$
$$S^- = b \;\;, \tag{4.1.9b}$$
$$S^z = b^\dagger b \;\; - \frac{1}{2} \tag{4.1.9c}$$

with creation ($b^\dagger$) and annihilation (b) operators describing **hard-core bosons** fulfilling the

Hard-Core Algebra (Real Space)

$$\left[b_i, b_j^\dagger\right] = \delta_{i,j}\left(1 - 2b_i^\dagger b_i\right) \,, \tag{4.1.10a}$$
$$[b_i, b_j] = \left[b_i^\dagger, b_j^\dagger\right] = 0 \,, \quad \forall i \neq j \,, \tag{4.1.10b}$$
$$\{b_i, b_i\} = \left\{b_i^\dagger, b_i^\dagger\right\} = 0 \,. \tag{4.1.10c}$$

Note the similarity to the commutation relations (3.1.3). The only difference lies in the fact that the hard-core bosons described here are flavorless, i.e. instead of four states $|s\rangle$, $|x\rangle$, $|y\rangle$ and $|z\rangle$ per site with three different triplon flavors $\alpha \in \{x, y, z\}$, only two states $|0\rangle$ (no excitation) and $|1\rangle$ (hard-core bosonic excitation) per site exist. Aside from that, the algebra describes similar particles to triplons: the local Hilbert space is finite, allowing only for two possible local energies and, since the hard-core bosons are flavorless, two possible local states. In that sense, hard-core bosons are similar to fermions, which fulfill the Pauli exclusion principle. This motivates the name "hard-core", because this principle can be understood as a hard-core repulsion of the quasi-particle excitations. On the other hand, they can also be understood as bosons, because hard-core operators on different sites commute rather than anticommute. This can be shown explicitly by rearranging (4.1.10a) for the two cases $i = j$ and $i \neq j$

$$\begin{aligned}\left[b_i, b_j^\dagger\right] = \delta_{i,j}\left(1 - 2b_i^\dagger b_i\right) &= \begin{cases} 1 - 2b_i^\dagger b_i & , i = j \,, \\ 0 & , i \neq j \end{cases} \\ \Leftrightarrow \begin{cases} \left\{b_i, b_i^\dagger\right\} = b_i b_i^\dagger + b_i^\dagger b_i = 1 & , i = j \,, \\ \left[b_i, b_j^\dagger\right] = 0 = \delta_{i,j} & , i \neq j \,. \end{cases}\end{aligned} \tag{4.1.11}$$

One can apply (4.1.9) to formulate (4.1.8) in terms of hard-core operators

$$\frac{H}{\Gamma_z} = \sum_{i=0}^{N-1}\left(b_i^\dagger b_i - \frac{1}{2}\right) - \frac{x}{2}\sum_{i=0}^{N-1}\left(b_i^\dagger b_{i+1} + b_i^\dagger b_{i+1}^\dagger + \text{h.c.}\right) \,. \tag{4.1.12}$$

4.1.2 Model in Momentum Space

For the discussion of CUT methods in momentum space, it is necessary to first describe the model in momentum space with Fourier transformations. For trivial systems consisting of only bilinear hopping terms $b_i^\dagger b_j$, a Fourier transformation already fully diagonalizes H. Fourier transformations are also useful for less trivial systems if they are translationally invariant, because this discrete invariance corresponds to conservation of total momentum up to summands $n2\pi/a$ with $n \in \mathbb{Z}$. For the TFIM model considered here, the Fourier transformed hard-core operators

$$b_k = \frac{1}{\sqrt{N}} \sum_{j=0}^{N-1} e^{\mathrm{i}kx_j} b_j \,, \qquad b_k^\dagger = \frac{1}{\sqrt{N}} \sum_{j=0}^{N-1} e^{-\mathrm{i}kx_j} b_j^\dagger \,, \tag{4.1.13a}$$

$$b_j = \frac{1}{\sqrt{N}} \sum_{k}^{1.\mathrm{BZ}} e^{-\mathrm{i}kx_j} b_k \,, \qquad b_j^\dagger = \frac{1}{\sqrt{N}} \sum_{k}^{1.\mathrm{BZ}} e^{\mathrm{i}kx_j} b_k^\dagger \tag{4.1.13b}$$

with $x_j := ja$ fulfill the algebra

$$[b_k, b_{k'}] \overset{(4.1.13a)}{=} \frac{1}{N} \sum_{j,l=0}^{N-1} e^{\mathrm{i}(kx_j + k'x_l)} \underbrace{[b_j, b_l]}_{\overset{(4.1.10b)}{=} 0} = 0 \,, \tag{4.1.14a}$$

$$\left[b_k^\dagger, b_{k'}^\dagger\right] = [b_{k'}, b_k]^\dagger \overset{(4.1.14a)}{=} 0 \,, \tag{4.1.14b}$$

$$\begin{aligned} \left[b_k, b_{k'}^\dagger\right] &\overset{(4.1.13a)}{=} \frac{1}{N} \sum_{j,l=0}^{N-1} e^{\mathrm{i}(kx_j - k'x_l)} \underbrace{\cdot \left[\, b_j \,,\, b_l^\dagger \,\right]}_{\overset{(4.1.10a)}{=} \delta_{j,l}(1 - 2b_j^\dagger b_j)} \\ &= \underbrace{\frac{1}{N} \sum_{j=0}^{N-1} e^{\mathrm{i}(k-k')x_j}}_{\delta_{k,k'}} - \frac{2}{N} \sum_{j=0}^{N-1} e^{\mathrm{i}(k-k')x_j} b_j^\dagger b_j \\ &\overset{(4.1.13b)}{=} \delta_{k,k'} - \frac{2}{N} \sum_{q,q'}^{1.\mathrm{BZ}} \underbrace{\frac{1}{N} \sum_{j=0}^{N-1} e^{i(k-k'+q-q')x_j}}_{\delta_{k-k'+q,q'}} b_q^\dagger b_{q'} \\ &= \delta_{k,k'} - \frac{2}{N} \sum_{q}^{1.\mathrm{BZ}} b_q^\dagger b_{k-k'+q} \,. \end{aligned} \tag{4.1.14c}$$

While the commutators $[b_k, b_{k'}]$ vanish just like in real space, the commutator $[b_k, b_{k'}^\dagger]$ is more involved, introducing a summation over various momenta. This is relevant for CUTs, because it causes more operator monomials to arise during the calculation of the commutator (2.2.7) in second quantization, i.e. more coefficients that must be tracked during integration.

The anticommutation relations in momentum space are less trivial than in real space. The real-space operators only anticommute if they act on the same site, so an

analogous calculation to (4.1.14a) for the momentum-space anticommutators is not possible. One finds

$$b_k b_{k'}^\dagger - b_{k'}^\dagger b_k \overset{(4.1.14c)}{=} \delta_{k,k'} - \frac{2}{N}\sum_q^{1.\mathrm{BZ}} b_q^\dagger b_{k-k'+q}\,, \tag{4.1.15a}$$

$$\Leftrightarrow b_k b_{k'}^\dagger + b_{k'}^\dagger b_k = \delta_{k,k'} - \frac{2}{N}\sum_q^{1.\mathrm{BZ}} \left(1 - N\delta_{k',q}\right) b_q^\dagger b_{k-k'+q} = \{b_k, b_{k'}\}\,. \tag{4.1.15b}$$

Consequently, the trivial hard-core repulsion $\{b_i, b_i\} = 0$ in real space, i.e. the constraint of the number of hard-core excitation per site to $n_i \in \{0, 1\}$, does not translate to a more complicated constraint in momentum space, i.e. multiple hard-core excitations with the same momentum can, in principle, exist. We discuss how to correctly describe the hard-core repulsion in momentum space in Sec. 4.2.3 . For now, it suffices to summarize the most useful commutation relations

Hard-Core Algebra (Momentum Space)

$$\left[b_k, b_{k'}^\dagger\right] = \delta_{k,k'} - \frac{2}{N}\sum_q^{1.\mathrm{BZ}} b_q^\dagger b_{k-k'+q}\,, \tag{4.1.16a}$$

$$[b_k, b_{k'}] = \left[b_k^\dagger, b_{k'}^\dagger\right] = 0\,. \tag{4.1.16b}$$

The TFIM (4.1.12) can be expressed in terms of the Fourier-transformed hard-core operators (4.1.13a) by applying the relation $\delta_{k,k'} = \frac{1}{N}\sum_{x_i} e^{\mathrm{i}x_i(k-k')}$ to apply conservation of momentum. The final Hamiltonian in momentum space reads

$$\begin{aligned}\frac{H}{\Gamma_z} = &\sum_k^{1.\mathrm{BZ}} \left[\Big(1 - x\cos(ka)\Big) b_k^\dagger b_k\right] \\ &- \frac{x}{2}\sum_k^{1.\mathrm{BZ}} \left[\cos(ka)\left(b_k^\dagger b_{-k}^\dagger + \text{h.c.}\right)\right] - \frac{N}{2}\,.\end{aligned} \tag{4.1.17}$$

The last summand is a constant energy shift and can be omitted, because we are not interested in the ground state energy, but in the relative energy of excited states in relation to the ground state.

4.1.3 Analytical Results

The TFIM can be solved using a Jordan-Wigner transformation in real space to obtain spinless fermionic operators, a subsequent Fourier transformation to obtain momentum-conserving operator terms and a final Bogoliubov transformation to treat the pair-creation and pair-annihilation terms. The full calculation is discussed in

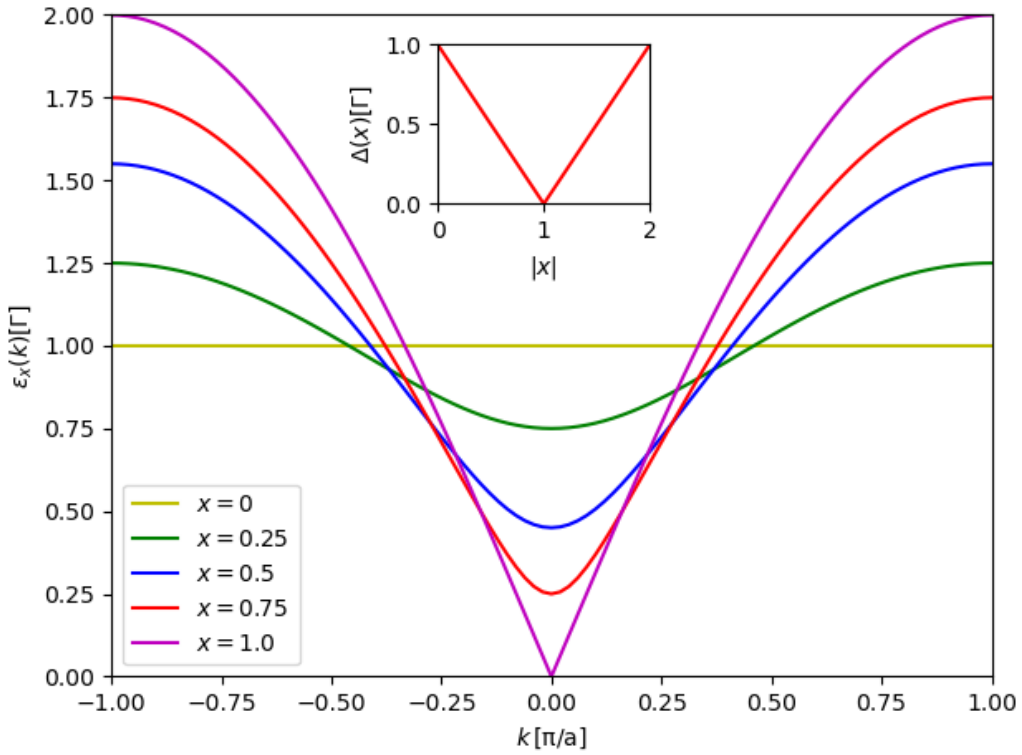

Figure 4.2: Dispersion $\epsilon_x(k)$, see (4.1.18b), and energy gap $\Delta(x)$, see (4.1.19), of the TFIM.

App. E. The resulting Hamiltonian for the ferromagnetic case $x \in [0, 1]$ is

$$\frac{H}{\Gamma_z} = \sum_k^{1.\mathrm{BZ}} \epsilon(k) \left(f_k^\dagger f_k - \frac{1}{2} \right) , \tag{4.1.18a}$$

$$\epsilon(k) = \sqrt{\Big(1 - x\Big)^2 + 2x\Big(1 - \cos(ka)\Big)} \tag{4.1.18b}$$

with the fermionic annihilation and creation operators $f_k^{(\dagger)}$ and the dispersion relation (4.1.18b). The dispersion and the energy gap

$$\Delta(x) := \min_k\big(\epsilon(k)\big) = |1 - x| \tag{4.1.19}$$

are plotted in Fig. 4.2. At $|x| = 1$, a the gap closes and a second order phase transition occurs, i.e. this is a quantum critical point. The antiferromagnetic case $x \in [-1, 0]$ has the same dispersion shifted by $k \to k + \pi/a$, since it is related to the ferromagnetic case by the flip of every second spin.

We use the analytical results of the gap (4.1.19) as a reference to check the accuracy of the CUT method in momentum space with various truncation schemes.

4.2 Momentum Continuous Unitary Transformations

In this section, we discuss why it can be advantageous to perform the CUT in momentum space to treat a system with a vanishing energy gap. We also point out challenges of this approach for hard-core systems.

4.2.1 Advantages

A vanishing or extremely small gap complicates renormalizing methods, such as CUTs. Local spatial truncation schemes fail because the correlation length diverges. Additionally, perturbative expansions fail, since the energy denominator vanishes, which makes it necessary to sum over an arbitrary number of orders. Furthermore, energies from different particle-spaces can overlap, e.g. the three-particle continuum with the one-quasi-particle dispersion, causing the particle picture to break down.

In momentum space, each single operator term is maximally delocalized. In this way, a finite number of operator monomials can describe strongly delocalized processes. While the real-space approach is suitable for systems with strongly localized elementary excitations, a momentum-space approach can perform better for strongly delocalized elementary excitations.

To perform an efficient calculation, all symmetries of a given system should be exploited. Symmetries in real space can be applied in momentum space as well and sometimes even easier than in real space. For instance, the real-space Hamiltonian (4.1.12) exhibits translational invariance, i.e. coefficients C_{ij} of operator monomials related to sites i and j depends only on the difference of sites, i.e. $C_{ij} = C_{i-j}$. In momentum space, this symmetry appears in the form of conservation of total momentum, e.g. $C_{k,k'} b_k b_{k'} = C_{k,k} b_k b_{-k} \delta_{k',-k}$ and $C^k_{k'} b^\dagger_k b_{k'} = C^k_k b^\dagger_k b_{-k} \delta_{k',k}$. Note that we use subscripts for the annihilation indices and superscripts for the creation indices. Translation invariance in real space implies that, for instance, all operator monomials $b^\dagger_{i+\Delta} b_i$ with the same Δ share a single coefficient, so the number of tracked coefficients is reduced by a factor $1/N$ when N sites are tracked. In momentum space, this translates to the last momentum index being determined unambiguously by all other momenta. Other symmetries can also be used analogously in momentum space. For instance, mirror symmetry $C^{j_1,\cdots}_{i_1,\dots} = C^{-j_1,\cdots}_{-i_1,\dots}$ can be applied directly in the form $C^{q_1,\cdots}_{k_1,\dots} = C^{-q_1,\cdots}_{-k_1,\dots}$ and so can Hermiticity $C^{k_1,\cdots}_{q_1,\dots} = (C^{q_1,\cdots}_{k_1,\dots})^*$. Both symmetries are valid for the TFIM (4.1.12).

4.2.2 Challenges

The real-space formulation of the TFIM (4.1.12) with hard-core operators contains highly localized operator monomials that span only next neighbors. When deriving the flow equations, the number of tracked coefficients increases with each

commutation (2.2.7) and is often only limited by the truncation scheme. Nevertheless, a small number of finite coefficients in the initial Hamiltonian $H(\ell = 0)$ is advantageous to reduce the number of significant operator monomials that should not be truncated. When taking symmetries into account, the initial real-space TFIM (4.1.12) effectively only contains three finite initial coefficient: Those for the operator monomials $b_i^\dagger b_i$, $b_i^\dagger b_{i+1}$ and $b_i^\dagger b_{i+1}^\dagger$. In contrast, the initial formulation in momentum space (4.1.17) contains various bilinear operator monomials, specifically $b_k^\dagger b_k$ and $b_k^\dagger b_{-k}^\dagger$ for all values of k in the Brillouin zone. This is not surprising, since the initial real-space Hamiltonian is highly localized, requiring a large number of delocalized operator terms in momentum space. This drastically increases the number of tracked coefficients in momentum space and therefore the computational cost.

Additionally, the hard-core algebra in momentum space (4.1.16a) is more involved than in real space (4.1.10a). In real space, each commutation introduces the term $[b_i, b_j^\dagger] = \delta_{i,j}\left(1 - 2b_i^\dagger b_i\right)$ with two new summands: one with two less operators and one with the same amount of operators, which act on the same site as the original operators. In momentum space, each commutation $[b_k, b_{k'}^\dagger] = \delta_{k,k'} - \frac{2}{N}\sum_q^{1.\mathrm{BZ}} b_q^\dagger b_{k-k'+q}$ introduces $N+1$ new summands: one with two fewer operators and N with the same amount of operators, which can act on different momentum sites than the original operators. This way, the number of tracked coefficients increases even more rapidly in momentum space. Note that this problem only occurs for hard-core excitations, since simple bosonic and fermionic excitations fulfill the same algebra in real and momentum space.

4.2.3 Hard-Core Repulsion in Momentum Space

In real space, the local Hilbert space at each site is finite, i.e. only $n_i \in \{0, 1\}$ hard-core excitations are allowed, due to the anticommutator $\{b_i, b_i\} = 0$, see (4.1.10c). This restriction also reduces the number of tracked coefficients in the flow equations, since operator monomials containing terms $b_i^\dagger b_i^\dagger$ or $b_i b_i$, i.e. two subsequent creations (or annihilations) on the same site, have vanishing coefficients. In momentum space, however, the anticommutator is more complicated, so it is not explicitly forbidden to create two excitations and operator monomials containing terms such as $b_k^\dagger b_k^\dagger$ or $b_k b_k$ do not have a vanishing coefficient. The hard-core repulsion can be reformulated as a more involved condition in momentum space. In this section, we motivate and introduce a general formula for the hard-core repulsion (4.1.10c) in momentum space. We use the notation $h[A]$ for the coefficient of an operator monomial A, see Sec. 2.2 .

The hard-core condition in momentum space can be derived most easily for bi-

linear operators

$$\begin{aligned} 0 \overset{(4.1.10c)}{=} \delta_{\Delta,0} \sum_{j=0}^{N-1} b_j^\dagger b_{j+\Delta}^\dagger &= \delta_{\Delta,0} \sum_{k,k'}^{1.\mathrm{BZ}} \underbrace{\frac{1}{N} \sum_{j=1}^{N-1} e^{\mathrm{i}j(k+k')}}_{=\delta_{k,-k'}} e^{\mathrm{i}k'\Delta} b_k^\dagger b_{k'}^\dagger \\ &= \delta_{\Delta,0} \sum_{k}^{1.\mathrm{BZ}} e^{-\mathrm{i}k\Delta} b_k^\dagger b_{-k}^\dagger = \sum_{k}^{1.\mathrm{BZ}} b_k^\dagger b_{-k}^\dagger \,. \end{aligned} \tag{4.2.20}$$

Hence, the bilinear condition in momentum-space is

$$0 = \sum_k h[b_k^\dagger b_{-k}^\dagger] \,. \tag{4.2.21}$$

This result is hardly surprising, because the Fourier transform of the real-space term $b_i^\dagger b_i^\dagger$ is the sum over all momentum space terms $b_k^\dagger b_k^\dagger$. Note that in real-space all N bilinear hard-core conditions $b_i^\dagger b_i^\dagger = 0$ for $i \in \{0, 1, ..., N-1\}$ are linear dependent due to translation invariance. Consequently, the single condition (4.2.21) in momentum space fully captures the hard-core restraint on the bilinear level.

For a quartic operator of the form $b_k^\dagger b_{k'}^\dagger b_q b_{k+k'-q}$ one obtains

$$0 \overset{(4.1.10c)}{=} \delta_{\Delta_i,0} N \sum_{j=1}^{N-1} b_j^\dagger b_{j+\Delta_1}^\dagger b_{j+\tilde{\Delta}} b_{j+\tilde{\Delta}+\Delta_2} \quad \forall i \in \{1,2\} \tag{4.2.22a}$$

$$= \delta_{\Delta_i,0} \sum_{k,k',q,q'}^{1.\mathrm{BZ}} \underbrace{\frac{1}{N} \sum_{j=1}^{N-1} e^{\mathrm{i}j(k+k'-q-q')}}_{=\delta_{k+k'-q,q'}} e^{\mathrm{i}(k'\Delta_1 - q'\Delta_2 - (q+q')\tilde{\Delta})} b_k^\dagger b_{k'}^\dagger b_q b_{q'} \tag{4.2.22b}$$

$$= \delta_{\Delta_i,0} \sum_{k,k',q}^{1.\mathrm{BZ}} e^{\mathrm{i}(k'\Delta_1 - (k+k'-q)\Delta_2 - (k+k')\tilde{\Delta})} b_k^\dagger b_{k'}^\dagger b_q b_{k+k'-q'} \,, \tag{4.2.22c}$$

which leads to $2N^2$ rules

$$\begin{aligned} 0 = \delta_{\Delta_i,0} \sum_{k,q,q'} e^{\mathrm{i}(k'\Delta_1 - (k+k'-q)\Delta_2 - (k+k')\tilde{\Delta})} h[b_k^\dagger b_{k'}^\dagger b_q b_{k+k'-q}] \\ \forall i \in \{1,2\}, j \neq i : \Delta_j, \tilde{\Delta} \in \{0, ..., N-1\} \,. \end{aligned} \tag{4.2.23}$$

For the coefficients of general operator monomials $h[b_{k_1}^\dagger \dots b_{k_m}^\dagger b_{q_1} \dots b_{q_n}]$ with m creators and n annihilators, one can perform an analogous calculation to derive the

conditions

$$0 = \delta_{c_i,0} \sum_{\substack{k_1=0,\dots \\ q_1=0,\dots \\ \sum_i q_i = \sum_i k_i}} \gamma^{c_1,\dots;a_1,\dots;\tilde{\Delta}}_{k_1,\dots;q_1,\dots} h[b^\dagger_{k_1} \dots b^\dagger_{k_m} b_{q_1} \dots b_{q_n}] \,, \tag{4.2.24a}$$

$$0 = \delta_{a_i,0} \sum_{\substack{k_1=0,\dots \\ q_1=0,\dots \\ \sum_i q_i = \sum_i k_i}} \gamma^{c_1,\dots;a_1,\dots;\tilde{\Delta}}_{k_1,\dots;q_1,\dots} h[b^\dagger_{k_1} \dots b^\dagger_{k_m} b_{q_1} \dots b_{q_n}] \,, \tag{4.2.24b}$$

$$\gamma^{c_1,\dots;a_1,\dots;\tilde{\Delta}}_{k_1,\dots;q_1,\dots} = \exp\left(\mathrm{i} \sum_{j=2}^{m} (c_j k_j) - \mathrm{i} \sum_{j=2}^{n} (a_j q_j) - \mathrm{i}\tilde{\Delta} \sum_{j=1}^{m} k_m \right) . \tag{4.2.24c}$$

These conditions can be interpreted geometrically as orthogonality $0 = \boldsymbol{\gamma} \cdot \boldsymbol{h}$ with the components $\gamma^{c_1,\dots;a_1,\dots;\tilde{\Delta}}_{k_1,\dots;q_1,\dots}$ of $\boldsymbol{\gamma}$ and the components $h[b^\dagger_{k_1} \dots b^\dagger_{k_m} b_{q_1} \dots b_{q_n}]$ of $\boldsymbol{h}$. Some of the conditions can be linear dependent, i.e. due to the Hermiticity of the TFIM Hamiltonian.

In real space, the hard-core conditions are fulfilled automatically if the commutation relations are applied consistently. In momentum space, our calculations show that the conditions must be implemented explicitly in order to obtain the same results as the real-space calculation. This can be done in two different ways. (i) One can implement this restriction explicitly when setting up the tensor D_{ijk} of the flow equations, which can unfortunately increase the number of tracked coefficients. (ii) To avoid introducing new coefficients, one can check this restriction in each integration step of the flow equations and correct the coefficients accordingly. The first approach is preferable despite the increased number of tracked coefficients, because it does not require hard-coded changes of the coefficients during the flow, which can lead to numerical instability.

Note that for testing purposes one can derive the flow equations in real space while considering the hard-core repulsion and then perform a Fourier transformation to obtain the flow equations in momentum space. In that case, the hard-core restriction is already fulfilled. For realistic applications, however, this approach can be less viable if one want to apply specialized truncation schemes in momentum space.

To conclude, the hard-core repulsion can be expressed explicitly in momentum space, but is considerably more intricate that in real space.

4.2.4 Alternative Approach using Bond-Operators

As an alternative to the hard-core operator description (4.1.9) with the rather complicated hard-core commutator (4.1.10a), one can apply a bond-operator description similar to the one proposed for triplons [112, 113]. For the flavorless hard-core

bosons in the TFIM, one can define

$$b_i^\dagger =: B_i^\dagger s_i \tag{4.2.25a}$$
$$|g\rangle = s_i^\dagger |0_i\rangle \tag{4.2.25b}$$
$$|B_i\rangle = B_i^\dagger |0_i\rangle \tag{4.2.25c}$$

with the bosonic operator $[s_i\,, s_j^\dagger] = \delta_{ij}$ and $[B_i\,, B_j^\dagger] = \delta_{ij}$ and real-space sites i. The state $|g\rangle$ contains no hard-core excitation and $|B_i\rangle$ contains a single excitation at site i. The state $|0_i\rangle$ is a mathematical reference state that lies outside the physical Hilbert space. Subsequently, one can define multi-particle states $|B_iB_j...0_a0_b...\rangle$. The advantage of the bond-operator description is that the hard-core condition is no longer encoded in the algebra, but instead in the condition

$$1 = b_i^\dagger b_i + s_i^\dagger s_i\,, \quad \forall i \in \{0, 1, ...N-1\}\,. \tag{4.2.26}$$

Since Fourier transformations do not alter bosonic commutation relations, the commutators $[s_k, s_{k'}^\dagger] = \delta_{kk'}$ and $[B_k, B_{k'}^\dagger] = \delta_{kk'}$ in momentum space are trivial. Condition (4.2.26), however, takes a more complicated form in momentum space. For instance, by summing over all N conditions (4.2.26) and Fourier transforming the operators, similar to the derivation (4.2.20), one finds the less trivial relation

$$N = \sum_k \left(b_k^\dagger b_k + s_k^\dagger s_k^\dagger \right)\,. \tag{4.2.27}$$

Consequently, the bond-operator description does not completely remove the complexity of the hard-core condition in momentum space, but only changes in which equation the complexity arises.

However, the difficulty of the momentum space CUT arises primarily due to the increased number of terms created in each commutation. These are a result of the hard-core algebra (4.1.16a) in momentum space, which contains a summation over all momenta. One could argue that the bosonic commutation relation of the bond-operators avoids this problem. Unfortunately, this is not correct. The bond-operator description increases the number of operators in all monomials. For instance, bilinear hard-core monomials are quartic bond-monomials $bb \to BBss$ and quartic hard-core monomials are octic bond-monomials $bbbb \to BBBBssss$. Bosonic commutation of a term with n_1 operators and a term with n_2 operators yields terms containing $n_1 + n_2 - 2$ operators. Since the initial bilinear hard-core monomials in (4.1.12) are quartic in the bond language ($n_i = 4$), commutation always increases the number of operators. Additionally, momentum conservation is only fulfilled for the sum of all indices. For instance, the Fourier transform of bilinear hard-core terms should create

terms with only one independent momentum. However, in bond-operator language

$$\sum_{n\Delta} b_n b_{n+\Delta} = \sum_{n\Delta} B_n s_n^\dagger B_{n+\Delta} s_{n+\Delta}^\dagger \tag{4.2.28a}$$

$$= \sum_{\Delta} \frac{1}{N} \sum_{nkk'qq'} e^{\mathrm{i}n(-k-k'+q+q')} e^{\mathrm{i}\Delta(q'-k')} B_k s_q^\dagger B_{k'} s_{q'}^\dagger \tag{4.2.28b}$$

$$= \sum_{\Delta} \sum_{kk'q} e^{\mathrm{i}\Delta(k-q)} B_k s_q^\dagger B_{k'} s_{k+k'-q}^\dagger \tag{4.2.28c}$$

terms containing three independent momentum indices are created. A Fourier transform in hard-core language only creates terms with one independent momentum, see (4.2.20). It should be noted that the coefficients of the bond-operator term differ only by the factor $e^{\mathrm{i}\Delta(k-q)}$ and therefore only depend on a single momentum difference $k-q$. Therefore, it should be possible to reduce the bond-operator description in such a way that the number of tracked terms is the same as in the hard-core description. Nevertheless, the bond-operator does not solve the problem that various new operator terms emerge in momentum space, which drastically increases the computational load of the momentum CUT.

For our purpose, the bond-operator formalism complicates the computation of the flow equations and does not offer any meaningful advantage compared to the hard-core operators (4.1.9). Therefore, this description is not pursued further in this work.

4.2.5 Scaling Argument

One advantage of the momentum-space description is the fact that scaling arguments based on the energy are more viable. The scaling dimension is used, for instance, in operator product expansions [21, 22]. In this section, we calculate the scaling dimension of one-dimensional hard-core bosonic systems to motivate a truncation based on the number of operators [148].

For simplicity, we assume that the energy gap is found at $k = 0$, which is the case for the TFIM for $x \in [0, 1]$. For gapless excitations, the lower edges of multi-particle continua overlap with the dispersion. The low-energy multi-particle states contain many particles at $k \approx 0$. Therefore, it is reasonable to assume that the low-temperature physics is dominated by processes with momenta $k \approx 0$ and that these processes are most relevant for the renormalizing CUT flow. To quantify which terms are most important for small energies, one can rescale the momenta $k \to \lambda k$ with $\lambda < 1$.

In the thermodynamic limit

$$\sum_{k}^{1.\ \mathrm{BZ}} \to \frac{L}{2\pi} \int_{-\pi/a}^{\pi/a} \mathrm{d}k\,, \quad \delta_{k,k'} \to \frac{2\pi}{L}\delta(k-k')\,, \quad b_k \to \frac{1}{\sqrt{L}} b(k)\,. \tag{4.2.29}$$

the commutation relation (4.1.16a) in momentum space becomes

$$[b(k), b^\dagger(k')] = 2\pi\delta(k-k') - \frac{a}{\pi}\int_{-\pi/a}^{\pi/a} \mathrm{d}q b^\dagger(q) b(k-k'+q)\,. \tag{4.2.30}$$

Rescaling the momenta yields

$$\begin{aligned}\Big[b(\lambda k), b^\dagger(\lambda k')\Big] = \;& 2\pi\delta(\lambda k - \lambda k') - \frac{a}{\pi}\int_{-\pi/a}^{\pi/a} \mathrm{d}q b^\dagger(q) b(\lambda k - \lambda k' + q) \\ \overset{q':=q/\lambda}{=}\; & \frac{2\pi}{\lambda}\delta(k-k') \quad - \lambda\frac{a}{\pi}\int_{-\pi/(\lambda a)}^{\pi/(\lambda a)} \mathrm{d}q' b^\dagger(\lambda q') b(\lambda k - \lambda k' + \lambda q').\end{aligned} \tag{4.2.31}$$

Since the rescaling should not change the algebra, the prefactor $1/\lambda$ in front of the delta function must vanish. With this it follows

$$\tilde{b}^\dagger(k) = \lambda^{\frac{1}{2}} b^\dagger(\lambda k) \tag{4.2.32}$$

for the one-dimensional TFIM. In D-dimensional systems, one finds the more general scaling relation $\tilde{b}^\dagger(\boldsymbol{k}) = \lambda^{\frac{D}{2}} b^\dagger(\lambda\boldsymbol{k})$ through an analogous calculation. Since each operator increases the scaling order in λ, it follows that operator monomials with a higher number of operators become less relevant for small energies.

This scaling behavior motivates a truncation scheme, where one considers only operator monomials up to a maximum number of operators, e.g. up to quartic order. Note, however, that this truncation scheme can also be applied in real space and does not exploit that momentum space operators are highly delocalized in real space.

4.3 Strategies and Results

4.3.1 Numerical Implementation

The CUT of the TFIM is implemented in quartic order, i.e. with operator monomials containing up to four operators, with the pc-generator (2.3.23). In the following, we use the symbol $C^{n_1,n_2,\cdots}_{m_1,m_2,\ldots}(\ell)$ for the coefficient of the real-space monomial $b^\dagger_{n_1} b^\dagger_{n_2} \ldots b_{m_1} b_{m_2} \ldots$ and $C^{k_1,k_2,\cdots}_{q_1,q_2,\ldots}(\ell)$ for the coefficient of the momentum-space monomial $b^\dagger_{k_1} b^\dagger_{k_2} \ldots b_{q_1} b_{q_2} \ldots$.

In real space, the Hamiltonian and generator

$$H(\ell) = \sum_{n,m=0}^{N-1} \frac{C_m^n(\ell)}{2} b_n^\dagger b_m + \sum_{n_1,n_2,m_1,m_2=0}^{N-1} C_{m_1,m_2}^{n_1,n_2}(\ell) b_{n_1}^\dagger b_{n_2}^\dagger b_{m_1} b_{m_2} + \sum_{n_1,n_2=0}^{N-1} C^{n_1,n_2}(\ell) b_{n_1}^\dagger b_{n_2}^\dagger + \sum_{n_1,n_2,n_3,m_1=0}^{N-1} C_{m_1}^{n_1,n_2,n_3}(\ell) b_{n_1}^\dagger b_{n_2}^\dagger b_{n_3}^\dagger b_{m_1} + \text{h.c.} \tag{4.3.33a}$$

$$\eta(\ell) = \sum_{n_1,n_2=0}^{N-1} C^{n_1,n_2}(\ell) b_{n_1}^\dagger b_{n_2}^\dagger + \sum_{n_1,n_2,n_3,m_1=0}^{N-1} C_{m_1}^{n_1,n_2,n_3}(\ell) b_{n_1}^\dagger b_{n_2}^\dagger b_{n_3}^\dagger b_{m_1} - \text{h.c.} \tag{4.3.33b}$$

are initialized with

$$C_m^n(0) = \delta_{n,m} - \frac{x}{2}(\delta_{n,m+1} + \delta_{n,m-1})\,, \tag{4.3.34a}$$

$$C^{n_1,n_2}(0) = -\frac{x}{4}(\delta_{n_1,n_2+1} + \delta_{n_1,n_2-1})\,, \tag{4.3.34b}$$

$$C_{m_1,m_2}^{n_1,n_2}(0) = C_{m_1}^{n_1,n_2,n_3}(0) = 0\,. \tag{4.3.34c}$$

In momentum space, the Hamiltonian and generator

$$H(\ell) = \sum_{k,q=0}^{1.\text{BZ}} \frac{C_q^k(\ell)}{2} b_k^\dagger b_q + \sum_{k_1,k_2,q_1,q_2=0}^{1.\text{BZ}} C_{q_1,q_2}^{k_1,k_2}(\ell) b_{k_1}^\dagger b_{k_2}^\dagger b_{q_1} b_{q_2} + \sum_{k_1,k_2=0}^{1.\text{BZ}} C^{k_1,k_2}(\ell) b_{k_1}^\dagger b_{k_2}^\dagger + \sum_{k_1,k_2,k_3,q_1=0}^{1.\text{BZ}} C_{q_1}^{k_1,k_2,k_3}(\ell) b_{k_1}^\dagger b_{k_2}^\dagger b_{k_3}^\dagger b_{q_1} + \text{h.c.} \tag{4.3.35a}$$

$$\eta(\ell) = \sum_{k_1,k_2=0}^{1.\text{BZ}} C^{k_1,k_2}(\ell) b_{k_1}^\dagger b_{k_2}^\dagger + \sum_{k_1,k_2,k_3,q_1=0}^{1.\text{BZ}} C_{q_1}^{k_1,k_2,k_3}(\ell) b_{k_1}^\dagger b_{k_2}^\dagger b_{k_3}^\dagger b_{q_1} - \text{h.c.} \tag{4.3.35b}$$

are initialized with

$$C_q^k(0) = (1 - x\cos(ka))\delta_{k,q}\,, \tag{4.3.36a}$$

$$C^{k_1,k_2}(0) = -\frac{x}{2}\cos(ka)\delta_{k_1,-k_2}\,, \tag{4.3.36b}$$

$$C_{q_1,q_2}^{k_1,k_2}(0) = C_{q_1}^{k_1,k_2,k_3}(0) = 0\,. \tag{4.3.36c}$$

The real-space Hamiltonian is translation invariant. Therefore, the effective number of independent coefficients is N for bilinear terms and N^3 for quartic terms. Additionally, mirror symmetry and permutations of creators (or annihilators) decrease

the number of independent terms. Numerically, only a single value is stored for all equivalent terms, see Sec. 2.5 .

In momentum space, only N bilinear terms and N^3 quartic terms of each type must be tracked due to momentum conservation. Like in real space, all symmetries are applied to reduce the number of tracked coefficients and consequently the computational effort. In (4.3.36), each bilinear term fulfilling momentum conservations starts with a finite coefficient, while only strongly localized real-space terms have finite initial values (4.3.34a). The momentum is discretized with N equidistant values $k \in \{\frac{n}{N}\frac{2\pi}{a}\}$, $n \in \{0, 1, ..., N-1\}$, which always include the dispersion minimum at $k = 0$.

The commutator (2.2.7) of the flow equations is first computed symbolically for arbitrary N and then explicitly for specific N. The detailed process of solving the commutators symbolically is explained in full detail in my master thesis [148]. The program was extended with a non-symbolic evaluation of (2.2.7) in order to facilitate a deepCUT expansion in x for hexatic terms. However, this approach did not improve the CUT results significantly, because the significant increase in runtime and memory cost did not allow tracking a significant number of hexatic terms. The results will not be discussed in the scope of this work.

The flow equations is solved numerically in C++. Matrix arithmetics are implemented using the Eigen library [136]. The flow equations are integrated using the Runge-Kutta-Dopri5 algorithm from the Boost library [149]. A controlled stepper adjusts the step size $\Delta\ell$ to reduce the absolute and relative error below 10^{-8}.

4.3.2 Results of Quartic Calculation

Fig. 4.3 depicts the gap Δ of the TFIM computed with a quartic CUT and the pc-generator. The results for the real-space CUT (RCUT) and the momentum-space CUT (KCUT) for various numbers of sites N are compared to results with exact diagonalization (for the same N) and the exact result (4.1.19) for $N \to \infty$. As one would expect, the real-space and momentum-space results are equivalent. Remember, however, that the momentum-space calculation for hard-core particles requires exceptionally more computational effort and a program implementing this approach is significantly more prone to programming errors. Not surprisingly, the difference between exact diagonalization and quartic CUT increases with N because the quartic truncation excludes n-particle interactions with $n > 2$. These truncated terms are less relevant for very small N. Furthermore, larger N lead to results closer to the exact solution in the thermodynamic limit. However, the quartic CUT does not converge for $N = 9$ at $x \geq 0.98$. For larger N, the minimal x for which the quartic CUT does not converge decreases even further. Since the full quartic

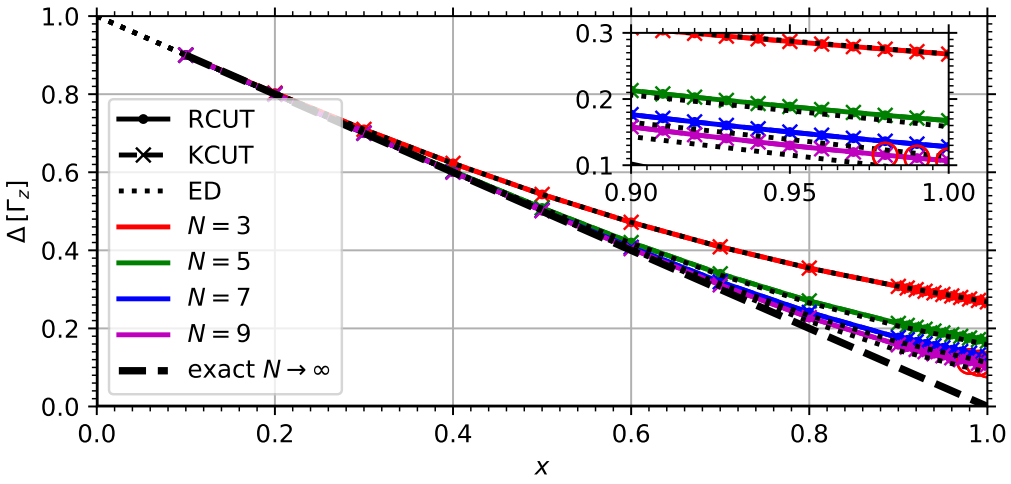

Figure 4.3: Computed gap with quartic CUT of the TFIM in real space (RCUT) and momentum space (KCUT) for various system sizes N. The results are compared to exact diagonalization results with the respective N and with the analytical result (4.1.19) in the thermodynamic limit. The inset to the top right depicts the results close to $x = 1$. If the quartic CUT does not converge, the gap at the minimal ROD is plotted and highlighted with a red circle. Here, this occurs for $N = 9$ and $x \in \{0.98, 0.99, 1\}$.

calculation in momentum space requires a long runtime, however, this work focuses only on calculations up to $N = 9$.

In principle, incorporating hexatic terms, i.e. monomials containing six operators, could lead to more stable convergence for $x \approx 1$. However, this greatly increases the computational cost. First calculations using a deepCUT-expansion in real-space did not provide better convergence. Full hexatic calculations, especially in momentum space, did not prove computationally feasible.

To conclude, the momentum-space CUT is capable of reproducing the results of the real-space CUT, but requires considerably more effort and is more error-prone. Both approaches do not converge for $N \geq 9$ and $x \approx 1$. This problem could be approached with more sophisticated momentum-space approaches, which we explore in the following sections.

4.3.3 Truncation Based on Momentum Extension

To describe highly delocalized excitations in real space, it is reasonable to use localized operators in momentum space. This motivates a truncation scheme based on the extension of operator monomials in momentum space, akin to truncation based on real space extension, see Sec. 2.4.2. By truncating all terms that do not fulfill $d < d_{\max}$ with an appropriate extension definition d, only terms with small momenta are considered. Normally, monomials containing a larger number of op-

erators have larger d and are, therefore, truncated more strictly. On the one hand, this is convenient since such terms are less important due to the scaling argument presented in Sec. 4.2.5 . On the other hand, a more controlled truncation can be achieved by using different maximal extensions for monomials with the respective number of operators, similar to the spatial truncation scheme explored in Sec. 2.4.2 . In the following, three definitions of d are considered to explore truncation schemes in momentum space.

The most straightforward definition of the extension is a direct application of the spatial extension defined in Sec. 2.4.2

$$d_{\text{direct}}[b^\dagger_{k_1}...b_{k_n}] = \max_{ij} |k_i - k_j| \tag{4.3.37}$$

with a truncation criterion $d_{\text{direct}} < d_{\max}$. The definition d_{direct} is difficult to justify physically, since translational invariance is valid in real space, but not in momentum space. Note that the periodicity of the Brillouin zone is considered when calculating $|k_i - k_j|$, so a more rigorous definition is given by substituting

$$|k_i - k_j| \to \min_{n\in\mathbb{Z}} \left| k_i - k_j + \frac{n}{N}\frac{2\pi}{a} \right| . \tag{4.3.38}$$

An alternative extension definition is based on the extension of momenta relative to a reference momentum. The reference momentum is chosen to be the momentum at which the one-particle dispersion is minimal, i.e. $k = 0$ for the TFIM at $x \in [0, 1]$. The reasoning is that low-energy processes are dominated by particles at low energies and, therefore, processes acting on these particles should dominate. To this end, the **reference-point momentum extension**

$$d_{\text{ref-point},k_{\text{ref}}}[b^\dagger_{k_1}...b_{k_n}] = \sum_{i=1}^{n} |k_i - k_{\text{ref}}|/2 \tag{4.3.39}$$

is defined with the summation over all indices k_i in a given operator monomial. The factor $1/2$ is introduced because $\sum_{i=1}^{n} |k_i - k_{\text{ref}}|$ is always even due to total momentum conservation.

The third definition is based on the extension of the momenta appearing in an operator monomial relative to one another. The idea is that particles with a large momentum difference, e.g. one particle with small momentum and another particle with large momentum, have a large energy difference according to the dispersion. Therefore, processes connecting such particles span large energy differences and are least relevant in a renormalizing scheme. Incorporating this idea in a truncation scheme is not straightforward. For particle-conserving processes, it might seem effective to sum over the difference between the momenta of the creation and annihilation operators by choosing pairs containing one creation and one annihilation operator, i.e.

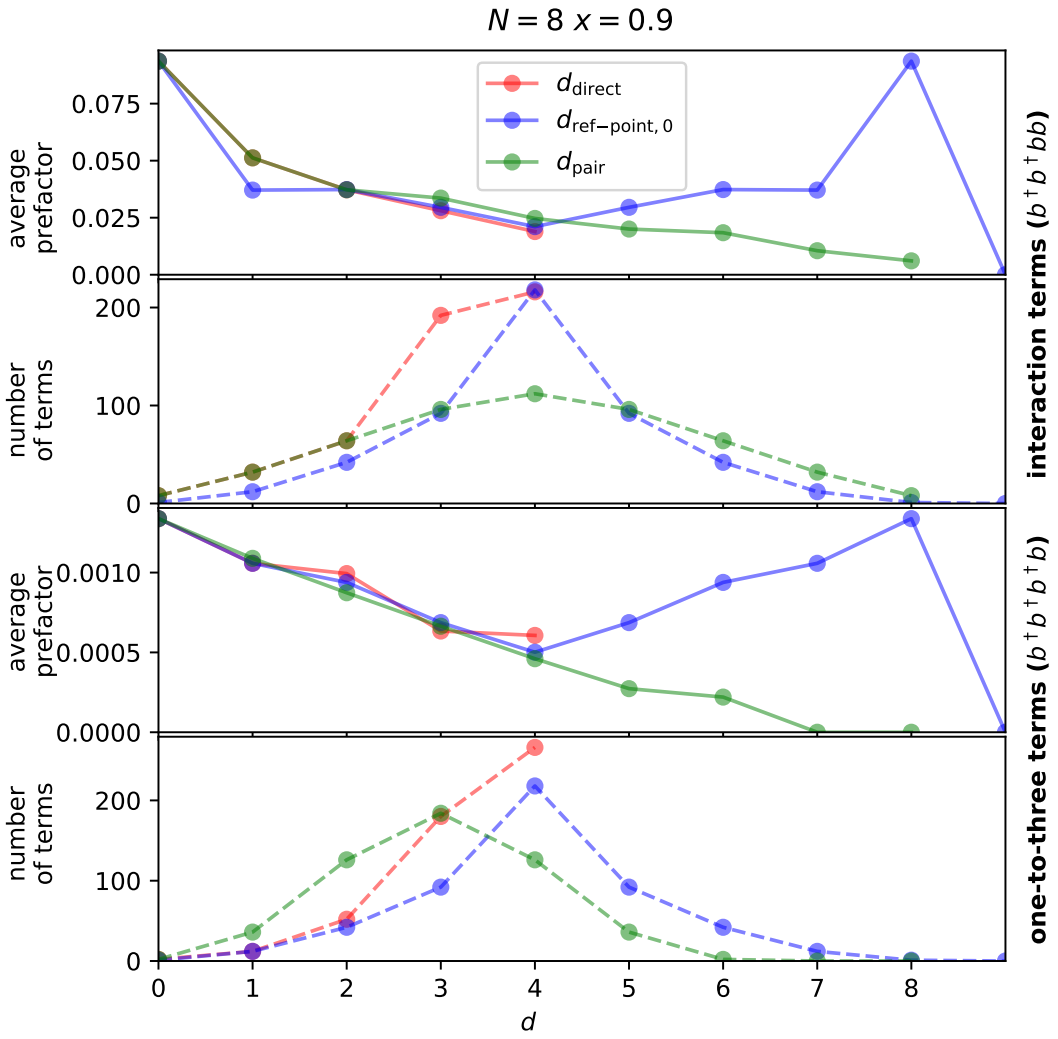

Figure 4.4: Average coefficients and total number of quartic operator monomials of given extension during the full quartic momentum-space flow of the TFIM-Hamiltonian (4.3.35a) for $N = 8$ and $x = 0.9$ at $\ell \approx 4.5/\Gamma_z$, i.e. in the early phase of the flow. For all three definition of the extension d in Sec. 4.3.3, small extension $d \approx 0$ correspond to a small number of monomials with the largest coefficients. However, for $d_{\text{ref-point},0}$ half of the largest coefficients are found at the maximal extension $d \approx N$.

$d_{\text{pair}}[b^\dagger_{k_1}...b^\dagger_{k_n} b_{q_1} b_{q_n}] = \sum_{i=1}^{n} |k_i - q_i|$. These pairs can be chosen, for instance, such that for each monomial the sum of momentum differences is minimized. However, it is not possible to find distinct pairs unambiguously for non-particle-conserving processes such as $b^\dagger_{k_1} b^\dagger_{k_2}$ or $b^\dagger_{k_1} b^\dagger_{k_2} b^\dagger_{k_3} b_{q_1}$. A more general definition is provided by a summation over all possible differences of momenta between all operators, the **pair-wise momentum extension**

$$d_{\text{pair}}[b^\dagger_{k_1}...b^\dagger_{k_n} b_{q_1} b_{q_m}] = \sum_{i=1}^{n} \sum_{j=1}^{n} |k_i - q_j| \,. \tag{4.3.40}$$

Note that this definition has the disadvantage that it cannot be applied to monomials

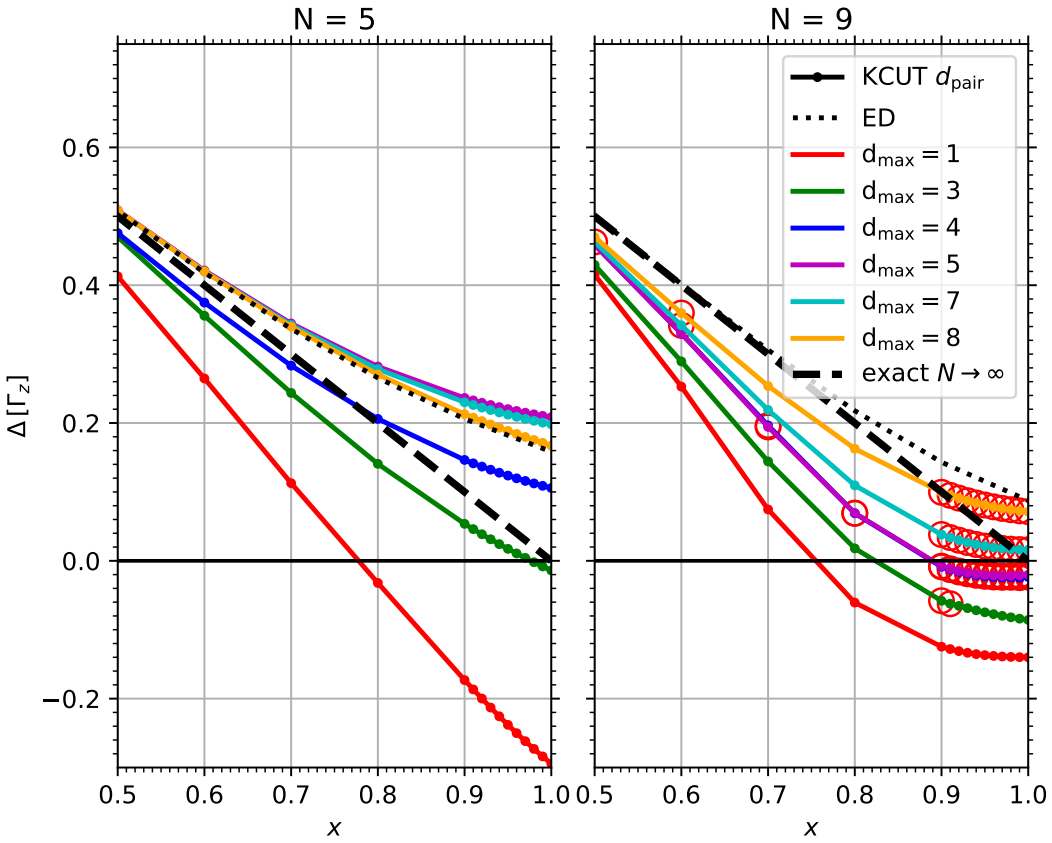

Figure 4.5: Computed gap with quartic CUT in momentum space and truncation based on the extension d_{pair}, see Sec. 4.3.3. If the quartic CUT does not converge, the gap at the minimal ROD is plotted and marked with a red circle. No convergence is achieved for $N = 9$ and $x \geq 0.9$ for $d_{\text{max}} \geq 4$.

containing only one type of operator. For the TFIM, this does not pose a problems, since the only terms of this form are bilinear and already present in the initial Hamiltonian $H(\ell = 0)$. Therefore, none of these terms should be truncated.

For the above extension definitions to be reasonable, terms of high extension should (i) have relatively small coefficients in a non-truncated calculation so that truncating them does not introduce large errors and (ii) be numerous enough that truncating them improves the computational performance significantly. Both of these conditions are verified in Fig. 4.4. Surprisingly, the naive definition d_{direct} fulfills both conditions. The second definition $d_{\text{ref-point},0}$ has the problem that some of the largest coefficients are also found at $d_{\text{ref-point},0} = N$, i.e. when all four momenta are π/a. The third definition d_{pair} fulfills both conditions. Since d_{pair} can be as large as N, while d_{direct} cannot be larger than $N/2$, the third definition d_{pair} allows for more precise adjustments of how many terms to truncate. Therefore, d_{pair} is the best candidate for a truncation scheme in momentum space.

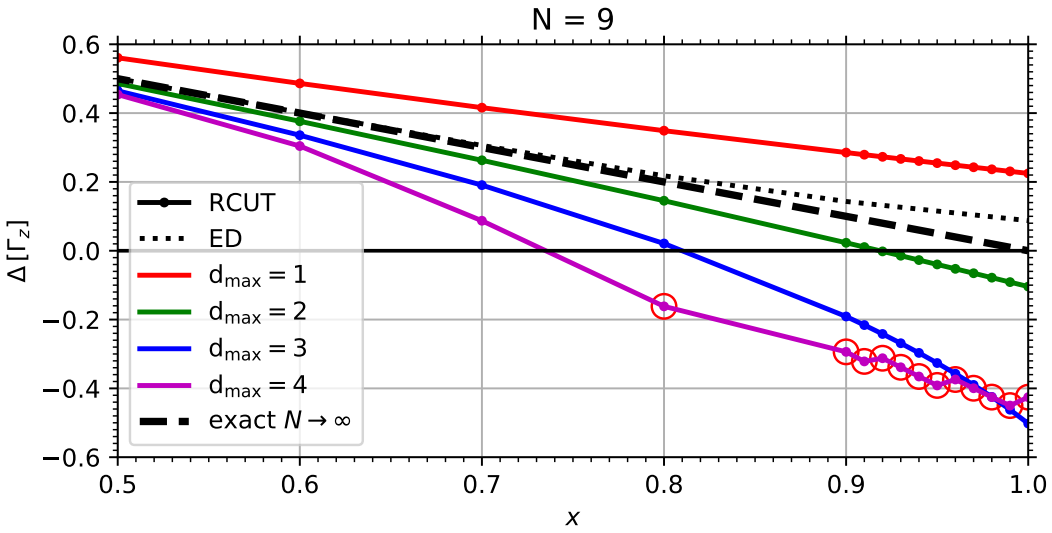

Figure 4.6: Computed gap with quartic CUT in real space and truncation based on the spatial extension $d = \max_{ij} |r_i - r_j|$, see Sec. 2.4. If the quartic CUT does not converge, the gap at the minimal ROD is plotted and marked with a red circle. No convergence is achieved for $N = 9$ and $x \geq 0.9$ for $d_{\max} \geq 4$.

The truncation scheme using d_{pair} is applied to the TFIM-Hamiltonian (4.3.35a) by considering bilinear terms of all extensions and quartic terms of extension up to $d_{\max}$. Fig. 4.5 shows the computed gap for $N \in \{5, 9\}$ and $d_{\max} \in \{1, 2, ..., 8\}$. Obviously, the computed gaps converge to the results obtained with a full quartic CUT in the limit $d_{\max} \to \infty$. For small $d_{\max}$, the gap is often closer to the correct result than the full quartic gap, see Fig. 4.3. However, this must be understood as a coincidence rather than a systematic improvement. Unfortunately, the truncated CUT does not converge for all $x \in [0, 1]$ at $N = 9$ (and larger N, despite not being shown explicitly), unless $d_{\max} = 1$ is chosen, which neglects all but the most trivial quartic terms. This problem was also observed without truncation in Sec. 4.3.2. Ideally, a good truncation scheme would improve the convergence behavior, but this is not the case here. While the truncation scheme does reduce the number of tracked terms, the description in momentum space is still computationally more expensive than a comparable calculation in real space. Additionally, Fig. 4.6 depicts the computed gap with a truncated CUT in real space, which appears to converge more reliably than the truncated momentum space CUT for small $d_{\max}$.

To conclude, the presented truncation schemes in momentum space can be motivated physically and the truncated terms are numerous and have small coefficients, which makes the approach computationally reasonable. However, the computed flows using these truncation schemes do not converge more reliably than a truncation based on spatial extension. Considering the increased computational burden of a calculation in momentum space for hard-core systems, truncation in momentum space does not offer significant advantages.

4.3.4 Asymptotic Convergence

The momentum-space description offers another potential advantage beyond truncation schemes based on momenta. Due to the renormalizing property of the pc-generator, off-diagonal matrix elements most generally converge asymptotically with $\exp(c_{\text{asym}}\ell)$ in the vicinity of the fixed point, see Sec. 2.3.1. The coefficient $c_{\text{asym}} < 0$ depends on the energy difference of the states that are connected by the off-diagonal element. This relation is straightforward for explicit matrix representations, but can be more involved in second quantization. Bilinear Hamiltonians $H(\ell)$ can be expressed by a matrix $\mathbf{M}(\ell)$

$$H(\ell) = \boldsymbol{b}^\dagger \mathbf{M}(\ell) \boldsymbol{b}\,, \quad \boldsymbol{b} := \left(b_0, b_1, ..., b_0^\dagger, b_1^\dagger, ...\right)^{\mathrm{T}} \tag{4.3.41}$$

in second quantization, i.e. the matrix elements are the coefficients $C^{k_1\cdots}_{q_1\cdots}(\ell)$ of the monomials. For such bilinear Hamiltonians, one finds asymptotic convergence of the non-particle-conserving terms $C^{k,-k}(\ell) \propto \exp(-2C_k^k\ell)$. Indeed, the flow equations of the TFIM-Hamiltonian (4.3.35a) calculated with a bosonic algebra $[b_q, b_k^\dagger] = \delta_{kq}$ are $\partial_\ell C_k^k = -8C^{k,-k}C^{k,-k}$ and $\partial_\ell C^{k,-k} = -2C^{k,-k}C_k^k$ [148]. Therefore, the Hamiltonian remains bilinear in the bosonic case and the non-particle-conserving terms converge with $C^{k,-k}(\ell) \propto \exp(-2\int_0^{\ell'} C_k^k(\ell')\mathrm{d}\ell')$.

The Hamiltonian does not remain bilinear during the flow obtained with the hard-core algebra (4.1.16a). Therefore, the convergence behavior close to the fixed point is more complicated, but it is conceivable that the convergence behavior can be described well by the dispersion coefficients $C_k^k(\ell')$. For instance, a naive assumption for one-to-three-terms $b_{k_1}^\dagger b_{k_2}^\dagger b_{k_3}^\dagger b_{q_1}$ is an asymptotic convergence with coefficient $c_{\text{asym}} = -|C_{k_1}^{k_1} + C_{k_2}^{k_2} + C_{k_3}^{k_3} - C_{q_1}^{q_1}|$. If such a systematic asymptotic convergence behavior could be found, it could be exploited (i) to drastically reduce the number of tracked coefficients by expressing various quartic coefficients in terms of a small number of quartic coefficients and bilinear energies or (ii) to find an analytic solution. Note that such an approach is only viable close to the fixed point, e.g. to describe the macroscopic physics of an effective low-energy model after the microscopic details of high-momentum terms has been treated with a different method, such as the Schrieffer-Wolff transformation [150]. To work towards such an application of flow equations, we study the asymptotic convergence of the quartic one-to-three terms in this section.

Fig. 4.7 depicts an analysis of the asymptotic convergence of quartic one-to-three processes in momentum space for $N \in \{7, 9\}$ and $x = 0.9$. The value $x = 0.9$ is chosen because it is close to $x = 1$, but still small enough that the CUT converges. As the top row of Fig. 4.7 shows, asymptotic convergence $C_{q_1}^{k_1,k_2,k_3}(\ell) \propto \exp(c_{\text{asym}}\ell)$ can be observed during large sections of the flow both for the bilinear and quartic non-particle-conserving terms. Deviations from this convergence occur mostly during

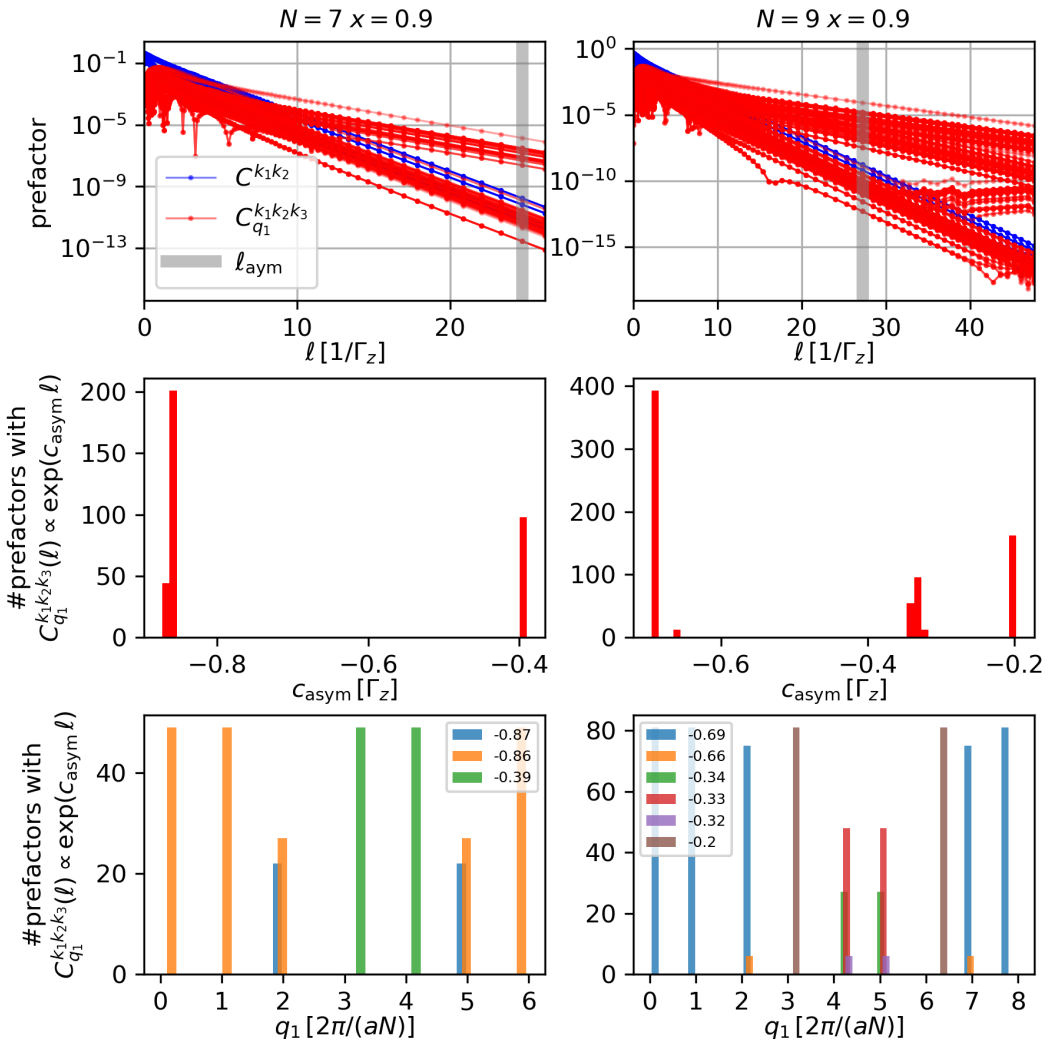

Figure 4.7: Analysis of the convergence behavior of quartic three-to-one coefficients $C^{k_1,k_2,k_3}_{q_1}$ for $N \in \{7, 9\}$ and $x = 0.9$. The top row shows the flow of the coefficients of the bilinear (C^{k_1,k_2}) and quartic ($C^{k_1,k_2,k_3}_{q_1}$) non-particle-conserving operator monomials. The grey areas mark the value of ℓ at which the asymptotic convergence exponent c_{asym} is evaluated, i.e. where the coefficients converges with $C^{k_1,k_2,k_3}_{q_1}(\ell) \propto \exp(c_{\text{asym}}\ell)$. The middle row shows histograms of the number of coefficients found for each value of c_{asym}, using 50 bins over the range of all found values for c_{asym}. For each bin, the monomials are sorted by the value of the annihilator momentum q_1 and displayed in the histograms in the bottom row.

the initial flow, where significant reordering happens and the signs of the coefficients often change, and during the late stage of the flow, where numerical errors can cause significant deviations. Notably, many quartic coefficients $C^{k_1,k_2,k_3}_{q_1}(\ell)$ appear to converge with the same speed, i.e. have the same convergence exponent c_{asym}. Furthermore, all bilinear coefficients $C^{k_1,k_2}(\ell)$ converge with the same exponent as the fastest converging quartic terms.

To quantify this finding, a flow paramater ℓ_{asym} is chosen at which all terms decrease exponentially and c_{asym} is then determined for each individual $C_{q_1}^{k_1,k_2,k_3}(\ell)$ by interpolating the flow at this ℓ_{asym}. All these coefficients are counted and plotted in histograms in the middle row of Fig. 4.7, which show that only two (for $N = 7$) or three (for $N = 9$) relevant values of c_{asym} are found aside from small deviations. Therefore, all $C_{q_1}^{k_1,k_2,k_3}(\ell)$ converge, in good approximation, with one of these c_{asym}. However, the fact that common coefficients exist by itself does not clarify how one finds the correct value c_{asym} for a given monomial.

To gain a better understanding, the histograms in the bottom row of Fig. 4.7 count the number of one-to-three terms $b_{k_1}^\dagger b_{k_2}^\dagger b_{k_3}^\dagger b_{q_1}$ with respect to the annihilator momentum q_1. Different colors are used depending on the convergence exponent c_{asym} of the respective coefficients. Note that due to the discrete spatial translation invariance, all momenta $q_1 = \frac{2\pi}{a}n$ with $n \in \mathbb{Z}$ correspond to $q_1 = 0$. Furthermore, mirror symmetry implies that $q_1 = \frac{2\pi}{aN}n$ and $q_1 = \frac{2\pi}{aN}(N-n)$ correspond to one another. Keeping this in mind, one finds in the bottom row of Fig. 4.7 that fastest convergence is achieved when q_1 is close to 0, i.e. the momentum with minimal energy. Let us assume that only two (for $N = 7$) and three (for $N = 9$) correct values of c_{asym} exist and that the small deviations are negligible. In this case, all coefficients with the same q_1 share the same convergence exponent c_{asym}. Specifically, the most rapid convergence is found for the smallest momenta $|q_1 \frac{aN}{2\pi}| \leq 2$. For each additional momentum $|q_1 \frac{aN}{2\pi}| \in \{3, ..., \lfloor \frac{N}{2} \rfloor\}$, an additional convergence exponent exists, which explains why $N = 9$ has one more exponent than $N = 7$. However, additional data for $N > 9$ is required to test if this trend continues for larger N.

No trivial way to calculate the concrete value of c_{asym} from k_1, k_2, k_3 and q_1 has been found. For instance, when the histograms in the bottom row of Fig. 4.7 are computed with respect to $|C_{k_1}^{k_1} + C_{k_2}^{k_2} + C_{k_3}^{k_3} - C_{q_1}^{q_1}|$ or $|C_{k_1}^{k_1} + C_{k_2}^{k_2} + C_{k_3}^{k_3} + C_{q_1}^{q_1}|$ instead of q_1, no correlation between these energy terms and c_{asym} can be found. Nevertheless, the fact that many coefficients share the same convergence behavior and that the convergence speed is connected to the trivial momentum q_1 is quite promising.

The analysis shows that up to quartic level, various monomial coefficients share a common convergence behavior close to the fixed point. This could be exploited to reformulate them as $C_{q_1}^{k_1,k_2,k_3}(\ell) = C_{q_1}^{k_1,k_2,k_3}(0)\exp(c_{\text{asym}}\ell)$ and subsequently perform analytic or numerical simplifications.

4.4 Conclusion

Traditional truncation schemes based on spatial extension fail in the vicinity of quantum critical points, i.e. when the energy gap closes and the elementary excitations delocalize. A description in momentum space offers the advantages that (i) delocalized excitations can be described more naturally and (ii) the asymptotic convergence of quartic terms can be related more easily to bilinear energy terms. However, the algebra of hard-core particles is much more involved in momentum space and vastly increases the computational cost of flow equations.

We studied the TFIM, which hosts flavorless hard-core bosonic excitations, in order to investigate a momentum-space approach. Our computations show that a direct implementation of a CUT in momentum space up to quartic order in the number of operators requires significantly more computational effort, but is possible and yields the same result as a similar calculation in real space.

We proposed three definitions of an extension d for operator monomials in momentum space in order to find new truncation schemes. While the analysis shows that two of the definitions could provide effective truncation schemes, our CUT calculations show that they do not offer significant improvements over spatial truncations for the TFIM. Such truncation schemes could, however, prove useful in the future for other models or in combination with other optimizations.

For Hamiltonians without second quantization and bilinear Hamiltonians in second quantization, the off-diagonal or non-particle-conserving terms have an exponential asymptotic convergence behavior. We investigated the flow of the bilinear and quartic non-particle-conserving terms and found that their asymptotic convergence can be described by a small number of exponents. For the small systems that we investigated, the convergence speed is directly connected to one of the momenta, which allows for a trivial mapping of operator monomials to a common convergence class. Future works could apply this knowledge to express various coefficients $C_{q_1}^{k_1,k_2,k_3}(\ell)$ by terms $C_{q_1}^{k_1,k_2,k_3}(\ell) = C_{q_1}^{k_1,k_2,k_3}(0)\exp(c_{\mathrm{asym}}\ell)$, which only differ by a constant factor $C_{q_1}^{k_1,k_2,k_3}(0)$. This could allow for elegant analytic solutions or significant numerical simplifications. However, we stress that this shared convergence behavior only arises if the system is close enough to the fixed point, that means close to the particle-conserving Hamiltonian $H(\ell \to \infty)$. Future works could attempt to treat the microscopic high-momentum details of a physical system using different methods, such as the Schrieffer-Wolff transformation [150], to find an effective low-energy system. This effective system could then be treated efficiently in momentum space by exploiting the common convergence behavior.

Chapter 5

Dissipative Flow Equations

In the previous chapter, we discussed a generalization of distance-based truncation schemes to momentum space for hard-core systems. In this chapter, we investigate a generalization of flow equations to dissipative flow equations, which are no longer restricted to Hermitian matrices and non-Hermitian matrices with real eigenvalues, but can also treat non-Hermitian matrices with complex eigenvalues.

Specifically, we aim to generalize the particle-conserving generator (pc-generator) scheme from Sec. 2.3.1 to non-Hermitian matrices, in general, and Lindblad master equations as an important application field. Lindblad master equations provide the most general description of Markovian dynamics of open quantum system. The term 'Markovian' specifies that the past of the physical state does not affect the dynamics. We prove important properties of our proposed generator and compare it with generator schemes proposed previously [86]. We show that our generator, which inherits the renormalizing properties of the pc-generator, offers an excellent tradeoff between convergence speed and accuracy in spite of truncation. Parts of this chapter are published in Ref. [151].

In Sec. 5.1 , we discuss the Lindblad master equations for open quantum systems as an important example in quantum physics where one faces non-Hermitian matrices. In Sec. 5.2 we generalize the formalism of flow equations, see Sec. 2.1 , to non-unitary flow equations. We show the limitations of the pc-generators for the dissipative case in Sec. 5.3 and introduce a more suitable generalization of the pc-generator in Sec. 5.4 . Additionally, we present three previously suggested generators for non-unitary flow equations in Sec. 5.5 . We compare all four generators with one another analytically in Sec. 5.6 and numerically in Sec. 5.7 and conclude our findings in Sec. 5.8 .

5.1 Lindblad Master Equations

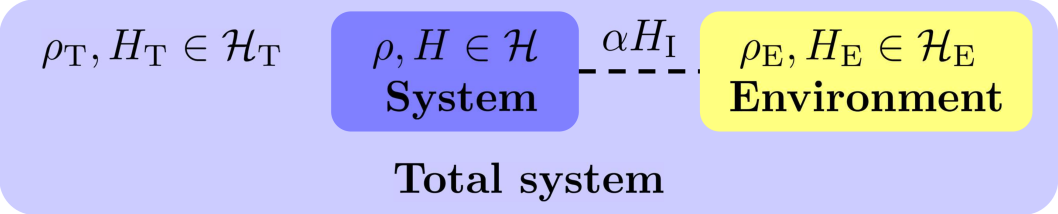

Figure 5.1: Schematic picture of an open quantum system consisting of a system (blue) coupled to an external environment (yellow). The density matrix ρ, Hamiltonian H and Hilbert space $\mathcal{H}$ are denoted by the subscript E for the environment and T for the total system. System and environment are coupled by αH_I.

An important application case of non-Hermitian matrices in quantum physics are **Lindblad master equations** [152]. They describe the time evolution of a unitary system interacting with an external environment, which leads to dissipation in the system. This division is depicted schematically in Fig. 5.1. In App. F, we discuss a full derivation of the simplified

Lindblad Master Equations

$$\mathrm{i}\frac{\mathrm{d}}{\mathrm{d}t}\rho(t) = [H, \rho(t)] + \mathrm{i}\hbar \sum_\alpha \gamma_\alpha \left(L_\alpha \rho(t) L_\alpha^\dagger - \frac{1}{2}\left\{ L_\alpha^\dagger L_\alpha, \rho(t) \right\} \right). \tag{5.1.1}$$

The operators L_α are often called Lindblad operators [60] or (quantum) jump operators [86,152] and the corresponding gain and loss rates are denoted by γ_α. The first summand describes the unitary von-Neumann dynamics of the density operator $\rho(t)$ and the Hamiltonian H of the small system. The Lindbladian describes Markovian dynamics of the system, i.e. the time evolution of the system does not depend on past events. More details can be found in the derivation.

The equation of motion can be formulated as a single superoperator, the Lindbladian $\mathcal{L}$ with

$$\mathrm{i}\hbar\frac{\mathrm{d}}{\mathrm{d}t}|\rho(t)\rangle = \mathcal{L}|\rho(t)\rangle\,, \tag{5.1.2}$$

which acts on the density matrices $|\rho(t)\rangle$ in Fock-Liouville space, which are treated like vectors [152]. The time evolution of the eigenstates $\mathcal{L}|\rho_\lambda(t)\rangle = \lambda|\rho_\lambda(t)\rangle$ is

$$|\rho_\lambda(t)\rangle = \exp\left(-\mathrm{i}\frac{\lambda t}{\hbar}\right)|\rho_\lambda(0)\rangle\,. \tag{5.1.3}$$

The real part of the eigenvalue is determined by the Hamiltonian in $[H, \rho(t)]$ and describes oscillations, i.e. $\exp(-\mathrm{i}\,\mathrm{Re}(\lambda)t/\hbar)$. The imaginary part originates from the second, dissipative summand and describes dissipations, i.e. decaying states

$\exp(-|\mathrm{Im}(\lambda)|t/\hbar)$. Note that $\mathrm{Im}(\lambda) \leq 0$, i.e. one does not observe unphysical exponentially increasing time evolutions. The eigenvectors to the eigenvalue $\lambda = 0$ corresponds to a steady state $\rho_0(t) = \rho_0$, which can be degenerate, and eigenvectors to eigenvalues with $\mathrm{Im}(\lambda) = 0$ but finite $\mathrm{Re}(\lambda)$ are quasi-stationary. These states do not vanish in the temporal evolution. Also note that all eigenvalues with $\mathrm{Re}(\lambda) \neq 0$ appear in pairs $(\lambda, -\lambda^*)$ because of the symmetry $\mathcal{L} = -\mathcal{L}^\dagger$ of the map. In literature, the prefactor $-\mathrm{i}/\hbar$ is sometimes defined to be part of the Lindbladian, so the time evolution is then $\mathcal{L}[\rho(t)] = \frac{\mathrm{d}}{\mathrm{d}t}\rho(t)$ and non-real eigenvalues appear in pairs (λ, λ^*), instead.

5.2 Non-Unitary Flow Equations

The flow equation mechanism from Sec. 2.1 can be generalized to non-Hermitian matrices M by introducing a non-unitary transformation

$$M(\ell) = S(\ell)M(0)S(\ell)^{-1}\,, \tag{5.2.4a}$$

$$S(\ell) := \mathcal{T}_\ell \exp\left(\int_0^\ell \eta(\ell')\mathrm{d}\ell'\right) \tag{5.2.4b}$$

with the transformation matrix $S(\ell)$, which needs not necessarily be unitary so that the generator $\eta(\ell)$ needs not necessarily be Antihermitian. Aside from this, the mechanism works the same as for Hermitian matrices: One arrives at an effective matrix M_{eff} at $\ell \to \infty$, or in good approximation for large enough ℓ, and can formulate the transformation with infinitesimal flow equations

$$\frac{\mathrm{d}}{\mathrm{d}\ell}M(\ell) = \big[\,\eta[M(\ell)], M(\ell)\,\big]\,. \tag{5.2.5}$$

Choosing a suitable generator $\eta[M(\ell)]$ is more involved than for the Hermitian case and the generator schemes from Sec. 2.3 must be adapted accordingly.

5.3 Limitations of the PC-Generator for Non-Hermitian Matrices

We begin by showing that the pc-generator introduced in Sec. 2.3.1 is not guaranteed to converge for non-Hermitian matrices M. We work with (2.3.11) here, which is the original definition by Mielke, but recall that the pc-generator scheme can be used in a more universal fashion, see Sec. 2.3.1.2 .

The proof of convergence for the pc-generator presented in Sec. 2.3.1.1 does not hold for non-Hermitian matrices M. One reason is the fact that the variational principle does not apply for M, another is the more intricate flow

$$\partial_\ell \left(\sum_{n=1}^{r} m_{nn}\right) = \sum_{n=1}^{r}\sum_{k>r} (-2m_{nk}m_{kn})\,. \tag{5.3.6}$$

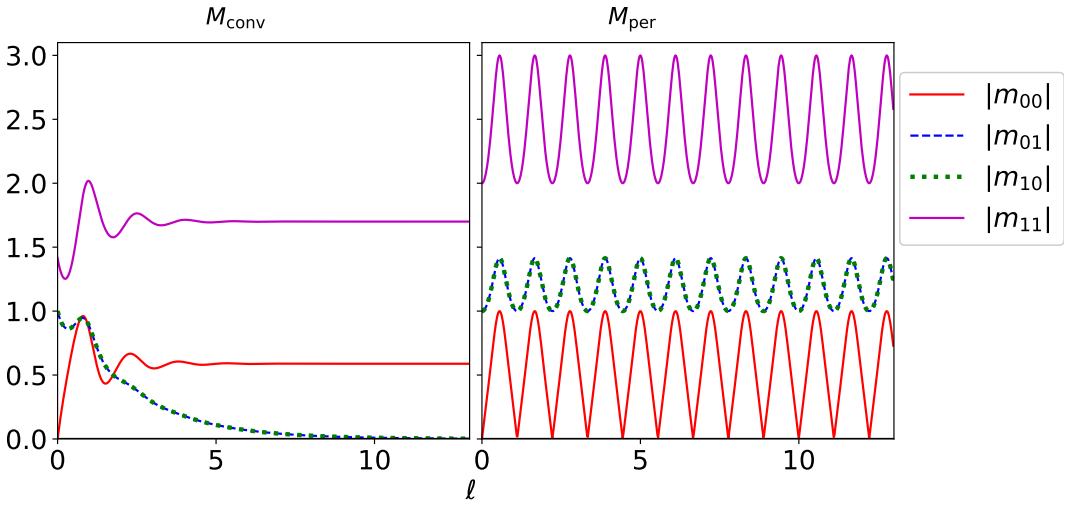

Figure 5.2: Exemplary flows induced by the pc-generator for the two non-Hermitian matrices (5.3.11). The left panels depicts a convergent flow, the right panel a periodic flow where the off-diagonal elements do not converge to 0.

For a Hermitian matrix $h_{nk}h_{kn} = |h_{nk}|^2 > 0$ is known, but this relation is not fulfilled for $m_{nk}m_{kn} \in \mathbb{C}$. One can get a better understanding of the flow equations by decomposing $M = H + A$ into a Hermitian component $H = H^\dagger$ with a real spectrum and an Antihermitian component $A = -A^\dagger$ with an imaginary spectrum

$$H := \frac{M + M^\dagger}{2}, \quad h_{nj} := (H)_{nj}\,, \tag{5.3.7a}$$

$$A := \frac{M - M^\dagger}{2}, \quad a_{nj} := (A)_{nj}\,. \tag{5.3.7b}$$

The flow equations decompose to the matrix form

$$\partial_\ell H = \big[\eta[H],\, H\big] + \big[\eta[A],\, A\big]\,, \tag{5.3.8a}$$

$$\partial_\ell A = \big[\eta[H],\, A\big] + \big[\eta[A],\, H\big]\,. \tag{5.3.8b}$$

and the element-wise form

$$\begin{aligned}\partial_\ell h_{nj} = {}& \operatorname{sign}(n-j)\,[h_{nj}(h_{jj} - h_{nn}) + a_{nj}(a_{jj} - a_{nn})] \\ & + \sum_{k\neq n,j} \left[\operatorname{sign}(n-k)\,(h_{nk}h_{kj} + a_{nk}a_{kj}) + \operatorname{sign}(j-k)\,(h_{nk}h_{kj} + a_{nk}a_{kj})\right]\end{aligned} \tag{5.3.9a}$$

$$\Rightarrow \partial_\ell h_{nn} = \sum_k 2\operatorname{sign}(n-k)\left(|h_{nk}|^2 - |a_{nk}|^2\right) \in \mathbb{R} \tag{5.3.9b}$$

and

$$\partial_\ell a_{nj} = \operatorname{sign}(n-j)\left[h_{nj}(a_{jj}-a_{nn}) + a_{nj}(h_{jj}-h_{nn})\right] + \sum_{k\neq n,j}\left[\operatorname{sign}(n-k)\left(h_{nk}a_{kj}+a_{nk}h_{kj}\right) + \operatorname{sign}(j-k)\left(a_{nk}h_{kj}+h_{nk}a_{kj}\right)\right] \tag{5.3.10a}$$

$$\Rightarrow \partial_\ell a_{nn} = \sum_k 2\operatorname{sign}(n-k)\left(a_{nk}h^*_{nk} + a_{kn}h^*_{kn}\right) \in \mathrm{i}\mathbb{R}\,. \tag{5.3.10b}$$

If the Hermitian components are dominant, i.e. if $|a_{nk}| \ll |h_{ml}|\,\forall n,k,m,l$, then the flow equations are approximately equivalent to the ones in the Hermitian case, e.g. $\partial_\ell h_{nn} \approx \sum_k 2\operatorname{sign}(n-k)|h_{nk}|^2$, and convergence is still likely. Non-Hermitian matrices M with real eigenvalues also lead to convergence, as will be explained briefly in Sec. 5.4. This has been observed, for instance, when applying the Dyson-Maleev representations of spin observables [30, 31] and when studying spin lattices subject to a non-Hermitian staggered magnetic field [69]. However, convergence is not guaranteed for non-Hermitian matrices and it is simple to find examples for which the flow does not converge. In Fig. 5.2 we show the pc-flows for the two non-Hermitian initial matrices

$$M_{\mathrm{conv}}(0) = \begin{pmatrix} 0 & 1 \\ -1 & 1+\mathrm{i} \end{pmatrix} \tag{5.3.11a}$$

$$M_{\mathrm{per}}(0) = \begin{pmatrix} 0 & 1 \\ -1 & 2\mathrm{i} \end{pmatrix}. \tag{5.3.11b}$$

The left panel shows the flow of the non-Hermitian matrix $M_{\mathrm{conv}}(\ell)$, which converges nicely. The right panel depicts the flow of $M_{\mathrm{per}}(\ell)$, which does not converge, but oscillates periodically.

5.3.1 Special Case: Antihermitian Matrix

To understand how a generalization of the pc-generator can be constructed, let us first consider the trivial case of an Antihermitian matrix A. This matrix can be expressed by a Hermitian matrix H, using

$$A = -A^\dagger\,, \tag{5.3.12a}$$

$$H := \mathrm{i}A = H^\dagger\,. \tag{5.3.12b}$$

Since we know that the pc-generator induces a convergent flow for Hermitian matrices H, it is straightforward to define an extension, the **imaginary particle-conserving (ipc-) generator**

$$\eta^{\mathrm{ipc}}_{nj}[A] = \mathrm{i}\eta^{\mathrm{pc}}_{nj}[H] = \operatorname{sign}(n-j)\mathrm{i}a_{nj}\,, \tag{5.3.13}$$

which induces an imaginary flow $\partial a_{nn} \in \mathrm{i}\mathbb{R}$ that is convergent for Antihermitian matrices instead of Hermitian matrices, but otherwise behaves analogous to the pc-generator. For Hermitian matrices, however, the ipc-generator often either converges very slowly or does not converge at all.

By considering the ipc-generator, one can find a pattern that helps to generalize the pc-generator to general non-Hermitian matrices:

- Hermitian matrices H with real eigenvalues $h_{nn} \in \mathbb{R}$ and real eigenvalues difference $(h_{nn} - h_{jj}) \in \mathbb{R}$ can be solved with the pc-generator $\eta^{\mathrm{pc}}_{nj}[H]$.
- Antihermitian matrices A with imaginary eigenvalues $a_{nn} \in \mathrm{i}\mathbb{R}$ and imaginary eigenvalue differences $(a_{nn} - a_{jj}) \in \mathrm{i}\mathbb{R}$ can be solved with the pc-generator, modified by a phase factor i, i.e. $\mathrm{i}\eta^{\mathrm{pc}}_{nj}[\mathrm{i}A]$.
- One can surmise that general non-Hermitian matrices M can be solved with a modification of the pc-generator in which the phase of the eigenvalue differences φ_{nj} with

$$\exp(\mathrm{i}\varphi_{nj}) := \frac{m_{nn} - m_{jj}}{|m_{nn} - m_{jj}|}, \qquad \exp(-\mathrm{i}\varphi_{nj}) = \frac{m^*_{nn} - m^*_{jj}}{|m^*_{nn} - m^*_{jj}|} \tag{5.3.14}$$

  is taken into account.

5.4 Generalized PC-Generator

We generalize the pc-generator by replacing the signum-function by a complex prefactor $\exp(-\mathrm{i}\varphi_{nj})$ and obtain at the **generalized particle-conserving generator (gpc-generator)**

$$\eta^{\mathrm{gpc}}_{nj}[M] = \begin{cases} \frac{m^*_{nn} - m^*_{jj}}{|m^*_{nn} - m^*_{jj}|} m_{nj} & \forall m_{nn} \neq m_{jj}\,, \\ 0 & \forall m_{nn} = m_{jj} \end{cases} \tag{5.4.15}$$

with the special cases

$$\eta^{\mathrm{gpc}}_{nj}[H] = \ \mathrm{sign}(\ h_{nn} - \ h_{jj}) h_{nj} = \eta^{\mathrm{pc}}_{nj}[H] \qquad \forall H = H^\dagger\,, \tag{5.4.16a}$$

$$\eta^{\mathrm{gpc}}_{nj}[A] = \mathrm{i}\,\mathrm{sign}(\mathrm{i}a_{nn} - \mathrm{i}a_{jj}) a_{nj} = \eta^{\mathrm{ipc}}_{nj}[A] \qquad \forall A = -A^\dagger\,. \tag{5.4.16b}$$

Therefore, the gpc-generator is equivalent to the pc-generator for Hermitian matrices and non-Hermitian matrices with real eigenvalues ($\exp(\mathrm{i}\varphi_{nj}) = \pm 1$) and to the ipc-generator for Antihermitian matrices and non-Hermitian matrices with imaginary eigenvalues ($\exp(\mathrm{i}\varphi_{nj}) = \pm\mathrm{i}$). Assuming that the gpc-generator converges for any non-Hermitian matrix, this also explains why the pc-generator leads to a convergent flow for non-Hermitian matrices with real eigenvalues, because such matrices still contain only real differences of the eigenvalues.

Note that the special cases discussed above correspond to definition (2.3.12) of the pc-generator, where the value of the diagonal elements is taken into account,

so the diagonal elements do not have to be sorted in ascending order. This is a consequence of how the prefactor in (5.4.15) is chosen and is actually advantageous, because providing a sorted diagonal is not always possible for complex eigenvalues.

In addition to the gpc-generator, we also investigated other generalizations of the pc-generator. However, those do not prove suitable for real applications, since they either suffer from slow convergence or do not correctly converge to diagonal matrices for all initial non-Hermitian matrices. For completeness sake and to inform the reader about less fruitful trials, these generalizations are discussed in App. G.

Note that the gpc-generator can be further generalized to obtain block-diagonality instead of diagonality, e.g. by using the definition

$$\eta_{nj}^{\mathrm{gpc}}[M] = \begin{cases} \operatorname{sign}(q_{nn} - q_{jj}) \frac{m_{nn}^* - m_{jj}^*}{|m_{nn}^* - m_{jj}^*|} m_{nj} & \forall m_{nn} \neq m_{jj}\,, \\ 0 & \forall m_{nn} = m_{jj} \end{cases} \tag{5.4.17}$$

where q_{nn} are the elements of a diagonal operator Q that is not transformed during the flow, similar to the formulation (2.3.22) of the pc-generator. Only decoupling selective blocks, similar to the ps-generator (2.3.25), is also possible. Further extension, such as a truncation based on the deepCUT approach are also conceivable, but are not investigated in this thesis.

In the following sections, we focus only on the definition (5.4.15) of the gpc-generator and compare the analytical and numerical results to previously suggested generators.

5.5 Previously Suggested Generators

In 2020, Rosso et al. introduced three generator schemes for dissipative systems [86], which are defined by

$$\eta^{\mathrm{R1}} = \left[M^\dagger, M_{\mathrm{nondiag}}\right]\,, \tag{5.5.18a}$$

$$\eta^{\mathrm{R2}} = \left[M_{\mathrm{diag}}^\dagger, M_{\mathrm{nondiag}}\right]\,, \quad \eta_{nj}^{\mathrm{R2}} = (m_{nn} - m_{jj})^* m_{nj}\,, \tag{5.5.18b}$$

$$\eta_{nj}^{\mathrm{R3}} = \begin{cases} \frac{m_{nj}}{m_{nn} - m_{jj}}, & \text{if } m_{nn} \neq m_{jj}\,, \\ 0, & \text{if } m_{nn} = m_{jj}\,. \end{cases} \tag{5.5.18c}$$

The first two generators R1 and R2 are a generalization of the Wegner generator (2.3.26) to non-Hermitian matrices and R3 is inspired by White's suggestion for quantum chemistry in 2002 [153]. In the following sections, we will compare the gpc-generator with these three generators analytically as well as numerically.

5.6 Analytical Analysis of the GPC-Generator

5.6.1 General Analysis of the Flow Equations

We begin with a general comparison between the gpc-flow and the flow of the three R-generators. Since R1 and R2 lead to very similar flow equations, which will be shown in the following sections, we do not discuss R1 explicitly in this section. A discussion of R2 suffices for a qualitative understanding of both generators. One can rewrite the generators on the matrix element level by using the prefactor $\exp(\mathrm{i}\varphi_{nj})$ from (5.3.14). The resulting generators

$$\eta^{\mathrm{R2}}_{nj}[M] = \quad e^{-\mathrm{i}\varphi_{nj}}|m_{nn} - m_{jj}|m_{nj}\,, \tag{5.6.19a}$$

$$\eta^{\mathrm{gpc}}_{nj}[M] = \begin{cases} e^{-\mathrm{i}\varphi_{nj}} m_{nj} & \forall m_{nn} \neq m_{jj}\,, \\ 0 & \forall m_{nn} = m_{jj}\,, \end{cases} \tag{5.6.19b}$$

$$\eta^{\mathrm{R3}}_{nj}[M] = \begin{cases} e^{-\mathrm{i}\varphi_{nj}} \frac{1}{|m_{nn}-m_{jj}|} m_{nj} & \forall m_{nn} \neq m_{jj}\,, \\ 0 & \forall m_{nn} = m_{jj}\,. \end{cases} \tag{5.6.19c}$$

share the basic layout

$$\eta^{(r)}_{nj}[M] := \begin{cases} e^{-\mathrm{i}\varphi_{nj}}|m_{nn} - m_{jj}|^r m_{nj} & \forall m_{nn} \neq m_{jj}\,, \\ 0 & \forall m_{nn} = m_{jj}\,, \end{cases} \tag{5.6.20a}$$

$$\eta^{(r)}[M] = \begin{cases} \eta^{\mathrm{R2}}[M] & , r = 1\,, \\ \eta^{\mathrm{gpc}}[M] & , r = 0\,, \\ \eta^{\mathrm{R3}}[M] & , r = -1\,, \end{cases} \tag{5.6.20b}$$

so they only differ in the power of the factor $|m_{nn} - m_{jj}|$.

The value of r also determines the physical dimension: The generator η and the flow parameter ℓ have dimension

$$\left[\eta^{(r)}\right] = 1\mathrm{J}^{1+r}, \quad \left[\ell^{(r)}\right] = \frac{1}{\mathrm{J}^{1+r}}\,, \tag{5.6.21}$$

in the general case, so R1 and R2 ($r = 1$) scale quadratically with the inherent energy scales of the system, gpc ($r = 0$) linearly and R3 ($r = -1$) does not scale with the energy at all. Note that these generators have the same scaling behavior as the Wegner, pc- and White generator, respectively, which they are based on.

To investigate the qualitative behavior of the flows of the various generators, one can analytically compare the flow equations and the asymptotic convergence behavior when the matrix is close to a diagonal form. The most general form of the

flow equations with arbitrary r is

$$\partial_\ell m_{nj}\big|_{(r)} = \sum_k (\eta^{(\mathrm{r})}_{nk} m_{kj} - m_{nk}\eta^{(\mathrm{r})}_{kj}) \tag{5.6.22a}$$

$$= e^{-\mathrm{i}\varphi_{nj}}|m_{nn}-m_{jj}|^r m_{nj}m_{jj} - e^{\mathrm{i}\varphi_{nj}}|m_{nn}-m_{jj}|^r m_{nj}m_{nn} + \sum_{k\neq n,j}\left(e^{\mathrm{i}\varphi_{kn}}|m_{nn}-m_{kk}|^r + e^{\mathrm{i}\varphi_{kj}}|m_{jj}-m_{kk}|^r\right) m_{nk}m_{kj} \tag{5.6.22b}$$

$$= -\underbrace{|m_{nn}-m_{jj}|^{r+1}}_{=:|\Delta E_{nj}|^{r+1}} \underbrace{m_{nj}}_{\mathcal{O}(M_{\mathrm{nondiag}})} + \sum_{k\neq n,j}\left(e^{\mathrm{i}\varphi_{kn}}|m_{nn}-m_{kk}|^r + e^{\mathrm{i}\varphi_{kj}}|m_{jj}-m_{kk}|^r\right) \underbrace{m_{nk}m_{kj}}_{\mathcal{O}(M^2_{\mathrm{nondiag}})} . \tag{5.6.22c}$$

Explicitly, the flow equations for R2 ($r=1$) read

$$\partial_\ell m_{nj}\big|_{\mathrm{R2}} = -\underbrace{|m_{nn}-m_{jj}|^2}_{=:|\Delta E_{nj}|^2} \underbrace{m_{nj}}_{\mathcal{O}(M_{\mathrm{nondiag}})} + \sum_{k\neq n,j}\left(m^*_{nn}+m^*_{jj}-2m^*_{kk}\right) \underbrace{m_{nk}m_{kj}}_{\mathcal{O}(M^2_{\mathrm{nondiag}})} . \tag{5.6.23}$$

It is apparent that the second summand is negligible when M is close to diagonal. In this case, the first summand is dominant and $m_{nn}(\ell) \approx m_{nn}(\infty)$ is fulfilled in good approximation, so the generators induce an asymptotic convergence of $m_{nj}(\ell) \propto \exp\left[-|\Delta E_{nj}|^2\ell\right]$, where $\Delta E_{nj} := h_{nn} - h_{jj}$. With this, the R1- and R2-generator are renormalizing just like the Wegner generator which inspired them.

The gpc-generator ($r=0$) induces the flow

$$\partial_\ell m_{nj}\big|_{\mathrm{gpc}} = -\underbrace{|m_{nn}-m_{jj}|}_{=:|\Delta E_{nj}|} \underbrace{m_{nj}}_{\mathcal{O}(M_{\mathrm{nondiag}})} + \sum_{k\neq n,j}\left(\frac{m^*_{nn}-m^*_{kk}}{|m^*_{nn}-m^*_{kk}|} + \frac{m^*_{jj}-m^*_{kk}}{|m^*_{jj}-m^*_{kk}|}\right) \underbrace{m_{nk}m_{kj}}_{\mathcal{O}(M^2_{\mathrm{nondiag}})} . \tag{5.6.24}$$

Analogous to the flow of R2, the first summand dominates if M is close to a diagonal form, in which case one finds the asymptotic convergence $m_{nj}(\ell) \propto \exp\left[-|\Delta E_{nj}|\ell\right]$. For this generator, the convergence scales linearly with the energy difference, just like for the pc-generator. One important difference to the pc-generator, however, is the fact that the gpc-generator does not preserve the diagonal width of M unless M is either Hermitian or Antihermitian. We examine this in more detail in App. H. One can calculate the flow of the diagonal elements $m_{nn}(\ell)$ as a special case of (5.6.24)

$$\partial_\ell m_{nn}\big|_{\mathrm{gpc}} = 2\sum_{k\neq n,j} \frac{m^*_{nn}-m^*_{kk}}{|m^*_{nn}-m^*_{kk}|} \underbrace{m_{nk}m_{kn}}_{\mathcal{O}(M^2_{\mathrm{nondiag}})} . \tag{5.6.25}$$

The R3-generator ($r=-1$) does not depend on the energy scale and induces a

flow

$$\partial_\ell m_{nj}\big|_{\mathrm{R3}} = -\underbrace{m_{nj}}_{\mathcal{O}(M_{\mathrm{nondiag}})} + \sum_{k\neq n,j}\left(\frac{1}{m_{nn}-m_{kk}}+\frac{1}{m_{jj}-m_{kk}}\right)\underbrace{m_{nk}m_{kj}}_{\mathcal{O}(M^2_{\mathrm{nondiag}})}\,, \quad (5.6.26)$$

which converges asymptotically with $\exp(-\ell)$ [86]. This offers a significant advantage, but also an even greater disadvantage: The advantage is the fact that the convergence speed is constant and does not decrease for nearly degenerate energies, i.e. for small ΔE. This is also this generator's greatest disadvantage, because this renders it not renormalizing. We will show in the numerical tests in Sec. 5.7 how this leads to large errors when truncations are used. Another issue of the R3-generator in numerical implementations is the fact that to calculate the generator elements η_{nj}, one divides by ΔE_{nj} if $\Delta E_{nj} \neq 0$, which leads to extremely large generator elements in the case of near degeneracy ($\Delta E_{nj} \approx 0$), which switch signs according to the sign of ΔE_{nj}. If the energies are actually degenerate ($\Delta E_{nj} = 0$), the corresponding generator elements $\eta^{\mathrm{R3}}_{nj} = 0$ vanish. To differentiate between these cases, one has to define a numerical cutoff ΔE_{min}. The strong discontinuity and the numerical cutoff can cause numerical instability, especially if the energy differences of the system are in the same order of magnitude as the cutoff. While a similar cutoff is necessary for the gpc-generator as well, the R3-generator is impacted more significantly because the elements η^{R3}_{nj} scale inversely with $|\Delta E_{nj}|$.

Generator	$[\eta]$	$[\ell]$	Convergence Behavior
R1, R2	E^2	$1/E^2$	$\exp[-\lvert\Delta E\rvert^2\,\ell]$
gpc	E	$1/E$	$\exp[-\lvert\Delta E\rvert\,\ell]$
R3	1	1	$\exp[-\ell]$
$\eta^{(r)}$	E^{1+r}	$1/E^{1+r}$	$\exp[-\lvert\Delta E\rvert^{1+r}\,\ell]$

Table 5.1: Comparison of the dimension and convergence behavior of the generators considered in this work.

The comparison of the generators is summarized in Tab. 5.1. In principle, one can define various generators with $r \in \mathbb{R}$. The numerical results in Sec. 5.7 , however, will suggest that it is reasonable to choose $|r| < 1$. The case $r = 1$ converges slowly and it stands to reason that convergence decreases further for $r > 1$, because the power of the energy scaling increases. The case $r = -1$ offers excellent convergence speed, but is not robust against trunations and numerical instability. We surmise that these problems are worse for $r < -1$, because for these values of r the renormalizing property is inverted, so processes of low energy are treated before processes of high energy, and the generator elements increase even further for near degenerate energies. By choosing $|r| < 1$, one can define generators which fill the gap between the gpc-, R1-, R2- and R3-generator and potentially offer tradeoffs between their properties.

5.6.2 Proof of Convergence

We show convergence of the flow induced by the gpc-generator using perturbative arguments in an expansion parameter x for a matrix M without degeneracy. We assume that all off-diagonal elements can be expanded in x, i.e.

$$m_{nn}(\ell) = m_n(\ell) \in \mathcal{O}(x^0) \qquad \text{with } m_a(\ell) \neq m_b(\ell)\ \forall a \neq b\,, \tag{5.6.27a}$$

$$m_{nl}(\ell) = \sum_{i>0} a_{nl}^{(i)}(\ell)\, x^i \quad , n \neq l,\,. \tag{5.6.27b}$$

In the following, we do not denote the ℓ-dependencies explicitly for brevity. One can define the factor

$$c_{nkl} := \left(\frac{m_n^* - m_k^*}{|m_n^* - m_k^*|} + \frac{m_l^* - m_k^*}{|m_l^* - m_k^*|} \right) = e^{\mathrm{i}\varphi_{kn}} + e^{\mathrm{i}\varphi_{kl}} \;\Rightarrow\; |c_{nkl}| \leq 2\,, \tag{5.6.28}$$

which is obviously bounded from above by 2. One can calculate the flow of the off-diagonals

$$\partial_\ell \left(\sum_{i>0} a_{nl}^{(i)} x^i \right) = -\,|m_n - m_l| \left(\sum_{i>0} a_{nl}^{(i)} x^i \right) \tag{5.6.29a}$$

$$+ \sum_{k\neq n,l} c_{nkl} \left(\sum_{i>0} a_{nk}^{(i)} x^i \right) \left(\sum_{j>0} a_{kl}^{(j)} x^j \right) \tag{5.6.29b}$$

$$\Rightarrow \partial_\ell a_{nl}^{(i)} = -\,|m_n - m_l| a_{nl}^{(i)} + \sum_{k\neq n,l} c_{nkl} \left(\sum_{0<\delta<i} a_{nk}^{(\delta)} a_{kl}^{(i-\delta)} \right). \tag{5.6.29c}$$

In the last step we compare the coefficients of the monomials in x to selectively calculate the derivative of individual orders $a_{nl}^{(i)}$. For the flow to converge, all of these coefficients should become exponentially small during the flow. One can prove this using induction in i by showing that all orders $j \leq i$ of the non-diagonal elements $m_{nl}(\ell)$ are exponentially small beyond a minimum value ℓ_i of the flow paramter ℓ, i.e.

$$\left| a_{nl}^{(j)}(\ell) \right| \ll 1 \quad \forall 0 \leq j \leq i;\, \ell > \ell_i\,. \tag{5.6.30}$$

The induction basis is

$$a_{nl}^{(0)}(\ell) = 0\,, \tag{5.6.31}$$

which is trivially fulfilled with $\ell_0 = 0$ since the expansion (5.6.27b) is assumed to start at $i = 1$ and, therefore, $a_{nl}^{(0)}(\ell) = 0$ by definition of the initial conditions. For the induction step, one can assume that all coefficients of order $j \in \{0, 1, ..., i-1\}$ are exponentially small beyond a large enough $\ell_{\max,i}$

$$\left| a_{nl}^{(j)}(\ell) \right| \ll 1 \quad \forall 0 \leq j < i;\, \ell > \ell_{\max,i} \max(\ell_0, ...\ell_{i-1})\,. \tag{5.6.32}$$

In that case, obviously $\left| a_{nk}^{(\delta)} a_{kl}^{(i-\delta)} \right| \lll 1$ is extremely small for all $\delta \in \mathbb{N}$ with $0 < \delta < i$. Since $|c_{nkl}| \leq 2$ is bounded from above, the second summand in (5.6.29c) is negligibly small and the flow is dominated by the first summand. Furthermore, the

diagonal elements can approximated to be diagonal, i.e. $m_n(\ell) \approx m_n(\infty)$, because the error made by this approximation is of order $\mathcal{O}(x^{2j})$, see (5.6.25). It follows

$$\partial_\ell a_{nl}^{(i)}(\ell) \approx -|m_n(\infty) - m_l(\infty)| a_{nl}^{(i)}(\ell)\,, \qquad \forall \ell > \ell_{\max,i}\,, \tag{5.6.33a}$$

$$\Rightarrow \quad a_{nl}^{(i)}(\ell) \approx a_{nl}^{(i)}(\ell_{\max,i}) e^{-|m_n(\infty)-m_l(\infty)|\,\ell}\,, \qquad \forall \ell > \ell_{\max,i}\,, \tag{5.6.33b}$$

$$\Rightarrow \quad \left|a_{nl}^{(i)}(\ell)\right| \ll 1\,, \qquad \forall \ell > \ell_i \text{ with } \ell_i \gg \ell_{\max,i}\,. \tag{5.6.33c}$$

One sees that $|a_{nl}^{(i)}(\ell)| \ll 1$ $\forall \ell > \ell_i$ is fulfilled if ℓ_i is chosen large enough, which concludes the induction step. Note that no explicit value for ℓ_i is determined in the derivation. The convergence speed and therefore the value of ℓ_i depends on the concrete flow of the matrix elements $m_n(\ell)$ and $m_l(\ell)$, but the proof shows that convergence is eventually achieved for an arbitrarily large ℓ_i. □

We must point out, however, that the series in x can be ill-behaved if the series ℓ_i grows too quickly with i. In that case, despite the convergence of $a_{nl}^{(i)}(\ell)$, the series (5.6.27b) in $m_{nl}(\ell)$ does not converge and thus the off-diagonal elements do not vanish for large ℓ. Nevertheless, all our numerical calculations presented in the following sections yield convergent gpc-flows, so all evidence suggests that the gpc-generator consistently induces convergent flows.

5.6.3 Analytical Example: Fermionic Mode with Losses and Gains

5.6.3.1 Physical Model

We consider a simple physical example to analytically compare the flow of the generators for a concrete problem. The example is also discussed for the R-generators in Ref. [86] and consists of a single fermionic mode of energy ϵ, which is coupled to a bath with a loss rate Γ_1 and a gain rate Γ_2. The Lindblad operators (or jump operators) can be described by the canonical fermionic creation and annihilation operators $\hat{c}$ and $\hat{c}^\dagger$. With this, one obtains the Lindblad master equations

$$\mathrm{i}\hbar \frac{\mathrm{d}}{\mathrm{d}t}\rho(t) = [H, \rho(t)] + \mathrm{i}\hbar \sum_j \Gamma_j L_j \rho(t) L_j^\dagger - \frac{\mathrm{i}\hbar}{2}\Gamma_j \left\{ L_j^\dagger L_j, \rho(t) \right\}, \tag{5.6.34a}$$

$$\hat{H} = \epsilon \hat{c}^\dagger \hat{c}, \quad L_1 = \hat{c}, \quad L_2 = \hat{c}^\dagger\,. \tag{5.6.34b}$$

One can treat this problem using a Lindbladian superoperator in matrix form $M = \mathcal{L}$, which acts on the density state $|\rho(t)\rangle$, see (5.1.2). To obtain this form, one can use **superfermion representation** to treat the open quantum system as a fermionic two-mode problem. The full derivation can be found in Refs. [86, 154, 155]. In this thesis, we only present the general idea to understand how the superfermionic representation can be used to derive the Lindbladian matrix.

One can express the density matrix $\rho = \sum_{n,m=1}^{N} \rho_{nm} |n\rangle\langle m|$ by a vector of dimen-

sion N^2 in Fock-Liouville space

$$|\rho\rangle = \sum_{nm} \rho_{nm} |n\rangle \otimes |m\rangle = \rho \otimes \mathbb{1} |I\rangle \,, \tag{5.6.35a}$$

$$|I\rangle := \sum_{n} |n\rangle \otimes |n\rangle \,, \tag{5.6.35b}$$

where the identity matrix is expressed by $|I\rangle$. In this space, one can work with fermionic superoperators

$$c := \hat{c} \otimes \mathbb{1} \,, \tag{5.6.36a}$$

$$\tilde{c} := (-1)^{c^\dagger c} \otimes \hat{c} \,, \tag{5.6.36b}$$

which describe the action of the fermionic operators $\hat{c}$ and $\hat{c}^\dagger$ on the left or right side of the density matrix. The operators c and $\tilde{c}$ are called fermionic superoperators because they fulfill the fermionic anticommutation relations

$$\{c, c\} = 0 \,, \qquad \{c, c^\dagger\} = 1 \,, \tag{5.6.37a}$$

$$\{\tilde{c}, \tilde{c}\} = 0 \,, \qquad \{\tilde{c}, \tilde{c}^\dagger\} = 1 \,, \tag{5.6.37b}$$

$$\{c, \tilde{c}\} = 0 \,, \qquad \{c, \tilde{c}^\dagger\} = 0 \,. \tag{5.6.37c}$$

Note that a similar superoperator representation is possible for bosons [156] and that the last two anticommutation relations (5.6.37c) follow from the factor $(-1)^{c^\dagger c}$ in (5.6.36b). By applying the superfermion formalism, one obtains the bilinear expression

$$M = \begin{pmatrix} c^\dagger & \tilde{c} \end{pmatrix} \begin{pmatrix} \epsilon - \frac{\mathrm{i}\hbar}{2}\Delta\Gamma_{12} & \hbar\Gamma_2 \\ -\hbar\Gamma_1 & \epsilon + \frac{\mathrm{i}\hbar}{2}\Delta\Gamma_{12} \end{pmatrix} \begin{pmatrix} c \\ \tilde{c}^\dagger \end{pmatrix} - \epsilon - \frac{\mathrm{i}\hbar}{2}(\Gamma_1 + \Gamma_2) \tag{5.6.38}$$

with $\Delta\Gamma_{12} := \Gamma_1 - \Gamma_2$. This matrix can be diagonalized with a non-unitary, but invertible transformation $M_{\text{eff}} = SMS^{-1}$. In the new basis, one can define the operators

$$\begin{pmatrix} d \\ \tilde{d}^\dagger \end{pmatrix} = S \begin{pmatrix} c \\ \tilde{c}^\dagger \end{pmatrix} \,, \qquad (D^\dagger,\ \tilde{D}) = (c^\dagger,\ \tilde{c})\, S^{-1} \,, \tag{5.6.39}$$

which satisfy the fermionic anticommutation relations. Note that $(d)^\dagger \neq D^\dagger$ and $(\tilde{D})^\dagger \neq \tilde{d}^\dagger$, but the anticommutators of the operators fulfill the relations $\{d, D^\dagger\} = 1$ and $\{\tilde{d}^\dagger, \tilde{D}\} = 1$. Using these operators, one obtains the diagonal form

$$M_{\text{eff}} = \begin{pmatrix} D^\dagger & \tilde{D} \end{pmatrix} \begin{pmatrix} \epsilon - \frac{\mathrm{i}\hbar}{2}(\Gamma_1 + \Gamma_2) & 0 \\ 0 & \epsilon + \frac{\mathrm{i}\hbar}{2}(\Gamma_1 + \Gamma_2) \end{pmatrix} \begin{pmatrix} d \\ \tilde{d}^\dagger \end{pmatrix} - \epsilon - \frac{\mathrm{i}\hbar}{2}(\Gamma_1 + \Gamma_2) \,. \tag{5.6.40}$$

To compare the flows of the generators introduce in Sec. 5.4 and Sec. 5.5 , we perform this diagonalization via flow equations. To that end, we parameterize the matrix

elements

$$M(\ell) = \begin{pmatrix} \epsilon(\ell) + \mathrm{i}\alpha(\ell) & \mu_2(\ell) \\ -\mu_1(\ell) & \epsilon(\ell) - \mathrm{i}\alpha(\ell) \end{pmatrix}, \quad \alpha(\ell), \epsilon(\ell), \mu_{1,2}(\ell) \in \mathbb{R}\,, \tag{5.6.41a}$$

$$\alpha(0) = -\frac{\hbar}{2}\Delta\Gamma_{12}\,, \qquad \mu_{1,2}(0) = \hbar\Gamma_{1,2}\,, \qquad \epsilon(0) = \epsilon \tag{5.6.41b}$$

and check if the flow converges to a diagonal matrix with the correct eigenvalues

$$\lambda_\pm = -\epsilon \pm \frac{\mathrm{i}\hbar}{2}(\Gamma_1 + \Gamma_2)\,. \tag{5.6.42}$$

This means that the parameters must converge to

$$\epsilon(\infty) = \epsilon, \quad \alpha(\infty) = \pm\frac{\hbar}{2}(\Gamma_1 + \Gamma_2), \quad \mu_1(\infty) = \mu_2(\infty) = 0\,. \tag{5.6.43}$$

5.6.3.2 Flow and Stationary State

The gpc-generator for the matrix (5.6.41a) reads

$$\eta^{\mathrm{gpc}} = \begin{pmatrix} 0 & \frac{(\epsilon-\mathrm{i}\alpha)-(\epsilon+\mathrm{i}\alpha)}{|(\epsilon-\mathrm{i}\alpha)-(\epsilon+\mathrm{i}\alpha)|}\mu_2 \\ \frac{(\epsilon+\mathrm{i}\alpha)-(\epsilon-\mathrm{i}\alpha)}{|(\epsilon+\mathrm{i}\alpha)-(\epsilon-\mathrm{i}\alpha)|}(-\mu_1) & 0 \end{pmatrix} = \begin{pmatrix} 0 & -\mathrm{i}\mu_2\mathrm{sign}(\alpha) \\ -\mathrm{i}\mu_1\mathrm{sign}(\alpha) & 0 \end{pmatrix} \tag{5.6.44}$$

and the resulting flow

$$\partial_\ell M\big|_{\mathrm{gpc}} = [\eta^{\mathrm{gpc}}, M] \tag{5.6.45a}$$

$$= \begin{pmatrix} \mathrm{i}2\mu_1\mu_2\mathrm{sign}(\alpha) & -2\mu_2|\alpha| \\ 2\mu_1|\alpha| & -\mathrm{i}2\mu_1\mu_2\mathrm{sign}(\alpha) \end{pmatrix}. \tag{5.6.45b}$$

One can formulate the flow equations as one-dimensional equations for the parameters

$$\text{gpc: } \partial_\ell\alpha = 2\mu_1\mu_2\mathrm{sign}(\alpha)\,, \qquad \partial_\ell\mu_1 = -2\mu_1|\alpha|\,, \qquad \partial_\ell\mu_2 = -2\mu_2|\alpha|\,. \tag{5.6.46a}$$

and do the same for the other three generators [86]

$$\text{R1: } \partial_\ell\alpha = 4\mu_1\mu_2\alpha\,, \qquad \partial_\ell\mu_1 = -2\mu_1(2\alpha^2 + \mu_1^2 - \mu_2^2)\,, \tag{5.6.47a}$$

$$\partial_\ell\mu_2 = -2\mu_2(2\alpha^2 - \mu_1^2 + \mu_2^2)\,, \tag{5.6.47b}$$

$$\text{R2: } \partial_\ell\alpha = 4\mu_1\mu_2\alpha\,, \qquad \partial_\ell\mu_1 = -4\mu_1\alpha^2\,, \tag{5.6.47c}$$

$$\partial_\ell\mu_2 = -4\mu_2\alpha^2\,, \tag{5.6.47d}$$

$$\text{R3 } (\forall\alpha \neq 0)\text{: } \partial_\ell\alpha = \mu_1\mu_2/\alpha\,, \qquad \partial_\ell\mu_1 = -\mu_1\,, \tag{5.6.47e}$$

$$\partial_\ell\mu_2 = -\mu_2\,. \tag{5.6.47f}$$

Note that we do not write down the flow equations for $\epsilon(\ell)$, because the real parts of the diagonals do not change, hence $\partial_\ell\epsilon = 0$. Furthermore, all of the above flow

equations are quite simple due to the small matrix size, but one can see that R1 creates a slightly more involved equation with more summands. The gpc-flow also appears as if it was slightly more complicated for analytical calculations due to the sign(α). This can be solved by using the absolute value $|\alpha|$, but we will keep using α for the brief discussion presented here. One can use the two invariants of motion

$$\mathrm{Tr}[M] = 2\epsilon = \text{const.} \qquad \Rightarrow \qquad \epsilon = \text{const}\,, \tag{5.6.48a}$$

$$\mathrm{Tr}[M^2] = 2(\epsilon^2 - \alpha^2) - 2\mu_1\mu_2 = \text{const.} \quad \Rightarrow \quad \alpha^2 + \mu_1\mu_2 = \hbar^2\frac{(\Gamma_1+\Gamma_2)^2}{4} \tag{5.6.48b}$$

to simplify the flow equation for α and to decouple it from μ_1 and μ_2, obtaining

$$\text{gpc: } \partial_\ell\alpha(\ell) = \frac{1}{2}\left(\hbar^2(\Gamma_1+\Gamma_2)^2 - 4\alpha^2(\ell)\right)\mathrm{sign}(\alpha)\,, \tag{5.6.49a}$$

$$\text{R1, R2: } \partial_\ell\alpha(\ell) = \left(\hbar^2(\Gamma_1+\Gamma_2)^2 - 4\alpha^2(\ell)\right)\alpha(\ell)\,, \tag{5.6.49b}$$

$$\text{R3 } (\forall\alpha\neq 0)\text{: } \partial_\ell\alpha(\ell) = \frac{\hbar^2(\Gamma_1+\Gamma_2)^2}{4\alpha(\ell)} - \alpha(\ell)\,. \tag{5.6.49c}$$

Note that α, μ_i and $\hbar\Gamma_i$ all have the dimension of an energy, thus one can clearly see the energy scaling of the different generators. For all generators, one finds the two fixed points $\tilde{\alpha}_{1,2} = \pm\hbar(\Gamma_1+\Gamma_2)/2$. A third fixed point $\tilde{\alpha}_3 = 0$ appears directly for R1, R2 and gpc. For R3, $\tilde{\alpha}_3 = 0$ is also a fixed point, since the generator vanishes for $\alpha(\ell) = 0$. In the trivial case $\Gamma_1 = -\Gamma_2$ these three fixed points collapse to a single one, but we will consider the more interesting case $\Gamma_1 \neq -\Gamma_2$.

One can easily see that the correct eigenvalues of $M(\ell)$ are found at the two fixed points $\tilde{\alpha}_{1,2}$, but the flow only converges to these fixed points if they are attractive. One can check the stability by differentiating the flow equation $\partial_\ell\alpha =: f(\alpha)$ with respect to α. The derivative fulfills $f'(\alpha) < 0$ for attractive fixed points and $f'(\alpha) > 0$ for repulsive fixed points. This is not possible for R3 at $\tilde{\alpha}_3 = 0$ due to the discontinuity of the flow equation, so one must check this case, instead, by calculating the signum of $\partial_\ell\alpha(\ell)$. The results of this analysis are

$$\text{gpc: } f'(\tilde{\alpha}_{1,2}) = -2\hbar|\Gamma_1+\Gamma_2| \leq 0 \qquad f'(\tilde{\alpha}_3) = \hbar^2(\Gamma_1+\Gamma_2)^2\delta(0) > 0\,, \tag{5.6.50a}$$

$$\text{R1, R2: } f'(\tilde{\alpha}_{1,2}) = -2\hbar^2(\Gamma_1+\Gamma_2)^2 \leq 0 \qquad f'(\tilde{\alpha}_3) = (\Gamma_1+\Gamma_2)^2 > 0\,, \tag{5.6.50b}$$

$$\text{R3: } f'(\alpha) < 0\ \forall\alpha\neq 0 \qquad \mathrm{sign}\left(\partial_\ell\alpha(\ell)\right) = \mathrm{sign}(\alpha) \text{ for } \alpha \approx \tilde{\alpha}_3 = 0 \tag{5.6.50c}$$

and confirm that for all generators $\tilde{\alpha}_{1,2}$ are attractive fixed points of the flow and $\tilde{\alpha}_3$ is a repulsive fixed point. Therefore, all four generators converge to the same, correct fixed points. The concrete speed of the flow in the space of possible (α, μ_1, μ_2), however, differs. The flow $\alpha(\ell)$ is plotted in Fig. 5.3 for all four generators for three different initial conditions, i.e. with different rates Γ_1 and Γ_2. For small energy differences (left panel), R3 converges most quickly, followed by gpc and finally by R1

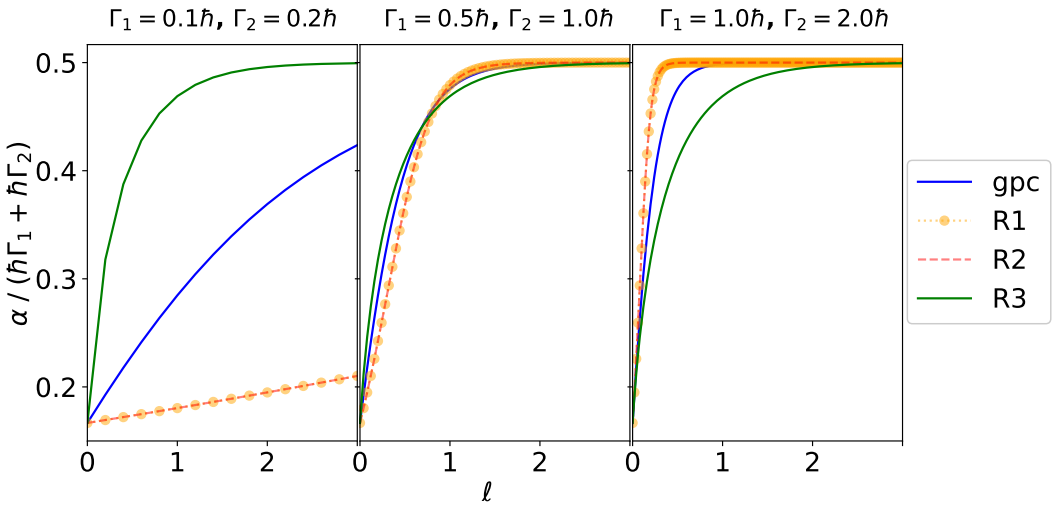

Figure 5.3: Exemplary flows $\alpha(\ell)$ of the analytical example (5.6.41a) induced by the gpc-generator (5.6.46a) and the R-generators (5.6.47f). Each panel depicts the flow for different rates Γ_1 and Γ_2. The flows are plotted based on the numerical values of ℓ for each generator, but recall that analytically, the physical dimensions of ℓ differ.

and R2. For larger energy differences the difference in convergence speed decreases (middle panel) or the order of the generators is reversed (right panel).

To better understand the correlation between convergence speed and energy differences, Fig. 5.4 displays exemplary flow trajectories $(\alpha(\ell), \mu_1(\ell))$ and the speed of the flow with the initial condition $\mu_2(0) = \mu_1(0) + 2\alpha(0)$. For the gpc-generator (third panel), the speed increases when the difference $2\mathrm{i}\alpha(\ell)$ between the eigenvalues increases. For the R1- and R2-generator (first and second panel), this effect is even more pronounced and one observes extremely slow flows at $\alpha \approx 0$. The R3-flow (fourth panel) converges faster when the energy difference is small. All four generators induce faster flows if the off-diagonals μ_1 and μ_2 are larger. These observation corresponds perfectly with the energy scaling of the generators discussed in Sec. 5.6.1 .

Note that the observations made above are based on a simple two-level system. More complex systems exhibit a multitude of energy scales and the corresponding flow often cannot be evaluated analytically. Furthermore, the physical dimension of the flow parameter ℓ differs between the generators, complicating the comparison further. For this reason, we will only study one last simplified analytical case before performing numerical benchmarks of the real time convergence speed for more realistic system sizes.

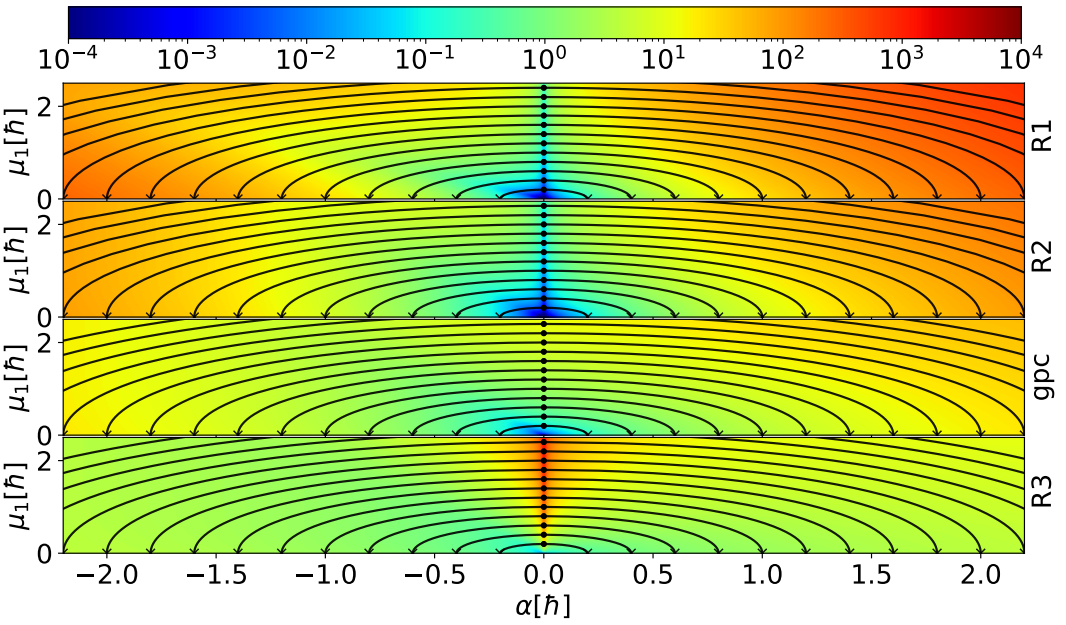

Figure 5.4: Exemplary flow $(\alpha(\ell), \mu_1(\ell))$ of the analytical example (5.6.41a). The black lines depict the flow for exemplary initial parameters $(\alpha, \mu_1, \mu_2) = (\pm 10^{-8}\hbar, \mu_1, \mu_1 \pm 2 \cdot 10^{-8}\hbar)$ and the heatmaps indicate the logarithmic norm of the gradient $\log[(\partial_\ell \alpha)^2 + (\partial_\ell \mu_1)^2 + (\partial_\ell \mu_2)^2]$ for exemplary initial parameters with $\mu_2 = \mu_1 + 2\alpha$. Red color indicates large gradients while blue color indicates small gradients.

5.6.3.3 Simple Analytical Case $\Gamma_2 = 0$

As an even simpler analytical example, we set $\Gamma_2 = 0$ for the gain rate. In this case $\mu_2(\ell) = 0$, so one degree of freedom disappears. Using the second invariant, one derives $\alpha(\ell) = -\Gamma_1/2$, losing another degree of freedom. Only the flow equation for $\mu_1(\ell)$ remains and takes the form

$$\text{gpc: } \partial_\ell \mu_1(\ell) = -\hbar\Gamma_1 \mu_1(\ell)\,, \tag{5.6.51a}$$

$$\text{R1: } \partial_\ell \mu_1(\ell) = -2(\hbar^2\Gamma_1^2 + \mu_1^2(\ell))\mu_1(\ell)\,, \tag{5.6.51b}$$

$$\text{R2: } \partial_\ell \mu_1(\ell) = -\hbar^2\Gamma_1^2 \mu_1(\ell)\,, \tag{5.6.51c}$$

$$\text{R3: } \partial_\ell \mu_1(\ell) = -\mu_1(\ell)\,. \tag{5.6.51d}$$

The respective scalings in energies appear quite clearly, again. The solutions are trivial

$$\text{gpc: } \mu_1(\ell) = \hbar\Gamma_1 \exp(-\hbar\Gamma_1 \ell)\,, \tag{5.6.52a}$$

$$\text{R1: } \mu_1(\ell) = \frac{\hbar\Gamma_1}{\sqrt{2\exp(4\hbar^2\Gamma_1^2\ell) - 1}}\,, \tag{5.6.52b}$$

$$\text{R2: } \mu_1(\ell) = \hbar\Gamma_1 \exp(-\hbar^2\Gamma_1^2 \ell)\,, \tag{5.6.52c}$$

$$\text{R3: } \mu_1(\ell) = \hbar\Gamma_1 \exp(-\ell) \tag{5.6.52d}$$

and demonstrate the convergence behaviors that one generally observes in the asymptotic case of the respective generator, see Sec. 5.6.1 . All four generators succeed in

the diagonalization with varying convergence speeds. The R3-generator is slightly favored, but the convergence speed ultimately depends on the concrete value of Γ_1. Since all flows can be computed without approximations, a final statement on truncation errors is not possible based on these results alone, but they provide a qualitative understanding of the convergence speed.

5.7 Numerical Analysis of the GPC-Generator

In this section, we perform numerical benchmarks of the gpc-generator and compare the results with the results for the R1-, R2- and R3-generator. For these benchmarks, we diagonalize matrix representations of various mathematical and physical systems without bias. The benchmarking process is explained in detail in Sec. 5.7.1 .

All calculations are implemented in C++ and use the Eigen library [136] for matrix arithmetics. The flow equations are integrated using the Runge-Kutta-Dopri5 algorithm from the Boost library [149] with a controlled stepper, which adjusts the step size $\Delta\ell$ so that the absolute and relative error stay below 10^{-8}.

All calculations are performed on the same machine. The computation times are measured in seconds, but absolute values are not representative, because the computation times depend strongly on the specific hardware and software implementations. Nevertheless, the relative computation times of various generators provide information on their relative performance in most scenarios.

5.7.1 Benchmark Parameters

5.7.1.1 Benchmark of Convergence Speed

To ensure that the integration of the flow equations is feasible for complicated systems, rapid convergence to an attractive fixed point of the flow is favorable. To benchmark the convergence speed, we fully diagonalize various models and generators until the ROD (2.6.50) falls below the threshold $\mathrm{ROD}_{\min} = 10^{-8}J$, where $J = [m_{00}]$ is the energy dimension of the matrix elements. For purely mathematical models, one can set $J = 1$, but for physical models J is typically an energy. Note that for purely numerical benchmarks, one could measure convergence with other methods, e.g. by calculating the square norm of the differences between the diagonal elements of the matrix $M(\ell)$ and the exact spectrum. We choose the ROD-criterion because it is simple to check and $\mathrm{ROD}(\ell) = 0$ implies $\eta(\ell) = 0$ and hence $\partial_\ell M(\ell) = 0$. Furthermore, in realistic applications of flow equations one often does not know the spectrum beforehand, but can easily calculate the ROD for any given $M(\ell)$. Recall that one can also use flow equations for block-diagonalization, e.g. to obtain a system with preservation of quasi-particles, see Sec. 2.3.1 . Full diagonalization, however, is useful for the numerical benchmarks presented here.

One can examine the convergence speed by studying the full flow of the function $\mathrm{ROD}(\ell)$, but it is also useful to quantify the convergence speed by a single number. To that end, we introduce the **convergence coefficient**

$$C_{\mathrm{Conv}}^{(\ell)} = \begin{cases} -\ln[\mathrm{ROD}(\ell_2)/\mathrm{ROD}(\ell_1)]/(\ell_2 - \ell_1) & \text{if flow converges}\,, \\ 0 & \text{else}\,, \end{cases} \tag{5.7.53}$$

with two reference points ℓ_1 and ℓ_2 with $\ell_2 > \ell_1$. Assuming asymptotic behavior $\mathrm{ROD} \propto \exp(-C_{\mathrm{Conv}}^{(\ell)}\ell)$ (see Sec. 5.6.1) between these reference points, the convergence coefficient describes the coefficient of the exponent and faster convergence coincides with a larger $C_{\mathrm{Conv}}^{(\ell)}$. The reference points ℓ_1 and ℓ_2 should be chosen such that the convergence behavior of the ROD is captured well. Initially, $\mathrm{ROD}(0)$ is often of the order of magnitude of $10^0 = 1$ and asymptotic convergence starts only after an initial transient, so ℓ_1 should not be chosen too small. When the flow is close to convergence, i.e. for large $\ell \gg J$, numerical fluctuations of the ROD can obscure the true convergence, so ℓ_2 should not be chosen too large. For the following benchmarks, we choose ℓ_2 such that $\mathrm{ROD}(\ell_2) \approx 10^{-6}\, J$ and ℓ_1 such that $\mathrm{ROD}(\ell_1) \approx 0.5\mathrm{ROD}(\ell_2)$. Note that we only use the approximate values because of the finite step size in ℓ in numerical calculations.

As long as one only compares generators that share a similar definition and identical physical dimensions, $C_{\mathrm{Conv}}^{(\ell)}$ can be a suitable choice for a convergence measure. However, we discussed in Sec. 5.6.1 that the generators depend differently on the energy scales, so not even the physical dimension of ℓ is comparable. Additionally, even for generators with the same energy dependence, constant coefficients change the convergence speed in ℓ. To understand this, consider the effect of rescaling a generator $\eta' = 2\eta$. According to (5.2.5), this implies $\partial_\ell H' = 2\partial_\ell H$, which is equivalent to the transformation $\ell' = \ell/2$ and causes a doubling $(C_{\mathrm{Conv}}^{(\ell)})' = 2C_{\mathrm{Conv}}^{(\ell)}$ of the convergence coefficient. Hence, η' has a higher convergence coefficient than η, but the calculation takes the same computation time, because the integration must be performed with halved step size to obtain the same precision. This simple example demonstrates that large values of $C_{\mathrm{Conv}}^{(\ell)}$ are not guaranteed to imply fast computation.

A better convergence measure that circumvents this problem is the time-dependent convergence coefficient

$$C_{\mathrm{Conv}}^{(t)} = \begin{cases} -\ln[\mathrm{ROD}(t_2)/\mathrm{ROD}(t_1)]/(t_2 - t_1) & \text{if flow converges}\,, \\ 0 & \text{else}\,, \end{cases} \tag{5.7.54}$$

which measures the convergence speed in accordance with the asymptotic behavior $\mathrm{ROD} \propto \exp(-C_{\mathrm{Conv}}^{(t)}t)$ with the actual computation time t. Measuring the real time is

prone to artifacts such as heat throttling of the CPU. Nevertheless, $C^{(t)}_{\mathrm{Conv}}$ quantifies the realistic performance of the generators better than $C^{(\ell)}_{\mathrm{Conv}}$. It also takes into account that the computation time increases if the calculation of a generator requires computationally expensive operations.

Note that the convergence coefficient assumes asymptotic behavior inside the interval $t \in [t_1, t_2]$ (or $\ell \in [\ell_1, \ell_2]$). For a vanishing energy gap, the convergence follow a power law. While $C^{(t)}_{\mathrm{Conv}}$ allows one to quickly compare the asymptotic convergence speed of various generators with one another, it is still useful to check the full flow of $\mathrm{ROD}(\ell)$, since it conveys further information, such as

- the full computation time necessary until convergence $\mathrm{ROD}(\ell) < \mathrm{ROD}_{\mathrm{min}}$ is achieved,
- the flow before the beginning of the asymptotic interval, i.e. $t < t_1$ and $\ell < \ell_1$,
- whether true asymptotic, i.e. exponentially decreasing, behavior occurs at all,
- if the ROD increases momentarily.

5.7.1.2 Benchmark of Truncation Error

While rapid convergence speed is desirable to reduce computational cost, it is also necessary that the results are accurate. Since one generally uses the flow equation method with truncation, see Sec. 2.4 , one must ensure that the truncation error remains small. Naturally, low computational cost allows one to perform the calculation in higher truncation orders, i.e. to consider more terms and therefore increase the accuracy of the results. Yet, it is preferable to choose a generator which combines speed with a calculation that is highly accurate at its core. Rapid convergence and minimal truncation errors are two orthogonal requirements and one has to choose a generator scheme which represents a good compromise of both.

We benchmark the truncation error by preparing an initial matrix M_{prep} based on one of the physical or mathematical models M used for the speed benchmark. The preparation consists of truncating M in order on_{max}, so that M_{prep} is band-diagonal with diagonal width n_{max}. This scheme is easy to implement for the benchmark, but in a real physical scenario, it would only be reasonable if off-diagonal elements far from the diagonal are small. If this assumption is not true for a given M, one can additionally rescale the elements $m_{nj,\,\mathrm{prep}} = \lambda^{|n-j|} m_{nj}$ with an expansion parameter $\lambda \in (0, 1)$. Additionally, it can be useful to reorder the diagonals of M_{prep} so that $|m_{nn} - m_{jj}| > |m_{nn} - m_{kk}|$ for $|n - j| > |n - k|$ is fulfilled. Note that this ordering is not trivial for $m_{nj} \in \mathbb{C}$. For the following benchmarks, we always perform the truncation based on diagonal width, while we only rescale the off-diagonals or reorder the diagonals if we state so explicitly.

To illustrate the preparation process, consider a 4x4 matrix that is truncated in order o2 in λ with rescaled off-diagonals

$$M = \begin{pmatrix} m_{11} & m_{12} & m_{13} & m_{14} \\ m_{21} & m_{22} & m_{23} & m_{24} \\ m_{31} & m_{32} & m_{33} & m_{34} \\ m_{41} & m_{42} & m_{43} & m_{44} \end{pmatrix} \Rightarrow M_{\text{prep}} = \begin{pmatrix} m_{11} & \lambda m_{12} & \lambda^2 m_{13} & 0 \\ \lambda m_{21} & m_{22} & \lambda m_{23} & \lambda^2 m_{24} \\ \lambda^2 m_{31} & \lambda m_{32} & m_{33} & \lambda m_{34} \\ 0 & \lambda^2 m_{42} & \lambda m_{43} & m_{44} \end{pmatrix}. \tag{5.7.55}$$

After the initialization of M_{prep}, we solve the flow equations with various generators in order o$n_{\max}$, i.e. any emerging elements $m_{nj}(\ell)$ with $|n-j| > n_{\max}$ are truncated. This way, truncation errors arise in the effective model $M_{\text{eff}} = M(\ell_{\text{eff}})$ at the end point ℓ_{eff} of numerical integration. We terminate the integration when a sufficiently small $\text{ROD}(\ell_{\text{eff}}) \leq 10^{-8}$ is obtained. To quantify the truncation error Δ_{trunc}, we compare the spectrum Λ_{trunc} of M_{eff} with the numerically exact spectrum Λ_{exact} of M_{prep} obtained with standard diagonalization

$$M_{\text{prep}}, \quad \text{with spectrum } \Lambda_{\text{exact}} = (\lambda_1, \lambda_2, ..., \lambda_D) \tag{5.7.56a}$$

$$\xrightarrow{\text{flow equations}} M_{\text{eff}}, \quad \Delta_{\text{trunc}} = \left|\Lambda_{\text{trunc}} - \Lambda_{\text{exact}}\right| = \sqrt{\sum_n \left|\lambda_{i,\,\text{trunc}} - \lambda_i\right|^2}. \tag{5.7.56b}$$

Note that the initial matrix M_{prep} is always truncated in the same order as the flow equations, i.e. the diagonal width of M_{prep} can increase with the truncation order. For this reason, the truncation error Δ_{trunc} can increase upon increasing $n_{\max}$. This is different from real physical examples, where the initial system is typically already a band matrix and one uses a truncation scheme which does not truncate any of the initial terms present at $\ell = 0$. In such realistic scenarios, increasing the truncation order normally decreases truncation errors. Since the benchmark presented here does not aim at comparing truncation orders with one another, but rather at comparing generator schemes, this behavior does not cause any problems.

5.7.2 Random Matrices

5.7.2.1 Matrix Generation

The first benchmark of the generators is performed for various non-Hermitian matrices with varying degrees of Hermiticity and Antihermiticity. To that end, random (DxD)-matrices R are sampled with real part and imaginary part of each matrix element r_{nm} from a uniform distribution on the interval $[-1, 1]$. The uniform distribution is chosen to avoid extremely large matrix elements. The Hermiticity of the matrix M is controlled by the transformation

$$M := (1-\alpha)(R + R^\dagger) + \alpha(R - R^\dagger) = R + (1-2\alpha)R^\dagger \tag{5.7.57}$$

with the crossover ratio α. For $\alpha = 0$, the matrix M is Hermitian and for $\alpha = 1$ it is Antihermitian. One can choose $\alpha \in [0, 1]$ to select how close M is to the

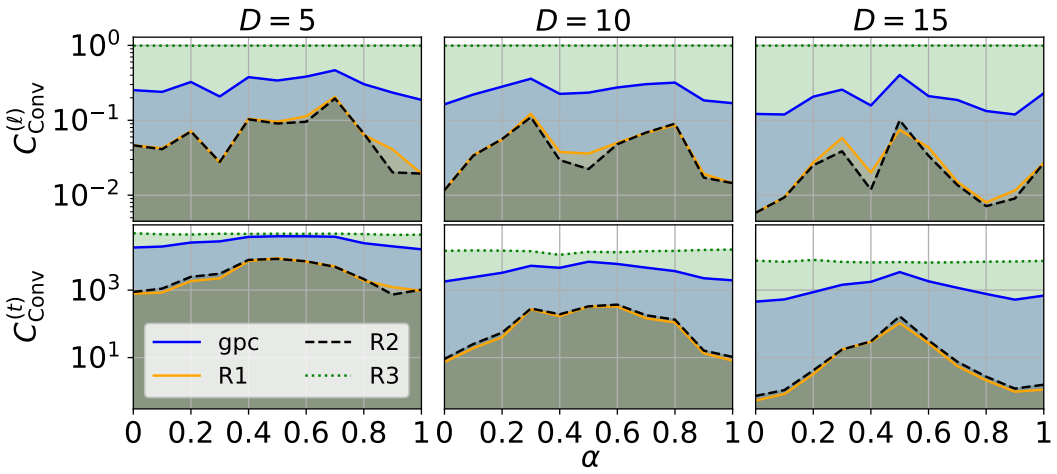

Figure 5.5: Convergence coefficients for ℓ-dependent (first row) and time-dependent (second row) flow of D-dimensional random matrices (5.7.57) for various crossover ratios α averaged over 100 samples. The flow induced by the gpc-generator is compared to the flows induced by the R1-, R2- and R3-generator. The dimension D is specified at the top of each column.

(Anti-)Hermitian case. We sample non-Hermitian matrices for various values of α.

5.7.2.2 Convergence Speed

We show the convergence coefficients in Fig. 5.5, averaged over 100 samples of random matrices for each value of α. We use the same samples for all four generators to ensure a fair comparison. The bottom row displays the coefficients $C^{(t)}_{\mathrm{Conv}}$ for the ROD(t) in real time and each column shows results for a different system size D. A larger coefficient is favorable, as it stands for faster convergence. For completeness sake, the top row also shows $C^{(\ell)}_{\mathrm{Conv}}$ for the ROD(ℓ), even though we established in Sec. 5.7.1.1 that it is not a reliable measure of convergence speed.

We first examine the results $C^{(\ell)}_{\mathrm{Conv}}$ in the top row. The R3-generator has a constant $C^{(\ell)}_{\mathrm{Conv}} = 1$, which is expected since it does not scale with energy differences ΔE. The generators R1 and R2 share a similar convergence coefficient with one another, because have share the same quadratic energy dependence. It is interesting to see that the convergence coefficient of the gpc-generator, which has a quadratic energy dependence, correlates strongly with the R1- and R2-coefficients. This is due to the fact that all three renormalizing generators depend on energy differences, albeit in different powers. If a matrix features near-degeneracy, all renormalizing flows are slowed down. Note that the convergence coefficients of the generators cannot be compared with one another quantitatively because of the different energy scales, as we discussed in Sec. 5.7.1.1 .

To compare the convergence speeds quantitatively, we examine the more reliable $C^{(t)}_{\mathrm{Conv}}$ in the bottom row of Fig. 5.5. We see that the R2- and R3-generators converge

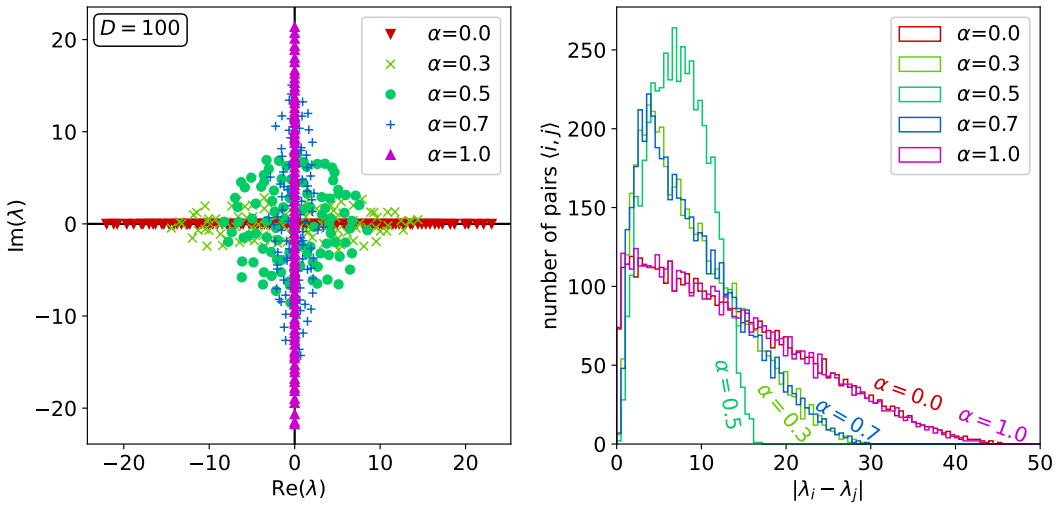

Figure 5.6: Left: Spectrum of a 100-dimensional random matrix (5.7.57) for various crossover ratios α. Right: Histogram of the distances between pairs of eigenvalues, calculated with 100 bins on the interval $[0, 50]$.

very slowly. Rapid convergence is achieved by the R3-generator and, close behind, the gpc-generator. Furthermore, we see that the renormalizing flows (gpc, R1 and R2) converge quickest at $\alpha \approx 0.5$ and slowest at $\alpha \in \{0, 1\}$. This is connected to the shape of the spectrum of eigenvalues. The sampling step (5.7.57), which combines R and $R^\dagger$ to achieve a crossover ratio α, causes the eigenvalues to be randomly distributed on a two-dimensional sphere. The width and height of this sphere are determined by α. For $\alpha = 0.5$ it is circular and for $\alpha \in \{0, 1\}$ it is compressed on a straight line on either the real or imaginary axis. In the latter cases, the diagonal elements stay on the same axis during the whole flow. Because they cannot leave this one-dimensional line, the chance of near-degeneracy increases, which slows down the renormalizing flow considerably.

We illustrate this in Fig. 5.6, which shows the spectrum $\{\lambda_i\}$ and a histogram of the distances $|\lambda_i - \lambda_j|$ between pairs of eigenvalues. The histogram shows a distribution of distances that is narrower for $\alpha \approx 0.5$. For $\alpha \approx 0$ and $\alpha \approx 1$, the maximum distance $|\lambda_i - \lambda_j|$ increases. The off-diagonal elements connecting these eigenvalues are rotated away by the renormalizing generators very quickly. The different shape of the histograms is a consequence of the spherical spectrum with width and height depending on α. More importantly, matrices M with $\alpha \approx 0$ and $\alpha \approx 1$ feature more extremely small differences $|\lambda_i - \lambda_j| \approx 0$ and therefore more off-diagonal elements that are rotated away very slowly. These slowly-rotating off-diagonal elements slow down the flow and dominate the asymptotic behavior. This causes the flows for matrices close to $\alpha \approx 0$ and $\alpha \approx 1$ to converge slowly.
Note that this observation is favorable for the renormalizing generators. The disadvantage of renormalizing flows is the fact that not all matrix elements are treated at

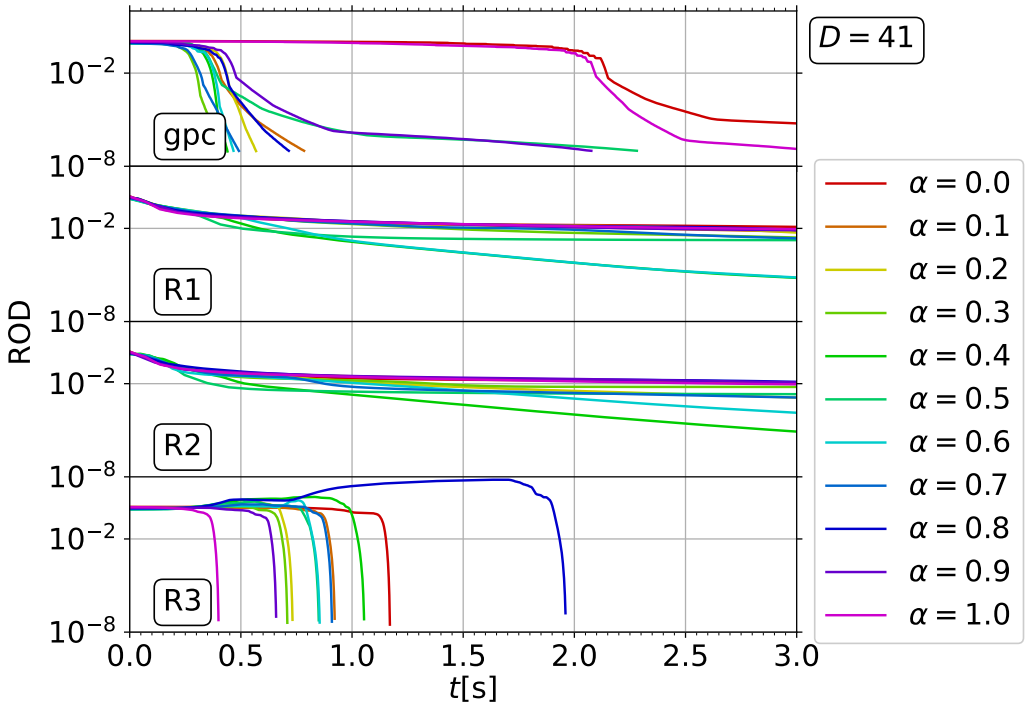

Figure 5.7: ROD flow vs. time for D-dimensional random matrices (5.7.57) and various crossover ratios α. The flow induced by the gpc-generator is compared to the flows induced by the R1-, R2- and R3-generator.

the same speed, which increases computation time. This is already well-known for Hermitian matrices. The fact that complex eigenvalues are less likely to approach degeneracy mitigates this increase of computation time.

By inspecting the panels in Fig. 5.5 from left to right, we see that both convergence coefficients $C^{(t)}_{\mathrm{Conv}}$ and $C^{(\ell)}_{\mathrm{Conv}}$ decrease with increasing matrix dimension D. This makes sense for $C^{(t)}_{\mathrm{Conv}}$, because a larger matrix requires a larger system of differential equations to be solved. For $C^{(\ell)}_{\mathrm{Conv}}$, we only see a decrease with D for the renormalizing generators gpc, R1 and R2. This can be explained by the fact that with increasing D it becomes more likely for initial diagonal elements $m_{nn}(0)$ to be close to each other, since they are restricted to the region $[-1,1]^2 \in \mathbb{C}^2$. This can slow down the flow in ℓ, especially in the initial phase. This effect should weaken as the flow proceeds, because the final spectrum $m_{nn}(\infty)$ is not restricted to $[-1,1]^2 \in \mathbb{C}^2$, but is actually spherical and its radius scales linearly with D. For the R3-generator, the coefficient $C^{(\ell)}_{\mathrm{Conv}} = 1$ does not change with D, because the asymptotic convergence of the R3-flow always takes the form $\exp(-\ell)$.

We show the full flow of $\mathrm{ROD}(t)$ for exemplary matrix samples in Fig. 5.7. Both the gpc-flow and the R3-flow exhibit a transient behavior at the beginning, where the ROD only decreases slowly, before rapid convergence begins. For the gpc-generator, this transient phase is longest for $\alpha \in \{0,1\}$, the two cases where the eigenvalues are

distributed on a straight line. For the R3-generator, it is especially noteworthy that the ROD can increase significantly during this transient phase. This is a consequence of the fact that the R3-generator is not renormalizing. Off-diagonal elements can be renormalized and reorganized significantly by the R3-flow, leading to a temporary increase of the ROD. This effect is relevant for the discussion of the truncation error, see below.

To conclude, the R3-generator offers the best convergence speed for the random matrices (5.7.57) with the gpc-generator close behind. The R1- and R2-flow convergence extremely slowly.

5.7.2.3 Truncation Error

The benchmark in the previous section shows rapid convergence of the R3-flow and slower but still fast convergence of the gpc-flow. Since flow equations are generally used in combination with truncations, rapid convergence is only desirable if it is not tied to large trunation errors. Renormalizing generators are commonly better at reducing the truncation error, which we confirm in this section.

To cover a large variety of matrices, we use two different models that are based on the random matrices from the previous section. The first model is an **unordered truncated random matrix**, which is sampled using (5.7.57) and then rescaled $m_{nj,\,\mathrm{prep}} = \lambda^{|n-j|} m_{nj}$ and truncated to diagonal width $n_{\max}$, see Sec. 5.7.1.2 . Renormalizing generators perform better when the diagonal elements and the spectrum are ordered. Ordering complex values is not trivial, but can potentially increase the accuracy of renormalizing generators. For this reason, we introduce a second model, the **ordered truncated random matrix**. We sample this model the same way as the unordered truncated random matrix, but then replace the diagonal elements with

$$m_{00,\mathrm{ordered}} = \exp\left(\mathrm{i}\frac{\alpha\pi}{2}\right) r_0\,, \tag{5.7.58a}$$

$$m_{nn,\mathrm{ordered}} = m_{n-1,n-1,\mathrm{ordered}} + \exp\left(\mathrm{i}\frac{\alpha\pi}{2}\right) r_n \quad \forall n \in \{1,2,...,D\}\,, \tag{5.7.58b}$$

where r_n are real random numbers sampled from a uniform distribution on $[0,1]$. Note that α is the crossover ratio, see (5.7.57), and that the off-diagonal elements are not changed by the ordering (5.7.58). By defining the ordered truncated random matrix in this way, all diagonal elements are placed on a straight line in the complex plane and the distances of neighboring eigenvalues fluctuate on the interval $[0,1]$. In Fig. 5.8 we show exemplary diagonal elements of ordered truncated random matrices in the left panel and the corresponding eigenvalues in the right panel. While the spectrum does not form a perfect line because of the random off-diagonal elements m_{nj}, both the spectrum and the diagonals are ordered to a great extent.

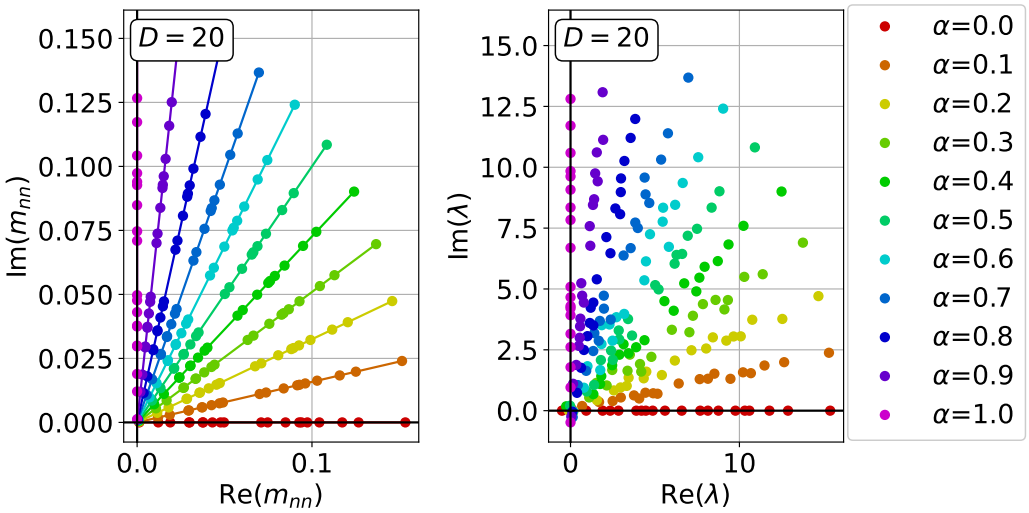

Figure 5.8: Representative diagonal elements (left) and eigenvalues (right) of the sorted truncated random matrices (5.7.58).

The truncation errors Δ_{trunc} in order o1, o2 and o3 are shown in Fig. 5.9. The top row displays the results for the unordered truncated matrix. We see that the errors are similar for different generators, but the R3-generator generally performs slightly worse than the renormalizing generators. For some individual sampled matrices, the gpc-generator shows a significantly smaller error than the other generators, but this does not show up as a significant effect in the averaged data presented in the figure.

For the ordered model displayed in the bottom row, the difference between the generators are more pronounced. For a small expansion parameter $\lambda = 0.1$, the gpc-generator clearly shows the highest accuracy, while the R1- and R2-generator perform only slightly better than the R3-generator. The R3-generator has the highest truncation error, which is a tradeoff for the high convergence speed achieved by treating all matrix elements simultaneously at the same speed. While this reduces computation time, it introduces significant renormalizations of the truncated off-diagonal elements far from the diagonal. The initially rising ROD in Fig. 5.7 is a strong indicator for these major reorderings happening in the off-diagonal elements. The renormalizing generators tackle this problem by treating off-diagonals connecting large energy differences first, but surprisingly only the gpc-generator decreases the truncation error significantly. Since the gpc-generator is a generalization of the pc-generator and the latter conserves diagonal width, it is possible that the gpc-generator is especially robust against truncation errors, even more than the R1- and R2-generators.

For larger $\lambda = 0.5$, i.e. a weaker downscaling $\lambda^{|n-j|}$ of the off-diagonals m_{nj}, the differences between the generators are less noticeable. A possible explanation is the fact that larger off-diagonals lead to more reordering, i.e. points of the flow

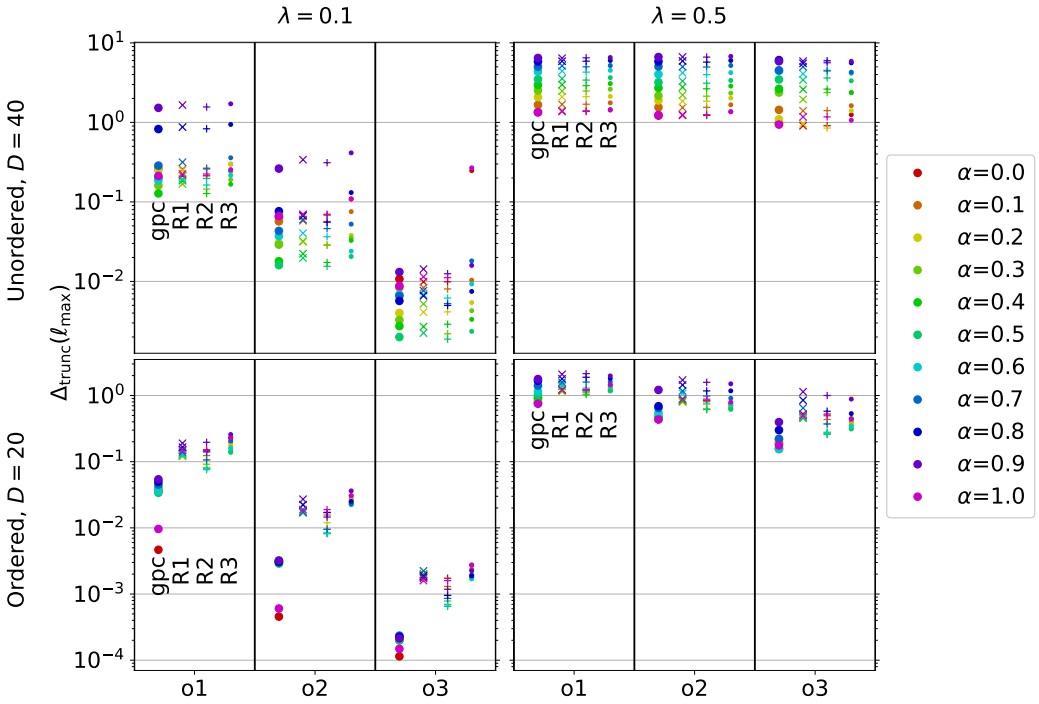

Figure 5.9: Truncation error $\Delta_{\text{trunc}}(\ell_{\text{max}})$ between exact spectrum and flow equation results for the (un)ordered truncated random matrix (5.7.58), averaged over 100 samples. The top row shows results for unordered matrices M, the bottom row shows results for ordered matrices. The left column displays results for $\lambda = 0.1$, the right column does for $\lambda = 0.5$. The truncation order is denoted by (o1,o2,o3) for truncation in order (1,2,3).

where the diagonal elements are no longer ordered and hence the far off-diagonals are renormalized more strongly. If such reordering occurs, the renormalizing property of the gpc-, R1- and R2-generator can actually be detrimental, because the off-diagonals far away from the diagonal can become elements connecting small energy differences during the reordering. In that case, the renormalizing generators rotate these elements away last, after they are already renormalized significantly. In fact, the R1- and R2-errors sometimes exceed the R3-error. Despite this caveat, the gpc-generator reliably yields more accurate results than the three other generators.

Special attention should be given to the cases $\alpha = 0$ and $\alpha = 1$. In these cases, the gpc-generator is equivalent to the pc-generator (2.3.12) for $\alpha = 0$ or to the ipc-generator (5.3.13) for $\alpha = 1$, which both conserve the diagonal width. Naively, one could assume that this would lead to a vanishing truncation error, but we observe finite, albeit small, errors for $\alpha \in \{0, 1\}$ in Fig. 5.9. This can be explained by the fact that the diagonal elements do not stay ordered during the whole integration, i.e. the flows of two diagonal elements $m_{nn}(\ell)$ and $m_{jj}(\ell)$ can cross, effectively leading to a reordering of the basis.

To conclude this example, we note that the gpc-generator offers the highest ac-

curacy in spite of truncations. This advantage is much more distinct when the diagonal elements are ordered and when the off-diagonal elements are significantly smaller than the diagonal elements. Together with the high convergence speed discussed in the previous section, this confirms that the gpc-generator is a beneficial generator choice. The R3-generator suffers from the largest truncation errors, which is the cost of the high convergence speed.

5.7.3 Ordered Dissipative Scattering Model

While the benchmark in Sec. 5.7.2 revealed some important properties of the generators, we only considered random matrices with spherical- or line-shaped spectra. The spectra of real physical systems are often more complicated, so it stands to reason that the observations made in Sec. 5.7.2 cannot be generalized to such systems. For this reason, we examine the convergence speed and truncation errors for more realistic physical examples, specifically open quantum systems, in this and the following sections. The Lindblad formalism was introduced in Sec. 5.1 . In this section, we consider an open quantum system with a spectrum that is mostly ordered.

5.7.3.1 Physical Model

Consider a gas of spinless fermions in d dimensions restricted to a box of volume L^d. The system has a loss mechanism that is localized at $\mathbf{x} = 0$. The Lindblad master equations of this system read

$$\mathrm{i}\hbar\frac{\mathrm{d}}{\mathrm{d}t}\rho(t) = [H,\rho(t)] + \mathrm{i}\hbar\int \mathrm{d}\mathbf{x}\,\Gamma(\mathbf{x})\left(\Psi(\mathbf{x})\rho(t)\Psi^\dagger(\mathbf{x}) - \frac{1}{2}\left\{\Psi^\dagger(\mathbf{x})\Psi(\mathbf{x}),\rho(t)\right\}\right), \tag{5.7.59a}$$

$$\hat{H} = \sum_{\mathbf{k}} \epsilon_{\mathbf{k}}\hat{c}^\dagger_{\mathbf{k}}\hat{c}_{\mathbf{k}}, \quad \Gamma(\mathbf{x}) = \gamma\delta(\mathbf{x})\,. \tag{5.7.59b}$$

One can formulate the full master equations completely in momentum space

$$\mathrm{i}\hbar\frac{\mathrm{d}}{\mathrm{d}t}\rho(t) = \left[\sum_{\mathbf{k}}\epsilon_{\mathbf{k}}\hat{c}^\dagger_{\mathbf{k}}\hat{c}_{\mathbf{k}},\rho(t)\right] + \mathrm{i}\frac{\hbar\gamma}{L^d}\sum_{\mathbf{k},\mathbf{q}}\left(\hat{c}_{\mathbf{k}}\rho(t)\hat{c}^\dagger_{\mathbf{q}} - \frac{1}{2}\left\{\hat{c}^\dagger_{\mathbf{k}}\hat{c}_{\mathbf{q}},\rho(t)\right\}\right). \tag{5.7.60}$$

By applying the superfermion representation (5.6.36), one obtains

$$M' = \sum_{\mathbf{k}}\epsilon_{\mathbf{k}}\left(c^\dagger_{\mathbf{k}}c_{\mathbf{k}} + \tilde{c}_{\mathbf{k}}\tilde{c}^\dagger_{\mathbf{k}}\right) - \mathrm{i}\frac{\hbar\gamma}{2L^d}\sum_{\mathbf{k},\mathbf{q}}\left(c^\dagger_{\mathbf{k}}c_{\mathbf{q}} - \tilde{c}_{\mathbf{k}}\tilde{c}^\dagger_{\mathbf{q}}\right) - \frac{\hbar\gamma}{L^d}\sum_{\mathbf{k},\mathbf{q}}\tilde{c}_{\mathbf{k}}c_{\mathbf{q}} - \sum_{\mathbf{k}}\left(\epsilon(\mathbf{k}) + \mathrm{i}\frac{\hbar\gamma}{2L^d}\right). \tag{5.7.61}$$

This leads to a triangular block matrix

$$M' = \begin{pmatrix} H - \frac{\mathrm{i}\hbar}{2}\Lambda_1 & 0 \\ -\Lambda_1 & H + \frac{\mathrm{i}\hbar}{2}\Lambda_1 \end{pmatrix}, \tag{5.7.62a}$$

$$h_{nj} = \epsilon(\mathbf{k}_n)\delta_{nj}\,, \qquad (\Lambda_1)_{nj} = \frac{\hbar\gamma}{L^d} \quad \forall n,j\,, \tag{5.7.62b}$$

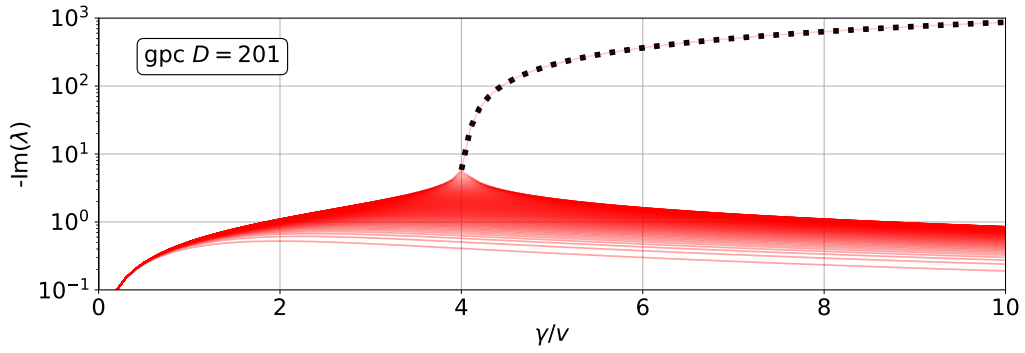

Figure 5.10: Eigenvalues of the ordered dissipative scattering model (5.7.63), calculated with the gpc-generator and dimension $D = 201$, i.e. $N = 100$. The eigenvalues are represented by transparent lines, and the eigenvalue of the strongly dissipative state for $\gamma \geq 4v$ is additionally marked by a dotted black line.

which allows one to narrow the problem down to finding the eigenvalues of the upper left block $H - \frac{\mathrm{i}\hbar}{2}\Lambda_1$. One can simplify the problem further by assuming a one-dimensional system with a linear dispersion $\epsilon(k)$. The final problem is described by the matrix

$$M = H - \frac{\mathrm{i}\hbar}{2}\Lambda_1\,, \qquad m_{nj} = \epsilon(k_n)\delta_{nj} - \mathrm{i}\frac{\hbar^2\gamma}{2L}\,, \tag{5.7.63a}$$

$$\epsilon(k_n) = \hbar v \frac{2\pi}{L} n \qquad \forall n \in [-N, -N+1, ..., N-1, N]\,, \tag{5.7.63b}$$

where an energy cutoff $|\epsilon| \leq \Lambda_N = \hbar v \frac{2\pi}{L} N$ is used so the matrix has finite dimension $D = 2N + 1$.

The imaginary, i.e. dissipative, components of the eigenvalues are plotted in Fig. 5.10. The results agree perfectly with prior findings [86]. For $\gamma > 4v$, the system exhibits a **strongly dissipative state**, denoted by the subscript 'sds', i.e. a dominant imaginary eigenvalue

$$\lambda_{\mathrm{sds}} = -\mathrm{i}\Lambda_N \tan\left(\frac{\pi}{2}\left(\frac{4v}{\gamma} - 1\right)\right) \qquad \forall \gamma > 4v \tag{5.7.64}$$

with $\lambda_{\mathrm{sds}} \gg \lambda_i$ for all other eigenvalues λ_i [86]. The strongly dissipative state decays much faster than all other states of the system.

5.7.3.2 Convergence Speed

Similar to the benchmark we performed for the previous model in Sec. 5.7.2 , we start with an analysis of the convergence speed. This time, we do not study the convergence coefficients, but rather focus solely on the flow of the ROD(ℓ), because the asymptotic convergence does not capture all relevant effects. Furthermore, we only benchmark the two most efficient generator, gpc and R3, because the R1- and

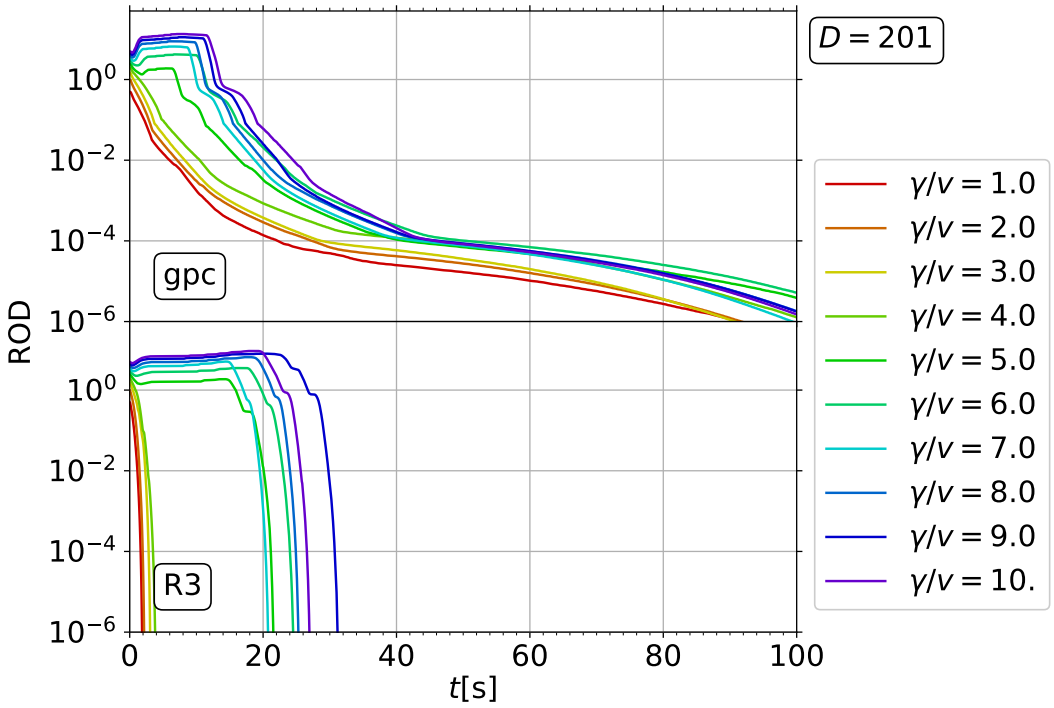

Figure 5.11: ROD flow of the ordered dissipative scattering model (5.7.63) of dimension $D = 201$, calculated with the gpc-generator and R3-generator.

R2-flows converge far too slowly for large system sizes. We choose the matrix size $D = 201$, which is achieved by choosing an energy cutoff with $N = 100$.

The results are plotted in Fig. 5.11. The R3-generators shows rapid convergence, as before, while the gpc-generator converges less quickly. Both generators suffer from a rising ROD in the initial transient for $\gamma > 4v$, i.e. in when γ is large enough for the strongly dissipative state to emerge. It is surprising that the renormalizing gpc-generator induces a temporarily increasing ROD as well but this suggests that the strongly dissipative state leads to major renormalizations for both generators. Nevertheless, the R3-generator sees a larger increase of computation time during this phase. The computation time increases because of the large initial changes in the off-diagonals, which requires a reduction of the step size $\Delta\ell$ in the integration algorithm to ascertain a small integration error.

Just like for random matrices, the R3-generator exhibits the best convergence speed of all four generators, but the computational cost increases in presence of the strongly dissipative state because of the initially rising ROD.

5.7.3.3 Truncation Error

The ordered dissipative scattering model (5.7.63) can provide a more realistic insight to the truncation error than the random matrices considered in Sec. 5.7.2 . We rescale the matrix elements $m_{nj,\text{prep}} = \lambda^{|n-j|} m_{nj}$ to ensure that off-diagonals

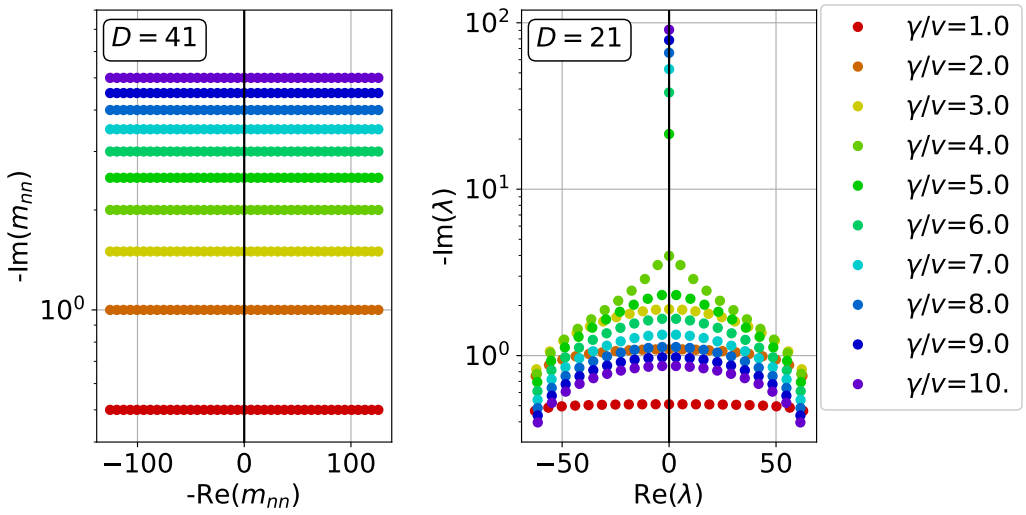

Figure 5.12: Representative diagonal elements (left) and spectra (right) of the ordered dissipative scattering model, see (5.7.63).

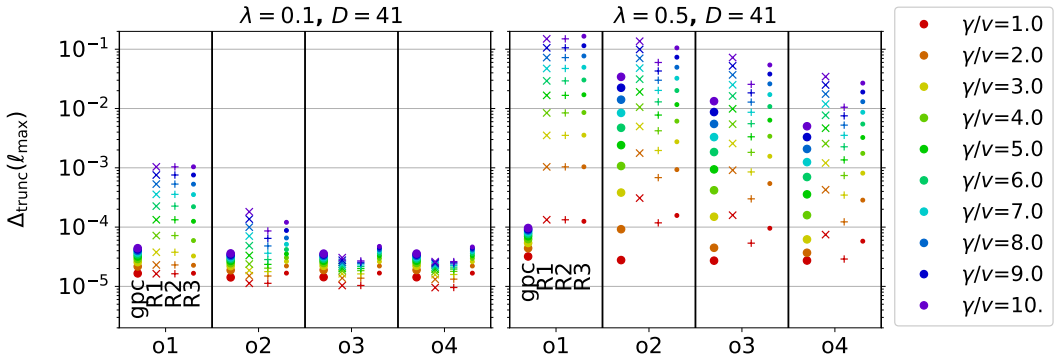

Figure 5.13: Truncation error $\Delta_{\text{trunc}}(\ell_{\text{max}})$ between the exact spectrum of the truncated matrix and the flow equation result for the ordered dissipative scattering model (5.7.63). The truncation order is denoted by (o1,o2,o3,o4) for truncation in order (1,2,3,4).

become less relevant with increasing distance to the diagonal, see Sec. 5.7.1.2 . We calculate the truncation error for all four generators. Since the diagonal elements of (5.7.63) are already ordered, we do not perform any subsequent ordering. In Fig. 5.12 we show that both the diagonal elements and spectrum of the ordered dissipative scattering model (5.7.63) are ordered. Aside from the strongly dissipative state, all eigenvalues lie on a one-dimensional curve in the complex plane. Note that the plot shows the spectrum of the full system without truncation. We expect such ordering to be advantageous for the renormalizing generators (gpc, R1 and R2).

The truncation error Δ_{trunc} is plotted in Fig. 5.13. The gpc-generator performs best out of all generators, especially in order o1. We stress that this is quite surprising, because we saw in Sec. 5.7.3.2 that the gpc-generator exhibits an initially rising ROD, just like the R3-generator. Since the gpc-generator is renormalizing, the increasing ROD mainly manifests in an increase of the off-diagonals which are

close to the diagonal, i.e. elements that are not truncated, while the R3-generator increases off-diagonals that are truncated, leading to a larger truncation error. This argument is supported by the fact that Δ_{trunc} increases with γ/v, i.e. it increases when the strongly dissipative state becomes more dominant, which correlates with a more pronounced initial increase of the ROD. Note that the excellent accuracy of the gpc-generator agrees with the properties summarized in Tab. 5.1, which places the gpc-generator between R2 and R3. Unlike the gpc-generator, the generators R1 and R2 provide less reliable results. In some cases they are slightly more accurate than the gpc-generator, but in most cases their accuracy is as bad as, or even worse than, the R3-generator's accuracy.

Note that it is not surprising that the truncation error Δ_{trunc} increases with the truncation order for the gpc-generator and a relatively large expansion parameter $\lambda = 0.5$. The additional matrix elements $m_{nj} = -\mathrm{i}\lambda^{|n-j|}\hbar^2\gamma/(2L)$ are not negligible for $\lambda = 0.5$ and lead to a more involved flow, implying a larger Δ_{trunc}. This effect was discussed in Sec. 5.7.1.2 and does not contradict the fact that in realistic applications, an increase of the truncation order normally increases accuracy.

To conclude, the gpc-generator clearly provides the highest accuracy for the ordered physical system (5.7.63). Surprisingly, the renormalizing R1- and R2-generators do not reliably offer better accuracy than the R3-generator.

5.7.4 Disordered Dissipative Scattering Model

The previous example provided a benchmark for a realistic open quantum system with ordering of the eigenvalues. In this section, we examine an open quantum system with an unordered spectrum, which is less favorable for the renormalizing generators gpc, R1 and R2.

5.7.4.1 Physical Model

We consider a fermionic disordered tight-binding model on a one-dimensional chain with periodic boundaries

$$\hat{H} = -J\sum_j \left[\hat{c}_j^\dagger \hat{c}_{j-1} + \text{h.c.}\right] + \sum_j h_j \hat{n}_j\,, \qquad h_j = \text{random}([-W, W])\,, \tag{5.7.65}$$

where the local site energies h_j are sampled from a uniform distribution and j denotes the lattice sites. We add a localized loss mechanism with loss rate γ at site 0 and obtain the Lindblad master equations

$$\mathrm{i}\hbar\frac{\mathrm{d}}{\mathrm{d}t}\hat{\rho}(t) = [\hat{H}, \hat{\rho}(t)] + \mathrm{i}\hbar\gamma\left(\hat{c}_0\rho(t)\hat{c}_0^\dagger - \frac{1}{2}\left\{\hat{n}_0, \rho(t)\right\}\right)\,. \tag{5.7.66}$$

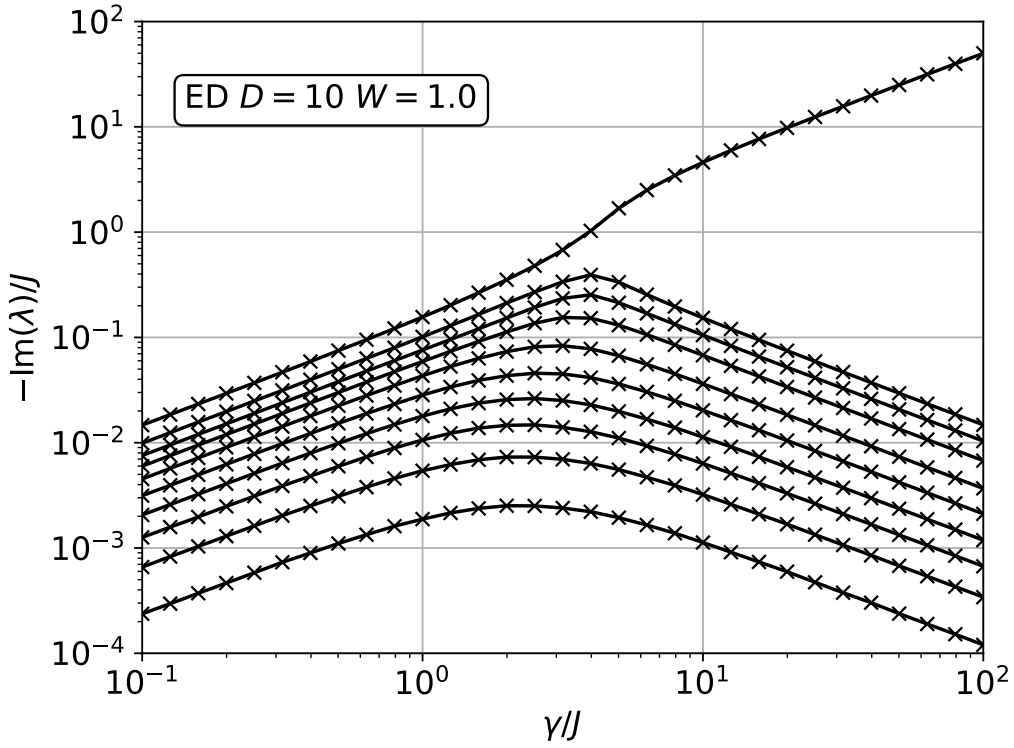

Figure 5.14: Imaginary parts of the eigenvalues of the disordered scattering model (5.7.67) with $N = 10$. The data for these plots was calculated using exact diagonalization and averaged over 100.000 disordered samples. One strongly dissipative state with a large imaginary part emerges for $\gamma \geq 4J$.

One can apply the superfermion representation (5.6.36) to obtain the matrix form (5.1.2) with $M = \mathcal{L}$ and matrix elements

$$m_{nn} = h_n - \mathrm{i}\frac{\hbar\gamma}{2}\delta_{n,0}\,, \tag{5.7.67a}$$

$$m_{nj} = -J(\delta_{n,j+1} + \delta_{n,j-1})\,. \tag{5.7.67b}$$

The definition of m_{nn} suggests that a large value of γ leads to a single strongly dissipative state, which has a large negative imaginary part, dominating all other imaginary parts of the spectrum. Indeed, just like for the ordered system (5.7.63), a strongly dissipative state emerges for $\gamma \geq 4J$, which we show in Fig. 5.14.

5.7.4.2 Convergence Speed

The flow of ROD(ℓ) for the two generators with the best convergence speed, gpc and R3, is plotted in Fig. 5.15. The data is averaged over 10 samples because the model (5.7.67) contains randomly sampled matrix elements. Surprisingly, the gpc-flow converges more quickly to $\mathrm{ROD}_{\mathrm{min}} = 10^{-8}$ than the R3-flow in most cases, although the R3-generator shows a rapid convergence after the intial transient, al-

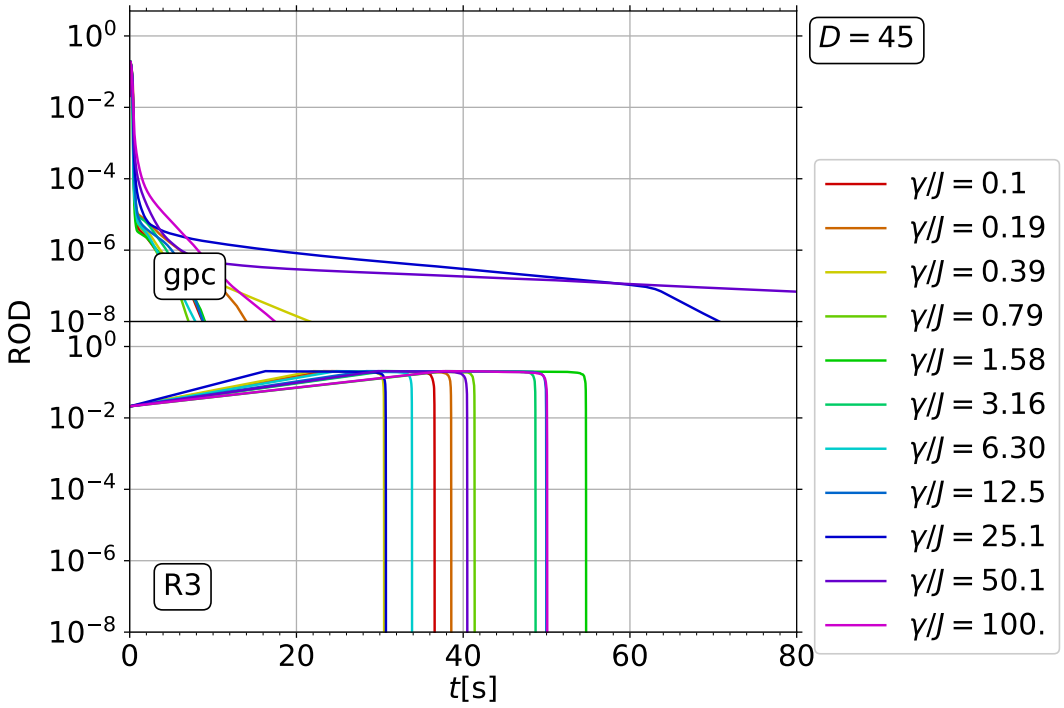

Figure 5.15: Exemplary ROD flow of the disordered dissipative scattering model (5.7.67), for $N = 45$ and $W = J$, calculated with the gpc-generator and R3-generator, averaged over 10 samples.

lowing for a quick calculation of even smaller RODs. An initial transient, which exhibits an increasing ROD and requires much computation time, only occurs in the R3-flow. As discussed for the previous models, this is connected to major reorderings of the off-diagonals. Contrary to the ordered system discussed in Sec. 5.7.3.2 , in the disordered system the initial transient of the R3-flow occurs even in absence of the strongly dissipative state. No initial transient is observed for the gpc-generator.
It is surprising that the gpc-generator converges more quickly than the R3-generator, since disorder is unfavorable for renormalizing generators. A possible explanation is the fact that in the ordered model the eigenvalues are close to each other (see Fig. 5.12), while they are spread out more randomly in the disordered model. This leads to larger 'energy' differences $|\Delta E|$, i.e. differences of pairs of diagonal elements, and faster asymptotic convergence $\exp(-|\Delta E|\,\ell)$ of the gpc-flow.

We conclude that the gpc-generator can surprisingly lead to faster converge than the R3-generator for the disordered model (5.7.67), despite the fact that disordering is unfavorable for a renormalizing generator such as the gpc-generator.

5.7.4.3 Truncation Error

The matrix (5.7.67) is already tridiagonal aside from the two furthest off-diagonal elements $m_{0,D-1} = m_{D-1,0} = -J/\mathrm{i}$, which are finite due to the periodic boundaries. Therefore, the diagonal width of the initial matrix $M(0)$ does not increase with the

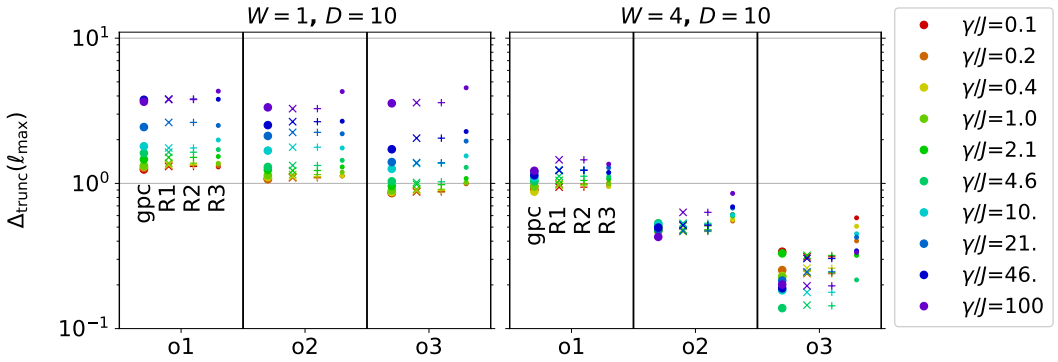

Figure 5.16: Truncation error $\Delta_{\mathrm{trunc}}(\ell_{\mathrm{max}})$ between exact spectrum and the flow equation result for the disordered dissipative scattering model (5.7.67), averaged over 100 samples. The truncation order is denoted by (o1,o2,o3) for truncation in order (1,2,3).

truncation order, unlike the models discussed previously. For this reason, it is not necessary to rescale the off-diagonals with a factor λ. We also refrain from sorting the matrix elements before solving the flow equations, since the aim of this section is to investigate the truncation error for a realistic disordered system.

The truncation error Δ_{trunc} is plotted in Fig. 5.16 for matrix dimension $D = 10$ and two different maximum spreads $W \in \{1, 4\}$ of the local site energies h_n. In all cases, the truncation error $\Delta_{\mathrm{trunc}} \in [10^{-1}, 10^{1}]$ is quite large for all generators in the orders used here. The large errors are a result of the disordered energies, since they cause even the renormalizing generator to significantly renormalize off-diagonals inside the truncated zone, i.e. far from the diagonal. High accuracy can only be achieved in higher truncation orders.

The gpc-generator shows the highest accuracy in most cases, but the R1- and R2-generator also perform well for $W = 4$. At first, this is surprising, because the results for unordered random matrices in Sec. 5.7.2.3 suggest that the truncation error of those two generators is similar to the R3-error for unordered matrices. However, note the different scales of the errors in Fig. 5.9 and Fig. 5.16. The increase in accuracy of the R1- and R2-generator compared to the R3-generator is similar for both models, but appears less pronounced in Fig. 5.9 because that plot covers a wider range of values of Δ_{trunc}.

This benchmark shows that the renormalizing generators still provide higher accuracy than the R3-generator, even for a realistic disordered system. The gpc-generator provides the highest accuracy, but by a narrower margin than for the previous examples.

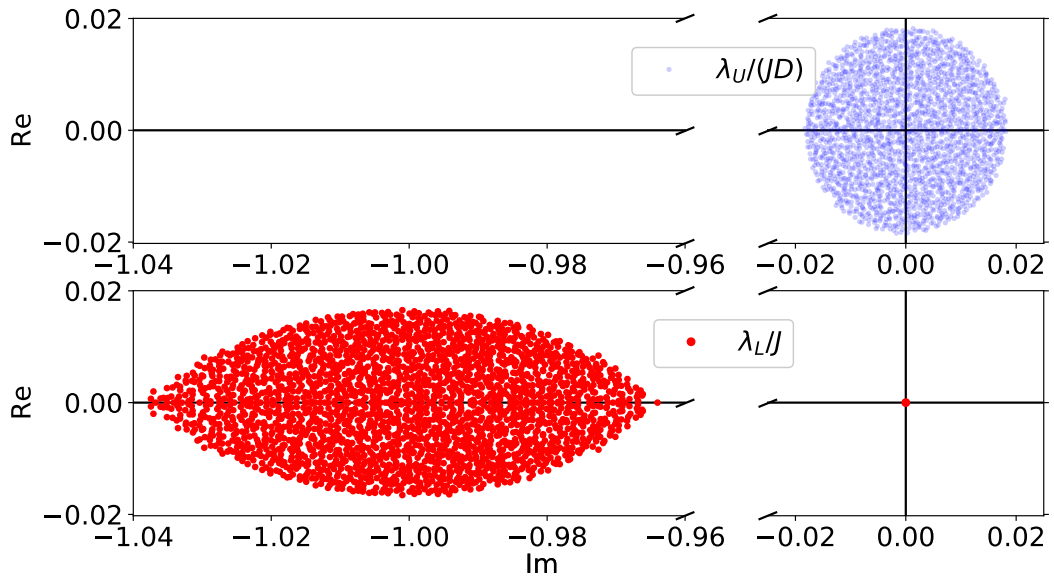

Figure 5.17: Top: Circular spectrum $\{\lambda_U\}$ of a matrix with uniformly random complex elements sampled with (5.7.57) for $\alpha = 0.5$ and dimension $D = 2000$. The spectrum is normalized to the matrix dimension D and energy scale J. Bottom: Spectrum $\{\lambda_L\}$ of a random Lindbladian (5.7.69), normalized to the energy scale J. The Lindbladian is sampled with $N = 50$ states, yielding $D = N^2 = 2500$ eigenvalues. The spectrum consists of a single stationary state $\lambda_L = 0$ and a lemon-shaped cluster around $-\mathrm{i}$.

5.7.5 Random Lindbladians

In Sec. 5.7.2 we sampled random non-Hermitian matrices to examine the flow for various matrices. In Sec. 5.7.3 we considered a physical open quantum system with ordered energies and in Sec. 5.7.4 we examined an open quantum system with disordered energies. Now, we want to combine the idea sampling random matrices with more realistic open quantum systems by sampling random Lindbladians, because the Lindblad master equations (5.1.1) is the most general Markovian description of open quantum systems. Sampling of realistic Lindbladians is still a subject of current studies [157]. The aim is to benchmark the convergence speed for a variety of Lindbladian systems.

5.7.5.1 Matrix Generation

First, we illustrate why the random matrices (5.7.57) used in the first numerical benchmark do not represent realistic Lindbladians. To this end, we examine the spectrum of random matrices with $\alpha = 0.5$, which corresponds to $M = R$, i.e. all elements have real and imaginary parts drawn from a uniform distribution on the interval $[-1, 1]$. In the top panel of Fig. 5.17 we see that the spectrum is circular and centered at 0 and the radius scales with the matrix dimension D. Note that half of the eigenvalues have a positive imaginary part, which is unphysical for a Lindbladian, since it corresponds to exponentially increasing solutions in (5.1.2). In contrast, the Lindbladians discussed in this section have a spectrum that is shown in

the bottom panel of Fig. 5.17. A single stationary state with $\lambda = 0$ exists alongside a lemon-shaped cluster of dissipative states around $-\mathrm{i}$. A detailed discussion of random Linbladians can be found in Ref. [158].

For the sampling process, we use the Gorini-Kossakowski-Sudarshan-Lindblad form [159, 160]

$$\mathcal{L}(\rho) = [H, \rho] + \mathcal{L}_D(\rho) = \mathcal{L}_U(\rho) + \mathcal{L}_D(\rho) \ . \tag{5.7.68}$$

For the sake of the benchmark, we neglect the unitary part $L_U(\rho)$ and focus on sampling only the dissipative part

$$\mathcal{L}_D(\rho) = \mathrm{i}\hbar \sum_{m,n=1}^{N^2-1} K_{mn} \left[F_n \rho F_m^\dagger - \frac{1}{2} \left(F_m^\dagger F_n \rho + \rho F_m^\dagger F_n \right) \right] \tag{5.7.69}$$

of dimension $N^2 \times N^2$. The traceless matrices $\{F_n\}$, $n = 1, 2, ..., N^2 - 1$ form an orthonormal Hilbert-Schmidt basis in Fock-Liouville space with $\mathrm{Tr}(F_n) = 0$ and $\mathrm{Tr}(F_n F_m^\dagger) = \delta_{n,m}$, while K is a positive semidefinite, complex Kossakowski matrix. Since the spectral features of the random Lindbladians are universal, the particular method for sampling the Kossakowski matrix does not matter. We sample $\mathcal{L}_D(\rho)$ in the following way, which is based on the method discussed in Ref. [158]:

1. Before staring the sampling process, we set up the orthonormal, traceless Hilbert-Schmidt basis of $N \times N$-dimensional matrices $\{F_n\}$, $n = 1, 2, ..., N^2 - 1$ with the $N^2 - 1$ Hermitian generators of SU(N) [161]. The basis consists of

$$\frac{N(N-1)}{2} \text{ symmetric matrices } S_{jk} = \frac{1}{\sqrt{2}} \left(|j\rangle\langle k| + |k\rangle\langle j| \right) , \tag{5.7.70a}$$

$$\frac{N(N-1)}{2} \text{ antisymmetric matrices } J_{jk} = -\frac{\mathrm{i}}{\sqrt{2}} \left(|j\rangle\langle k| - |k\rangle\langle j| \right) , \tag{5.7.70b}$$

$$N-1 \text{ diagonal matrices } D_l = \frac{1}{\sqrt{l(l+1)}} \left(\sum_{n=1}^{l} |n\rangle\langle n| - l|l+1\rangle\langle l+1| \right) \tag{5.7.70c}$$

$$\text{with } j, k \in \{1, 2, ..., N\} \text{ and } l \in \{1, 2, ..., N-1\} .$$

   For $N = 2$, one obtains the famous Pauli matrices and for $N = 3$ the standard eight Gell-Mann matrices.

2. For each sample of a random Lindbladian, we compute a $(N \times N)$-dimensional complex square Ginibre matrix G. The real and imaginary parts of the matrix elements g_{nm} of G are sampled from a normal distribution with expectation value $\mu = 0$ and standard deviation $\sigma = 1/\sqrt{2N}$. Using G, the complex square Wishart matrix W and the Kossakowski matrix K are computed

$$W = GG^\dagger \geq 0 \, , \tag{5.7.71}$$

$$K = \frac{NW}{\mathrm{Tr}(W)} \, . \tag{5.7.72}$$

3. To obtain a matrix representation of $\mathcal{L}_D(\rho)$, one can choose an arbitrary basis $\{B_n\}_n$ with $n \in \{1, 2, ..., N^2\}$ of density matrices ρ in Fock-Liouville space. For simplicity, we choose the N^2 matrices B_n which have a single finite element 1, and compute the Lindbladian supermatrix elements m_{nm} using the relation

$$\mathcal{L}_D[B_j] = \sum_n m_{nj} B_n \,. \tag{5.7.73}$$

In principle, we apply the Lindbladian on each basis state $B_j \, \forall j \in \{1, 2, ..., N^2\}$ and express the results in the basis $\{B_n\}_n$ to obtain all m_{nm}. Our basis choice makes it trivial to express the results $L_D[B_j]$ in the basis $\{B_n\}_n$. After computing all elements m_{nj}, we obtain the $(N^2 \times N^2)$-dimensional supermatrix representation M of $\mathcal{L}_D(\rho)$.

The process of sampling random Lindbladians and calculating their matrix representation is computationally expensive and scales with $\mathcal{O}(N^7)$ in the worst case, i.e. if the matrix multiplications scale with $\mathcal{O}(N^3)$. One can see this in (5.7.69), where the summation over m and n are of order $\mathcal{O}(N^2)$, respectively, and the matrix product of the $(N \times N)$-dimensional matrices is of order $\mathcal{O}(N^3)$. For sparse matrices, such as F_n and ρ, matrix products can often be calculated more efficiently, so the overall scaling can be slightly better, i.e. $\mathcal{O}(N^\alpha)$ with non-integer scaling dimension $\alpha \in [6, 7]$. To reduce computation time, we use the sparse matrix representation of the Eigen library for C++ [136] and calculate all possible products $F_n\rho$ and $\rho F_m^\dagger$ only once, outside of the innermost loop. Using all these optimizations, the computation time for the sampling process is negligible compared to the time necessary for integration the flow equations.

5.7.5.2 Convergence Speed

Fig. 5.18 shows the flow of ROD(ℓ) for all four considered generators and two exemplary Lindbladians of dimension $D = 100$ and $D = 400$, respectively. In both cases, the R1- and R2-generator induce an extremely slow convergence. This coincides with the convergence speed for other models and the fact that the asymptotic scaling with $|\Delta E|^2$ can reduce convergence speed significantly if many eigenvalues with near-degeneracy exist. Recalling Fig. 5.17, the radius of the spectrum of the random Lindbladians (5.7.69) does not scale with D, unlike the spectrum of random matrices (5.7.57). Therefore, the amount of nearly-degenerate eigenvalues increases with D, exacerbating this problem. It is surprising to see that even tough the gpc-generator is also renomalizing, its $|\Delta E|$-scaling does not inhibit rapid convergence. Instead, the gpc-generator shows fast convergence despite an initial transient with a temporarily rising ROD.

Recalling the results for previous models, one would expect the R3-generator, which does not depend on energy differences, to show the rapid convergence for

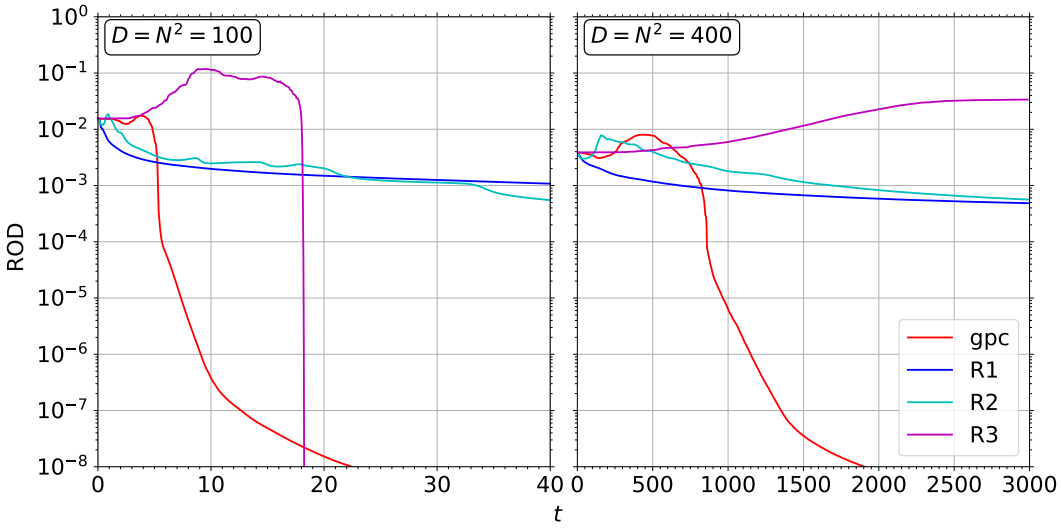

Figure 5.18: ROD flow of Random Lindbladians (5.7.69) with $D = N^2 = 100$ (left) and $D = N^2 = 400$ (right) eigenvalues, calculated with the gpc-generator, R1-, R2- and R3-generator.

random Lindbladians as well. For $D = 100$ (left panel of Fig. 5.18), this is true. The ROD rises during the initial transient, which costs significant computation time, but finally converges to 0 rapidly and overtakes the rapid convergence of the gpc-generator. For larger system sizes, however, the R3-generator no longer induces rapid convergence. In fact, we do not observe convergence of the R3-flow over the course of the computation time, anymore. One such example, $D = 400$, is depicted in the right panel of Fig. 5.18. While the gpc-flow converges nicely for $D = 400$, the R3-flow does not converge at any point during a calculation up to $t = 150000\,\mathrm{s}$ (not shown). Instead, the ROD increases during the computed R3-flow.

For all system sizes D, i.e. even when the R3-flow converges, the ROD-increase during the initial transient of the R3-flow is significantly greater than the ROD-increase observed during the gpc-flow. A possible explanation is the denominator $m_{nn} - m_{jj}$ appearing in the R3-generator (5.5.18c). While the generator does not explicitly scale with energy differences, near-degeneracies can still cause numerical problems, because the denominator is then numerically close to 0. The generator avoids the singularity by defining $\eta_{nj}^{\mathrm{R3}} = 0$ for $m_{nn} - m_{jj} = 0$, but the distinctive discontinuity and large generator elements for $m_{nn} - m_{jj} \approx 0$ remain. We tackle the problem with a cutoff $\eta_{nj}^{\mathrm{R3}} = 0$ for $|m_{nn} - m_{jj}| < 10^{-10}$, but the results for large D suggest that the R3-generator can still be numerically unstable.

To conclude, the R3-flow converges slightly faster than the gpc-flow for random Lindbladians of small size, but for larger system sizes the R3-generators does not converge in our calculations. The gpc-generator appears more robust against numerical instabilities caused by near-degeneracy and still provides fast convergence.

5.8 Concluding Comparison of Dissipative Generators

Understanding open quantum systems, i.e. quantum systems in interaction with a dissipative bath, is crucial for the theoretical description of novel physics. Important application areas are non-equilibrium physics, pump-probe experiments and quantum information processing. Lindblad master equations provide the most general description for Markovian baths and feature non-Hermitian matrices, which cannot be treated with continuous unitary transformations. They can, however, be treated with dissipative flow equations, which require generalizations of existing generator schemes. We cannot overemphasize that truncations are the critical issue of flow equations, since simple systems which are tractable without any truncation can also be solved by other methods. Therefore, an appropriate generator scheme must offer a good compromise between two orthogonal requirements: (i) rapid convergence to allow the treatment of complicated systems and (ii) accuracy in spite of truncations to capture the physics correctly. Renormalizing generators like the pc-generator provide such a compromise, because they treat high-energy excitations before low-energy excitations. This causes less flow into truncated matrix elements and therefore reduces truncation errors significantly, but increases computation time. Previous works in the field of dissipative flow equations have focused solely on convergence speed [86].

We introduced a generalization of the pc-generator, the gpc-generator, for dissipative flow equations. In the special cases of Hermitian and Antihermitian matrices, this generator is equivalent to the pc-generator and ipc-generator. We presented a perturbative proof that the gpc-generator converges for any non-Hermitian matrix. Unlike the pc-generator, however, the gpc-generator does not preserve the diagonal width, except for the very limited class of complex-sorted matrices. We compared the gpc-flow with the flows for the R-generators introduced in Ref. [86]. Furthermore, we introduced the generator scheme $\eta^{(r)}$, which is generalized even further and encapsulates three of four dissipative generators: $\eta^{(1)} = \eta^{\mathrm{R2}}$, which has a quadratic energy dependence and suffers from extremely slow convergence speed, the non-renormalizing generator $\eta^{(-1)} = \eta^{\mathrm{R3}}$ which has excellent convergence speed at the cost of large truncation errors and our proposed generator $\eta^{(0)} = \eta^{\mathrm{gpc}}$, which has a linear energy dependence and is placed between the other two.

We compared all four generators analytically and benchmarked the convergence speed and truncations errors numerically. The speed benchmark is based on real computation time, because the physical dimension of the flow parameter ℓ differs between the generators. The truncation error is quantified by the difference between the exact spectrum and the spectrum obtained via flow equations.
As expected, the R3-generator shows the highest convergence speed with the largest truncation errors, because it treats all matrix elements at the same time and speed.

Generator	$[\eta]$	$[\ell]$	Asymp. Convergence	Convergence Speed	Accuracy
R1, R2	E^2	$1/E^2$	$\exp[-\lvert\Delta E\rvert^2\,\ell]$	−	∼
gpc	E	$1/E$	$\exp[-\lvert\Delta E\rvert\,\ell]$	+	+
R3	1	1	$\exp[-\ell]$	++	−

Table 5.2: Results of the analytical analysis and numerical benchmark for the generators considered in this work. The dimension of η and ℓ are given in terms of the energy E and the asymptotic convergence in terms of the energy differences ΔE of the system. The convergence speed and the accuracy (in spite of truncation) are depicted by the symbol + for positive results, − for negative results and ∼ for mixed results.

The other three generators are renormalizing, and accordingly induce a less rapid convergence, but smaller truncation errors. As expected, the gpc-generator converges quicker than the R1- and R2-generators and is more robust against truncations than the R3-generator.
Surprisingly, the truncations errors induced by the gpc-generator are significantly smaller than the errors induced by the R1- and R2-generator in most cases. In the rare cases where R1 and R2 exhibit slightly smaller truncation errors, the fast convergence speed of the gpc-generator allows calculations in higher truncation orders, which provide higher accuracy. Therefore, our results suggest that gpc is always a better choice than R1 and R2.
Furthermore, we are surprised to find that the gpc-generator sometimes provides better convergence speed than the R3-generator. In particular, the R3-flow does not converge for large random Lindbladians, most likely due to numerical instability in presence of near-degeneracy, while the gpc-flow remains robust. This puts the excellent convergence speed of the R3-generator into perspective. The results for all generators are summarized in Tab. 5.2.

We conclude that the gpc-generator $\eta^{(0)} = \eta^{\mathrm{gpc}}$ surpasses all previously suggested generators in regards to the accuracy in spite of truncation. This exceeds the expectations made by choosing it to fill the gap between $\eta^{(1)} = \eta^{\mathrm{R2}}$ and $\eta^{(-1)} = \eta^{\mathrm{R3}}$. The R3-generator provides higher convergence speed, but the gpc-generator is more robust against truncation errors and near-degeneracy.
In the past, the pc-generator has been further developed with novel truncation and approximation schemes like the deepCUT approach [32,59], see Sec. 2.4.3 . We expect similar advances for the gpc-generator in future studies, which could provide even more powerful tools for open quantum system. In addition, the generator scheme $\eta^{(r)}$ could be investigated for other values of r. For instance, generators with non-integer values $r \in (-1, 0)$ or $r \in (0, 1)$ are promising candidates for efficient and robust flow equations, because they could fill the gap between η^{R3} and η^{gpc} and between η^{gpc} and η^{R2}, respectively.

Chapter 6

Final Conclusion and Outlook

The flow equation method, also known as CUT method, provides a powerful renormalization tool to obtain effective models, especially in low-energy physics. It improves traditional renormalization methods by not discarding high-energy processes completely. Instead, it takes care of processes spanning large energy differences first before going to processes spanning small energy differences. The method has been expanded considerably in the past, including various sophisticated truncation schemes and combinations with other methods such as Floquet theory.

In this thesis, we applied the flow equation method to describe novel physics and extended its scope. We began with the introduction of basic CUT concepts such as generator and truncation schemes in Chap. 2 . In the following chapters, we investigated flow equations in three different contexts.

In Chap. 3 , we introduced a Heisenberg spin-ladder system with triplon excitations and discussed various excitation channels for scattering experiments, specifically INS and RIXS. We argued that RIXS offers many promising prospects, such as probing of the SC channel, which is unavailable to INS measurements. Unfortunately, the prediction of RIXS results requires the calculation of spectral weights for more complicated observables. To find the most relevant observables in both the SC and NSC channel, we performed the UCL expansion and calculated the corresponding spectral weights in the two leading orders by using the deepCUT method, Lanczos tridiagonalization and the continued fraction expansion. The CUT method transforms the problem to an effective model with conserved triplons. We showed that the deepCUT method provides many advantages over other methods, such as (i) the computation of real continua instead of discretized eigenvalues, (ii) a high resolution of the spectral weights, (iii) results of remarkable accuracy, (iv) an effective Hamiltonian in the basis of the real elementary excitations that are a conserved quantity,

and (v) the ability to selectively turn off n-particle interactions. The last advantage turned out to be especially useful when we discovered a three-triplon bound state. By selectively turning off the three-triplon interactions, we were able to show that the three-triplon bound states occur only in presence of true three-triplon interactions. In contrast, most binding effect in nature are induced by two-body interactions. We proposed realistic physical systems to confirm our predictions experimentally with RIXS or THz spectroscopy.
This research can be extended in various ways. For instance, one could investigate higher orders of the UCL expansion or consider the cross terms that are neglected in our study. One could also apply the CUT method to compute the RIXS response for more sophisticated systems, e.g. coupled spin ladders or systems with more involved interactions such as the Dzyaloshinskii-Moriya-interaction proposed for the compound $BiCu_2PO_6$ [36]. Furthermore, one could investigate n-triplon bound states for $n > 3$ and assess whether triplon-strings arise in spin ladders, i.e. many-triplon bound states analogous to Bethe strings [121, 122].

In Chap. 4 we studied the TFIM, a spin-ladder model that hosts hard-core bosons. Close to the critical point, the correlation length diverges and truncation schemes that rely on the spatial extension fail to capture the physics. To tackle this challenge and track delocalized excitations, we introduced truncation schemes that are local in momentum space and therefore delocalized in real space. The new truncation schemes do not offer advantages for the TFIM at the current stage, but future works could study if similar truncation schemes prove useful in other settings. Furthermore, we analyzed the asymptotic convergence of the non-particle-conserving terms. Our computations show that the asymptotic convergence can be described by a small number of exponents that are connected trivially to the momenta of the operators. Because of the computational cost of calculating the flow equations for hard-core bosons in momentum space, only small systems with up to $N = 9$ sites were studied, so far. Future works could investigate whether these observations can be extended to larger systems and explore ways to utilize this finding. For instance, the flow equation method could be improved for effective low-energy models with small or vanishing gaps by vastly reducing the number of tracked coefficient.

In Chap. 5 we introduced dissipative flow equations, i.e. non-unitary flow equations that can be applied to non-Hermitian matrices. Such matrices occur in open quantum systems that are coupled to an external bath. As an important application field, we discussed Lindblad master equations, which provide the most general description of the Markovian dynamics of open quantum systems. We proposed the gpc-generator, which generalizes the famous pc-generator to non-Hermitian matrices, and discussed important properties of this novel generator. To this end, we compared it to previously suggested generator schemes for dissipative systems both

analytically and numerically by investigating various benchmark problems. Some of these problems are purely mathematical models, while others describe realistic physical systems with dissipation. A previous study [86] concerning dissipative flow equations focused only on the convergence speed, which is important to reduce computational cost and to tackle large systems. We explained that high accuracy despite truncation is an equally important requirement because truncations are ubiquitous in the field of flow equations and the physics of a system can only be captured correctly if the truncation error remains small. Moreover, we showed that previous generator schemes provide either excellent convergence speed or reasonable accuracy against truncations, but not both at the same time. Our proposed gpc-generator fills the gap between the existing schemes. It provides a good compromise of the desired properties and its performance in the numerical benchmarks even exceeds the expectations. Additionally, we introduced the more general dissipative generator scheme $\eta^{(r)}$, where the gpc-generator corresponds to the special case $r = 1$ and the other generators correspond to $r \in \{-1, 1\}$. This emphasizes that the gpc-generator can be understood as an intermediate choice between the other generators.
The field of dissipative flow equations is still in its infancy, but our results offer promising prospects for future research. While we focused on establishing the advantageous properties of the gpc-generator, keeping the application simple, future studies could apply it to more sophisticated open quantum systems. Furthermore, one could extend the scope of the gpc-generator by combining it with advances made previously for the pc-generator, such as the deepCUT scheme, where one performs a perturbative expansion in second quantization to decide which operator monomials should be tracked during the integration of the flow equations. Moreover, one could investigate the more general generator scheme $\eta^{(r)}$ for other values of r, i.e. non-integer values $r \in (-1, 0)$ or $r \in (0, 1)$.

In conclusion, we applied flow equations to calculate the response functions of RIXS measurements and predicted novel physics, specifically three-triplon bound states induced by irreducible three-triplon interactions arising in realistic Heisenberg spin ladders. Furthermore, we extended the scope of flow equations by proposing truncation schemes in momentum space and finding common asymptotic behavior, which could facilitate improvements of the flow equation method for gapless systems. Finally, we generalized the pc-generator to the gpc-generator, which can be applied to non-Hermitian matrices and dissipative systems, and showed that it has more advantageous properties than previously suggested generators.
The flow equation method, which was established in physics by Wegner in 1994 [4], has seen vast improvements and extensions in the past decades. Considering our findings in this thesis, it is obvious that the full scope of this method has not been exhausted yet and one can still await exciting future developments.

Appendix A

Ultra-Short Core-Hole Lifetime Expansion at Cu L_3-Edge

We approximate the indirect RIXS response for a Heisenberg spin ladder (3.1.1) in the ultra-short core-hole lifetime (UCL) expansion [47, 48, 50]. As its name suggests, the leading orders of the UCL expansion provide a good approximation of the full response if the core-hole lifetime $1/\Gamma$ of the intermediate state is much shorter than the timescales of the spin exchange couplings $1/J$ and the elementary excitations of the system. In the following, we derive the UCL expansion for the special case of the Cu L_3-edge, but an analogous calculation can be performed for different edges. The derivation presented here is based on the Kramers-Heisenberg formalism [50, 162], but the UCL expansion can also be derived with Green's functions [45].

In the Kramers-Heisenberg formalism, the response intensity is

$$I(\boldsymbol{q},\omega) \propto \sum_f \left| \langle f | D^\dagger_{\boldsymbol{k}_f} R D_{\boldsymbol{k}_i} | g \rangle \right|^2 \delta(\omega_f - \omega_g + \omega) \tag{A.1}$$

with the initial momentum $\boldsymbol{k}_i$ and final momentum $\boldsymbol{k}_f$ in the Fourier transformed dipole operators

$$D_{\boldsymbol{k}} = \sum_{i,\tau,\sigma} e^{\mathrm{i}\boldsymbol{k}\boldsymbol{R}_{i,\tau}} D_{i,\tau,\sigma} \tag{A.2}$$

for spins at rung i and leg τ with spin orientation $\sigma \in \{\uparrow, \downarrow\}$. The symbol R is the resolvent

$$R = \frac{1}{\omega - H_{\mathrm{UCL}} + \mathrm{i}\Gamma} = \sum_{|\nu\rangle} \frac{|\nu\rangle\langle\nu|}{\omega - \epsilon_n + \mathrm{i}\Gamma} \tag{A.3}$$

with the intermediate Hamiltonian

$$H_{\mathrm{UCL}} = \tilde{H} + H_{\mathrm{soc}}\,, \tag{A.4a}$$

$$\tilde{H} = H_0 + U_{\mathrm{C}} \sum_{i,\tau} n_{i,\tau} n^c_{i,\tau}\,, \tag{A.4b}$$

$$H_0 = J_{\mathrm{rung}} \sum_{i=1} \boldsymbol{S}_{i,1} \cdot \boldsymbol{S}_{i,2} + J_{\mathrm{leg}} \sum_{i,\tau=0,1} \boldsymbol{S}_{i,\tau} \cdot \boldsymbol{S}_{i+1,\tau}\,, \tag{A.4c}$$

$$H_{\mathrm{soc}} = \epsilon^{\alpha}_c \sum_{i,\tau,\alpha} n^c_{i,\tau,\alpha}\,. \tag{A.4d}$$

Here, $|\nu\rangle$ denotes the eigenstates of H_{UCL}, $n_{i,\tau}$ is the valence band occupation, $n^c_{i,\tau}$ the core-level occupation and U_{C} is the strength of the Coulomb interaction between these levels. The term H_{soc} represents the spin-orbit coupling in the core-level with $\alpha \in \{\mathrm{L}_2, \mathrm{L}_3\}$, i.e. it is necessary to differentiate between the energies for different total angular momenta $\boldsymbol{J} = \boldsymbol{L} + \boldsymbol{S}$ in the 2p-orbital, which are well separated for Cu atoms [50]. In the following, creation and annihilation operators describe the creation and annihilation of holes. Note that because of the short core-hole lifetime, (i) the dynamics on the intermediate state are limited, (ii) the core-hole potential can be treated as a local potential and (iii) the core-hole is immobile [45]. The strong Coulomb interaction U_{C} inhibits hoppings to the d-orbital in the intermediate state. With completely suppressed hopping, the intermediate state factorizes

$$|\nu\rangle = |n\rangle|n_c\rangle\,, \tag{A.5a}$$

$$H_{\mathrm{UCL}}|\nu\rangle = \epsilon_n|\nu\rangle\,, \tag{A.5b}$$

$$\tilde{H}|n\rangle = E_n|n\rangle\,, \tag{A.5c}$$

$$H_{\mathrm{soc}}|n_c\rangle = E_c|n_c\rangle\,. \tag{A.5d}$$

For this derivation, we focus on the L_3-edge with energy $E_c = E_{\mathrm{L}_3}$ and $|n_c\rangle = |\mathrm{L}_3\rangle$, but an analogous calculation can be performed for the L_2-edge. For the L_3-edge, the spectral composition of the resolvent is

$$R = |\mathrm{L}_3\rangle\langle\mathrm{L}_3| \sum_{|n\rangle} \frac{|n\rangle\langle n|}{\omega - E_n - E_{\mathrm{L}_3} + \mathrm{i}\Gamma} \tag{A.6a}$$

$$= |\mathrm{L}_3\rangle\langle\mathrm{L}_3| \frac{1}{\Delta - \tilde{H} + \mathrm{i}\Gamma} \tag{A.6b}$$

$$= |\mathrm{L}_3\rangle\langle\mathrm{L}_3| \frac{1}{\Delta + \mathrm{i}\Gamma} \sum_{l=0}^{\infty} \left(\frac{\tilde{H}}{\Delta + \mathrm{i}\Gamma} \right)^l \tag{A.6c}$$

with the difference $\Delta := \omega - E_{\mathrm{L}_3}$ between transferred energy and the energy of the edge. At resonance $\Delta \to 0$, one obtains

$$R = |\mathrm{L}_3\rangle\langle\mathrm{L}_3| \frac{1}{\mathrm{i}\Gamma} \sum_{l=0}^{\infty} \left(\frac{\tilde{H}}{\mathrm{i}\Gamma} \right)^l . \tag{A.7}$$

The dipole operator for the 2p→3d process at the Cu L_3-edge is

$$D_{i,\tau,\sigma} = \sum_{\alpha} d_{i,\tau,\sigma} p^{\dagger}_{i,\tau,\alpha} \tag{A.8}$$

where $p^{\dagger}_{i,\tau,\alpha}$ creates a core-hole in the p-orbital at rung i and leg τ and $d_{i,\tau,\sigma}$ annihilates a valence hole. One can define the local exchange Hamiltonian

$$H_{i,\tau} = \boldsymbol{S}_{i,\tau} \cdot \left(J_{\mathrm{rung}} \boldsymbol{S}_{i,\bar{\tau}} + J_{\mathrm{leg}} \big(\boldsymbol{S}_{i+1,\tau} + \boldsymbol{S}_{i-1,\tau} \big) \right) \tag{A.9}$$

which fulfills $H_{i,\tau} D_{i,\tau,\sigma} |g\rangle = 0$. The Coulomb interaction U_{C} inhibits the superexchange coupling to the core-hole site spin $\boldsymbol{S}_{i,\tau}$, so the Hamiltonian for the intermediate state can be written as $\tilde{H} = H_0 - H_{i,\tau}$, which fulfills $[\tilde{H}, D_{i,\tau,\sigma}] = 0$ and $\tilde{H}|g\rangle = (H_0 + H_c)|g\rangle = 0|g\rangle$ with the ground state energy set to $H_0|g\rangle = 0|g\rangle$. One can use these relations to obtain an expansion in powers of $H_{i,\tau}$

$$\frac{1}{\mathrm{i}\Gamma} \sum_{l=0}^{\infty} \left(\frac{\tilde{H}}{\mathrm{i}\Gamma} \right)^{l} D_{i,\tau,\sigma} |g\rangle = D_{i,\tau,\sigma} \frac{1}{\mathrm{i}\Gamma} \sum_{l=0}^{\infty} \left(\frac{H_0 - H_{i,\tau}}{\mathrm{i}\Gamma} \right)^{l} |g\rangle \tag{A.10a}$$

$$= D_{i,\tau,\sigma} \frac{1}{\mathrm{i}\Gamma} \sum_{l=0}^{\infty} \left(1 - \frac{H_{i,\tau}}{\mathrm{i}\Gamma} + \frac{H^2_{i,\tau}}{(\mathrm{i}\Gamma)^2} - \frac{H_0 H_{i,\tau}}{(\mathrm{i}\Gamma)^2} + \ldots \right) |g\rangle \,. \tag{A.10b}$$

By applying the relations

$$d^{\dagger}_{i,\tau,\sigma'} d_{i,\tau,\sigma} p_{i,\tau,\alpha} |\mathrm{L}_3\rangle \langle \mathrm{L}_3| p^{\dagger}_{i,\tau,\alpha} = \begin{cases} n_{i,\tau,\sigma} & , \sigma' = \sigma \,, \\ S^z_{i,\tau} & , \sigma' \neq \sigma \end{cases} \tag{A.11}$$

from Ref. [50] one can expand the scattering amplitude

$$\langle f | e^{\mathrm{i}\boldsymbol{k}\boldsymbol{R}_{i,\tau}} D^{\dagger}_{i,\tau,\sigma'} | L_3 \rangle \langle L_3 | D_{i,\tau,\sigma} \sum_{l=0}^{\infty} e^{\mathrm{i}\boldsymbol{k}\boldsymbol{R}_{i,\tau}} \frac{(H_0 - H_{i,\tau})^l}{(\mathrm{i}\Gamma)^{l+1}} |g\rangle$$

$$= \begin{cases} \langle f | \sum_i e^{\mathrm{i}\boldsymbol{k}\boldsymbol{R}_{i,\tau}} n_{i,\tau,\sigma} \sum_{l=0}^{\infty} \frac{(H_0 - H_{i,\tau})^l}{(\mathrm{i}\Gamma)^{l+1}} |g\rangle & , \sigma' = \sigma \,, \\ \langle f | \sum_i e^{\mathrm{i}\boldsymbol{k}\boldsymbol{R}_{i,\tau}} S^z_{i,\tau} \sum_{l=0}^{\infty} \frac{(H_0 - H_{i,\tau})^l}{(\mathrm{i}\Gamma)^{l+1}} |g\rangle & , \sigma' \neq \sigma \,. \end{cases} \tag{A.12}$$

If one neglects the cross term $H_0 H_{i,\tau}$, the leading orders are given by $H_{i,\tau}$ and $H^2_{i,\tau}$. The leading orders of the response in the SC ($\Delta S = 0$) and NSC ($\Delta S = 1$) channel are obtained with the expansion

$$S^{\mathrm{UCL}}_{\Delta S}(\boldsymbol{q}, \omega) = \sum_{k=0}^{\infty} \left(\frac{J^{2k}}{\Gamma^{2(k+1)}} \sum_f \left| \langle f | e^{\mathrm{i}\boldsymbol{k}\boldsymbol{R}_{i,\tau}} O^{\Delta S,k}_{i,\tau,\sigma} | g \rangle \right|^2 \right) \delta(\omega_f - \omega_g + \omega) \tag{A.13}$$

and with the SC observables

$$O^{0,k}_{i,\tau,\sigma} := \begin{cases} n_{i,\tau,\sigma} & , k = 0 \,, \\ \left(J_{\mathrm{rung}} \boldsymbol{S}_{i,\tau} \cdot \boldsymbol{S}_{i,\bar{\tau}} + J_{\mathrm{leg}} \boldsymbol{S}_{i,\tau} \cdot \big(\boldsymbol{S}_{i+1,\tau} + \boldsymbol{S}_{i-1,\tau} \big) \right)^k & , k > 0 \end{cases} \tag{A.14}$$

and the NSC observables

$$O^{1,k}_{i,\tau,\sigma} := S^z_{i,\tau}\left(J_{\mathrm{rung}}\boldsymbol{S}_{i,\tau}\cdot\boldsymbol{S}_{i,\bar{\tau}} + J_{\mathrm{leg}}\boldsymbol{S}_{i,\tau}\cdot\left(\boldsymbol{S}_{i+1,\tau}+\boldsymbol{S}_{i-1,\tau}\right)\right)^k. \tag{A.15}$$

Note that the NSC observables for $k > 0$ are not Hermitian because $[S^z_{i,\tau}, \boldsymbol{S}_{i,\tau}] \neq 0$ and that the index σ can be omitted for all observables aside from $O^{0,0}_{i,\tau,\sigma}$.

Appendix B

Emergence of Three-Triplon Processes

In Chap. 3 the deepCUT method is applied to the Hamiltonian of the spin-1/2 Heisenberg ladder. The initial Hamiltonian (3.1.5) features two-triplon interactions, but no irreducible three-triplon interactions, i.e. interactions that only emerge for three or more triplons. However, the Bogoliubov terms, i.e. pair creation terms and pair annihilation terms, lead to the emergence of new interaction terms in the course of the CUT. This way, one obtains irreducible three-triplon interactions in the effective Hamiltonian H_{eff}. In this section, we discuss two examples of the commutation (2.1.4) leading to the three-triplon interaction terms, both with and without considering the hard-core constraint. In both examples, we calculate the commutators between selected operator monomials to derive exemplary irreducible three-triplon interactions in leading order.

For the first example, we start with the commutation of a pair creation term (present in η and H) and a translation term (present in H)

$$\left[x\, t_i^{\alpha,\dagger} t_{i+1}^{\alpha,\dagger}\,,\, x\, t_{i+2}^{\beta,\dagger} t_{i+1}^{\beta}\right] = x^2 t_i^{\alpha,\dagger} t_{i+2}^{\beta,\dagger}\left[t_{i+1}^{\alpha,\dagger}\,,\, t_{i+1}^{\beta}\right] \tag{B.1a}$$

$$= x^2\,\delta_{\alpha,\beta}\left(-t_i^{\alpha,\dagger} t_{i+2}^{\beta,\dagger} + \sum_{\gamma} \underbrace{t_i^{\alpha,\dagger} t_{i+2}^{\beta,\dagger} t_{i+1}^{\gamma,\dagger} t_{i+1}^{\gamma}}_{\text{one-to-three process}}\right)$$
$$+ x^2\, \underbrace{t_i^{\alpha,\dagger} t_{i+2}^{\beta,\dagger} t_{i+1}^{\alpha,\dagger} t_{i+1}^{\beta}}_{\text{one-to-three process}}\,. \tag{B.1b}$$

The calculation yields a one-to-three process in order $\mathcal{O}(x^2)$. This process is not present in the initial Hamiltonian (3.1.5), hence it is added to the basis. Since this process does not conserve the number of quasi-particles, it also appears in the generator η. Next, we consider the commutation of this new process with a pair

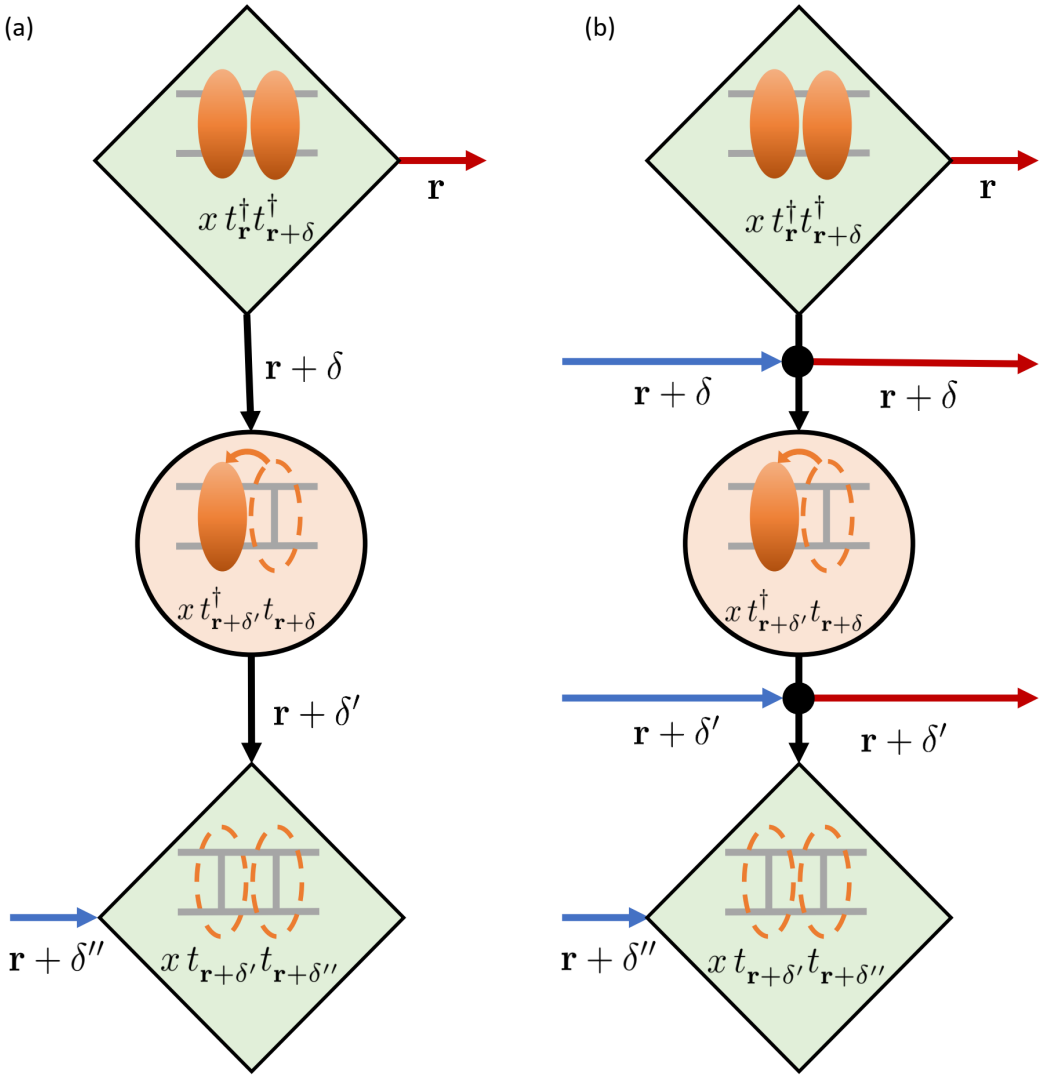

Figure B.1: Diagrammatic representation of an irreducible three-triplon interaction emerging from processes in the initial Hamiltonian (3.1.5) or similar processes in higher-dimensional systems with finite local Hilbert spaces. The dimer site r and the inter-dimer distances δ, δ' and δ'' are given in real space in dimension D. Blue arrows indicate incoming triplons, red arrows scattered, outgoing triplons and black arrows internal triplon propagations. (a) For normal bosons the combined process is single-particle ireducible and corresponds to an effective hopping, but (b) the hard-core constraint (black circles) induces three-triplon interactions in order $\mathcal{O}(x^3)$. We also published this figure in Ref. [44].

annihilation process, which is present both in η and H

$$\left[x^2\, t_i^{\alpha,\dagger} t_{i+2}^{\beta,\dagger} t_{i+1}^{\gamma,\dagger} t_{i+1}^{\gamma}\,,\; x\, t_{i+2}^{\mu} t_{i+3}^{\mu}\right] = x^3\, t_i^{\alpha,\dagger} \left[t_{i+2}^{\beta,\dagger}\,,\; t_{i+2}^{\mu}\right] t_{i+1}^{\gamma,\dagger} t_{i+1}^{\gamma} t_{i+3}^{\mu} \tag{B.2a}$$

$$= x^3\, \delta_{\beta,\mu} \left(-t_i^{\alpha,\dagger} t_{i+1}^{\gamma,\dagger} t_{i+1}^{\gamma} t_{i+3}^{\mu} + \sum_{\nu} \underbrace{t_i^{\alpha,\dagger} t_{i+1}^{\gamma,\dagger} t_{i+2}^{\nu,\dagger} t_{i+1}^{\gamma} t_{i+2}^{\nu} t_{i+3}^{\mu}}_{\text{three-triplon interaction}} \right)$$

$$+ x^3 \underbrace{t_i^{\alpha,\dagger} t_{i+1}^{\gamma,\dagger} t_{i+2}^{\beta,\dagger} t_{i+1}^{\gamma} t_{i+2}^{\mu} t_{i+3}^{\mu}}_{\text{three-triplon interaction}} . \tag{B.2b}$$

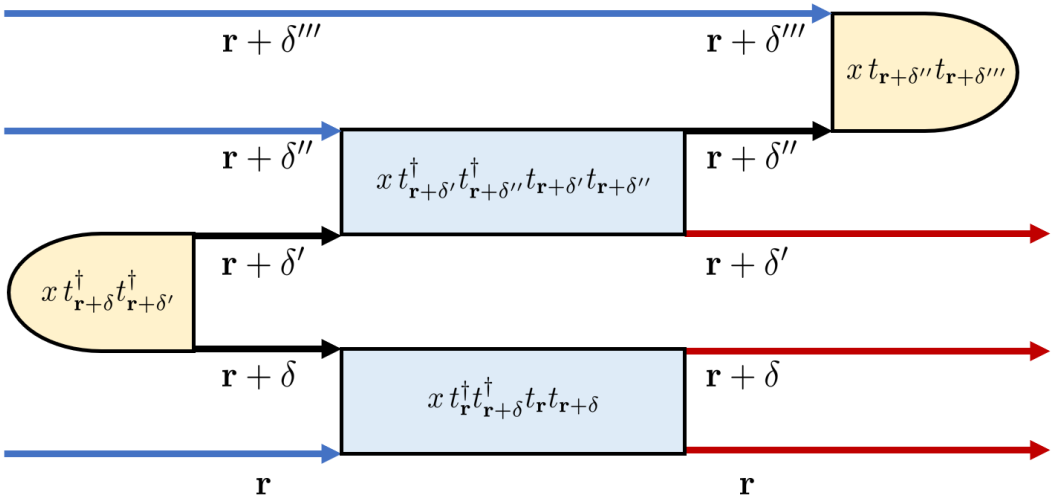

Figure B.2: Diagrammatic representation of an irreducible three-triplon interaction emerging without hard-core constraint from processes in the initial Hamiltonian (3.1.5) or similar processes in higher-dimensional systems with finite local Hilbert spaces. The dimer site r and the inter-dimer distances δ, δ', δ'' and δ''' are given in real space in dimension D. Blue arrows indicate incoming triplons, red arrows scattered, outgoing triplons and black arrows internal triplon propagations. Without the hard-core constraint, the three-triplon interactions emerge in order $\mathcal{O}(x^4)$.

and obtain an irreducible three-triplon interaction in order $\mathcal{O}(x^3)$. The emergence of this process from the three initial processes is depicted in analogy to the famous Feynman-Diagrams in Fig. B.1. Note that the above calculations are performed on a one-dimensional spin ladder, but irreducible three-triplon interactions can emerge by the same process for any dimerized system in any dimension D, which is indicated in Fig. B.1 by the dimer indices r and inter-dimer distances δ, δ' and δ''. The three-triplon interactions only arise in leading order $\mathcal{O}(x^3)$ because of the hard-core constraint, which appears in the triplon commutator (3.1.3) as bilinear operator terms, which allows one to obtain irreducible three-triplon interactions using no more than two commutations.

For the second example, we consider a bosonic approximations without the hard-core constraint and show that irreducible three-triplon interactions still emerge, albeit in order $\mathcal{O}(x^4)$ because three commutations are necessary. We start with the commutation of a two-body interaction and a zero-to-two process

$$\left[x\, t_i^{\alpha,\dagger} t_{i+1}^{\beta,\dagger} t_i^\beta t_{i+1}^\alpha\,,\, x\, t_{i+1}^{\gamma,\dagger} t_{i+2}^{\gamma,\dagger}\right] = x^2\, \delta_{\alpha,\gamma}\, t_i^{\alpha,\dagger} t_{i+1}^{\beta,\dagger} t_{i+1}^{\alpha,\dagger} t_{i+2}^{\alpha,\dagger} t_i^\beta\,. \tag{B.3}$$

Next, one can calculate the commutator of this one-to-three process with another two-body interaction

$$\left[x^2\, t_i^{\alpha,\dagger} t_{i+1}^{\beta,\dagger} t_{i+2}^{\alpha,\dagger} t_i^\beta\,,\, x\, t_{i+2}^{\gamma,\dagger} t_{i+3}^{\mu,\dagger} t_{i+2}^\mu t_{i+3}^\gamma\right] = -x^3\, \delta_{\alpha,\mu}\, t_i^{\alpha,\dagger} t_{i+1}^{\beta,\dagger} t_{i+2}^{\gamma,\dagger} t_{i+2}^{\alpha,\dagger} t_{i+3}^{\alpha,\dagger} t_i^\beta t_{i+3}^\gamma\,. \tag{B.4}$$

Finally, one can combine this two-to-four process with a two-to-zero process

$$\left[x^3\, t_i^{\alpha,\dagger} t_{i+1}^{\beta,\dagger} t_{i+2}^{\gamma,\dagger} t_{i+3}^{\alpha,\dagger} t_i^{\beta} t_{i+3}^{\gamma}\,,\; x\, t_{i+3}^{\mu} t_{i+4}^{\mu}\right] = -x^4\, \delta_{\alpha,\mu}\, t_i^{\alpha,\dagger} t_{i+1}^{\beta,\dagger} t_{i+2}^{\gamma,\dagger} t_i^{\beta} t_{i+3}^{\gamma} t_{i+4}^{\alpha}\,. \tag{B.5}$$

The final term is an irreducible three-body interaction. Note how this interaction emerges even without considering the hard-core nature of the quasi-particles. However, recall that this mechanism is only possible because the initial Hamiltonian contains terms which do not preserve the number of particles, namely Bogoliubov terms. The diagrammatic formation of a bosonic irreducible three-body interaction is shown in Fig B.2, where $\mathbf{r}$ is a dimer site in D dimension and $\delta, \delta', \delta''$ and δ''' are interdimer distances.

Appendix C

Numerical Parameters and Slices of the Dynamic Response

In Chap. 3 we apply the deepCUT method to calculate the dynamic response of the spin-1/2 Heisenberg ladder in RIXS experiments. In Sec. 3.4 , we discuss the results of the two leading nontrivial orders of the UCL expansion in both the SC and NSC channel. App. D presents additional data to assess the accuracy of the results. An extensive list of the numerical parameters used for the calculation of spectral densities is found here in Tab. C.1 (first leading orders) and Tab. C.2 (second leading orders).

The plots provided in Chap. 3 depict the spectral weight as heat maps for various x and q_x in each plot. This representation provides a good overview of the relative weight in different regions of phase space, but does not convey the shape of the function. For instance, square-root divergences at the continuum edges cannot be recognized easily. In Fig. C.1 to Fig. C.8, we provide plots of the spectral weight $S(\omega)$ for fixed q_x, where the form of the spectral weight can be discerned more easily.

Channel	UCL order	q_y	n_{QP}	$\hat{\eta}$	x	$o_{\max}$	$d_{\max}$	n_{LC}	n_{q_x}
NSC$_-$	$k=0$	π	1	(1:n)	0.25	o10	-	1	201
					0.5	o10	-	1	201
	(Fig. 3.9, Fig. 3.11)				1.2	o10	-	1	201
					2	o10	-	1	201
NSC$_+$	$k=0$	0	2	(2:n)	0.25	o10	2000	1000	201
					0.5	o10	2000	800	201
	(Fig. 3.8, Fig. 3.10, Fig. C.1)				1.2	o10	2000	600	201
					2	o10	2000	500	201
NSC$_-$	$k=0$	π	3	(3(2):n)	0.25	o8(10)	1000	600	201
					0.5	o8(10)	1000	600	201
	(Fig. 3.9, Fig. 3.11, Fig. C.2)				1.2	o6(10)	1000	500	201
					2	o5(10)	1000	400	201
SC$_+$	$k=1$	0	2	(2:n)	0.25	o10	2000	1000	201
					0.5	o10	2000	900	201
	(Fig. 3.15, Fig. 3.17, Fig. C.3)				1.2	o10	2000	600	201
					2	o10	2000	500	201
SC$_-$	$k=1$	π	3	(3(2):n)	0.25	o9(10)	1000	560	201
					0.5	o8(10)	1000	600	201
	(Fig. 3.16, Fig. 3.18, Fig. C.4)				1.2	o6(10)	1000	500	801
					2	o5(10)	1000	500	801
NSC$_+$	$k=0$	0	2	(2:n)	1	o9	1800	900	201
	(Fig. D.1)				1	o10	1800	900	201
SC$_+$	$k=1$	0	2	(2:n)	1	o10	2000	600	201
SC$_-$	$k=1$	π	3	(3:n)	1	o6	1000	500	201
	(Fig. 3.34)								
SC$_+$	$k=1$	0	2&4	(2:n)	0.25	o10	60	30	51
					0.5	o10	60	30	51
	(Fig. D.2, Fig. D.3)				1.2	o10	80	30	51
					2	o10	60	30	51

Table C.1: Numerical parameters of all plots in first leading order in Chap. 3 , App. C and App. D . The channel is characterized by (non-)-spin-conservation, (anti-)symmetry of the observable and order k of the UCL expansion. The (anti-)symmetry of the observable is directly related to the momentum q_y and number of excited triplons n_{QP}. The deepCUT is evaluated in order $o_{\max}$ in the expansion parameter $x = J_{\mathrm{leg}}/J_{\mathrm{rung}}$. The notation (3(2):$n$) is used when the accuracy of three-triplon computations is increased by combining (i) three-triplon interactions computed with the (3:n)-generator in maximum convergent order (see $o_{\max}$) with (ii) one- and two-triplon processes computed with the (2:n)-generator in order 10. The maximum distance $d_{\max}$ between triplons is used in the Lanczos algorithm with n_{LC} considered Lanczos coefficients and n_{q_x} is the number of evaluated discrete values q_x.

Channel	UCL order	q_y	n_{QP}	$\hat{\eta}$	x	$o_{\max}$	$d_{\max}$	n_{LC}	n_{q_x}
NSC_-	$k=1$	π	1	(1:n)	0.25	o10	-	1	201
					0.5	o10	-	1	201
	(Fig. 3.25, Fig. 3.27)				1.2	o10	-	1	201
					2	o10	-	1	201
NSC_+	$k=1$	0	2	(2:n)	0.25	o10	2000	1000	201
					0.5	o10	2000	900	201
	(Fig. 3.24, Fig. 3.26, Fig. C.5)				1.2	o10	2000	700	201
					2	o10	2000	550	201
NSC_-	$k=1$	π	3	(3(2):n)	0.25	o8(10)	1000	600	201
					0.5	o8(10)	1000	600	201
	(Fig. 3.25, Fig. 3.27, Fig. C.6)				1.2	o6(10)	1000	500	201
					2	o5(10)	1000	400	201
SC_+	$k=2$	0	2	(2:n)	0.25	o10	2000	1000	201
					0.5	o10	2000	900	201
	(Fig. 3.29, Fig. 3.31, Fig. C.7)				1.2	o10	2000	700	201
					2	o10	2000	550	201
SC_-	$k=2$	π	3	(3(2):n)	0.25	o8(10)	1000	600	201
					0.5	o8(10)	1000	600	201
	(Fig. 3.30, Fig. 3.32, Fig. C.8)				1.2	o6(10)	1000	500	201
					2	o5(10)	1000	400	201

Table C.2: Numerical parameters of all plots in second leading order in Chap. 3 , App. C and App. D . The channel is characterized by (non-)-spin-conservation, (anti-)symmetry of the observable and order k of the UCL expansion. The (anti-)symmetry of the observable is directly related to the momentum q_y and number of excited triplons n_{QP}. The deepCUT is evaluated in order $o_{\max}$ in the expansion parameter $x = J_{\mathrm{leg}}/J_{\mathrm{rung}}$. The notation (3(2):$n$) is used when the accuracy of three-triplon computations is increased by combining (i) three-triplon interactions computed with the (3:n)-generator in maximum convergent order (see $o_{\max}$) with (ii) one- and two-triplon processes computed with the (2:n)-generator in order 10. The maximum distance $d_{\max}$ between triplons is used in the Lanczos algorithm with n_{LC} considered Lanczos coefficients and n_{q_x} is the number of evaluated discrete values q_x.

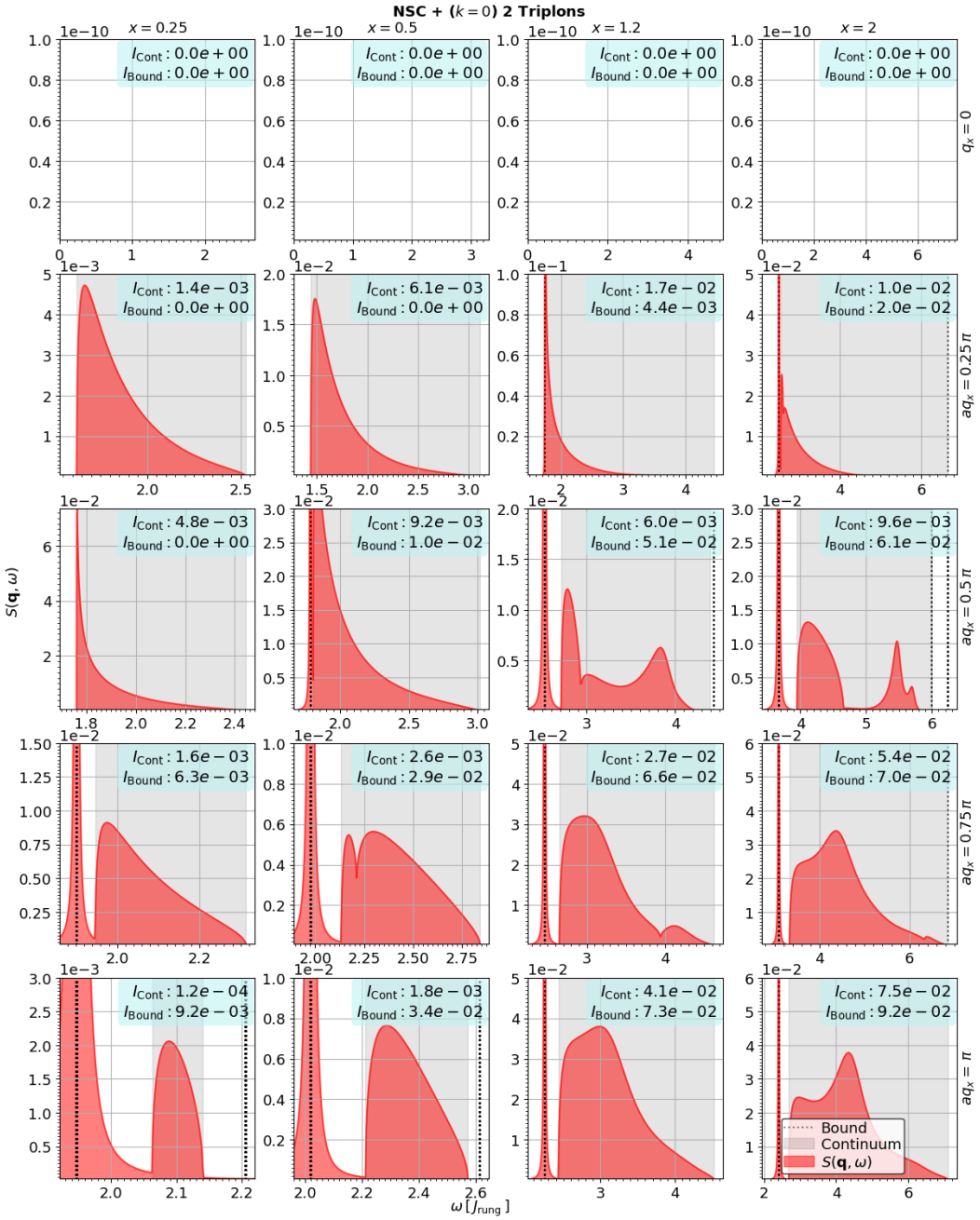

Figure C.1: Spectral density $S(q_x, \omega)$ slices of the leading order NSC observable in two-triplon space.

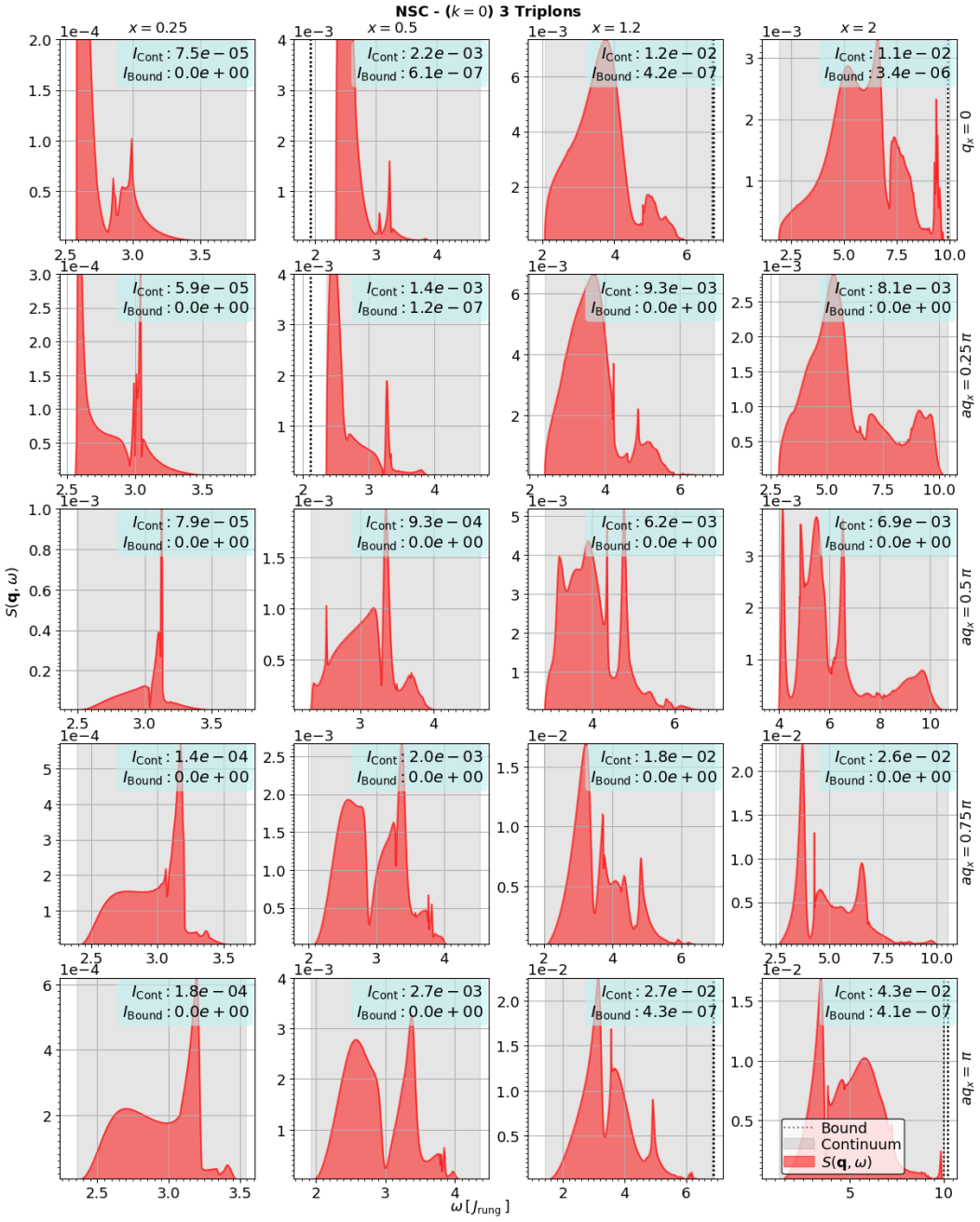

Figure C.2: Spectral density $S(q_x, \omega)$ slices of the leading order NSC observable in three-triplon space.

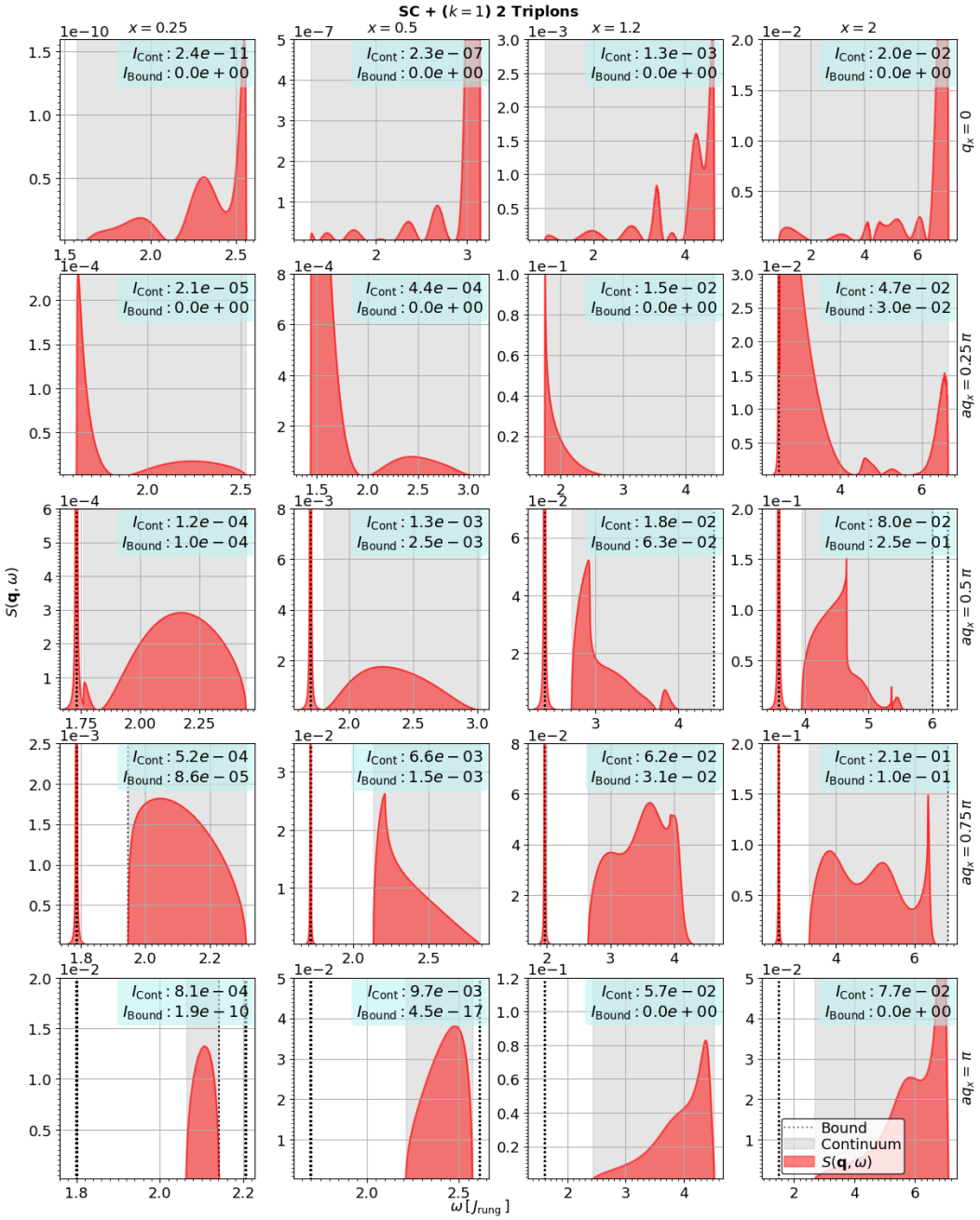

Figure C.3: Spectral density $S(q_x, \omega)$ slices of the leading order SC observable in two-triplon space.

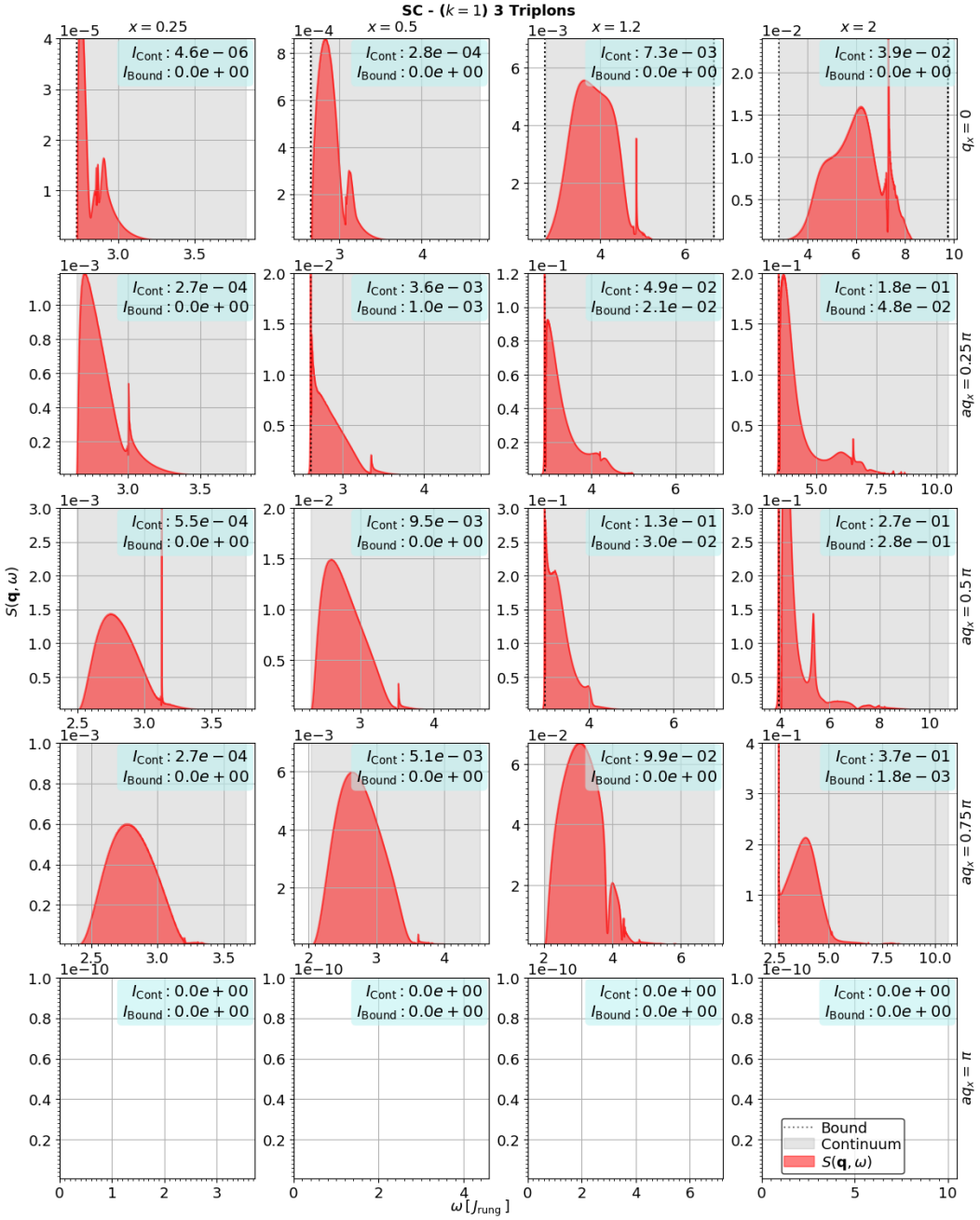

Figure C.4: Spectral density $S(q_x, \omega)$ slices of the leading order SC observable in three-triplon space.

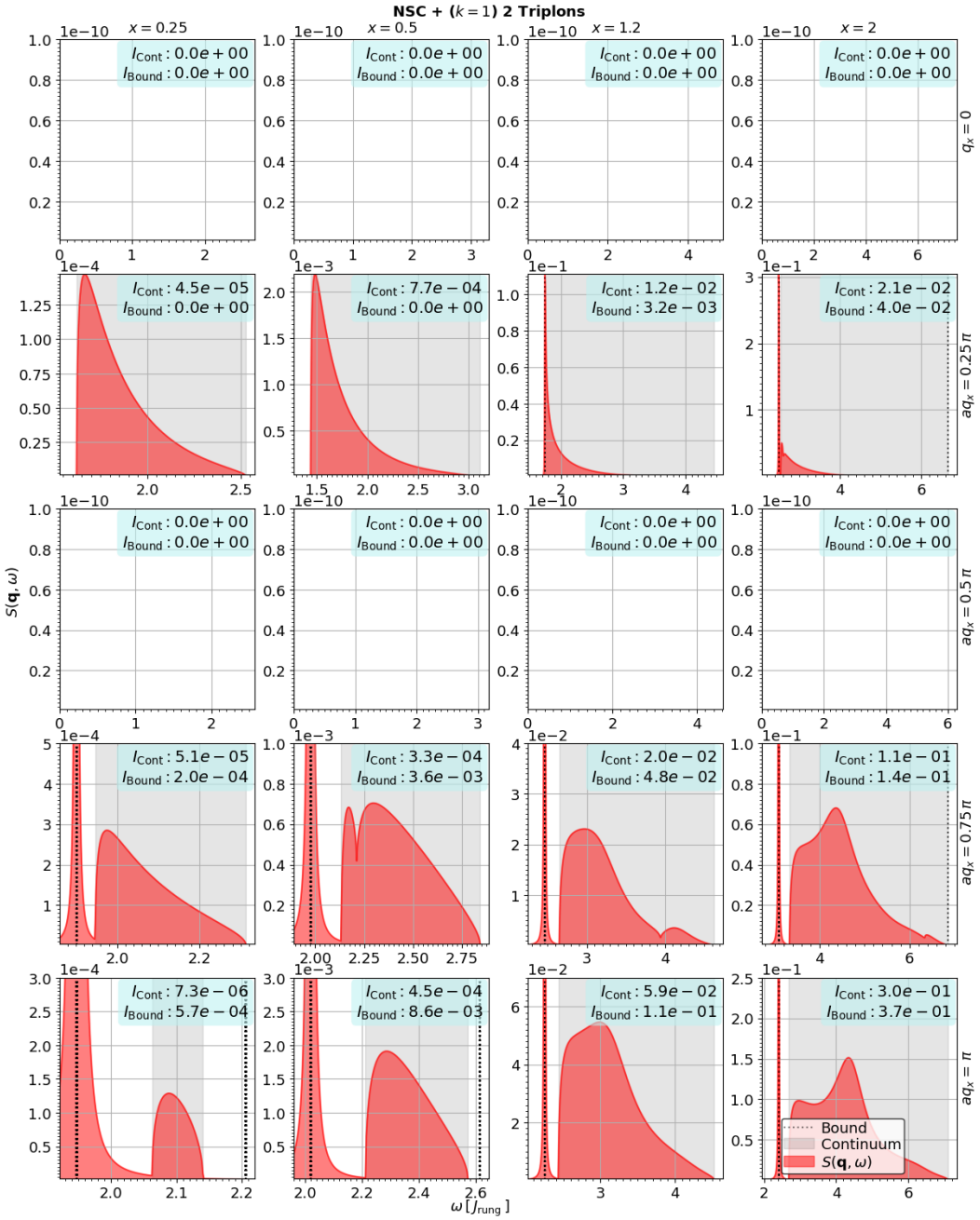

Figure C.5: Spectral density $S(q_x, \omega)$ slices of the second leading order NSC observable in two-triplon space.

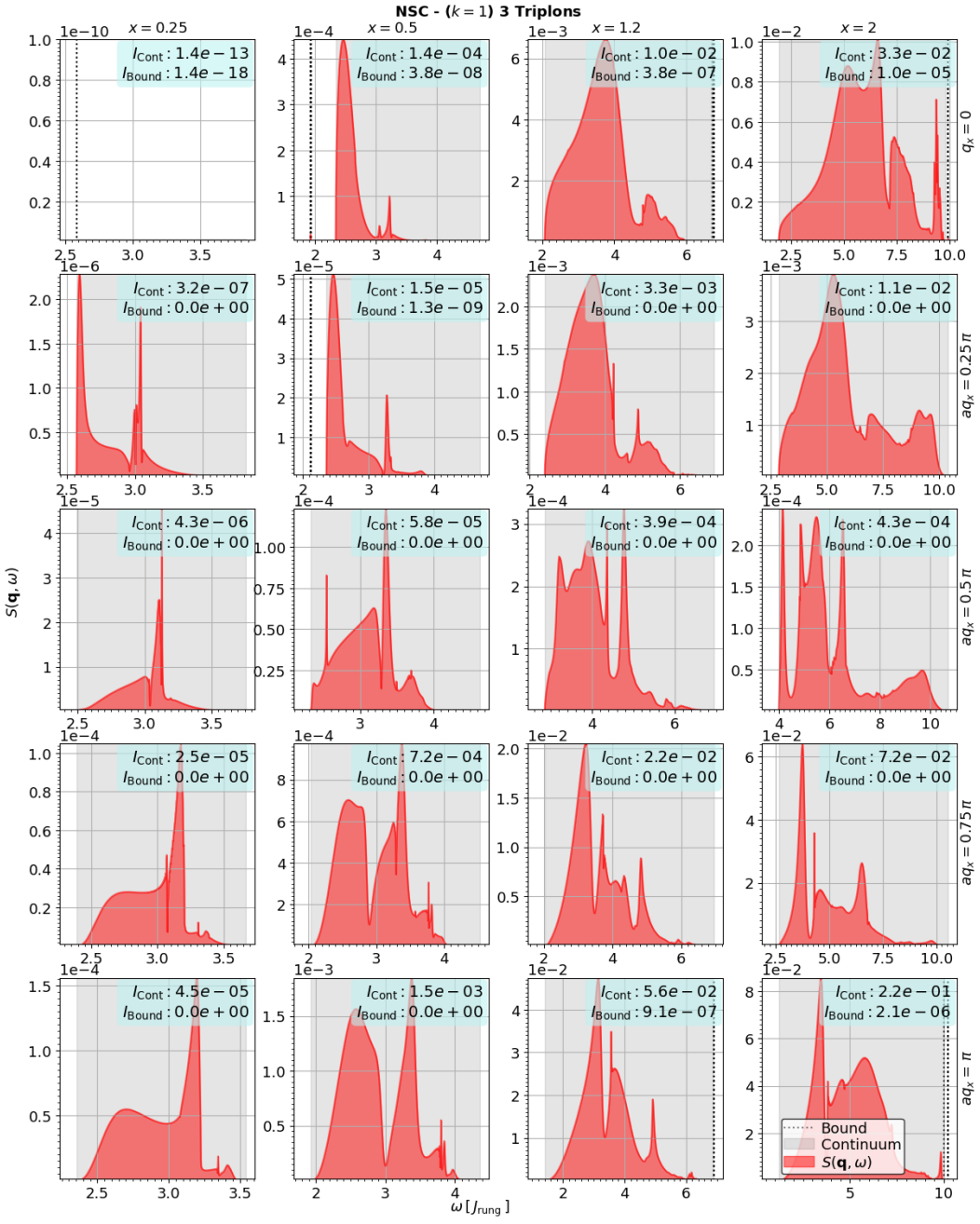

Figure C.6: Spectral density $S(q_x, \omega)$ slices of the second leading order NSC observable in three-triplon space.

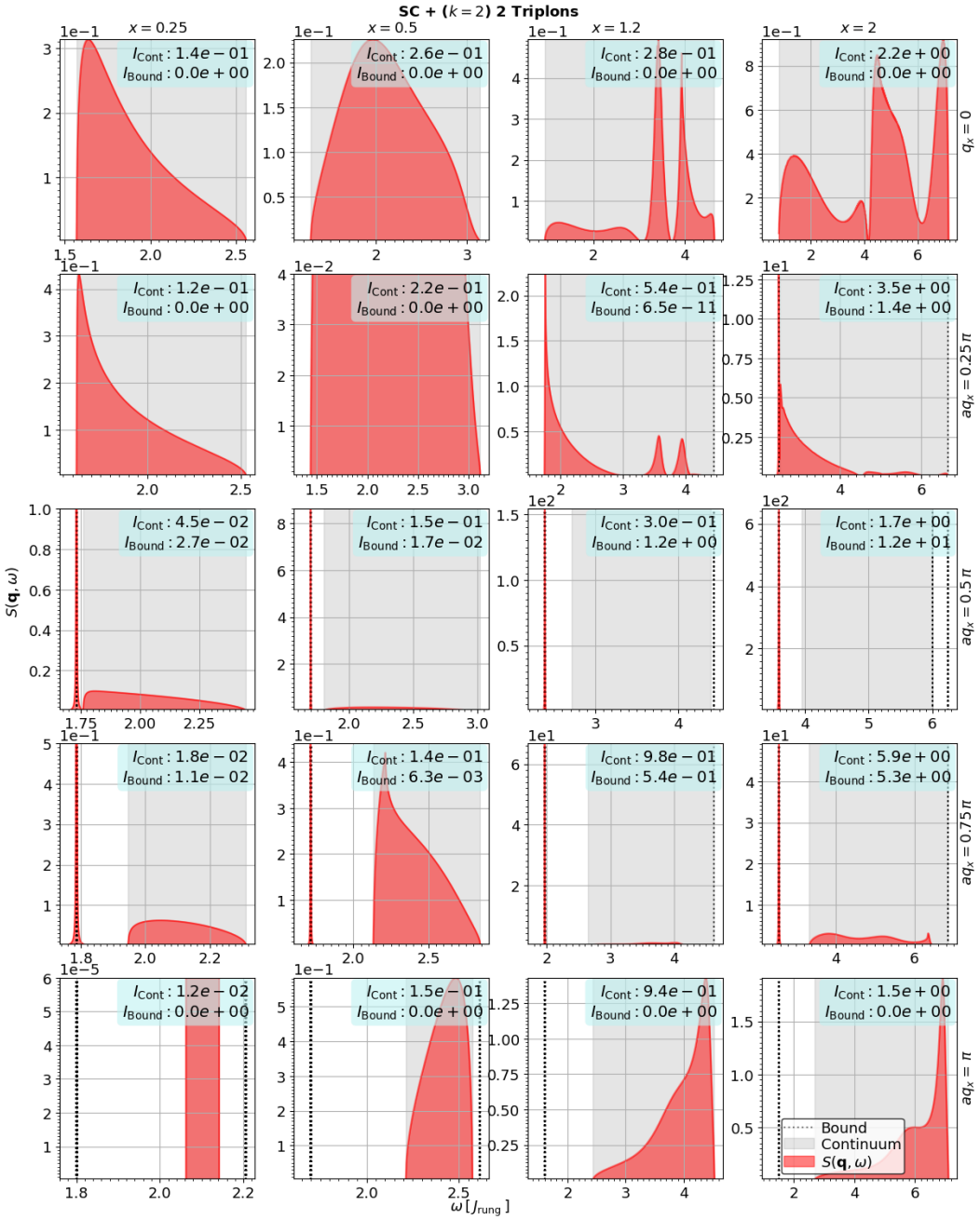

Figure C.7: Spectral density $S(q_x, \omega)$ slices of the second leading order SC observable in two-triplon space.

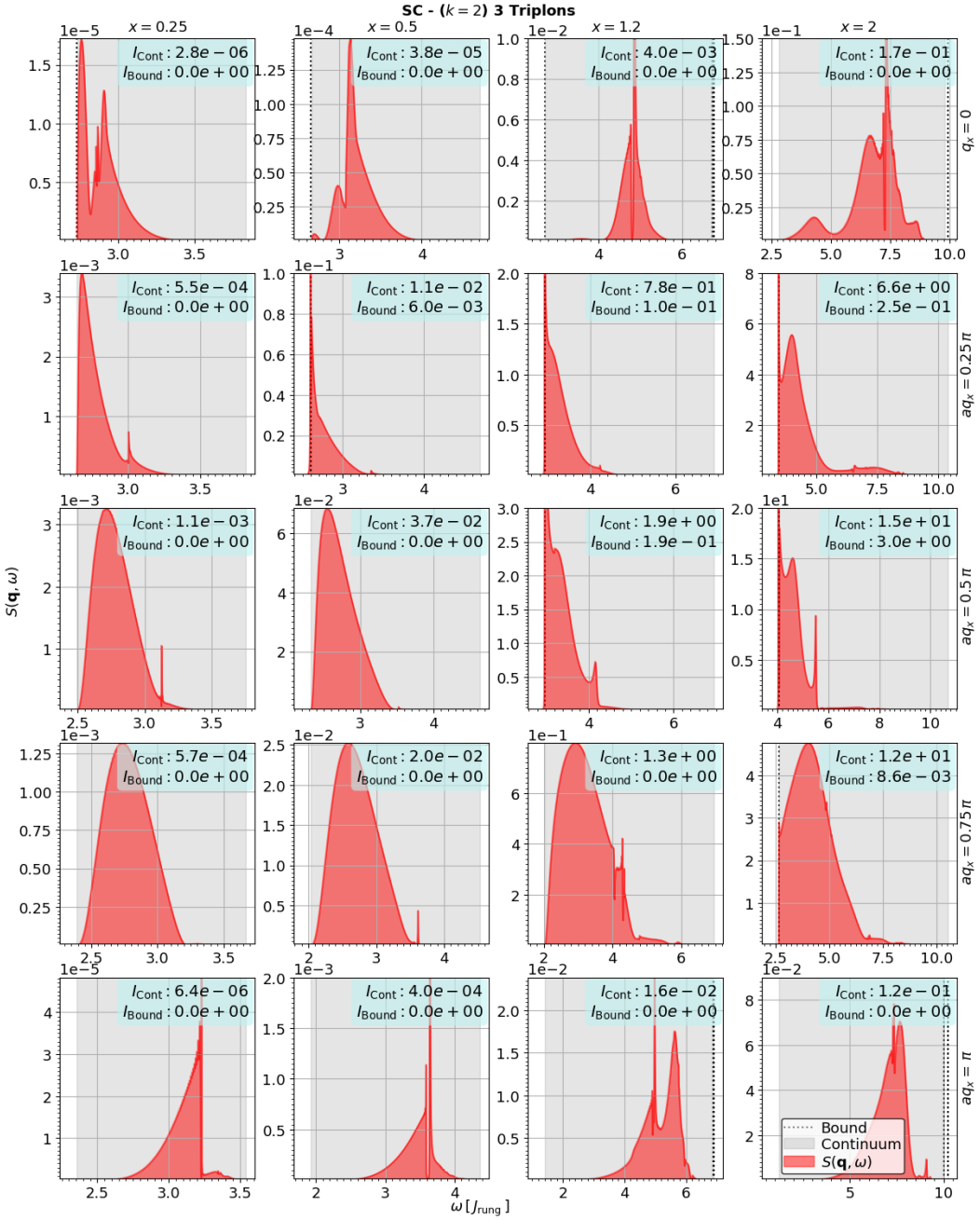

Figure C.8: Spectral density $S(q_x, \omega)$ slices of the second leading order SC observable in three-triplon space.

Appendix D

Accuracy of the Dynamic Response Predictions

In Chap. 3 we apply the deepCUT method to calculate the response of the spin-1/2 Heisenberg ladder in RIXS experiments. In Sec. 3.4 , we discuss the results of the two leading orders of the UCL expansion in both the SC and NSC channel. Here, we discuss the accuracy of the results by showing that convergence is achieved during the calculation and by arguing that no significant weight from states of more than three triplons interferes with the predicted response.

D.1 Convergence of the Numerical Results

If the numerical parameters (deepCUT-order, maximum extension $d_{\max}$ of terms in Lanczos algorithm, number n_{LC} of Lanczos coefficients) used for the calculation are not large enough, then the truncated results are not a good approximation of the exact results. When increasing the parameters, the results should converge to the correct results. Therefore, one can change the parameters slightly to check whether convergence has occurred up to numerical precision. The results might not be converged if

(i) the deepCUT truncation order is too low or

(ii) too few Lanczos coefficients are used, i.e. $d_{\max}$ is too small.

Fig. D.1 depicts an exemplary comparison of results for $x = 1$ between typical used parameters and slightly altered parameters. Panel (c) displays the results with typical parameters, o10 and $d_{\max} = 2000$, while panel (b) shows results for a smaller $d_{\max} = 1800$ and panels (a) results for a lower truncation order o9 and $d_{\max} = 1800$.

For the calculation with a lower truncation order in panel (a), $d_{\max} = 1800$ is chosen such that the same number of Lanczos coefficients can be used as in panel (c). A lower deepCUT expansion order allows for more Lanczos coefficients before the $d_{\max}$ truncation leads to errors in the coefficients. One observes that the results in the three panels do not differ in any significant way, indicating that the calculation is converged up to numerical precision for the used parameters.

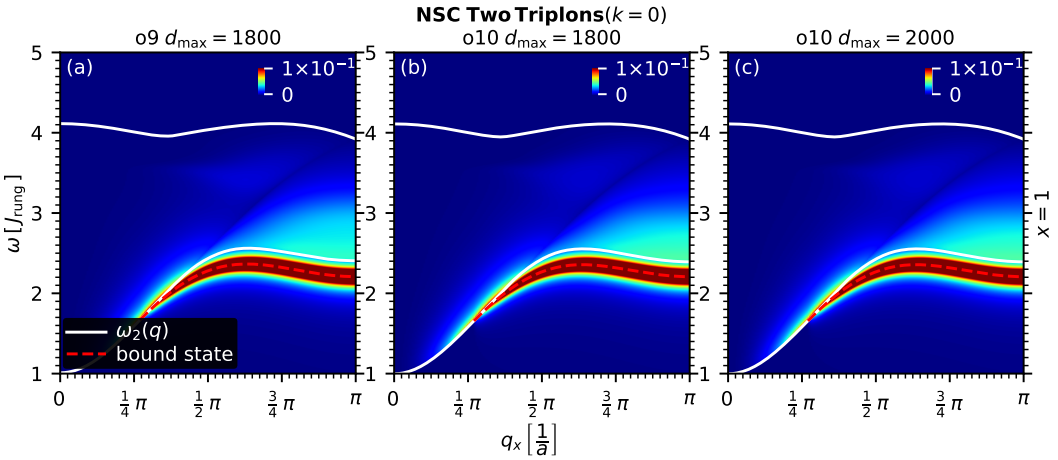

Figure D.1: Spectral density $S(q_x, \omega)$ of the leading NSC observable $O^{\text{NSC},0}_{i,\tau} = S^z_{i,\tau}$ (DSF, see (3.2.10)) in two-triplon space for perturbation parameter $x = 1$ for different deepCUT expansion orders (o9,o10,o10) and maximum Lanczos extension $d_{\max} \in \{1800, 1800, 2000\}$. Apart from numerical noise, all three calculations yield the same results, demonstrating that the parameters suffice for convergence.

D.2 Spectral Weight I_n in n-Triplon Channels

The numerical calculation of spectral densities becomes very memory consuming in higher n-triplon spaces. The calculations up to three-triplons space converge well and the results are discussed in Sec. 3.4 . Calculations in four-triplon space are currently only feasible with the (3:n)-generator and up to small $d_{\max}$, as can be seen in Tab. C.1. The four-triplon results in the SC channel are shown in Fig. D.2 and Fig. D.3 in panels (a-b), respectively, and the two-triplon results are added in panels (c-d). While the four-triplon results contain many ripples which indicate that the calculation is not fully converged due to too few Lanczos coefficients, it is apparent that the spectral weight of the four-triplon contributions is significantly smaller than the two-triplon spectral weight. This is especially important for experimental verification of the results, since both channels show contributions in the same region of phase space.

The four-triplon results should be treated with caution, since the (3:n)-generator was used during the deepCUT. This means that four-triplon contributions of the Hamiltonian are not decoupled from higher spaces, i.e. four triplons states are not

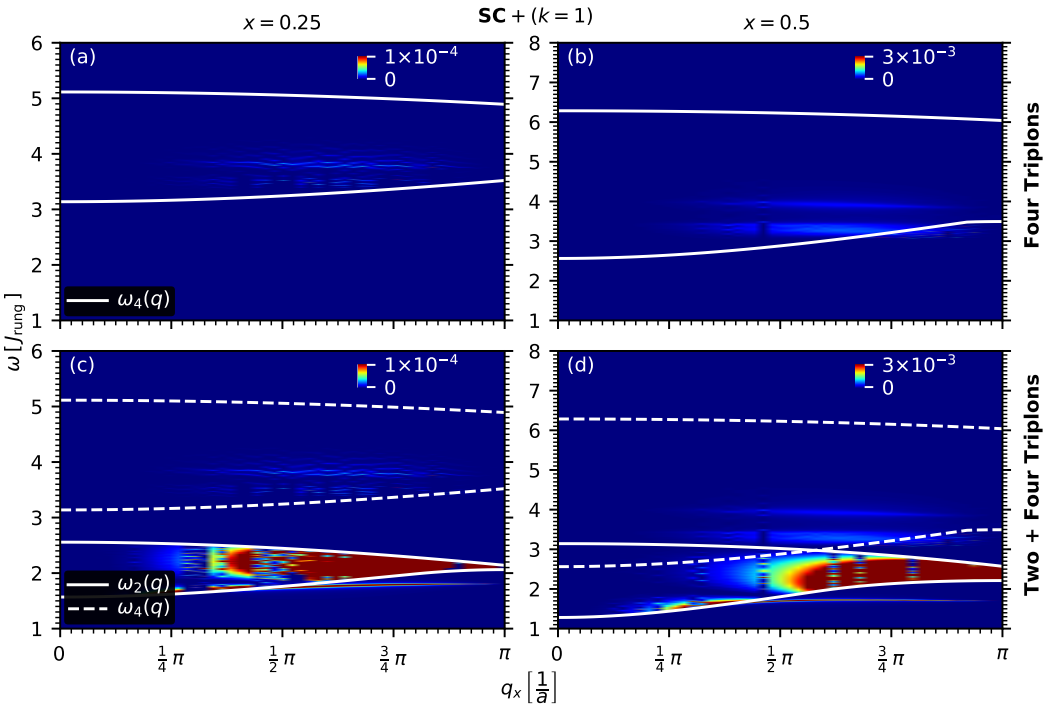

Figure D.2: Spectral density $S(q_x, \omega)$ of the leading SC observable $O^{\mathrm{SC},1}_{i,\pm}$ (DESF, see (3.2.15)) in (two+four)-triplon and four-triplon space for perturbation parameters $x \in \{0.25, 0.5\}$. Note that the calculation in four-triplon space is only feasible with a small value of $d_{\max}$, see Tab. C.1.

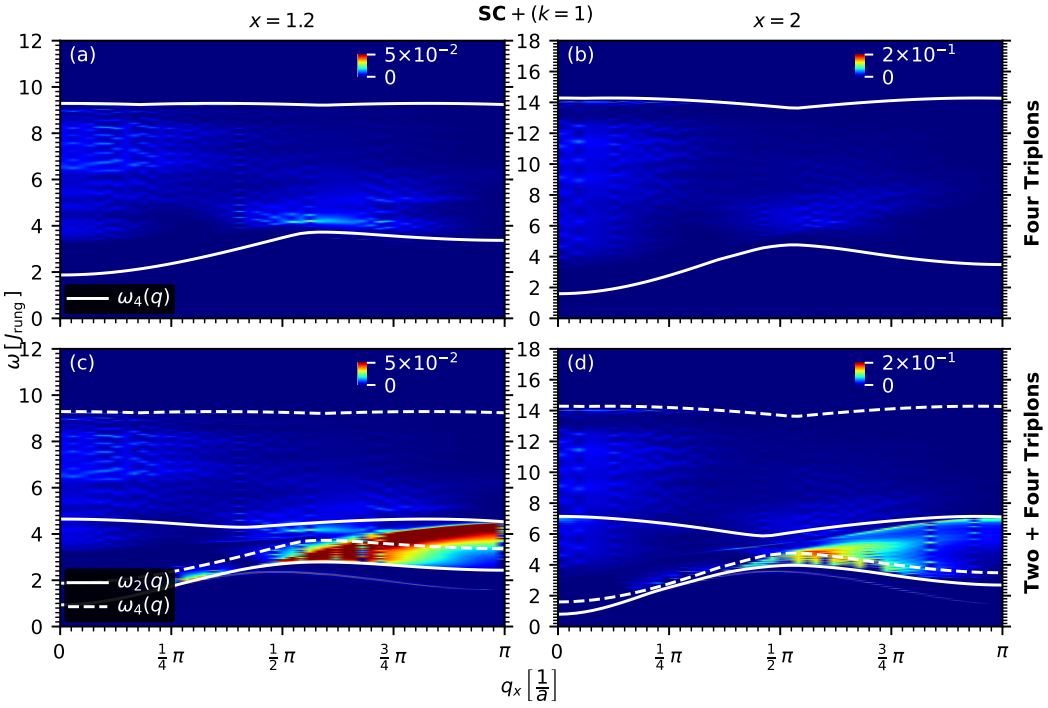

Figure D.3: Spectral density $S(q_x, \omega)$ of the leading SC observable $O^{\mathrm{SC},1}_{i,\pm}$ (DESF, see (3.2.15)) in (two+four)-triplon and four-triplon space for perturbation parameters $x \in \{1.2, 2\}$. Note that the calculation in four-triplon space is only feasible with a small $d_{\max}$, see Tab. C.1.

separated from six-triplon states, those are not separated from eight-triplon states and so forth. Consequently, the four-triplon results do not correctly portray the four-triplon channel of conserved triplons, but rather provides an estimate of the real results.

In the following, we show more rigorously that the results for $n \leq 3$ already describe the bulk of the weight and no significant weight is added by $n > 3$ triplons. To achieve this, we use the sum rule

$$I_{\text{total}}[O] = \sum_{n=0}^{\infty} I_n[O] = \left\langle O^2 \right\rangle - \langle O \rangle^2 , \tag{D.1}$$

which gives the total spectral weight $I_{\text{total}}[O]$ of all n-triplon subspaces by evaluating the expectation values $\left\langle O^2 \right\rangle$ and $\langle O \rangle$ on the ground state. We calculate the total weight numerically using the following scheme

1) We set up the Hamiltonian of a finite spin ladder with N rungs numerically in the spin basis. The basis states are characterized by the spin quantum numbers $(S^z_{1,1}, S^z_{1,2}, S^z_{2,1}, ..., S^z_{N,2})$. To increase efficiency, we use the sparse matrix representation of the Eigen library [136].

2) We calculate the ground state $|0\rangle$ of the system by using the power method [163]

   a) Initialize $|\Psi_0\rangle$ with a normalized random vector.

   b) Calculate normalized vectors

   $$|\Psi_{n+1}\rangle = \frac{\hat{H}|\Psi_n\rangle}{\left|\hat{H}|\Psi_n\rangle\right|} \tag{D.2}$$

   until the composition of the state no longer changes up to numeric precision, i.e. repeat the iteration until

   $$\left| \left(\frac{1}{\langle \Psi_n | \Psi_{n+1} \rangle} \right) |\Psi_{n+1}\rangle - |\Psi_n\rangle \right| < 10^{-8} . \tag{D.3}$$

   Note that the division by $\langle \Psi_n | \Psi_{n+1} \rangle$ is necessary since the eigenvalue can have a complex phase $\exp(\mathrm{i}\varphi)$.

   c) The final calculated state approximates the ground state $|0\rangle \approx |\Psi_{n_{\max}}\rangle$.

   We perform these calculations up to $N = 12$ rungs, which corresponds to 24 spins and a Hilbert space of dimension $2^{24} = 16777216$. For small N, we compare the result for the ground state and ground state energy with results using exact diagonalization as an additional check.

3) We extrapolate the results for finite N to $N = \infty$ with

$$I_{\text{total}}(N) = a + be^{c/N} \tag{D.4}$$

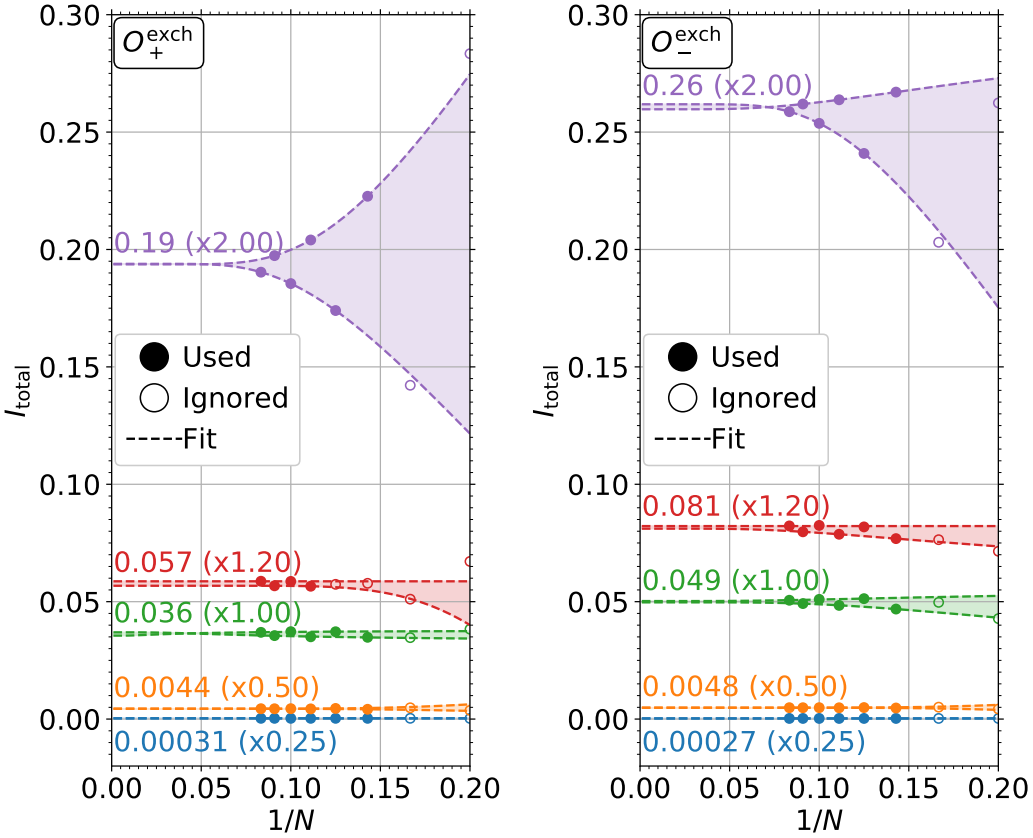

Figure D.4: Total weights $I_{\text{total}}(N)$ for the leading order SC observable $O_{\pm}^{\text{ex}}$, see(3.2.15), in the symmetric (O_{+}^{ex}, left) and antisymmetric (O_{-}^{ex}, right) case for finite spin ladders with N rungs, calculated using exact diagonalization. The filled data points are used for the fit, the empty data points are skipped. The dotted lines show the fits for even N and odd N, respectively.

with the fit parameters a, b and c. Since the ground state changes qualitatively between even and odd N, the extrapolation of these cases is performed separately. We average the extrapolated results

$$I_{\text{total}}(\infty) = \frac{I_{\text{total}}^{\text{even}}(\infty) + I_{\text{total}}^{\text{odd}}(\infty)}{2}\,. \tag{D.5}$$

To reduce finite size effect of extremely small N, which do not scale like (D.4), we only fit the data points for the largest available N, i.e. $N_{\text{even}} \in \{12, 10, 8\}$ and $N_{\text{odd}} \in \{11, 9, 7\}$. The caveat is that three data points for three parameters do not yield fit errors, which would be useful to estimate the accuracy of the extrapolation. However, one can use the difference between the even and odd result $\Delta I_{\text{total}}(\infty) = |I_{\text{total}}^{\text{even}}(\infty) - I_{\text{total}}^{\text{odd}}(\infty)|$ to estimate the error. The data points for finite N and the fitted curves are shown in Fig. D.4.

The total weights I_{total} calculated with the above method and the n-triplon weights I_n obtained with the deepCUT approach are compared in Fig. D.5. The

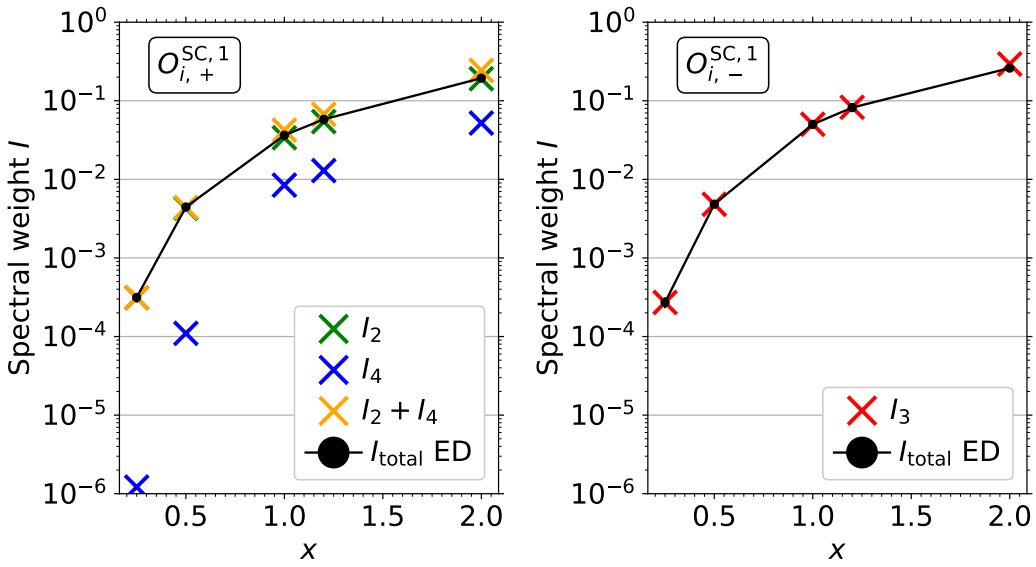

Figure D.5: Total weights I_n in n-triplon spectra for the exchange observable $O_{\pm}^{\mathrm{ex}}$, see (3.2.15), in the symmetric (O_{+}^{ex}, left) and antisymmetric (O_{-}^{ex}, right) case. The black crosses show the total weight (D.1) of the observable for all n-triplon spaces evaluated using exact diagonalization. The estimated error $\Delta I_{\mathrm{total}}(\infty) = |I_{\mathrm{total}}^{\mathrm{even}}(\infty) - I_{\mathrm{total}}^{\mathrm{odd}}(\infty)|$ is smaller than the symbol size for $x > 0.25$; even for $x = 0.25$, the vertical black lines indicating the error are barely visible. The errors increase with x, but this cannot be observed directly due to the logarithmic scale of the y-axis.

weights increase with x and most weight is found in the two-triplon and three-triplon channel. Furthermore, the total weight is already described well by the two-triplon and three-triplon contributions and consequently no additional, significantly large weight can appear in the channels with $n > 3$ triplons. However, one finds for large $x > 1$ that I_{total} is smaller than I_2 or I_3, respectively. This is an indicator for small errors in the RIXS results for large x. Three sources for these errors exist.

(i) The extrapolation (D.4) of the finite-size results to the infinite system. Results for higher N can give a better estimation of $I_{\mathrm{total}}(\infty)$. This error does not imply any errors in the calculated spectral densities using deepCUT.

(ii) The finite deepCUT expansion order. This error increases with x as the delocalization of the triplons increases.

(iii) The four-triplon sector not being decoupled from sectors with 6, 8, ... triplons due to the use of the (3:n)-generator. This tends to overestimate the weight of the 4-particle channel.

Despite these inaccuracies for large x, the results show clearly that hardly any weight is to be expected for $n > 4$ triplons.

Appendix E

Analytical Solution of the TFIM Model

We discuss flow equations in momentum space for the TFIM model in Chap. 4, which can be formulated with hard-core operators in real space

$$\frac{H}{\Gamma_z} = \sum_{i=0}^{N-1} \left(b_i^\dagger b_i - \frac{1}{2} \right) - \frac{x}{2} \sum_{i=0}^{N-1} \left(b_i^\dagger b_{i+1} + b_i^\dagger b_{i+1}^\dagger + \text{h.c.} \right) . \tag{E.1}$$

In the strong field limit $|x| \leq 1$, the system can be diagonalized by applying the

1. Jordan-Wigner transformation [164]

$$f_l = \exp\left(\mathrm{i}\pi \sum_{j<l} b_l^\dagger b_l \right) b_l \,, \qquad b_l = \exp\left(\mathrm{i}\pi \sum_{j<l} f_l^\dagger f_l \right) f_l \,, \tag{E.2}$$

$$f_l^\dagger = \exp\left(\mathrm{i}\pi \sum_{j<l} b_l^\dagger b_l \right) b_l^\dagger \,, \qquad b_l^\dagger = \exp\left(\mathrm{i}\pi \sum_{j<l} f_l^\dagger f_l \right) f_l^\dagger \,, \tag{E.3}$$

2. Fourier transformation

$$\bar{f}_k = \frac{1}{\sqrt{N}} \sum_j e^{+ikx_j} f_j \,, \qquad f_j = \frac{1}{\sqrt{N}} \sum_k e^{-ikx_j} f_k \,, \tag{E.4}$$

$$\bar{f}_k^\dagger = \frac{1}{\sqrt{N}} \sum_j e^{-ikx_j} f_j^\dagger \,, \qquad f_j^\dagger = \frac{1}{\sqrt{N}} \sum_k e^{+ikx_j} f_k^\dagger \,, \tag{E.5}$$

3. and Bogoliubov transformation [165]

$$\begin{pmatrix} f_k^\dagger \\ f_{-k} \end{pmatrix} = \begin{pmatrix} \cos(\theta_k) & +\mathrm{i}\sin(\theta_k) \\ +\mathrm{i}\sin(\theta_k) & \cos(\theta_k) \end{pmatrix} \begin{pmatrix} \bar{f}_k^\dagger \\ \bar{f}_{-k} \end{pmatrix} , \tag{E.6}$$

$$\begin{pmatrix} \bar{f}_k^\dagger \\ \bar{f}_{-k} \end{pmatrix} = \begin{pmatrix} \cos(\theta_k) & -\mathrm{i}\sin(\theta_k) \\ -\mathrm{i}\sin(\theta_k) & \cos(\theta_k) \end{pmatrix} \begin{pmatrix} f_k^\dagger \\ f_{-k} \end{pmatrix} \tag{E.7}$$

one after another. We consider only the ferromagnetic case $x \in [0,1]$ explicitly, but the antiferromagnetic $x \in [-1,0]$ result is treated analogously with a shifted momentum $k \to k + \pi/a$.

The Jordan-Wigner transformation introduces coefficients $e^{\mathrm{i}\pi n_{j<l}} = \pm 1$, where the signs depends on the number $n_{j<l} := \sum_{j<l} b_l^\dagger b_l$ of occupied sites $j \in \{0, ..., l-1\}$. This highly non-local transformation turns the symmetric commutation relations of hard-core operators between different sites into antisymmetric anticommutation relations of spinless fermions. Strictly speaking, this transformation is only possible for open systems, but not for systems with periodic boundaries. This does not restrict the application of the Jordan-Wigner transforamtion to obtain a solution of the TFIM in the thermodynamic limit, because in that limit the open and periodic case are equivalent. Note that the occupation number operators $f_i^\dagger f_i = b_i^\dagger b_i$ transform trivially. The Hamiltonian (E.1) expressed in terms of the fermionic operators reads

$$\frac{H}{\Gamma_z} = \sum_{i=0}^{N-1} \left(f_i^\dagger f_i - \frac{1}{2} \right) - \frac{x}{2} \sum_{i=0}^{N-1} \left(f_i^\dagger f_{i+1} + f_i^\dagger f_{i+1}^\dagger + \text{h.c.} \right) . \tag{E.8}$$

The next-neighbor hopping terms of this tight-binding Hamiltonian are diagonalized with the Fourier transformation

$$\frac{H}{\Gamma_z} = \sum_k^{1.\mathrm{BZ}} \left[\left(1 - x\cos(ka) \right) \bar{f}_k^\dagger \bar{f}_k - \frac{1}{2} \right] + \mathrm{i}\frac{x}{2} \sum_k^{1.\mathrm{BZ}} \left[\sin(ka) \left(\bar{f}_k^\dagger \bar{f}_{-k}^\dagger - \text{h.c.} \right) \right] . \tag{E.9}$$

Note that the prefactor of the pair creation and annihilation terms in the fermionic momentum-space formulation (E.9) differs significantly from the hard-core bosonic momentum-space formulation (4.1.17). The most important difference, however, is not the different prefactor, but the fact that the fermionic operators fulfill the simpler fermionic anticommutation relations. The Bogoliubov transformation diagonalizes the remaining pair creation and annihilation terms. It must fulfill the condition

$$\cos\theta_k = \cos\theta_{-k} , \qquad \sin\theta_k = -\sin\theta_{-k} \tag{E.10}$$

and conserve the anticommutation relations

$$\begin{aligned}
\{f_k, f_{k'}\} &= \mathrm{i}\cos\theta_k \sin\theta_{k'} \underbrace{\{\bar{f}_k, \bar{f}^\dagger_{-k'}\}}_{=\delta_{k,-k'}} + \mathrm{i}\sin\theta_k \cos\theta_{k'} \underbrace{\{\bar{f}^\dagger_{-k}, \bar{f}_{k'}\}}_{\delta_{k,-k'}} \\
&= \mathrm{i}\delta_{k,-k'} \left[\cos\theta_k \sin(-\theta_k) + \cos(-\theta_k)\sin\theta_k\right] = 0\,, \qquad \text{(E.11a)} \\
\{f^\dagger_k, f^\dagger_{k'}\} &= \{f_{k'}, f_k\}^\dagger = 0\,, \qquad \text{(E.11b)} \\
\{f_k, f^\dagger_{k'}\} &= \cos\theta_k \cos\theta_{k'} \underbrace{\{\bar{f}_k, \bar{f}^\dagger_{k'}\}}_{=\delta_{k,k'}} + \sin\theta_k \sin\theta_{k'} \underbrace{\{\bar{f}^\dagger_{-k}, \bar{f}_{-k'}\}}_{\delta_{k,-k'}} \\
&= \delta_{k,k'}(\cos^2\theta_k + \sin^2\theta_k) = \delta_{k,k'}\,. \qquad \text{(E.11c)}
\end{aligned}$$

The transformed Hamiltonian

$$\begin{aligned}
\frac{H}{\Gamma_z} = \sum_k^{1.\mathrm{BZ}} \Bigg\{ &\left[\left(1 - x\cos(ka)\right)\cos(2\theta_k) + x\sin(ka)\sin(2\theta_k)\right] f^\dagger_k f_k \\
&+ \left[\left(1 - x\cos(ka)\right)\sin^2(\theta_k) - \frac{x}{2}\sin(ka)\sin(2\theta_k) - \frac{1}{2}\right] \\
&+ \left[-\frac{\mathrm{i}}{2}\left(1 - x\cos(ka)\right)\sin(2\theta_k) + \mathrm{i}\frac{x}{2}\sin(ka)\cos(2\theta_k)\right]\left(f^\dagger_k f^\dagger_{-k} - \text{h.c.}\right)\Bigg\}\,.
\end{aligned} \qquad \text{(E.12)}$$

The coefficient of the pair creation and annihilation terms vanish for

$$\tan(2\theta_k) = \frac{x\sin(ka)}{1 - x\cos(ka)}\,. \qquad \text{(E.13)}$$

By applying this condition and the relations

$$\begin{aligned}
\cos(2\theta_k) &= \frac{1}{\sqrt{1+\tan^2(2\theta_k)}} = \frac{1 - x\cos(ka)}{\sqrt{(1-x)^2 + 2x(1-\cos(ka))}}\,, \qquad \text{(E.14a)} \\
\sin(2\theta_k) &= \frac{\tan(2\theta_k)}{\sqrt{1+\tan^2(2\theta_k)}} = \frac{x\sin(ka)}{\sqrt{(1-x)^2 + 2x(1-\cos(ka))}}\,, \qquad \text{(E.14b)} \\
\sin^2(\theta_k) &= \frac{1}{2}\Big(1 - \cos(2\theta_k)\Big)\,, \qquad \text{(E.14c)} \\
\sum_k^{1.\mathrm{BZ}} \cos(ka) &= 0\,, \qquad \text{(E.14d)}
\end{aligned}$$

one obtains the diagonal Hamiltonian

$$\frac{H}{\Gamma_z} = \sum_k^{1.\mathrm{BZ}} \epsilon(k)\left(f^\dagger_k f_k - \frac{1}{2}\right)\,, \qquad \text{(E.15a)}$$

$$\epsilon(k) = \sqrt{\Big(1 - x\Big)^2 + 2x\Big(1 - \cos(ka)\Big)} \qquad \text{(E.15b)}$$

with the ground state energy

$$\epsilon_0 = \langle 0|H|0\rangle = -\frac{1}{2}\sum_k^{1.\mathrm{BZ}} \sqrt{\Big(1 - x\Big)^2 + 2x\Big(1 - \cos(ka)\Big)}\,. \qquad \text{(E.16)}$$

For $x \leq 1$, the ground state is described by the vacuum state $|0\rangle$ with $f_k^\dagger f_k|0\rangle = 0\,\forall k$ and the excitations are induced by the creation operators $f_k^\dagger$. The energy gap

$$\Delta(x) := \min_k\big(\epsilon(k)\big) = |1-x| \tag{E.17}$$

can be found at $k = 0$ in the ferromagnetic case $x > 0$ and at $k = \pi/a$ in the antiferromagnetic case $x < 0$. In principle, both cases are described in an analogous way and can be transformed into one another with a momentum shift $k \to k + \frac{\pi}{a}$, which one can check explicitly for the dispersion

$$\begin{aligned}
\epsilon_x(k) &= \sqrt{\left(1-x\right)^2 + 2x\left[2\sin^2\left(\frac{ka}{2}\right)\right]} \\
&= \sqrt{1+x^2+2x\left[2\sin^2\left(\frac{ka}{2}\right)-1\right]} \\
&= \sqrt{1+x^2+2x\left[\sin^2\left(\frac{ka}{2}\right)-\cos^2\left(\frac{ka}{2}\right)\right]}\,, \qquad \text{(E.18)}\\
\epsilon_{-x}\left(k+\frac{\pi}{a}\right) &= \sqrt{1+x^2-2x\left[\cos^2\left(\frac{ka}{2}\right)-\sin^2\left(\frac{ka}{2}\right)\right]} = \epsilon_x(k)\,. \qquad \text{(E.19)}
\end{aligned}$$

For simplicity, we only consider the antiferromagnetic case explicitly. At the quantum critical point $x = 1$, the gap closes linearly and a quantum phase transition between the magnetically ordered phase and the unordered phase occurs [146]

$$\epsilon_1(k) = \sqrt{2\Big(1-\cos(ka)\Big)} = 2\left|\sin\left(\frac{ka}{2}\right)\right| \overset{ka\ll 1}{\approx} |ka|\,. \tag{E.20}$$

Note that the phase transition occurs at $T = 0$ and is induced solely by quantum fluctuation. One can define the magnetization in x-direction

$$M(x) = \left\langle 0\middle|\sum_{i=0}^{N-1} S_i^x\middle|0\right\rangle = \begin{cases} \frac{1}{2}\left(1-\frac{1}{x^2}\right)^{\frac{1}{8}} & \text{if } x > 1\,, \\ 0 & \text{if } x \in [0,1]\,, \end{cases} \tag{E.21}$$

as an order parameter to characterize the phase with the critical exponent $\beta = \frac{1}{8}$ [146]. The magnetization is plotted in Fig. E.1.

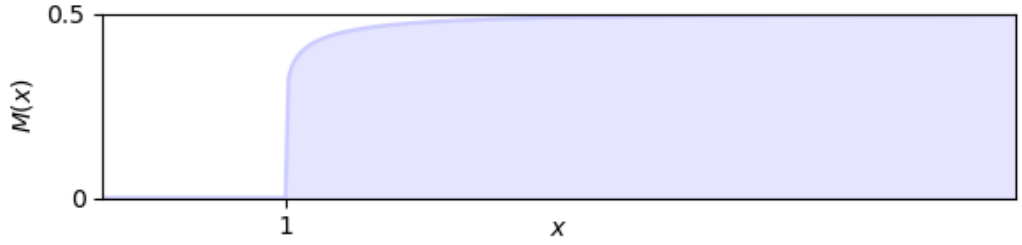

Figure E.1: Dispersion $M(x)$, see (E.21), of the TFIM.

Appendix F

Derivation of Lindblad Master Equations

In Chap. 5 we discuss flow equations for non-Hermitian matrices and in Sec. 5.1 we introduce Lindblad master equations (5.1.1). In the following, we present a derivation of the Lindblad master equations from unitary time evolution [152].

Consider a total system consisting of the main system of interest and the external environment, see Fig. 5.1. The Hilbert space $\mathcal{H}$, density matrix ρ and Hamiltonian H of the environment are denoted by the subscript E. For the total system we use the subscript T. The unitary time evolution of the total system is described by the von Neumann equation

$$\dot{\rho}_{\mathrm{T}}(t) = -\mathrm{i}\,[H_{\mathrm{T}}, \rho_{\mathrm{T}}(t)]\ . \tag{F.1}$$

Our goal is finding a Markovian equation of motion, i.e. an equation of motion that does not depend on past events, of the system $\rho(t)$, in which no knowledge of the exact time evolution of the environment $\rho_{\mathrm{E}}(t)$ is necessary. These equations of motion are non-unitary. We begin by introducing some necessary assumptions.

1) **The interaction between the system and environment is small** compared to the inherent energy scales

$$H_{\mathrm{T}} = H \otimes \mathbb{1}_{\mathrm{E}} + \mathbb{1}_{\mathrm{S}} \otimes H_{\mathrm{E}} + \alpha H_{\mathrm{I}}, \quad \alpha \ll 1\,. \tag{F.2}$$

Here, we explicitly denote the identity operators once for clarity, but we will omit them in the following calculations for brevity. The interaction Hamiltonian can be expressed as

$$H_{\mathrm{I}} = \sum_i S_i \otimes E_i\,. \tag{F.3}$$

with $S_i \in \mathcal{H}$ and $E_i \in \mathcal{H}_{\mathrm{E}}$.

1a) For all operators E_i appearing in H_I, one can safely assume

$$\langle E_i \rangle = \mathrm{Tr}[E_i \rho_\mathrm{E}(0)] = 0 \; \forall i \,. \tag{F.4}$$

If this assumption were not true for any E_i, one could always perform an energy shift on H_T and define H'_I with new operators E'_i, so that

$$H_\mathrm{T} = \left(H + \alpha \sum_i \langle E_i \rangle S_i \right) + H_\mathrm{E} + \alpha H'_\mathrm{I} \,, \tag{F.5a}$$

$$H'_\mathrm{I} = \sum_i S_i \otimes E'_i := \sum_i S_i \otimes \left(E_i - \langle E_i \rangle \right) \tag{F.5b}$$

and $\langle E'_i \rangle = 0$.

2) **At $t = 0$ the system and environment are not correlated** and, therefore, the density matrix is separable

$$\rho_\mathrm{T}(0) = \rho(0) \otimes \rho_\mathrm{E}(0) \,. \tag{F.6}$$

This is possible if the system and environment have not interacted at $t < 0$ or if the correlations are short-lived.

2a) Combining assumptions 1) and 2), it is reasonable to assume that the system and the environment stay uncorrelated during the time evolution

$$\rho_\mathrm{T}(t) = \rho(t) \otimes \rho_\mathrm{E}(t) \,. \tag{F.7}$$

This is not true exactly because the interaction can create correlations. However, due to the small coupling strength α one can assume that the timescale of correlations τ_corr and the timescale of relaxations in the environment τ_E are much smaller than the typical system timescale τ, i.e.

$$\tau_\mathrm{corr}, \tau_\mathrm{E} \ll \tau \,. \tag{F.8}$$

2b) The assumption that the system and environment have not interacted in the past implies

$$H_\mathrm{I}(t) = 0 \; \forall t < 0 \,. \tag{F.9}$$

3) **The environment is thermal initially**

$$\rho_\mathrm{E}(0) = \frac{1}{\mathrm{Tr}\left[e^{-\beta H_\mathrm{E}}\right]} e^{-\beta H_\mathrm{E}} \quad , \beta = \frac{1}{k_\mathrm{B} T} \,, \tag{F.10}$$

where k_B is the Boltzmann constant and T the temperature.

3a) Combining assumptions 2a) and 3), it is safe to assume that the environment always stays thermal

$$\rho_\mathrm{E}(t) = \rho_\mathrm{E}(0) = \frac{1}{\mathrm{Tr}\left[e^{-\beta H_\mathrm{E}}\right]} e^{-\beta H_\mathrm{E}} \,. \tag{F.11}$$

With this, one finds

$$\rho_\mathrm{T}(t) = \rho(t) \otimes \rho_\mathrm{E}(0) \,. \tag{F.12}$$

We will now use these assumptions to derive the Lindblad master equations. We work in the interaction picture, where the time evolution of operators $O(t)$ is described by the inherent Hamiltonians $H+H_\mathrm{E}$ and the time evolution of the density matrix is described by the interaction Hamiltonian H_I

$$O(t) = e^{\mathrm{i}(H+H_\mathrm{E})t} O(0) e^{-\mathrm{i}(H+H_\mathrm{E})t}\,, \tag{F.13a}$$

$$\frac{\mathrm{d}}{\mathrm{d}t}\rho_\mathrm{T}(t) = -\mathrm{i}\alpha[H_\mathrm{I}(t), \rho_\mathrm{T}(t)]\,. \tag{F.13b}$$

The time evolution of the density matrix can, in principle, be integrated

$$\rho_\mathrm{T}(t) = \rho_\mathrm{T}(0) - \mathrm{i}\alpha \int_0^t \mathrm{d}s \big[H_\mathrm{I}(s), \rho_\mathrm{T}(s)\big]\,. \tag{F.14}$$

This formula poses two problems: One still needs to solve an integral in the total Hilbert space $\mathcal{H}_\mathrm{T}$ and requires knowledge of the time evolution $\rho_\mathrm{T}(s)$ for all previous times $s \in [0,t]$. One can tackle these issues by inserting (F.14) in (F.13b) once

$$\frac{\mathrm{d}}{\mathrm{d}t}\rho_\mathrm{T}(t) = -\mathrm{i}\alpha\big[H_\mathrm{I}(t), \rho_\mathrm{T}(0)\big] - \alpha^2 \int_0^t \mathrm{d}s \Big[H_\mathrm{I}(t), \big[H_\mathrm{I}(s), \rho_\mathrm{T}(s)\big]\Big] \tag{F.15}$$

and once more

$$\frac{\mathrm{d}}{\mathrm{d}t}\rho_\mathrm{T}(t) = -\mathrm{i}\alpha\big[H_\mathrm{I}(t), \rho_\mathrm{T}(0)\big] - \alpha^2 \int_0^t \mathrm{d}s \Big[H_\mathrm{I}(t), \big[H_\mathrm{I}(s), \rho_\mathrm{T}(t)\big]\Big] + \mathcal{O}(\alpha^3)\,. \tag{F.16}$$

At this point, $\rho_\mathrm{T}(s)$ only appears in order $\mathcal{O}(\alpha^3)$ and can be disregarded due to assumption 1). Now, one only requires knowledge of the density matrix $\rho_\mathrm{T}(t)$ at time 0 and t and the interaction Hamiltonian $H_\mathrm{I}(s)$ for all times $s \in [0,t]$. Since our goal is the derivation of an equation of motion for only the system of interest $\rho(t)$, we trace over all degrees of freedom of the environment

$$\frac{\mathrm{d}}{\mathrm{d}t}\rho(t) = \mathrm{Tr}_\mathrm{E}\left[\frac{\mathrm{d}}{\mathrm{d}t}\rho_\mathrm{T}(t)\right] \tag{F.17a}$$

$$= -\mathrm{i}\alpha \mathrm{Tr}_\mathrm{E}\big[H_\mathrm{I}(t), \rho_\mathrm{T}(0)\big] - \alpha^2 \int_0^t \mathrm{d}s \mathrm{Tr}_\mathrm{E}\Big[H_\mathrm{I}(t), \big[H_\mathrm{I}(s), \rho_\mathrm{T}(t)\big]\Big]\,. \tag{F.17b}$$

First, we focus on the first summand. We decompose H_I with (F.3), use the assumption of no correlation (F.6) and the cyclic invariance of the trace so that we can rewrite the summand to

$$\mathrm{Tr}_\mathrm{E}\big[H_\mathrm{I}(t), \rho_\mathrm{T}(0)\big] = \sum_i \Big(\big(S_i(t)\rho(0) - \rho(0)S_i(t)\big) \underbrace{\mathrm{Tr}_\mathrm{E}\big[E_i(t)\rho_\mathrm{E}(0)\big]}_{=\langle E_i\rangle \overset{(\mathrm{F.4})}{=} 0}\Big) = 0\,. \tag{F.18}$$

With this, the first summand of the equation of motion vanishes. One can rewrite the remaining summand

$$\frac{\mathrm{d}}{\mathrm{d}t}\rho(t) \overset{(\mathrm{F.12})}{=} -\alpha^2 \int_0^t \mathrm{d}s \mathrm{Tr}_\mathrm{E}\Big[H_\mathrm{I}(t), \big[H_\mathrm{I}(s), \rho(t)\otimes\rho_\mathrm{E}(0)\big]\Big]\,. \tag{F.19}$$

This result is already an independent equation of motion for $\rho(t)$ that is local in time, but it still depends on the initial state $\rho_{\mathrm{E}}(0)$ of the environment and is therefore non-Markovian. Using the assumption that no interaction occurs at $t < 0$, see (F.9), one can rewrite the equation of motion by performing a shift $s \to t - s$ and integrating up to ∞

$$\frac{\mathrm{d}}{\mathrm{d}t}\rho(t) = -\alpha^2 \int_0^\infty \mathrm{d}s \mathrm{Tr}_{\mathrm{E}}\Big[H_{\mathrm{I}}(t), \big[H_{\mathrm{I}}(t-s), \rho(t) \otimes \rho_{\mathrm{E}}(0)\big]\Big], \tag{F.20}$$

which is also known as the Redfield equation. This equation poses a problem: It does not warrant a positive map and can therefore give rise to non-positive density matrices. Therefore, we use a final approximation, the **rotating wave approximation**. To do so, we must first expand the commutators to

$$\begin{aligned}\frac{\mathrm{d}}{\mathrm{d}t}\rho(t) = -\alpha^2 \mathrm{Tr}\Big[&\int_0^\infty \mathrm{d}s H_{\mathrm{I}}(t)H_{\mathrm{I}}(t-s)\rho(t) \otimes \rho_{\mathrm{E}}(0) - \int_0^\infty \mathrm{d}s H_{\mathrm{I}}(t)\rho(t) \otimes \rho_{\mathrm{E}}(0)H_{\mathrm{I}}(t-s) \\ &- \int_0^\infty \mathrm{d}s H_{\mathrm{I}}(t-s)\rho(t) \otimes \rho_{\mathrm{E}}(0)H_{\mathrm{I}}(t) - \int_0^\infty \mathrm{d}s \rho(t) \otimes \rho_{\mathrm{E}}(0)H_{\mathrm{I}}(t-s)H_{\mathrm{I}}(t)\Big].\end{aligned} \tag{F.21}$$

We decompose the operators

$$S_i = \sum_\omega S_i(\omega) \tag{F.22}$$

in the basis of eigenstates $S_i(\omega)$ to the superoperator $[\cdot, H]$, i.e. operators that fulfill $[S_i(\omega), H] = \omega S_i(\omega)$ and, consequently, $[S_i^\dagger(\omega), H] = -\omega S_i^\dagger(\omega)$. To make use of this decomposition, one can switch to the Schrödinger picture for the operators of the interaction Hamiltonian

$$\tilde{S}_i = e^{\mathrm{i}Ht} S_i e^{-\mathrm{i}Ht}, \tag{F.23a}$$

$$\tilde{E}_i = e^{\mathrm{i}H_{\mathrm{E}}t} E_i e^{-\mathrm{i}H_{\mathrm{E}}t} \tag{F.23b}$$

$$\Rightarrow H_{\mathrm{I}}(t) = \sum_{i,\omega} e^{-\mathrm{i}\omega t} S_i(\omega) \otimes \tilde{E}_i(t) = \sum_{i,\omega} e^{\mathrm{i}\omega t} S_i^\dagger(\omega) \otimes \tilde{E}_i^\dagger(t). \tag{F.23c}$$

By using the decomposition in $S_i(\omega)$ for $H_{\mathrm{I}}(t-s)$ and the decomposition in $S_i^\dagger(\omega)$ for $H_{\mathrm{I}}(t)$, one can rewrite (F.21). Using $[H_{\mathrm{E}}, \rho_{\mathrm{E}}(0)] = 0$ and the cyclic invariance of the trace, one obtains

$$\frac{\mathrm{d}}{\mathrm{d}t}\rho(t) = \sum_{\substack{\omega,\omega' \\ n,j}} \left(e^{\mathrm{i}(\omega'-\omega)t} \Gamma_{nj}(\omega) \big[S_j(\omega)\rho(t), S_n^\dagger(\omega')\big] + e^{\mathrm{i}(\omega-\omega')t} \Gamma_{jn}^*(\omega') \big[S_j(\omega), \rho(t) S_n^\dagger(\omega')\big] \right), \tag{F.24a}$$

$$\Gamma_{nj}(\omega) = \int_0^\infty \mathrm{d}s\, e^{\mathrm{i}\omega s} \mathrm{Tr}_{\mathrm{E}}\Big[\tilde{E}_n^\dagger(t)\tilde{E}_j(t-s)\rho_{\mathrm{E}}(0)\Big], \tag{F.24b}$$

where the effect of the environment is hidden in $\Gamma_{nj}(\omega)$. Now, we can apply the rotating wave approximation, where we assume that $|\omega-\omega'| \gg \alpha^2$, i.e. the functions $e^{\pm \mathrm{i}(\omega'-\omega)t}$ oscillate much faster than the typical timescale of the system, which means that they do not contribute to the time evolution apart from resonant terms with $\omega = \omega'$. Using this, one obtains

$$\frac{\mathrm{d}}{\mathrm{d}t}\rho(t) = \sum_{\substack{\omega \\ n,j}} \left(\Gamma_{nj}(\omega) \big[S_j(\omega)\rho(t), S_n^\dagger(\omega) \big] + \Gamma_{jn}^*(\omega) \big[S_j(\omega), \rho(t) S_n^\dagger(\omega) \big] \right). \tag{F.25}$$

One can decompose this equation of motion into a unitary von Neumann term and a dissipative term. To do so, one has to divide Γ_{nj} into a Hermitian part γ_{nj} and an Antihermitian part π_{nj}, leading to

$$\Gamma_{nj}(\omega) = \frac{\gamma_{nj}(\omega)}{2} + \mathrm{i}\pi_{nj}(\omega)\,, \tag{F.26a}$$

$$\gamma_{nj}(\omega) = \Gamma_{nj}(\omega) + \Gamma_{nj}^*(\omega) = \int_{-\infty}^{\infty} \mathrm{d}s e^{\mathrm{i}\omega s} \mathrm{Tr}\left[\tilde{E}_n^\dagger(s) E_j(0) \rho_\mathrm{E}(0) \right], \tag{F.26b}$$

$$\pi_{nj}(\omega) = -\frac{\mathrm{i}}{2}\big(\Gamma_{nj}(\omega) - \Gamma_{nj}^*(\omega)\big)\,. \tag{F.26c}$$

One can use this decomposition and transform back to the Schrödinger picture, obtaining

$$\frac{\mathrm{d}}{\mathrm{d}t}\rho(t) = -\mathrm{i}[H + H_\mathrm{Lamb}, \rho(t)] + \sum_{\substack{\omega \\ n,j}} \gamma_{nj}(\omega) \left(S_j(\omega)\rho(t) S_n^\dagger(\omega) - \frac{1}{2}\left\{ S_n^\dagger(\omega) S_j(\omega), \rho(t) \right\} \right) \tag{F.27}$$

with the Lamb shift Hamiltonian

$$H_\mathrm{Lamb} = \sum_{\substack{\omega \\ n,j}} \pi_{nj}(\omega) S_n^\dagger(\omega) S_j(\omega)\,, \tag{F.28}$$

which renormalizes the energies of the system Hamiltonian because of the interaction with the environment. While this equation already presents a Markovian master equation, this is not yet the Lindblad form. The factors $\gamma_{nj}(\omega)$ are Fourier transforms of positive functions and therefore, the matrix $\gamma(\omega)$ formed by them is positive and can be diagonalized. In the diagonal basis, one obtains the celebrated Lindblad master equations

$$\mathrm{i}\frac{\mathrm{d}}{\mathrm{d}t}\rho(t) = [H + H_\mathrm{Lamb}, \rho(t)] + \mathrm{i}\hbar \sum_{\alpha,\omega} \gamma_\alpha \left(L_\alpha(\omega)\rho(t) L_\alpha^\dagger(\omega) - \frac{1}{2}\left\{ L_\alpha^\dagger(\omega) L_\alpha(\omega), \rho(t) \right\} \right) \tag{F.29}$$

where the operators L_α are often called Lindblad operators [60] or (quantum) jump operators [86, 152] and the corresponding rates are denoted by γ_α. In the simplest case, one only considers a single relevant frequency ω and the Lamb shift can be neglected, in which case one obtains

$$\mathrm{i}\frac{\mathrm{d}}{\mathrm{d}t}\rho(t) = [H, \rho(t)] + \mathrm{i}\hbar \sum_{\alpha} \gamma_\alpha \left(L_\alpha \rho(t) L_\alpha^\dagger - \frac{1}{2}\left\{ L_\alpha^\dagger L_\alpha, \rho(t) \right\} \right). \tag{F.30}$$

Appendix G

Dissipative Generalizations of PC-Generator

In Chap. 5 we discuss flow equations for non-Hermitian matrices and in Sec. 5.4 we introduce the gpc-generator, a generalization of the pc-generator (2.3.22) to the non-Hermitian case. During initial testing, we considered other generalizations of the pc-generator, as well, which are presented here to inform the reader about less promising trials.

G.1 Phase-Shifted PC-Generator

Definition

As discussed in Sec. 5.4 , the pc-generator can be adapted to Antihermitian matrices by introducing a phase factor $e^{\mathrm{i}\pi/2} = \mathrm{i}$, which is connected to the imaginary differences of diagonal elements. The gpc-generator generalizes this idea by calculating the phase factor $\exp(\mathrm{i}\varphi_{nj}) := \frac{m_{nn}-m_{jj}}{|m_{nn}-m_{jj}|}$ for each pair of diagonal elements. A different scheme to incorporate a phase factor to the pc-generator is the **phase-shifted particle-conserving generator (ppc-generator)**

$$\eta^{\mathrm{ppc}}_{nj}(\theta)[M] = \mathrm{sign}(n-j)e^{\mathrm{i}\theta}m_{nj} \qquad ,\theta \in \left[0, \frac{\pi}{2}\right] , \tag{G.1}$$

which uses a fixed phase factor $e^{\mathrm{i}\theta}$. The idea is that matrices with mostly Hermitian components can still be treated well by the pc-generator ($\theta = 0$) and matrices with mostly Antihermitian components can be treated well by the ipc-generator ($\theta = \pi/2$). Therefore, choosing a suitable θ can lead to convergence for matrices with various crossover ratios of Hermitian and Antihermitian components. One can use a fixed value $\theta = \frac{\pi}{4}$ for convenience sake, but calculating a suitable θ for each matrix M by comparing the norms of the Hermitian part $H = (M + M^\dagger)/2$ and the Antihermitian

part $A = (M - M^\dagger)/2$ is also possible, i.e.

$$\alpha = \frac{\|M - M^\dagger\| - \|M + M^\dagger\|}{2\|M\|} \,. \tag{G.2}$$

Convergence Speed

We benchmark the convergence speed with the convergence coefficients introduced in Sec. 5.7.1.1 and the random $(D \times D)$-dimensional matrices M defined in Sec. 5.7.2. During the benchmark, we vary two parameters , the phase ratio φ and the crossover ratio α with

$$\theta = \frac{\pi}{2}\varphi \,, \tag{G.3a}$$

$$M = (1-\alpha)(R + R^\dagger) + \alpha(R - R^\dagger) = R + (1-2\alpha)R^\dagger \,. \tag{G.3b}$$

Therefore, the parameters are restricted to the intervall $\varphi, \alpha \in [0, 1]$, where 0 corresponds to the Hermitian case and the pc-generator, respectively, while 1 corresponds to the Antihermitian case and the ipc-generator, respectively. For $\varphi = \alpha$ the phase ratio of the generator matches the crossover ratio of the Antihermitian and Hermitian components of M.

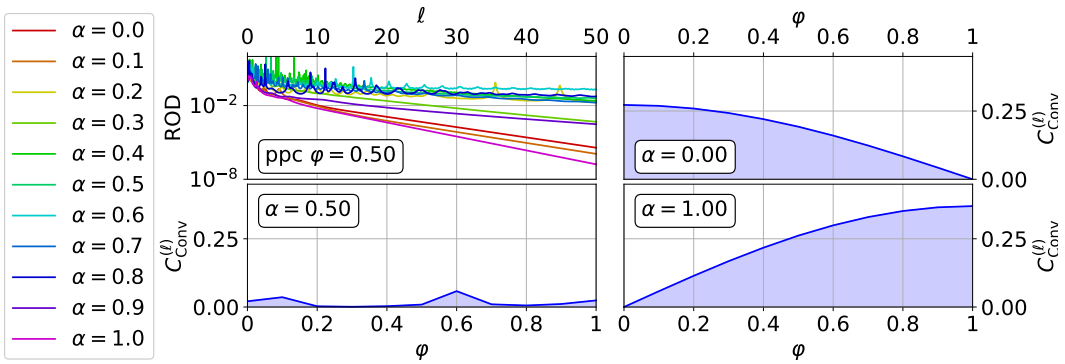

Figure G.1: Top left: Exemplary ROD flow of the ppc-generator, see (G.1), with fixed $\varphi = 0.5$ for mixed random matrices with varying α. The other three panels depict the convergence coefficients, each for a fixed random matrix with given α, diagonalized by the ppc-generator with various values of φ. All matrices are of dimension $D = 20$.

Fig. G.1 show exemplary flows $\mathrm{ROD}(\ell)$ and convergence coefficients $C^{(\ell)}_{\mathrm{Conv}}$ for various α and φ. A fast decrease of $\mathrm{ROD}(\ell)$ and larger values of $C^{(\ell)}_{\mathrm{Conv}}$ are favorable. Since the prefactor of the generator only changes by a phase factor, the scale of ℓ does not change with φ and one can compare the flow $\mathrm{ROD}(\ell)$ instead of $\mathrm{ROD}(t)$. The top left panel depicts the flow $\mathrm{ROD}(\ell)$ for the ppc-generator with $\varphi = 0.5$ and various matrix phase ratios α. Convergence is achieved in all cases, but the convergence speed varies. Contrary to expectation, fastest convergence is achieved for $\alpha \approx 0$ and $\alpha \approx 1$, i.e. for Hermitian and Antihermitian matrices. Convergence is very slow for $\alpha \approx 0.5$, which signifies that $\alpha \approx \varphi$ does not guarantee fast convergence speed. In fact, the

ROD(ℓ) increases periodically for $\alpha \approx 0.5$. We do not benchmark the truncation error, see Sec. 5.7.1.2 , for this generator, but note that a temporarily increasing ROD(ℓ) is an indicator for truncation errors and is therefore an unfavorable result. This problem does not occur when using the gpc-generator for random matrices, which is discussed in Sec. 5.7.2.2 and displayed in Fig. 5.7, in particular.

Additionally, the bottom left panel shows that the convergence coefficient $C_{\mathrm{Conv}}^{(\ell)}$ for fixed $\alpha = 0.5$ is not maximized by choosing $\varphi = \alpha$, i.e. $\varphi = 0.5$, and $C_{\mathrm{Conv}}^{(\ell)}$ is not related to $|\varphi - \alpha|$ in a trivial way. The exceptions are $\alpha = 0$ (top right panel), where the pc-generator ($\varphi = 0$) shows fastest convergence, and $\alpha = 1$ (bottom right panel), where the ipc-generator ($\varphi = 1$) is optimal. Note that $C_{\mathrm{Conv}}^{(\ell)}$ vanishes for $|\alpha - \varphi| = 1$ because our calculations show no convergence in these cases.

We conclude that by choosing the ppc-generator with $\varphi \in]0, 1[$ instead of the pc- or ipc-generator, one can potentially increase the convergence speed and achieve convergence for all $\alpha \in [0, 1]$. However, finding the optimal value of φ a priori is not trivial and in many cases, the optimal convergence speed is achieved with the pc- or ipc-generator. Overall, the ppc-generator is vastly inferior to the gpc-generator, which offers faster convergence without periodically increasing ROD(ℓ).

G.2 Hermitized PC-Generator

Definition

Since the pc-generator can be used to diagonalize Hermitian matrices, one approach for diagonalizing non-Hermitian matrices M is the construction of a Hermitian matrix

$$H := M^\dagger M, \qquad h_{nj} = \sum_k m_{kn}^* m_{kj} \,. \tag{G.4}$$

The matrix H can be diagonalized with the pc-generator while M is treated as an observable so that after integration one obtains M_{eff} in the effective basis. We call this approach the **hermitized particle-conserving generator (hpc-generator)**

$$\eta_{nj}^{\mathrm{hpc}}[M] := \eta_{nj}^{\mathrm{pc}}[H] = \mathrm{sign}(n - j) \sum_k m_{kn}^* m_{kj} \,. \tag{G.5}$$

For the concrete numerical implementation, one can either integrate the flow of $M(\ell)$ and $H(\ell)$ simultaneously, or only transform $M(\ell)$ explicitly, in which case one must calculate $H(\ell) = M^\dagger(\ell) M(\ell)$ in each integration step to obtain $\eta(\ell)$.

Fixed Points of the PC- and HPC-Generator

The attractive fixed points of the pc-generator are diagonal matrices [28]. By assuming that the flow has converged to a fixed point, i.e. a point where the flow

stops, one finds

$$\partial_\ell h_{nn} = 0 \tag{G.6a}$$

$$\Rightarrow \sum_{k>n} |h_{nk}| = 0 \tag{G.6b}$$

$$\Rightarrow |h_{nj}| = 0 \quad \forall n \neq j\,. \tag{G.6c}$$

The Hermitian matrix H is diagonal at the fixed point. Since one aims to diagonalize M when applying the generator $\eta_{nj}^{\mathrm{hpc}}[M]$, it is useful to express the fixed point by the elements m_{nj} of M

$$\forall n \neq j : 0 = h_{nj} \tag{G.7a}$$

$$= \sum_k m_{kn}^* m_{kj} \tag{G.7b}$$

$$= \boldsymbol{m}_n^\dagger \boldsymbol{m}_j\,. \tag{G.7c}$$

The last line uses the standard inner product of complex vectors. By including the case $n = j$, one can formulate this fixed point condition in the form

$$\boldsymbol{m}_n^\dagger \boldsymbol{m}_j = \delta_{nj} |\boldsymbol{m}_n|^2\,. \tag{G.8}$$

This condition strongly resembles the condition for a unitary matrix $\boldsymbol{m}_j^\dagger \boldsymbol{m}_n = \delta_{nj}$, where the column vectors form an orthonormal basis. The condition (G.8), however, only causes $\boldsymbol{m}_n$ to form an orthogonal basis without normalization.

To conclude, the fixed points of the hpc-flow are defined by (G.8) and include many matrices M which are not diagonal. Hence, the hpc-generator does not guarantee diagonalization of M.

Convergence Speed

We showed that the hpc-generator does not guarantee diagonalization. In this section, we confirm this finding numerically. To this end, we attempt to diagonalize random $(D \times D)$-dimensional matrices M, see Sec. 5.7.2 , with the hpc-generator. We show exemplary results in Fig. G.2. The top panel depicts the ROD of the Hermitian matrix $H = M^\dagger M$, which converges to 0 as expected. However, the bottom panel shows that the ROD$[M]$ of the matrix M of interest converges to a finite value, in most cases. For $\alpha \geq 0.5$, the ROD$[M]$ decreases extremely slowly and periodically increases, which is an indicator of unfavorable truncation errors. The computationally expensive integration of the hpc-generator is superfluous if it concludes with only a partial reduction of ROD$[M]$.

To conclude, the hpc-generator does not offer any benefits over the gpc-generator.

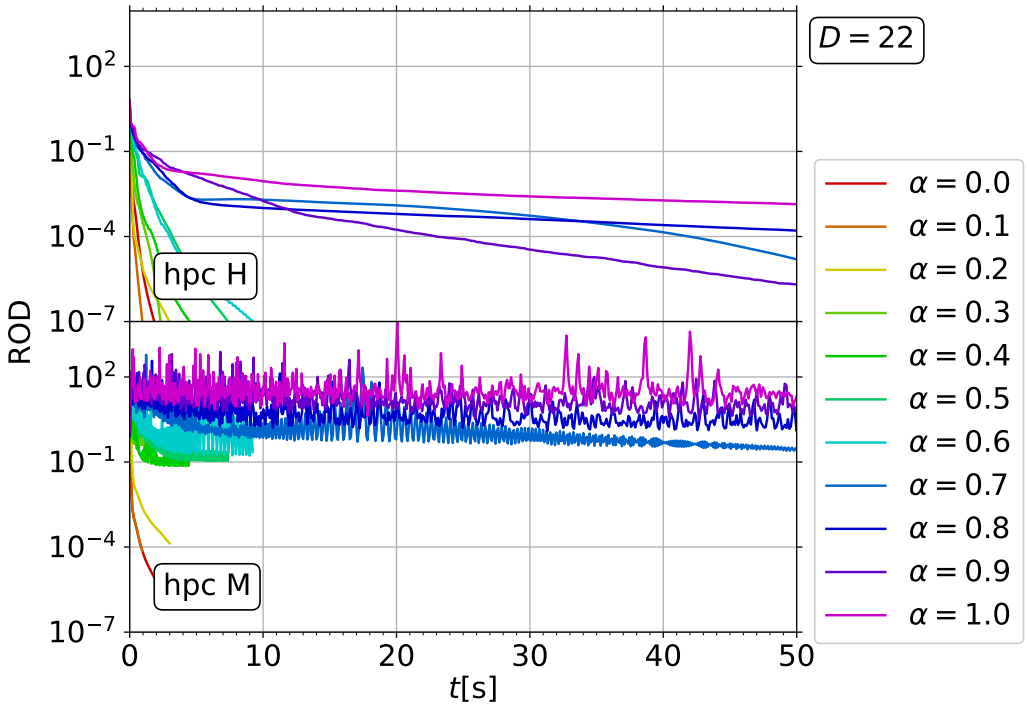

Figure G.2: Flow of ROD$[H = M^\dagger M](\ell)$ (top) and ROD$[M](\ell)$ (bottom) induced by the hpc-generator, see (G.5), for random matrices with different crossover ratios α, see Sec. 5.7.2 .

G.3 Switching between PC- and IPC-Generator

A non-Hermitian matrix can be expressed as a superposition $M = H + A$ of a Hermitian matrix H and an Antihermitian matrix A. Since the pc-generator works well for Hermitian matrices and the ipc-generator performs equally well for Antihermitian matrices, it seems reasonable to use them one after another

$$M = H + A := \frac{M + M^\dagger}{2} + \frac{M - M^\dagger}{2} \tag{G.9a}$$

$$\xrightarrow{\eta^{\mathrm{ipc}}[H]} M' = H' + A'_{\mathrm{diag}} \tag{G.9b}$$

$$\xrightarrow{\eta^{\mathrm{pc}}[A]} M'' = H''_{\mathrm{diag}} + A''_{\mathrm{diag}} \,. \tag{G.9c}$$

Note that for each step (M, M' and M''), H and A are defined as the Hermitian and Antihermitian part of the respective matrix M. Indeed, the ipc-flow diagonalizes A, yielding A'_{diag}, and the pc-flow diagonalizes H', yielding H''_{diag}. However, for the final matrix M'' to be diagonal, the pc-flow must preserve the band-diagonality of A'_{diag} so that A''_{diag} is also diagonal. This condition is not fulfilled, which one can show by

examining the flow equations of the Antihermitian components (5.3.10)

$$\begin{aligned}\partial_\ell a_{nj} = \operatorname{sign}(n-j)\left[h_{nj}(a_{jj}-a_{nn}) + a_{nj}(h_{jj}-h_{nn})\right] \\ + \sum_{k\neq n,j}\left[\operatorname{sign}(n-k)\left(h_{nk}a_{kj}+a_{nk}h_{kj}\right) + \operatorname{sign}(j-k)\left(a_{nk}h_{kj}+h_{nk}a_{kj}\right)\right] .\end{aligned} \tag{G.10}$$

For an Antihermitian matrix, the terms $a_{nk} = 0\ \forall n \neq k$ vanish initially, but one still obtains a finite flow to the off-diagonals

$$\partial_\ell a_{nj} = \operatorname{sign}(n-j) h_{nj}(a_{jj}-a_{nn})\,, \tag{G.11}$$

due to the fact that H' is not yet diagonalized. Therefore, the pc-generator does not preserve the diagonality of the Antihermitian matrix A'_{diag}. Consequently, A''_{diag} (and therefore M'') are not guaranteed to be diagonal. If one reverses the order of the generators, i.e. starts with the pc-generator and subsequently uses the ipc-generator, an analogous argument shows that the diagonality of the Hermitian part is not preserved by the ipc-flow. Numerical calculations for random $(D \times D)$-dimensional matrices M, see Sec. 5.7.2 , confirm that alternating application of the pc- and ipc-generator does not lead to better results than applying one of the generators once. We do not show plots of the results because they do not provide any additional information.

To conclude, switching between the pc- and ipc-generator increases the computational cost without significantly decreasing the ROD. Therefore, it does not offer any benefits over the gpc-generator or even the basic pc- and ipc-generator.

Appendix H

Loss of Band-Diagonality of GPC-Generator

A particular advantage of the pc-generator (2.3.22) is the fact that it preserves the band-diagonality of Hermitian matrices. This property reduces the number of tracked coefficients during the integration of the flow equations and, therefore, decreases both computational cost and truncation errors. Unfortunately, the gpc-generator (5.4.15) does not inherit this property for non-Hermitian matrices. In this section, we investigate to what extent the gpc-generator preserves the band-diagonality of various matrices.

It is trivial that the gpc-generator preserves the band-diagonality of Hermitian matrices and all other matrices with real diagonal elements, because it is equivalent to the pc-generator for these matrices. We now define a broader blass of matrices

$$M = \{m_{nj}\} \text{ is } \textbf{complex-sorted} \iff m_{nn} = cx_n, c \in \mathbb{C}, x_n \in \mathbb{R}, x_{j+1} > x_j \forall n, j\,. \tag{H.1}$$

This definition is equivalent to the two conditions

1. all diagonal elements lie on a straight line through the origin in $\mathbb{C}$ and
2. they are sorted on this line.

The first condition is fulfilled, for instance, by the ordered truncated random matrices introduced in Sec. 5.7.2.3 . While the first condition is a strong restriction, the second condition can always be met for matrices without degeneracies by reordering indices. However, this reordering can increase the diagonal width of the matrix, i.e.

the number of minor diagonals including the diagonals with non-vanishing elements. The first condition is always fulfilled by Hermitian and Antihermitian matrices with sorted diagonals. We show that

> if $M(\ell) = \{m_{nj}(\ell)\}$ is **complex-sorted**
> $\Rightarrow$ the gpc-generator preverses the diagonal width of M infinitesimally,
> i.e. $\partial_\ell m_{nj} = 0 \; \forall |n-j| > \delta$ if M has diagonal width δ.

(H.2)

Proof:
A matrix is band-diagonal with diagonal width δ if

$$m_{nj} = 0 \; \forall |n-j| > \delta \,. \tag{H.3}$$

We prove that (H.3) implies $\partial_\ell m_{nj} = 0 \; \forall |n-j| > \delta$ by showing

$$\frac{m^*_{nn} - m^*_{kk}}{|m^*_{nn} - m^*_{kk}|} + \frac{m^*_{jj} - m^*_{kk}}{|m^*_{jj} - m^*_{kk}|} \overset{\text{(H.1)}}{=} \frac{c^*}{|c|}\left(\frac{x_n - x_k}{|x_n - x_k|} + \frac{x_j - x_k}{|x_j - x_k|}\right) \tag{H.4a}$$

$$\overset{n<k<j}{=} \frac{c^*}{|c|}(-1+1) = 0 \qquad \forall n < k < j \tag{H.4b}$$

and

$$\partial_\ell m_{nj} = -|m_{nn} - m_{jj}| \cdot \underbrace{m_{nj}}_{=0} + \sum_{k \neq n,j} \underbrace{\left(\frac{m^*_{nn} - m^*_{kk}}{|m^*_{nn} - m^*_{kk}|} + \frac{m^*_{jj} - m^*_{kk}}{|m^*_{jj} - m^*_{kk}|}\right)}_{=0 \; \forall n<k<j} \cdot \underbrace{m_{nk} m_{kj}}_{=0 \; \forall k \notin [n,j]} \tag{H.5a}$$

$$= 0 \qquad \forall |n-j| > \delta \,, \tag{H.5b}$$

where the step $m_{nk} m_{kj} = 0 \; \forall k < n \vee k > j$ follows from the band-diagonality (H.3). □

Note that we only proved (H.2), which states that the renormalization of the off-diagonals $\partial_\ell m_{nj} = 0$ vanishes as long as the matrix $M(\ell)$ is complex-sorted. If, at any point of the integration, the ordering of $m_{nn}(\ell)$ changes because two flows $m_{nn}(\ell)$ and $m_{jj}(\ell)$ cross one another, the bandwidth is no longer preserved. Additionally, the proof does not work for all band-diagonal matrices (H.3), because (H.4b) is not fulfilled if the matrix is not complex-sorted. A simple example, for which the gpc-flow does not conserve bandwidth, is the non-Hermitian matrix

$$M_1 = \begin{pmatrix} 0 & 1 & 0 \\ 1 & 1 & 1 \\ 0 & 1 & \mathrm{i} \end{pmatrix} . \tag{H.6}$$

In fact, one can even find a Hermitian matrix

$$M_2 = \begin{pmatrix} 0 & 1 & 0 \\ 1 & 1 & 1 \\ 0 & 1 & 0 \end{pmatrix} \tag{H.7}$$

for which neither the gpc- nor the pc-generator preserve bandwidth, because the diagonal elements are not initially ordered. Note, however, that for a matrix with unsorted real diagonal elements such as M_2 this can be fixed by simply sorting the diagonals, i.e.

$$M_2' = \begin{pmatrix} 0 & 1 & 1 \\ 1 & 0 & 0 \\ 1 & 0 & 1 \end{pmatrix} . \tag{H.8}$$

During such initial sorting, the bandwidth of the matrix can increase, because elements can be moved to minor diagonals with a larger distance to the diagonal. For non-Hermitian matrices, such as M_1, the diagonals are complex and a rigorous ordering is not always possible.

In conclusion, we showed that for the class of complex-sorted matrices $M(\ell)$, the gpc-generator does not renormalize matrix elements beyond the diagonal width $\partial_\ell m_{nj} = 0 \ \forall |n-j| > \delta$ at the specific value ℓ. However, the bandwidth is not preserved if the ordering of the diagonal elements changes at any point, i.e. if the matrix ceases to be complex-sorted. While the bandwidth is preserved in special cases, it should be expected for most application cases that the bandwidth is not preserved by the gpc-generator.

Bibliography

[1] J. Bila, *Emergent phenomena in complex systems and their detection*, International Journal of Enhanced Research in Science, Technology & Engineering **6**(12), 40 (2017), http://www.erpublications.com/our-journals-dtl-pdf.php?pid=1&id=241.

[2] P. W. Anderson, *Basic Notions of Condensed Matter Physics*, Addison-Wesley, Reading, MA, 1th edn., ISBN 9780201328301 (1997).

[3] S. Kehrein, *The Flow Equation Approach to Many-Particle Systems*, vol. 217 of *Springer Tracts in Modern Physics*, Springer-Verlag, Berlin Heidelberg, 1th edn., doi: 10.1007/3-540-34068-8 (2006).

[4] F. Wegner, *Flow-equations for Hamiltonians*, Ann. der Phys. **3**, 77 (1994), doi: 10.1002/andp.19945060203.

[5] S. D. Glazek and K. G. Wilson, *Renormalization of Hamiltonians*, Phys. Rev. D **48**(12), 5863 (1993), doi: 10.1103/PhysRevD.48.5863.

[6] S. D. Glazek and K. G. Wilson, *Perturbative renormalization group for Hamiltonians*, Phys. Rev. D **49**(8), 4214 (1994), doi: 10.1103/PhysRevD.49.4214.

[7] M. T. Chu and K. R. Driessel, *The Projected Gradient Method for Least Squares Matrix Approximations with Spectral Constraints*, SIAM Journal on Numerical Analysis **27**(4), 1050 (1990), doi: 10.1137/0727062.

[8] R. W. Brockett, *Dynamical Systems That Sort Lists, Diagonalize Matrices, and Solve Linear Programming Problems*, Linear Algebra and Its Applications **146**, 79 (1991), doi: 10.1016/0024-3795(91)90021-N.

[9] M. T. Chu, *A List of Matrix Flows with Applications*, Fields Institute Communications **3**, 87 (1994), http://citeseerx.ist.psu.edu/viewdoc/summary?doi=10.1.1.69.736.

[10] S. K. Kehrein and A. Mielke, *Flow equations for the Anderson Hamiltonian*, Journal of Physics A **27**(12), 4259 (1994), doi: 10.1088/0305-4470/27/12/030.

[11] S. K. Kehrein and A. Mielke, *On the spin-boson model with a sub-ohmic bath*, Physics Letters A **219**(5-6), 313 (1996), doi: 10.1016/0375-9601(96)00475-6.

[12] S. K. Kehrein, A. Mielke and P. Neu, *Flow equations for the spin-boson problem*, Zeitschrift für Physik B **99**(269) (1996), doi: 10.1007/s002570050037.

[13] A. Mielke, *Calculating critical temperatures of superconductivity from a renormalized Hamiltonian*, Europhysics Letters **40**(2), 195 (1997), doi: 10.1209/epl/i1997-00445-5.

[14] A. Mielke, *Similarity renormalization of the electron-phonon coupling*, Annalen der Physik **509**(3), 215 (1997), doi: 10.1002/andp.19975090305.

[15] S. K. Kehrein and A. Mielke, *Low temperature equilibrium correlation functions in dissipative quantum systems*, Annalen der Physik **509**(2), 90 (1997), doi: 10.1002/andp.19975090203.

[16] S. K. Kehrein and A. Mielke, *Diagonalization of System plus Environment Hamiltonians*, Journal of Statistical Physics **90**(3-4), 889 (1998), doi: 10.1023/A:1023289323069.

[17] C. Knetter and G. S. Uhrig, *Perturbation theory by flow equations: dimerized and frustrated $S = 1/2$ chain*, European Physical Journal B **13**(2), 209 (2000), doi: 10.1007/s100510050026.

[18] K. P. Schmidt and G. S. Uhrig, *Excitations in One-Dimensional $S = \frac{1}{2}$ Quantum Antiferromagnets*, Phys. Rev. Lett. **90**(22), 2227204 (2003), doi: 10.1103/PhysRevLett.90.227204.

[19] M. Hafez-Torbati and G. S. Uhrig, *Singlet exciton condensation and bond-order-wave phase in the extended Hubbard model*, Phys. Rev. B **96**(12), 125129 (2017), doi: 10.1103/PhysRevB.96.125129.

[20] M. Hafez-Torbati and G. S. Uhrig, *Massive spinons in $S = 1/2$ spin chains: Spinon-pair operator representation*, Phys. Rev. B **95**(15), 155136 (2017), doi: 10.1103/PhysRevB.95.155136.

[21] S. Kehrein, *Flow Equation Solution for the Weak- to Strong-Coupling Crossover in the Sine-Gordon Model*, Phys. Rev. Lett. **83**(24), 4914 (1999), doi: 10.1103/PhysRevLett.83.4914.

[22] S. Kehrein, *Flow equation approach to the sine-Gordon model* , Nuclear Physics B **592**(3), 512 (2001), doi: 10.1016/S0550-3213(00)00507-1.

[23] C. Knetter, A. Bühler, E. Müller-Hartmann and G. S. Uhrig, *Dispersion and Symmetry of Bound States in the Shastry-Sutherland Model*, Phys. Rev. Lett. **85**(19), 3958 (2000), doi: 10.1103/PhysRevLett.85.3958.

[24] B. Fauseweh, F. Groitl, T. Keller, K. Rolfs, D. A. Tennant, K. Habicht and G. S. Uhrig, *Time-dependent correlations in quantum magnets at finite temperature*, Phys. Rev. B **94**(18), 180404(R) (2016), doi: 10.1103/PhysRevB.94.180404.

[25] M. Malki, L. Müller and G. S. Uhrig, *Absence of localized edge modes in spite of a non-trivial Zak phase in $BiCu_2PO_6$*, Phys. Rev. Research **1**(3), 033197 (2019), doi: 10.1103/PhysRevResearch.1.033197.

[26] A. Verdeny, A. Mielke and F. Mintert, *Accurate Effective Hamiltonians via Unitary Flow in Floquet Space*, Phys. Rev. Lett. **111**(17), 175301 (2013), doi: 10.1103/PhysRevLett.111.175301.

[27] M. Vogl, P. Laurell, A. D. Barr and G. A. Fiete, *Flow Equation Approach to Periodically Driven Quantum Systems*, Phys. Rev. X **9**(2), 021037 (2019), doi: 10.1103/PhysRevX.9.021037.

[28] A. Mielke, *Flow equations for band-matrices*, European Physical Journal B **5**(3), 605 (1998), doi: 10.1007/s100510050485.

[29] A. Reischl, E. Müller-Hartmann and G. S. Uhrig, *Systematic mapping of the Hubbard model to the generalized t-J model*, Phys. Rev. B **70**(24), 245124 (2004), doi: 10.1103/PhysRevB.70.245124.

[30] M. Powalski, G. S. Uhrig and K. P. Schmidt, *Roton Minimum as a Fingerprint of Magnon-Higgs Scattering in Ordered Quantum Antiferromagnets*, Phys. Rev. Lett. **115**(20) (2015), doi: 10.1103/PhysRevLett.115.207202.

[31] M. Powalski, K. P. Schmidt and G. S. Uhrig, *Mutually attracting spin waves in the square-lattice quantum antiferromagnet*, SciPost Physics **4**(1), 001 (2018), doi: 10.21468/SciPostPhys.4.1.001.

[32] H. Krull, N. A. Drescher and G. S. Uhrig, *Enhanced perturbative continuous unitary transformations*, Phys. Rev. B **86**(12), 125113 (2012), doi: 10.1103/PhysRevB.86.125113.

[33] S. W. Lovesey, *Theory of Neutron Scattering from Condensed Matter*, vol. 72 of *The International Series of Monographs on Physics*, Oxford University Press, Oxford, ISBN 9780198520283 (1987).

[34] H. Ibach and H. Lüth, *Solid-State Physics*, Springer-Verlag, Berlin Heidelberg, 4th edn., doi: 10.1007/978-3-540-93804-0 (2009).

[35] B. Fauseweh and G. S. Uhrig, *Multiparticle spectral properties in the transverse field Ising model by continuous unitary transformations*, Phys. Rev. B **87**(18), 184406 (2013), doi: 10.1103/PhysRevB.87.184406.

[36] L. Splinter, N. A. Drescher, H. Krull and G. S. Uhrig, *Minimal model for the frustrated spin ladder system $BiCu_2PO_6$*, Phys. Rev. B **94**(15), 155115 (2016), doi: 10.1103/PhysRevB.94.155115.

[37] C. Jia, K. Wohlfeld, Y. Wang, B. Moritz and T. P. Devereaux, *Using RIXS to Uncover Elementary Charge and Spin Excitations*, Phys. Rev. X **6**(2), 021020 (2016), doi: 10.1103/PhysRevX.6.021020.

[38] S. Kourtis, J. van den Brink and M. Daghofer, *Exact diagonalization results for resonant inelastic x-ray scattering spectra of one-dimensional Mott insulators*, Phys. Rev. B **85**(6), 064423 (2012), doi: 10.1103/PhysRevB.85.064423.

[39] J. Schlappa, T. Schmitt, F. Vernay, V. N. Strocov, V. Ilakovac, B. Thielemann, H. M. Rønnow, S. Vanishri, A. Piazzalunga, X. Wang, L. Braicovich, G. Ghiringhelli *et al.*, *Collective Magnetic Excitations in the Spin Ladder $Sr_{14}Cu_{24}O_{41}$ Measured Using High-Resolution Resonant Inelastic X-Ray Scattering*, Phys. Rev. Lett. **103**(4), 047401 (2009), doi: 10.1103/PhysRevLett.103.047401.

[40] U. Kumar, A. Nocera, E. Dagotto and S. Johnston, *Multi-spinon and anti-holon excitations probed by resonant inelastic x-ray scattering on doped one-dimensional antiferromagnets*, New Journal of Physics **20**(7), 073019 (2018), doi: 10.1088/1367-2630/aad00a.

[41] R. Bulla, A. C. Hewson and T. Pruschke, *Numerical renormalization group calculations for the self-energy of the impurity Anderson model*, Journal of Physics: Condensed Matter **10**(37), 8365 (1998), doi: 10.1088/0953-8984/10/37/021.

[42] C. Raas, G. S. Uhrig and F. Anders, *High-energy dynamics of the single-impurity Anderson model*, Phys. Rev. B **69**(4), 041102(R) (2004), doi: 10.1103/PhysRevB.69.041102.

[43] A. Nocera, U. Kumar, N. Kaushal, G. Alvarez, E. Dagotto and S. Johnston, *Computing Resonant Inelastic X-Ray Scattering Spectra Using The Density Matrix Renormalization Group Method*, Scientific Reports **8**(1), 11080 (2018), doi: 10.1038/s41598-018-29218-8.

[44] G. Ferkinghoff, L. Müller, G. S. Uhrig, U. Kumar and B. Fauseweh, *Accessing Multi-triplons in Spin Ladders using Resonant Inelastic X-ray Scattering*, preprint arXiv (submitted to Comm. Phys.) (2020), doi: 10.48550/arXiv.2012.01513.

[45] L. J. P. Ament, M. van Veenendaal, T. P. Devereaux, J. P. Hill and J. van den Brink, *Resonant inelastic x-ray scattering studies of elementary excitations*, Rev. Mod. Phys. **83**(2), 705 (2011), doi: 10.1103/RevModPhys.83.705.

[46] J. Schlappa, U. Kumar, K. J. Zhou, S. Singh, M. Mourigal, V. N. Strocov, A. Revcolevschi, L. Patthey, H. M. Rønnow, S. Johnston and T. Schmitt, *Probing multi-spinon excitations outside of the two-spinon continuum in the antiferromagnetic spin chain cuprate Sr_2CuO_3*, Nature Communications **9**, 5394 (2018), doi: 10.1038/s41467-018-07838-y.

[47] L. J. P. Ament, F. Forte and J. van den Brink, *Ultrashort lifetime expansion for indirect resonant inelastic x-ray scattering*, Phys. Rev. B **75**(11), 115118 (2007), doi: 10.1103/PhysRevB.75.115118.

[48] J. van den Brink and M. van Veenendaal, *Correlation functions measured by indirect resonant inelastic X-ray scattering*, Europhysics Letters **73**(1), 121 (2006), doi: 10.1209/epl/i2005-10366-9.

[49] U. Kumar, A. Nocera, E. Dagotto and S. Johnston, *Theoretical study of the spin and charge dynamics of two-leg ladders as probed by resonant inelastic x-ray scattering*, Phys. Rev. B **99**(20), 205130 (2019), doi: 10.1103/PhysRevB.99.205130.

[50] U. Kumar, A. Nag, J. Li, H. C. Robarts, A. C. Walters, M. García-Fernández, R. Saint-Martin, A. Revcolevschi, J. Schlappa, T. Schmitt, S. Johnston and K.-J. Zhou, *Unraveling higher-order corrections in the spin dynamics of RIXS spectra*, preprint arXiv (2021), doi: 10.48550/arXiv.2110.03186.

[51] S. Sachdev and B. Keimer, *Quantum criticality*, Physics Today **64**(2), 29 (2011), doi: 10.1063/1.3554314.

[52] T. Giamarchi, *Quantum Physics in One Dimension*, vol. 121 of *International Series of Monographs on Physics*, Oxford University Press, Great Clarendon Street, ISBN 9780198525004 (2004).

[53] A. Klauser, J. Mossel, J.-S. Caux and J. van den Brink, *Spin-Exchange Dynamical Structure Factor of the $S = 1/2$ Heisenberg Chain*, Phys. Rev. Lett. **106**(15), 157205 (2011), doi: 10.1103/PhysRevLett.106.157205.

[54] S. Sachdev, *Quantum Phase Transitions*, Cambridge University Press, 2th edn., doi: 10.1017/CBO9780511973765 (2011).

[55] Y. Nambu, *Quasi-Particles and Gauge Invariance in the Theory of Superconductivity*, Phys. Rev. **117**(3), 648 (1960), doi: 10.1103/PhysRev.117.648.

[56] J. Goldstone, *Field theories with «Superconductor» solutions*, Il Nuovo Cimento (1955-1965) **19**(1), 154 (1961), doi: 10.1007/BF02812722.

[57] J. Goldstone, A. Salam and S. Weinberg, *Broken Symmetries*, Phys. Rev. **127**(3), 965 (1962), doi: 10.1103/PhysRev.127.965.

[58] N. A. Drescher, T. Fischer and G. S. Uhrig, *Truncation errors in self-similar continuous unitary transformations*, European Physical Journal B **79**(2), 225 (2011), doi: 10.1140/epjb/e2010-10723-6.

[59] T. Fischer, S. Duffe and G. S. Uhrig, *Adapted continuous unitary transformation to treat systems with quasi-particles of finite lifetime*, New Journal of Physics **12**(3), 033048 (2010), doi: 10.1088/1367-2630/12/3/033048.

[60] H. P. Breuer and F. Petruccione, *The Theory of Open Quantum Systems*, Oxford University Press, Great Clarendon Street, doi: 10.1093/acprof:oso/9780199213900.001.0001 (2007).

[61] M. Beau, J. Kiukas, I. L. Egusquiza and A. del Campo, *Nonexponential quantum decay under environmental decoherence*, Phys. Rev. Lett. **119**, 130401 (2017), doi: 10.1103/PhysRevLett.119.130401.

[62] I. Carusotto and C. Ciuti, *Quantum fluids of light*, Rev. Mod. Phys. **85**(1), 299 (2013), doi: 10.1103/RevModPhys.85.299.

[63] N. Syassen, D. M. Bauer, M. Lettner, T. Volz, D. Dietze, J. J. García-Ripoll, J. I. Cirac, G. Rempe and S. Dürr, *Strong Dissipation Inhibits Losses and Induces Correlations in Cold Molecular Gases*, Science **320**(5881), 1329 (2008), doi: 10.1126/science.1155309.

[64] I. Carusotto, A. A. Houck, A. J. Kollár, P. Roushan, D. I. Schuster and J. Simon, *Photonic materials in circuit quantum electrodynamics*, Nature Physics **16**(3), 268 (2020), doi: 10.1038/s41567-020-0815-y.

[65] J. T. Barreiro, M. Müller, P. Schindler, D. Nigg, T. Monz, M. Chwalle, M. Hennrich, C. F. Roos, P. Zoller and R. Blatt, *An open-system quantum simulator with trapped ions*, Nature **470**(7335), 486 (2011), doi: 10.1038/nature09801.

[66] A. Browaeys and T. Lahaye, *Many-body physics with individually controlled Rydberg atoms*, Nature Physics **16**(2), 132 (2020), doi: 10.1038/s41567-019-0733-z.

[67] H. Y. Ling and B. Kain, *Topological study of a Bogoliubov-de Gennes system of pseudo spin-1/2 bosons with conserved magnetization in a honeycomb lattice*, Phys. Rev. A. **105**(2), 023319 (2022), doi: 10.1103/physreva.105.023319.

[68] R. L. Cook, L. Ko and K. B. Whaley, *A Quantum trajectory picture of single photon absorption and energy transport in photosystem II*, eprint arXiv (2021), doi: 10.48550/arXiv.2110.13811.

[69] L. Lenke, M. Mühlhauser and K. P. Schmidt, *High-order series expansion of non-Hermitian quantum spin models*, Phys. Rev. B **104**(19), 195137 (2021), doi: 10.1103/PhysRevB.104.195137.

[70] F. J. Dyson, *General Theory of Spin-Wave Interactions*, Phy. Rev. **102**(5), 1217 (1956), doi: 10.1103/PhysRev.102.1217.

[71] S. V. Maleev, *Scattering of Slow Neutrons in Ferromagnets*, Soviet Phys. JETP **6**(4), 776 (1958), [ZhÉTF, **33**(4), 1010], `http://jetp.ras.ru/cgi-bin/e/index/r/33/4/p1010?a=list`.

[72] F.-L. Xiong and W.-M. Zhang, *Controlling the dynamics of dissipationless localized bound states in open quantum systems with periodic driving fields*, Phys. Rev. A **104**(6), 062206 (2021), doi: 10.1103/PhysRevA.104.062206.

[73] M. Yarmohammadi, C. Meyer, B. Fauseweh, B. Normand and G. S. Uhrig, *Dynamical properties of a driven dissipative dimerized $S = 1/2$ chain*, Phys. Rev. B **103**(4), 045132 (2021), doi: 10.1103/PhysRevB.103.045132.

[74] E. Bairey, C. Guo, D. Poletti, N. H. Lindner and I. Arad, *Learning the dynamics of open quantum systems from their steady states*, New Journal of Physics **22**(3), 032001 (2020), doi: 10.1088/1367-2630/ab73cd.

[75] P. Hayden and J. Sorce, *A canonical Hamiltonian for open quantum systems*, Journal of Physics A **55**(22), 225302 (2021), doi: 10.1088/1751-8121/ac65c2.

[76] A. J. Daley, *Quantum trajectories and open many-body quantum systems, Advances in Physics*, Advances in Physics **63**(2), 77 (2014), doi: 10.1080/00018732.2014.933502.

[77] S. R. White and A. E. Feiguin, *Real-Time Evolution Using the Density Matrix Renormalization Group*, Phys. Rev. Lett. **93**(7), 076401 (2004), doi: 10.1103/PhysRevLett.93.076401.

[78] F. Verstraete, J. J. García-Ripoll and J. I. Cirac, *Matrix Product Density Operators: Simulation of Finite-Temperature and Dissipative Systems*, Phys. Rev. Lett. **93**(20), 207204 (2004), doi: 10.1103/PhysRevLett.93.207204.

[79] R. Cleve and C. Wang, *Efficient Quantum Algorithms for Simulating Lindblad Evolution*, 44th International Colloquium on Automata, Languages, and Programming (ICALP 2017) **80**, 17:1 (2017), doi: 10.4230/LIPIcs.ICALP.2017.17.

[80] J. Jin, A. Biella, O. Viyuela, L. Mazza, J. Keeling, R. Fazio and D. Rossini, *Cluster Mean-Field Approach to the Steady-State Phase Diagram of Dissipative Spin Systems*, Phys. Rev. X **6**(3), 031011 (2016), doi: 10.1103/PhysRevX.6.031011.

[81] H. Landa, M. Schiró and G. Misguich, *Multistability of Driven-Dissipative Quantum Spins*, Phys. Rev. Lett. **124**(4), 043601 (2020), doi: 10.1103/PhysRevLett.124.043601.

[82] P. Lenz and F. Wegner, *Flow equations for electron-phonon interactions*, Nuclear Physics B **482**(3), 693 (1996), doi: 10.1016/S0550-3213(96)00521-4.

[83] M. Ragwitz and F. Wegner, *Flow equations for electron-phonon interactions: phonon damping*, European Physical Journal B **8**(1), 9 (1999), doi: 10.1007/s100510050663.

[84] T. Stauber and A. Mielke, *Equilibrium correlation functions of the spin-boson model with sub-ohmic bath*, Physics Letters A **305**(5), 275 (2002), doi: 10.1016/S0375-9601(02)01416-0.

[85] S. P. Kelly, R. Nandkishore and J. Marino, *Exploring many-body localization in quantum systems coupled to an environment via Wegner-Wilson flows*, Nuclear Physics B **951**, 114886 (2020), doi: 10.1016/j.nuclphysb.2019.114886.

[86] L. Rosso, F. Iemini, M. Schirò and L. Mazza, *Dissipative flow equations*, SciPost Physics **9**(6), 91 (2020), doi: 10.21468/SciPostPhys.9.6.091.

[87] J.-P. Blazot and G. Ripka, *Quantum Theory of Finite Systems*, MIT Press, Cambridge, MA, ISBN 9780262022149 (1985).

[88] N. A. Drescher, *Variational and perturbative extensions of continuous unitary transformations for low-dimensional spin systems*, PhD thesis, TU Dortmund (2014), doi: 10.17877/DE290R-7051.

[89] H. Y. Yang and K. P. Schmidt, *Effective models for gapped phases of strongly correlated quantum lattice models*, Europhysics Letters **94**(1), 17004 (2011), `http://stacks.iop.org/0295-5075/94/i=1/a=17004`.

[90] A. C. Irving and C. J. Hamer, *Methods in Hamiltonian lattice field theory(II). Linked-cluster expansions*, Nuclear Physics **230**(3), 361 (1984), doi: 10.1016/0550-3213(84)90218-9.

[91] G. S. Uhrig and B. Normand, *Magnetic properties of $(VO)_2P_2O_7$ from frustrated interchain coupling*, Phys. Rev. B **58**(22), R14705(R) (1998), doi: 10.1103/PhysRevB.58.R14705.

[92] C. Knetter, K. P. Schmidt and G. S. Uhrig, *High order perturbation theory for spectral densities of multi-particle excitations: $S = 1/2$ two-leg Heisenberg ladder*, European Physical Journal B **36**(4), 525 (2003), doi: 10.1140/epjb/e2004-00008-2.

[93] S. Dusuel and G. S. Uhrig, *The quartic oscillator: a nonperturbative study by continuous unitary transformations*, Journal of Physics A **37**(39), 9275 (2004), doi: 10.1088/0305-4470/37/39/014.

[94] J. Stein, *Flow Equations and extended Bogoliubov transformation for the Heisenberg antiferromagnet near the classical limit*, European Physical Journal B **5**(2), 193 (1998), doi: 10.1007/s100510050434.

[95] C. Knetter, K. P. Schmidt and G. S. Uhrig, *The structure of operators in effective particle-conserving models*, Journal of Physics A **36**(29), 7889 (2003), doi: 10.1088/0305-4470/36/29/302.

[96] T. Fischer, S. Duffe and G. S. Uhrig, *Adapted continuous unitary transformation to treat systems with quasi-particles of finite lifetime*, New Journal of Physics **12**(3), 033048 (2010), doi: 10.1088/1367-2630/12/3/033048.

[97] S. Duffe and G. S. Uhrig, *Hole dispersions for antiferromagnetic spin-1/2 two-leg ladders by self-similar continuous unitary transformations*, European Physical Journal B **84**(3), 475 (2011), doi: 10.1140/epjb/e2011-20150-x.

[98] J. E. Moussa, *Approximate diagonalization method for many-fermion Hamiltonians*, eprint arXiv, Supplementary to APS March Meeting 2010 talk (2010), `arxiv.org/abs/1003.2596`.

[99] D. G. Pettifor and D. L. Weaire, *The Recursion Method and Its Applications: Proceedings of the Conference, Imperial College, London, England September 13–14, 1984*, vol. 58 of *Springer Series in Solid-State Sciences*, Springer-Verlag, Berlin Heidelberg, doi: 10.1007/978-3-642-82444-9 (1985).

[100] E. Dagotto and T. M. Rice, *Surprises on the Way from One- to Two-Dimensional Quantum Magnets: The Ladder Materials*, Science **271**(5249), 618 (1996), doi: 10.1126/science.271.5249.618.

[101] E. Dagotto, *Experiments on ladders reveal a complex interplay between a spin-gapped normal state and superconductivity*, Reports on Progress in Physics **62**(11), 1525 (1999), doi: 10.1088/0034-4885/62/11/202.

[102] C. P. Landee, M. M. Turnbull, C. Galeriu, J. Giantsidis and F. M. Woodward, *Magnetic properties of a molecular-based spin-ladder system: $(5IAP)_2CuBr_4{\cdot}2H_2O$*, Phys. Rev. B **63**(10), 100402(R) (2001), doi: 10.1103/PhysRevB.63.100402.

[103] M. T. Batchelor, X.-W. Guan and N. Oelkers, *Theoretical Analysis of the Double Spin Chain Compound $KCuCl_3$*, Differential geometry and physics. Proceedings, 23rd International Conference, Tianjin, China pp. 133–141 (2005), doi: 10.1142/9789812772527_0007.

[104] T. Nakamura and K. Okamoto, *Theoretical analysis of the experiments on the double-spin-chain compound – $KCuCl_3$*, Phys. Rev. B **58**(5), 2411 (1998), doi: 10.1103/PhysRevB.58.2411.

[105] C. A. Hayward, D. Poilblanc and L. P. Lévy, *The Magnetization of $Cu_2(C_5H_{12}N_2)_2Cl_4$: A Heisenberg Spin Ladder System*, Phys. Rev. B **54**(18), R12649(R) (1996), doi: 10.1103/PhysRevB.54.R12649.

[106] B. C. Watson, V. N. Kotov, M. W. Meisel, D. W. Hall, G. E. Granroth, W. T. Montfrooij, S. E. Nagler, D. A. Jensen, R. Backov, M. A. Petruska, G. E. Fanucci and D. R. Talham, *Magnetic Spin Ladder $(C_5H_{12}N)_2CuBr_4$: High-Field Magnetization and Scaling near Quantum Criticality*, Phys. Rev. Lett. **86**(22), 5168 (2001), doi: 10.1103/PhysRevLett.86.5168.

[107] M. Matsuda, K. Katsumata, R. S. Eccleston, S. Brehmer and H.-J. Mikeska, *Magnetic excitations and exchange interactions in the spin-$\frac{1}{2}$ two-leg ladder compound $La_6Ca_8Cu_{24}O_{41}$*, Phys. Rev. B **62**(13), 8903 (2000), doi: 10.1103/PhysRevB.62.8903.

[108] M. Windt, M. Grüninger, T. Nunner, C. Knetter, K. P. Schmidt, G. S. Uhrig, T. Kopp, A. Freimuth, U. Ammerahl, B. Büchner and A. Revcolevschi, *Observation of Two-Magnon Bound States in the Two-Leg Ladders of $(Ca, La)_{14}Cu_{24}O_{41}$*, Phys. Rev. Lett. **87**(12), 127002 (2001), doi: 10.1103/PhysRevLett.87.127002.

[109] S. Notbohm, P. Ribeiro, B. Lake, D. A. Tennant, K. P. Schmidt, G. S. Uhrig, C. Hess, R. Klingeler, G. Behr, B. Büchner, M. Reehuis, R. I. Bewley *et al.*, *One- and Two-Triplon Spectra of a Cuprate Ladder*, Phys. Rev. Lett. **98**(2), 027403 (2007), doi: 10.1103/PhysRevLett.98.027403.

[110] V. Bisogni, K. Wohlfeld, S. Nishimoto, C. Monney, J. Trinckauf, K. Zhou, R. Kraus, K. Koepernik, C. Sekar, V. Strocov, B. Büchner, T. Schmitt *et al.*, *Orbital Control of Effective Dimensionality: From Spin-Orbital Fractionalization to Confinement in the Anisotropic Ladder System $CaCu_2O_3$*, Phys. Rev. Lett. **114**(9), 096402 (2015), doi: 10.1103/PhysRevLett.114.096402.

[111] C. Knetter, K. P. Schmidt, M. Grüninger and G. S. Uhrig, *Fractional and Integer Excitations in Quantum Antiferromagnetic Spin* 1/2 *Ladders*, Phys. Rev. Lett. **87**(16), 167204 (2001), doi: 10.1103/PhysRevLett.87.167204.

[112] S. Sachdev and R. N. Bhatt, *Bond-operator representation of quantum spins: Mean-field theory of frustrated quantum Heisenberg antiferromagnets*, Phys. Rev. B **41**(13), 9323 (1990), doi: 10.1103/PhysRevB.41.9323.

[113] A. V. Chubukov, *A difference in the properties of one-dimensional antiferromagnets with integer and half-integer spins*, Soviet Phys. JETP Letters **49**(2), 108 (1989), [ZhÉTF **49**(2), 108 (1989)], `jetpletters.ru/ps/1113/article_16848.shtml`.

[114] C. Knetter and G. S. Uhrig, *Dynamic structure factor of the two-dimensional shastry-sutherland model*, Phys. Rev. Lett. **92**, 027204 (2004), doi: 10.1103/PhysRevLett.92.027204.

[115] P. A. McClarty, F. Krüger, T. Guidi, S. F. Parker, K. Refson, A. W. Parker, D. Prabhakaran and R. Coldea, *Topological triplon modes and bound states in a Shastry–Sutherland magnet*, Nature Physics **13**(8), 736 (2017), doi: 10.1038/nphys4117.

[116] D. G. Shelton, A. A. Nersesyan and A. M. Tsvelik, *Antiferromagnetic spin ladders: Crossover between spin s=1/2 and s=1 chains*, Phys. Rev. B **53**, 8521 (1996), doi: 10.1103/PhysRevB.53.8521.

[117] T. Barnes, E. Dagotto, J. Riera and E. S. Swanson, *Excitation spectrum of Heisenberg spin ladders*, Phys. Rev. B **47**(6), 3196 (1993), doi: 10.1103/PhysRevB.47.3196.

[118] S. Trebst, H. Monien, C. J. Hamer, Z. Weihong and R. R. P. Singh, *Strong-Coupling Expansions for Multiparticle Excitations: Continuum and Bound States*, Phys. Rev. Lett. **85**(20), 4373 (2000), doi: 10.1103/PhysRevLett.85.4373.

[119] K. P. Schmidt and G. S. Uhrig, *Spectral Properties of Magnetic Excitations in Cuprate Two-Leg Ladder Systems*, Mod. Phys. Lett. B **19**(24), 1179 (2005), doi: 10.1142/S0217984905009237.

[120] A. Honecker, F. Mila and B. Normand, *Multi-triplet bound states and finite-temperature dynamics in highly frustrated quantum spin ladders*, Phys. Rev. B **94**(9), 094402 (2016), doi: 10.1103/PhysRevB.94.094402.

[121] Z. Wang, J. Wu, W. Yang, A. K. Bera, D. Kamenskyi, A. T. M. N. Islam, S. Xu, J. M. Law, B. Lake, C. Wu and A. Loidl, *Experimental observation of Bethe strings*, Nature **554**(7691), 219 (2018), doi: 10.1038/nature25466.

[122] Z. Wang, M. Schmidt, A. Loidl, J. Wu, H. Zou, W. Yang, C. Dong, Y. Kohama, K. Kindo, D. I. Gorbunov, S. Niesen, O. Breunig *et al.*, *Quantum Critical Dynamics of a Heisenberg-Ising Chain in a Longitudinal Field: Many-Body Strings versus Fractional Excitations*, Phys. Rev. Lett. **123**(6), 067202 (2019), doi: 10.1103/PhysRevLett.123.067202.

[123] C. Lacroix, P. Mendels and F. Mila, *Introduction to Frustrated Magnetism*, vol. 164 of *Springer Series in Solid-State Sciences*, Springer-Verlag, Berlin Heidelberg, doi: 10.1007/978-3-642-10589-0 (2011).

[124] G. L. Squires, *Introduction to the Theory of Thermal Neutron Scattering*, Cambridge University Press, 3th edn., doi: 10.1017/CBO9781139107808 (2012).

[125] L. V. Hove, *Correlations in Space and Time and Born Approximation Scattering in Systems of Interacting Particles*, Phys. Rev. **95**(1), 249 (1954), doi: 10.1103/PhysRev.95.249.

[126] W. L. Bragg, *The Specular Reflection of X-rays*, Nature **90**(2250), 410 (1912), doi: 10.1038/090410b0.

[127] M. van Veenendaal, *Polarization Dependence of L- and M-edge Resonant Inelastic X-Ray Scattering in Transition-Metal Compounds* , Phys. Rev. Lett. **96**(11), 117404 (2006), doi: 10.1103/PhysRevLett.96.117404.

[128] D. S. Ellis, J. Kim, J. P. Hill, S. Wakimoto, R. J. Birgeneau, Y. Shvyd'ko, D. Casa, T. Gog, K. Ishii, K. Ikeuchi, A. Paramekanti, *et al.*, *Magnetic nature of the 500 meV peak in $La_{1-x}Sr_xCuO_4$ observed with resonant inelastic x-ray scattering at the Cu K-edge*, Phys. Rev. B **81**(8), 085124 (2010), doi: 10.1103/PhysRevB.81.085124.

[129] V. Bisogni, S. Kourtis, C. Monney, K. Zhou, R. Kraus, C. Sekar, V. Strocov, B. Büchner, J. van den Brink, L. Braicovich, T. Schmitt, M. Daghofer *et al.*, *Femtosecond Dynamics of Momentum-Dependent Magnetic Excitations from Resonant Inelastic X-Ray Scattering in $CaCu_2O_3$*, Phys. Rev. Lett. **112**(14), 147401 (2014), doi: 10.1103/PhysRevLett.112.147401.

[130] R. Fumagalli, L. Braicovich, M. Minola, Y. Y. Peng, K. Kummer, D. Betto, M. Rossi, E. Lefrançois, C. Morawe, M. Salluzzo, H. Suzuki, F. Yakhou *et al.*, *Polarization-resolved Cu L_3-edge resonant inelastic x-ray scattering of orbital and spin excitations in $NdBa_2Cu_3O_{7-\delta}$*, Phys. Rev. B **99**(13), 134517 (2019), doi: 10.1103/PhysRevB.99.134517.

[131] M. C. Beard, G. M. Turner and C. A. Schmuttenmaer, *Terahertz Spectroscopy*, J. Phys. Chem. B **106**(29), 7146 (2002), doi: 10.1021/jp020579i.

[132] D. Betto, R. Fumagalli, L. Martinelli, M. Rossi, R. Piombo, K. Yoshimi, D. Di Castro, E. Di Gennaro, A. Sambri, D. Bonn, G. A. Sawatzky, L. Braicovich *et al.*, *Multiple-magnon excitations shape the spin spectrum of cuprate parent compounds*, Phys. Rev. B **103**, L140409 (2021), doi: 10.1103/PhysRevB.103.L140409.

[133] G. Cazzoli and C. Puzzarini, *Sub-Doppler Resolution in the THz Frequency Domain: 1 kHz Accuracy at 1 THz by Exploiting the Lamb-Dip Technique*, The Journal of Physical Chemistry A **117**(50), 13759 (2013), doi: 10.1021/jp407980f, PMID: 24053662, `https://doi.org/10.1021/jp407980f`.

[134] H.-W. Hübers, H. Richter and M. Wienold, *High-resolution terahertz spectroscopy with quantum-cascade lasers*, Journal of Applied Physics **125**(15),

151401 (2019), doi: 10.1063/1.5084105, https://doi.org/10.1063/1.5084105.

[135] D. Chandler, *Introduction to Modern Statistical Mechanics*, Oxford University Press, doi: 10.1063/1.2811680 (1987).

[136] *Eigen library*, eigen.tuxfamily.org.

[137] *OpenMP*, openmp.org.

[138] V. S. Viswanath and G. Müller, *The Recursion Method: Application to Many-Body Dynamics*, vol. 23 of *Lecture Notes in Physics Monographs*, Springer-Verlag, Berlin Heidelberg, doi: 10.1007/978-3-540-48651-0 (1994).

[139] A. P. Higginbotham, S. M. Albrecht, G. Kiršanskas, W. Chang, F. Kuemmeth, P. Krogstrup, T. S. Jespersen, J. Nygård, K. Flensberg and C. M. Marcus, *Parity lifetime of bound states in a proximitized semiconductor nanowire*, Nature Physics **11**(12), 1017 (2015), doi: 10.1038/nphys3461.

[140] S. Weimann, M. Kremer, Y. Plotnik, Y. Lumer, S. Nolte, K. G. Makris, M. Segev, M. C. Rechtsman and A. Szameit, *Topologically protected bound states in photonic parity–time-symmetric crystals*, Nature Materials **16**(4), 433 (2017), doi: 10.1038/nmat4811.

[141] R. J. Fletcher, R. Lopes, J. Man, N. Navon, R. P. Smith, M. W. Zwierlein and Z. Hadzibabic, *Two- and three-body contacts in the unitary Bose gas*, Science **355**(6323), 377 (2017), doi: 10.1126/science.aai8195.

[142] W. Heisenberg, *Zur Theorie des Ferromagnetismus*, Zeitschrift für Physik **49**, 619 (1928), doi: 10.1007/BF01328601.

[143] W. Nolting, *Grundkurs Theoretische Physik 7: Viel-Teilchen-Theorie*, Springer-Lehrbuch. Springer Spektrum, Berlin Heidelberg, 8th edn., doi: 10.1007/978-3-642-25808-4 (2015).

[144] R. B. Stinchcombe, *Ising model in a transverse field*, Journal of Physics C **6**(15), 2549 (1973), doi: 10.1088/0022-3719/6/15/009.

[145] S. Suzuki, J. Inoue and B. K. Chakrabarti, *Quantum Ising Phases and Transitions in Transverse Ising Models*, vol. 862 of *Lecture Notes in Physics*, Springer-Verlag, Berlin Heidelberg, doi: 10.1007/978-3-642-33039-1 (2013).

[146] P. Pfeuty, *The one-dimensional Ising model with a transverse field*, Ann. of Phys. **57**(1), 79 (1970), doi: 10.1016/0003-4916(70)90270-8.

[147] T. Matsubara and H. Matsuda, *A Lattice Model of Liquid Helium*, Progress of Theoretical Physics **16**(6), 569 (1956), doi: 10.1143/PTP.16.569.

[148] G. Ferkinghoff, *Kontinuierliche unitäre Transformationen für Hardcore-Bosonen im Ising-Modell im transversalen Feld*, Master's thesis, TU Dortmund (2017), `https://cmt.physik.tu-dortmund.de/storages/cmt-physik/r/uhrig/master/master-gary-ferkinghoff.pdf`.

[149] *Boost library*, `boost.org`.

[150] J. R. Schrieffer and P. A. Wolff, *Relation between the Anderson and Kondo Hamiltonians*, Phys. Rev. **149**(2), 491 (1966), doi: 10.1103/PhysRev.149.491.

[151] G. Ferkinghoff and G. S. Uhrig, *Efficient flow equations for dissipative systems*, preprint arXiv (submitted to SciPost Physics) (2022), doi: 10.48550/arXiv.2203.15532.

[152] D. Manzano, *A short introduction to the Lindblad master equation*, AIP Advances **10**(2), 025106 (2020), doi: 10.1063/1.5115323.

[153] S. R. White, *Numerical canonical transformation approach to quantum many-body problems*, The Journal of Chemical Physics **117**(16), 7472 (2002), doi: 10.1063/1.1508370.

[154] A. A. Dzhioev and D. S. Kosov, *Super-fermion representation of quantum kinetic equations for the electron transport problem*, The Journal of Chemical Physics **134**(4), 044121 (2011), doi: 10.1063/1.3548065.

[155] E. Arrigoni and A. Dorda, *Out-of-Equilibrium Physics of Correlated Electron Systems, Chap. Master equation versus Keldysh Green's functions for correlated quantum systems out of equilibrium*, vol. 191 of *Springer Series in Solid-State Sciences*, ISBN 9783319949550 (2018).

[156] M. Schmutz, *Real-Time Green's Functions in Many Body Problems*, Zeitschrift für Physik B **30**(1), 97 (1978), doi: 10.1007/BF01323673.

[157] K. Wang, F. Piazza and D. J. Luitz, *Hierarchy of Relaxation Timescales in Local Random Liouvillians*, Phys. Rev. Lett. **124**(10), 100604 (2020), doi: 10.1103/PhysRevLett.124.100604.

[158] S. Denisov, T. Laptyeva, W. Tarnowski, D. Chruściński and K. Życzkowski, *Universal Spectra of Random Lindblad Operators*, Phys. Rev. Lett. **123**(14), 140403 (2019), doi: 10.1103/PhysRevLett.123.140403.

[159] V. Gorini, A. Kossakowski and E. C. G. Sudarshan, *Completely positive dynamical semigroups of N-level systems*, J. Math. Phys. **17**(5), 821 (1976), doi: 10.1063/1.522979.

[160] G. Lindblad, *On the generators of quantum dynamical semigroups*, Commun. Math. Phys. **48**, 119 (1976), doi: 10.1007/BF01608499.

[161] R. Alicki and K. Lendi, *Quantum Dynamical Semigroups and Applications*, vol. 717 of *Lecture Notes in Physics*, Springer-Verlag, Berlin Heidelberg, ISBN 9783540708612 (2007).

[162] H. A. Kramers and W. Heisenberg, *Über die Streuung von Strahlung durch Atome*, Zeitschrift für Physik **31**, 681 (1925), doi: 10.1007/BF02980624.

[163] S. Andrilli and D. Hecker, *Chapter 9 - Numerical Techniques*, In *Elementary Linear Algebra*, pp. 607–666. Academic Press, Boston, 5th edn., ISBN 978-0-12-800853-9, doi: https://doi.org/10.1016/B978-0-12-800853-9.00009-8 (2016).

[164] P. Jordan and E. Wigner, *Über das Paulische Äquivalenzverbot*, Zeitschrift für Phys. **47**(9-10), 631 (1928), doi: 10.1007/BF01331938.

[165] N. N. Bogoliubov, *On the Theory of Superfluidity*, Journal of Physics **11**(1), 23 (1947), `https://www.ufn.ru/pdf/jphysussr/1947/11_1/3jphysussr19471101.pdf`.

Acronyms

CUT continuous unitary transformation, also known as flow equation method, see Sec. 2
2, 3, 5, 8–11, 19, 23, 25, 30, 76–78, 80, 81, 83, 84, 88–90, 92, 93, 96–98, 101, 143, 144, 150

deepCUT directly evaluated enhanced perturbative continuous unitary transformation, a scheme to efficiently expand and truncate the flow equations, see Sec. 2.4.3
11, 26, 30, 43, 44, 46, 47, 52, 53, 62, 63, 72–76, 92, 93, 108, 142, 143, 145, 150, 154–156, 165, 166, 169, 170

DESF dynamic (spin) exchange structure factor, leading nontrivial order in the SC channel of RIXS, see (3.2.12)
41–44, 59–61, 64–66, 167

DSF dynamic (spin) structure factor, dynamic response for INS leading order in the NSC channel of RIXS, see (3.2.10)
38, 39, 41, 43, 55–57, 166

gpc generalized particle-conserving, see Sec. 5.4 for the definition of the gpc-generator
107–111, 113, 115–117, 119, 123, 125, 126, 128–136, 139–142, 144, 145, 180, 182, 183, 185–188

INS inelastic neutron scattering, see Sec. 3.2.2
3, 4, 35, 37–39, 41, 42, 54, 57, 66, 75, 143

ipc imaginary particle-conserving, see Sec. 5.3.1 for the definition of the pc-generator
106, 107, 128, 141, 180–182, 184, 185

NSC non-spin-conserving, used here to refer to a probing channel where spin $S = 1$ is transferred, as opposed to the spin-conserving channel
4, 36, 39, 41, 42, 54–60, 66–69, 72, 75, 143, 148, 149, 154, 157, 158, 161, 162, 165, 166, 189

pc particle-conserving, see Sec. 2.3.1 for the definition of the pc-generator
vi, 7, 8, 14, 15, 17–22, 77, 90, 92, 97, 102, 104–110, 128, 141, 142, 144, 145, 180–182, 184–186, 188

ps particle-sorting, see Sec. 2.3.2 for the definition of the ps-generator
vi, 20, 21, 44, 108

RIXS resonant inelastic X-ray scattering, see Sec. 3.2.3
4, 8, 39–43, 54, 57, 65–67, 69, 71, 75, 76, 143–146, 154, 165, 170, 189

ROD residual-off-diagonality, see Sec. 2.6
8, 29, 93, 96, 97, 119–123, 125, 126, 128, 130–135, 139, 140, 181–185

SC spin-conserving, used here to refer to a probing channel where no spin is transferred ($S = 0$), as opposed to the non-spin-conserving channel
4, 36, 39, 41–43, 54, 57–62, 64–66, 69–75, 143, 148, 154, 159, 160, 163–167, 169, 189

TFIM transverse-field Ising model, see Sec. 4.1
viii, 78, 79, 81–85, 87–90, 92–96, 98, 101, 144, 171, 172, 174

UCL ultra-short core-hole lifetime expansion, see App. A
4, 5, 41, 42, 66, 69, 75, 76, 143, 144, 146, 154–156, 165

List of Publications

G. Ferkinghoff, L. Müller, G. S. Uhrig, U. Kumar, and B. Fauseweh. Accessing Multi-triplons in Spin Ladders using Resonant Inelastic X-ray Scattering. *preprint arXiv (submitted to Comm. Phys.)*, 2020. doi: 10.48550/arXiv.2012.01513.

G. Ferkinghoff and G. S. Uhrig. Efficient flow equations for dissipative systems. *preprint arXiv (submitted to SciPost Physics)*, 2022. doi: 10.48550/arXiv.2203.15532.

Danksagung

Eine Dissertationsschrift entsteht niemals gänzlich allein, denn der Prozess wird stets von diversen Personen sowohl fachlich als auch persönlich unterstützt. An dieser Stelle möchte ich meinen Dank all jenen Menschen zukommen lassen, die mich in den letzten Jahren während der Erstellung dieser Arbeit unterstützt haben.

Meinem Doktorvater Prof. Götz S. Uhrig danke ich herzlich für die Vergabe des Forschungsthemas, für seine vielen hilfreichen Ideen und Hinweise, dafür, dass er als Betreuer stets geduldig und gut erreichbar war, und für die regelmäßige gute Zusammenarbeit in der Lehre. Herrn Prof. Dr. Frithjof Anders danke ich für die Übernahme des Zweitgutachtens.

Für das Korrekturlesen von Teilen dieser Arbeit danke ich Simon Ahlmann, Carolin Lüders, Katrin Bolsmann und Timo Gräßer, deren Hinweise äußerst hilfreich waren.

Ich danke Dr. Benedikt Fauseweh, Dr. Leanna Müller und Dr. Umesh Kumar für die exzellente Zusammenarbeit an unseren gemeinsamen Projekten.

Ich danke Leanna für die intensiven Gespräche während unserer gemeinsamen Doktorandenzeit. Besonders danke ich auch meinen Kommilitonen Simon and Caro für die gegenseitige Unterstützung während unserer Doktorandenzeit und darüber hinaus. Bei meinen Bürokollegen und der gesamten Arbeitsgruppe bedanke ich mich für die spannenden fachlichen und überfachlichen Diskussionen.

Während eines mehrjährigen Promotionsstudiums trifft man auf zahlreiche Menschen, mit denen man sich persönlich und professionell austauscht und zusammenarbeitet. Nicht alle davon finden hier namentlich Erwähnung, doch auch euch möchte ich dafür danken, dass ihr meine Zeit bereichert habt. Ausdrücklich möchte ich all jenen danken, mit denen ich in den vergangenen Jahren in der Lehre zusammengearbeitet habe.

Nicht zuletzt danke ich meiner Frau Mara und meiner ganzen Familie, die stets für mich da waren. Danke, dass ich mich auf euch verlassen kann.